



TECHNISCHE
UNIVERSITÄT
WIEN
Vienna | Austria

DISSERTATION

Experimental investigation of weak values in massive quantum systems

ausgeführt zum Zwecke der Erlangung des akademischen Grades eines Doktors
der technischen Wissenschaften unter der Leitung von

Associate Prof. Dipl.-Ing. Dr. Yuji Hasegawa
E141 - Atominstitut

eingereicht an der Technischen Universität Wien
Fakultät für Physik

von

DI Tobias Denkmayr

0726050

Habichergasse 19/28

1160 Wien

Wien, am 6. September 2016

Abstract

To investigate quantum ensembles between pre- and postselection the so-called weak value formalism was introduced by Aharonov, Albert, and Vaidman. Originally they constructed it in a non-relativistic quantum framework and hence it should be first and foremost applicable to massive quantum systems. However, due to the small coherence volume of massive particle beams, an experimental determination of a simple massive-particle system's weak value turned out to be difficult. Here, measurement protocols are presented which can be used to determine weak values of two-level quantum systems with arbitrary interaction strengths. It is implemented in several neutron optical experiments; the first successful determination of a massive particle's weak value is performed. In particular weak values of Pauli operators of the neutron's spin and path degree of freedom, as well as those of projection operators of the path degree of freedom are determined experimentally. The newly established experimental method is used to investigate quantum mechanics at a fundamental level: Neutron ensembles with a purely imaginary spin weak value are created to test the so called quantum pigeon hole principle. The path weak values are used to perform a so-called "direct" state tomography. Finally weak measurements are used to experimentally investigate the quantum Cheshire cat phenomenon. Neutron interferometry has been established as a powerful experimental method to investigate the foundations of quantum mechanics. In combination with the novel weak value measurement schemes presented in this thesis, it offers an experimental window into previously inaccessible parts of massive quantum systems. We expect applications in future experiments studying quantum dynamics.

Zusammenfassung

Um Quantensysteme im Zeitraum zwischen ihrer Präparation (preselection) und einer projektiven Messung (postselection) zu untersuchen, entwickelten Aharonov, Albert und Vaidman den sogenannten “Weak Value Formalismus”. Dieser wurde ursprünglich in einem nicht relativistischen Kontext eingeführt und sollte deshalb für massebehaftete Quantensysteme verwendet werden. Da das Kohärenzvolumen von Strahlen, welche aus massiven Teilchen bestehen, jedoch sehr klein ist, stellte sich die Messung eines Weak Values in einem massebehafteten Quantensystem als äußerst schwierig heraus. In dieser Dissertation werden Messprotokolle präsentiert, welche dazu verwendet werden können Weak Values von Zweizustandssystemen mittels beliebigen Mess stärken zu bestimmen. Diese werden folglich in neutronenoptischen Experimenten zur Anwendung gebracht, wodurch die erste erfolgreiche Messung eines Weak Values eines massiven Teilchens gelingt. Insbesondere werden Weak Values von Pauli Spin und Pfad Operatoren, sowie die von Pfad-Projektionsoperatoren gemessen. Die neue experimentelle Methode erlaubt es die Grundlagen der Quantenmechanik zu untersuchen: Neutronen Ensembles mit rein imaginären Spin Weak Values werden erzeugt um das “Quanten Taubenschlagprinzip” zu testen. Die Weak Values der Pfad Operatoren werden dazu verwendet um eine sogenannte direkte Quantenzustandstomographie durchzuführen. Außerdem wird das Phänomen der “Quantengrinsekatz” experimentell untersucht. Neutroneninterferometrie gilt als ein nützliches Werkzeug zur Untersuchung der Grundlagen der Quantenmechanik. Gemeinsam mit der neuen experimentellen Technik, welche in dieser Dissertation erarbeitet wird, werden neue Wege zur Analyse von massebehafteten Quantensystemen eröffnet. Wir erwarten eine Anwendung in zukünftigen Experimenten, welche die Dynamik von Quantensystemen studieren.

Acknowledgements

First of all I want to thank my parents Manfred and Helga Denkmayr for their support throughout the time of my studies. They made it possible for me to pursue a degree and gave me their full support from the very first moment.

Particular thanks go to my colleagues Stephan Sponar and Hermann Geppert. They shared their vast experience in theory and experiment with me, which came in handy more than once. They not only supported me during the experiments, but they made the time of my PhD studies so much more worthwhile.

I want to thank the Institute Laue-Langevin for its hospitality and continuous support. In particular I want to express my gratitude to Hartmut Lemmel, who helped me gain a deeper understanding of the workings of the neutron interferometer.

I also want to express my gratitude towards my supervisor Yuji Hasegawa. He guided me very well throughout the work on this thesis and continuously challenged me so that I could spread my full potential.

I want to thank my son Samuel to be quick in understanding the difference between night and day, which gave me the necessary rest to complete my studies in time.

The last words of acknowledgement are to Anna: Thank you for being there for me and supporting me no matter what!

Contents

1	Introduction	1
1.1	Neutron interferometry	1
1.1.1	Perfect crystal neutron interferometer	3
1.2	Experimental investigation of quantum mechanics using neutron in- terferometry	5
1.3	Weak measurements and weak values	9
1.3.1	Weak measurements of photonic systems	12
1.3.1.1	Weak value amplification	13
1.3.1.2	The weak value as a measurable complex value	14
1.3.1.3	The weak value as a conditioned average and quan- tum paradoxes	15
1.3.2	Weak values in massive quantum systems	17
2	Neutron optical setup and components	18
2.1	Neutron sources and detectors	18
2.1.1	Neutron sources	18
2.1.2	Counter tubes	19
2.2	Neutron interferometer and associated components	21
2.2.1	The neutron's path degree of freedom	23
2.2.2	The neutron's path degree of freedom as a two-level quantum system	25
2.2.3	Phase shifters	27
2.2.4	Absorbers	28
2.3	Neutron polarimeter and associated components	29

2.3.1	The neutron's spin degree of freedom as a two-level quantum system	30
2.3.2	Polarizing supermirrors	30
2.3.3	DC coils as spin rotators	33
2.3.4	Helmholtz coils producing homogenous magnetic Fields	33
3	Weak values of two-level quantum systems	36
3.1	Weak values of Pauli operators	36
3.1.1	Weak interactions	37
3.1.2	Expected intensities for ideal situations	42
3.1.3	Interactions with arbitrary strengths	44
3.2	Weak values of projection operators	51
3.2.1	Weak interaction	51
3.2.2	Strong interactions	52
3.3	Summary	55
4	Spin weak values	56
4.1	Background and motivation of the experiment	56
4.2	Experimental realizations of spin weak measurements	59
4.2.1	Interferometer experiment	59
4.2.1.1	Adjustment	61
4.2.1.2	Optimizing the measurement strength	77
4.2.1.3	Data acquisition	79
4.2.1.4	Background and contrast corrections	89
4.2.1.5	Results	93
4.2.2	Polarimeter experiment	98
4.2.2.1	Adjustment	98
4.2.2.2	Optimizing the measurement strength	101
4.2.2.3	Data acquisition	103
4.2.2.4	Results	104
4.2.3	Measurement of $\text{Im} [\langle \hat{\sigma}_z^s \rangle_w]$ using the interferometric setup . .	107
4.3	The quantum pigeon hole effect	109
4.3.1	Experimental realization	112
4.3.2	The quantum pigeon hole effect and contextuality	115
4.4	Summary and perspective	117

5	Path weak values	119
5.1	Underlying experimental idea	120
5.2	Experimental realization	122
5.2.1	Adjustment	123
5.2.2	Measurement of Pauli operators	127
5.2.2.1	Data	128
5.2.2.2	Results	132
5.2.3	Measurement of projection operators	135
5.2.3.1	Data	135
5.2.3.2	Results	138
5.2.4	Summary and conclusion	139
5.3	“Direct” state characterization	140
5.3.1	Characterizing the preselected path state via weak values . . .	140
5.3.2	Results	143
5.4	Summary and perspective	146
6	The quantum Cheshire cat effect	147
6.1	Theory	147
6.2	Experiment	150
6.2.1	Probing the location of the neutrons	151
6.2.2	Probing the location of the neutrons’ spin component	153
6.2.3	Quantifying the results	156
6.2.4	Discussion	159
6.3	Summary and perspective	160
7	Conclusion and outlook	162
	Bibliography	164
	Curriculum Vitae	176

CHAPTER 1

Introduction

Here we introduce the topics of neutron interferometry and weak measurements. The most important points of both subjects are discussed. It is shown how neutron interferometry is used to demonstrate purely quantum mechanical effects and how weak measurements and weak values appear in quantum mechanics.

1.1 Neutron interferometry

In introductory quantum mechanical courses, it is often taught that the phase of a wave function Ψ is not accessible. In general this is not correct. While an absolute phase is indeed inaccessible, relative phases between two wave functions Ψ_1 and Ψ_2 can be detected. The most suitable apparatus to investigate such relative phases are interferometers. If one is interested in the behavior of matter waves, neutron interferometers are ideal experimental tools. Neutron interferometry has many similarities to classical interferometry, e.g. using silicon perfect crystals Mach-Zehnder type interferometers can be constructed for neutrons [Rauch et al., 1974]. A schematic view of such an interferometer is depicted in Fig. 1.1.

In a Mach-Zehnder type interferometer, a monochromatic beam hits a 50:50 beam splitter and the beam is divided coherently by amplitude division. The beams get reflected towards a final 50:50 beam splitter, i.e. the analyzer, where they recombine to interfere. The interferometer has two exits, one in forward and one in reflected direction. The intensity gets divided into two exits, depending on the relative phase between the beams in two paths. The phase difference can be tuned

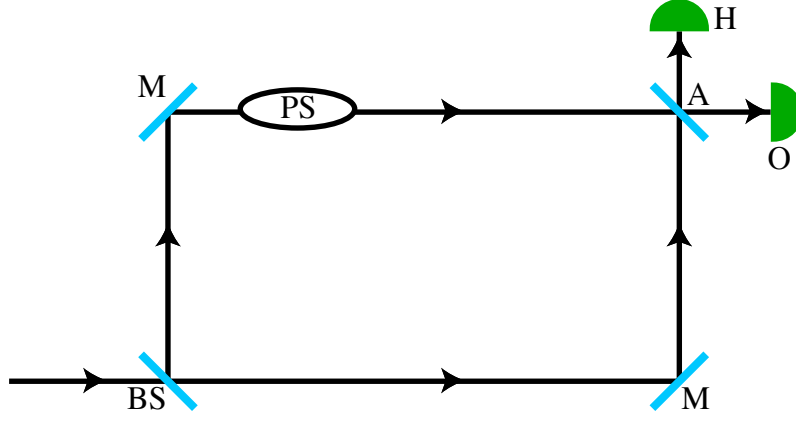


Figure 1.1: Schematic drawing of a Mach-Zehnder type interferometer: The interferometer consists of a beamsplitter (BS) that divides the incoming beam by amplitude division. The sub beams are reflected by the two mirrors (M) and recombined at the analyzer (A). The interferometer has two exits, one in forward and one in reflected direction. The phase shifter (PS) makes it possible to introduce a relative phase between the two beam paths.

by a difference in the optical path lengths, by introducing material with a different refraction index in one of the beams.

We now give a short general quantum mechanical introduction to Mach-Zehnder type interferometers. Subsequently the so called triple Laue (LLL) perfect crystal neutron interferometer's function is explained.

A wave function of the incident beam of the interferometer is given by

$$|\Psi_i\rangle = A_i e^{i\Phi}, \quad (1.1)$$

which describes a plane wave with amplitude A_i and phase ϕ . The wave function of the recombined beam after the interferometer's final plate is then

$$|\Psi_f\rangle = |\Psi_I\rangle \pm |\Psi_{II}\rangle \quad (1.2)$$

with $|\Psi_I\rangle$ and $|\Psi_{II}\rangle$ being the contributions from path I and II . The plus sign is valid for the forward direction and the minus sign for the reflected one. $|\Psi_I\rangle$ and $|\Psi_{II}\rangle$ are of the form

$$|\Psi_I\rangle = A_I e^{i\Phi_I}, \quad (1.3a)$$

$$|\Psi_{II}\rangle = A_{II} e^{i\Phi_{II}}. \quad (1.3b)$$

For simplicity's sake we assume that the amplitudes are of the form

$$A_I = A_{II} = \frac{1}{2}A_i. \quad (1.4)$$

The intensity exiting the interferometer is then

$$I_{\pm} = |\langle \Psi_f | \Psi_f \rangle|^2 = \frac{I_i}{2} [1 \pm \cos(\chi)], \quad (1.5)$$

where I_i is the incident intensity. The relative phase χ between the two beam paths is defined as $\chi = \Phi_{II} - \Phi_I$. Due to the conservation of particles, the intensities of the two exiting beams must sum to unity, i.e. $I_+ + I_- = 1$. One can now define the fringe contrast C as

$$C = \frac{I_{\max} - I_{\min}}{I_{\max} + I_{\min}}. \quad (1.6)$$

The contrast of an ideal interferometer is 1 (or 100%). The most general form for the intensity oscillation can then be expressed as

$$I = \bar{I} [1 + C \cos(\chi + \omega)] \quad (1.7)$$

with the average intensity \bar{I} and the interferometer's intrinsic phase ω [Sears, 1989a].

1.1.1 Perfect crystal neutron interferometer

As its name already suggest, a perfect crystal neutron interferometer is cut from a silicon perfect crystal rod and has a monolithic structure. One typical neutron interferometer design, called triple Laue, is depicted in Fig. 1.2. The design shows a top view of a symmetric neutron interferometer with three plates, which are parallel and equally separated. The interferometer is cut in a way that the crystal's net planes (220) are perpendicular to the plate's surfaces. Since the interferometer is cut from a single crystal, the parallel alignment of the Bragg planes in the three plates is guaranteed perfectly. The cutting of the crystal has to be performed with high precision. To ensure a good performance of the neutron interferometer, the thickness of all three plates has to be the same within an accuracy of 1 μm . Also the distance between the first and the second as well as the second and the third plate has to be equal within the same tolerance. Figure 1.3 shows a photograph of the so called Kaiser interferometer, which has the triple Laue configuration.

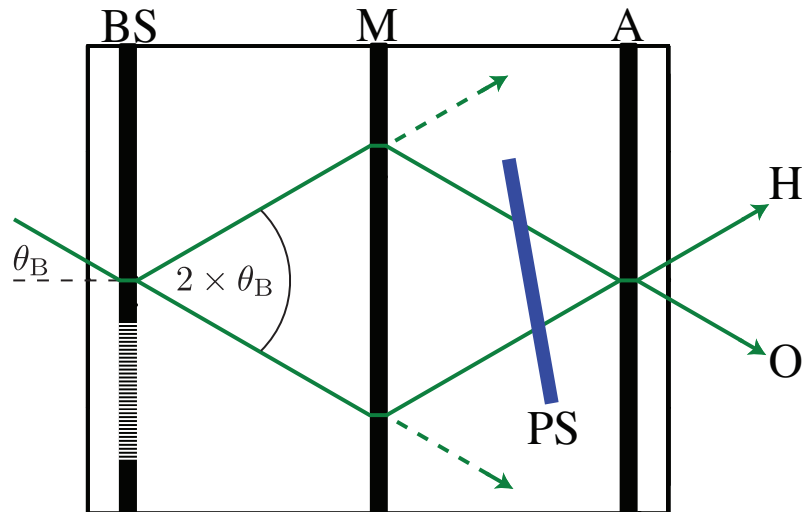


Figure 1.2: Schematic drawing of a neutron interferometer in triple Laue configuration: The beam hits the neutron interferometer under the angle θ_B then it is split coherently by amplitude division upon the first beam splitter plate (BS). In the Laue configuration the silicon's crystal planes are perpendicular to the surface of the plane, as is depicted by the white stripes of the first plate. All three plates are 50:50 beam splitters. Because of that two sub beams leave the middle plate (M). Upon the third analyzer plate (A) the beams are recombined. A slab can be inserted in both beam paths to introduce a phase shift.

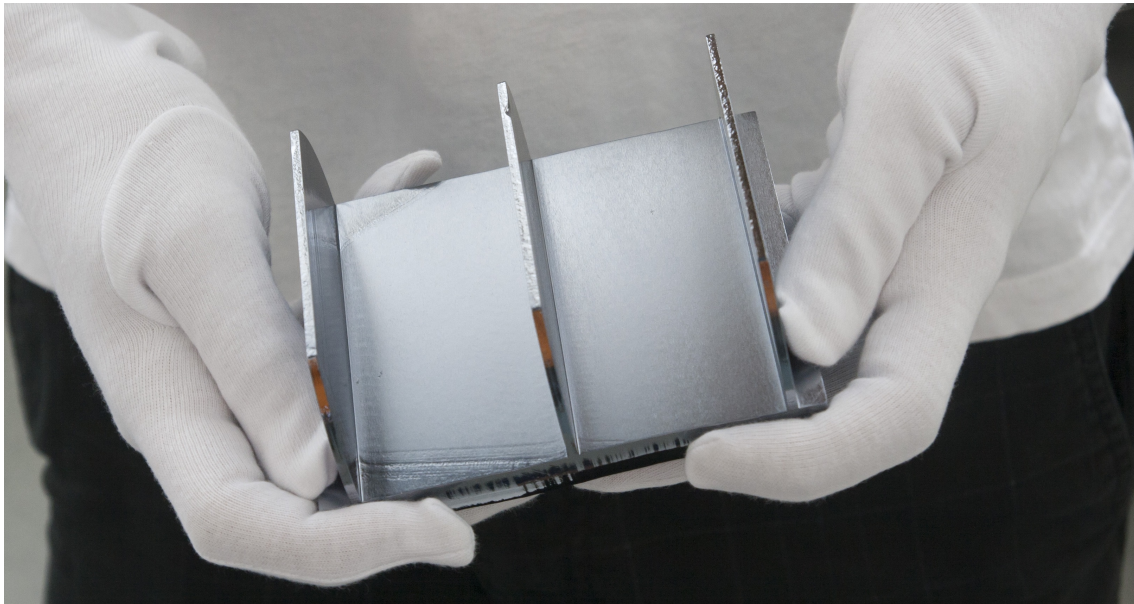


Figure 1.3: Picture of the Kaiser interferometer: The Kaiser interferometer is a symmetric three plate perfect crystal neutron interferometer, which realizes the triple Laue (LLL) configuration.

1.2 Experimental investigation of quantum mechanics using neutron interferometry

From an experimental point of view quantum mechanics is one of the best-verified theories of physics. Its predictions have been tested numerous times with many different quantum systems and so far all predictions are confirmed to be correct [Folger, 2009]. Until today novel theoretical predictions are made based on the framework of quantum mechanics and continuous tests of these predictions are absolutely essential for their experimental verification.

As we have seen from the previous section neutron interferometry in combination with spin polarimetry is a perfect tool to perform such tests (for a detailed review see e.g. [Hasegawa and Rauch, 2011, Klepp et al., 2014]). It offers access to two purely quantum mechanical systems under almost ideal circumstances. They can be utilized in the investigations of the foundations of quantum mechanics. Both degrees of freedom, the neutron interferometer's paths and the neutron spin, can be controlled coherently with high precision using various neutron optical components, which are explained in detail in chapter 2. Also, as compared to optical experiments with visible light, the approach using matter waves has the advantage that there is no overlap with a classical theory. Here we want to give a brief description of several historically important neutron interferometric experiments.

One of the first tests of the foundations of quantum mechanics using neutron interferometry dealt with the 4π spinor symmetry of spin- $1/2$ particles. The Schrödinger equation of a fermion with mass m and a wave function $\Psi(\vec{r}, t)$ which is subject to an externally applied magnetic field is given by

$$\hat{H}\Psi(\vec{r}, t) = \left[-\frac{\hbar}{2m}\nabla^2 - \mu\hat{\sigma} \cdot \hat{B}(\vec{r}, t) \right] \Psi(\vec{r}, t) = i\hbar\frac{\partial}{\partial t}\Psi(\vec{r}, t), \quad (1.8)$$

where μ is the magnetic moment of the particle. The solution of this differential equation is given by

$$\Psi(\vec{r}, t) = c_+(\vec{r}, t) \cos\left(\frac{\theta}{2}\right) |\Psi_z; +\rangle + c_-(\vec{r}, t) \sin\left(\frac{\theta}{2}\right) e^{i\phi} |\Psi_z; -\rangle \quad (1.9)$$

with polar and azimuthal angle θ and ϕ , as well as the spin base vectors $|\Psi_z; \pm\rangle$. $c_{\pm}(\vec{r}, t)$ are space time dependent coefficients of the wave function. The wave function given by Eq. (1.9) is obviously symmetric under a 4π rotation, since a 2π rotation would only yield a phase factor of minus ones. The first experimental investigation of the 4π spinor symmetry was performed using a neutron interferom-

eter. This was possible because of the macroscopic beam separation which occurs in the interferometer. While one beam served as a reference, the spin of the other beam was rotated by the angle α so that the beams accumulated a relative phase, which is then observable by the shift in the interference fringes. The experiment fully confirmed the quantum mechanical predictions [Rauch et al., 1975].

In 1975 Colella, Overhauser and Werner (COW) used a neutron interferometer setup to investigate the role of gravity in quantum mechanics [Colella et al., 1975]. Today the experiment is often referred to after its creators as the COW experiment.

Looking at the classical equation of motion of a falling body with mass m within the gravitational potential \hat{V}

$$m \frac{d^2 \vec{x}}{dt^2} = -m \nabla \hat{V} = -mg \vec{z} \quad (1.10)$$

one immediately sees that m does not play a role since it drops out on both sides of the equation. In quantum mechanics, one has to use Schrödingers equation in order to describe a particle under the influence of gravity:

$$\left[-\frac{\hbar^2}{2m} \Delta + m \hat{V} \right] \psi = i \hbar \frac{\partial \psi}{\partial t}. \quad (1.11)$$

Now the mass term does not cancel out any more. It remains in combination with \hbar . It is therefore necessary to find a quantum mechanical situation in which gravity plays an important role. This is very difficult, because of the weakness of the gravitational force. However exactly such a situation can be created using neutron interferometry seen from the schematic drawing in Fig. 1.4. A monochromatic neu-

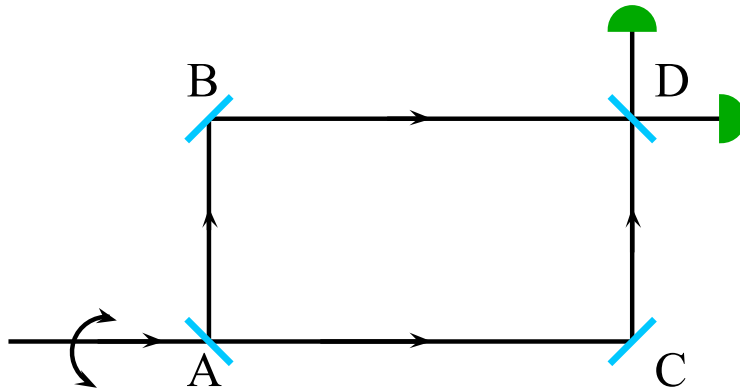


Figure 1.4: Setup of the COW experiment: A monochromatic neutron beam enters the interferometer along the axis going through A and C. If the interferometer is rotated around \overline{AC} the neutrons travelling along the upper beam path pick up a relative phase Φ compared to the ones travelling along the lower beam path due to the difference in gravitational potential $\Delta \hat{V}$.

tron beam enters the interferometer along the axis through A and C. If the points A, B, C and D all lie within the same horizontal plane the gravitational potential can be set to zero, i.e. $\hat{V} = 0$. By rotating the interferometer around \overline{AC} by the angle α , it is possible to introduce a height difference between the upper and the lower beam path. Then there are different gravitational potentials in the respective paths, leading to a relative phase between them. If the distance between A and C is l_1 and the distance between A and B is l_2 , the difference in the gravitational potential between the upper and the lower beam path is given by

$$\Delta\hat{V} = \hat{V}_{\overline{BD}} - \hat{V}_{\overline{AC}} = m_n g l_2 \sin(\alpha), \quad (1.12)$$

where m_n is the neutron's mass, g is the local gravitational acceleration and α is the angle by which the interferometer is rotated. The relative phase change accumulated by the neutrons travelling along \overline{ABD} , as compared to those travelling along \overline{ACD} , is therefore

$$\exp\left(\frac{-im_n g l_2 \sin(\alpha) \tau}{\hbar}\right), \quad (1.13)$$

where τ is the time spent for the neutron to go from B to D. Using the neutron's De-Broglie wave length given by $\lambda = h/p$ the expected relative phase shift is

$$\Phi = \frac{m_n^2 g l_1 l_2 \lambda \sin(\alpha)}{2\pi\hbar^2}. \quad (1.14)$$

The wave length of the neutrons used in the COW experiment, was $\lambda = 1.445 \text{ \AA}$. If the area $l_1 l_2$ enclosed by the interferometer's paths is $l_1 l_2 = 10 \text{ cm}^2$, we obtain 56.64 rad for the factor

$$q = \frac{m_n^2 g l_1 l_2 \lambda}{2\pi\hbar^2}. \quad (1.15)$$

This means that one should see $56.6/2\pi \approx 9$ maxima and minima if the interferometer is rotated by $\pi/2$. Hence the magnitude of the effect is just right to be observed by a neutron interferometer experiment. The experiment showed a slight deviation from the theoretical predictions. COW ascribed the difference between the theoretical and the experimental value to the bending of the interferometer's base during the rotation. A more recent experiment confirmed a deviation between quantum mechanical predictions and experimentally observed results, which cannot be attributed to experimental imperfections, by 1% [Littrell et al., 1997].

Another notable experiment investing the foundations of quantum mechanics is the

direct observation of fermion spin superposition by neutron interferometry [Summhammer et al., 1983]. Quantum mechanics predicts that a superposition of two spin states aligned along the positive and negative z -axis, i.e. a state constructed by the linear superposition of $|\Psi_z; \pm\rangle$, is not a classical mixture, but a new pure spin state. This behavior is investigated using neutron interferometry by preparing an incident beam so that its spin state is given by $|\mathbf{S}_z; +\rangle$, i.e. it is aligned along the positive z -axis. After the beam enters the interferometer and is split at the first plate, the spin is flipped in one of the beam paths. After the beams recombine at the third plate the spin state is given by

$$|\mathbf{S}\rangle = \frac{1}{\sqrt{2}} (|\mathbf{S}_z; +\rangle + e^{i\chi} |\mathbf{S}_z; -\rangle), \quad (1.16)$$

where χ is the phase caused by the phase shifter in the interferometer. The polarization vector of this spin state lies in the xy -plane and if a spin state lying in the same plane is analyzed, a sinusoidal intensity modulation is observed. In the actual experiment only the beam in forward direction was spin analyzed and indeed interference fringes were observed. In contrast to that the beam in reflected direction, which was not spin analyzed, showing no intensity modulation due to the orthogonality of the spin states inside the interferometer.

Yet another experiment demonstrating the non intuitive nature of quantum mechanics deals with absorbers present in the neutron interferometer: If neutrons are absorbed along either one of the two beam paths inside the interferometer, the amplitude of the observed interference fringes reduces. In the limiting case of total absorption in one beam path the interference vanishes and no intensity modulation can be observed at all. Interestingly enough, quantum mechanics predicts that there is a difference between stochastic and deterministic absorption. The former refers to the case in which it cannot be predicted if a neutron gets absorbed or not, while the latter one denotes the case in which one can predict with certainty if an absorption will happen or not. If a stochastic absorber is put inside the interferometer quantum mechanics predicts that the contrast of the observed interference fringes scales with $\sqrt{T_{\text{STO}}}$, where T is the transmissivity of the absorber. For a deterministic absorber the contrast is expected to scale with T_{DET} , i.e. one finds

$$I_{\text{STO}} \propto |\langle \Psi | \Psi \rangle|^2 \left[1 + 1 + T_{\text{STO}} + 2\sqrt{T_{\text{STO}}} \cos(\chi) \right], \quad (1.17a)$$

$$I_{\text{DET}} \propto |\langle \Psi | \Psi \rangle|^2 \left[1 + T_{\text{DET}} + 2T_{\text{DET}} \cos(\chi) \right]. \quad (1.17b)$$

In the actual experiment absorbing foils were used to test the stochastic case. Inside the foil, the neutron is absorbed with a certain probability. To test the deterministic case a small chopper was put inside the interferometer, which alternatingly blocked the beam and opened it again in time. By tuning the block/open ratio of the chopper different transmissivities could be realized. Indeed, for the same transmissivity different contrasts were observed, for stochastic and deterministic absorption [Summhammer et al., 1987].

In the four decades since its advent, neutron interferometry has put quantum mechanics to the test numerous times. In particular experiments have been performed to demonstrate geometric phases [Wagh et al., 1997, Hasegawa et al., 2001] and to show confinement induced phases [Rauch et al., 2002].

Furthermore entanglement between different degrees of freedom has been demonstrated successfully [Hasegawa et al., 2010, Sponar et al., 2010, Erdösi et al., 2013]. This technique has been used to investigate the contextual nature of quantum mechanics [Hasegawa et al., 2006, Bartosik et al., 2009] as well as to demonstrate a violation of a Bell like inequality [Hasegawa et al., 2003].

A very recent neutron interferometric experiment successfully demonstrated the coherent control of neutron orbital angular momentum degree of freedom [Clark et al., 2015], which opens up the possibilities for novel experiments utilizing the entanglement between different degrees of freedom.

1.3 Weak measurements and weak values

Observables of a quantum mechanical system are described by Hermitian operators. The eigenvalues of such operators are always real. The eigenvalue spectrum is discrete and non degenerate in the simplest case. Let \hat{A} be the operator corresponding to some physical quantity a , like energy, momentum or spin. The eigenvectors of \hat{A} given by $\{|a'\rangle\}$ span a basis of the Hilbert space of \hat{A} and any state can be expressed in that basis by a linear combination of the base vectors:

$$|\Psi\rangle = \sum_{a'} c_{a'} |a'\rangle, \quad (1.18)$$

with $c_{a'} = \langle a' | \Psi \rangle$ being the probability amplitudes for obtaining one of the possible measurement outcomes a' .

According to von Neumann [von Neumann, 1932] the measurement apparatus itself must also be described by a state in a Hilbert space. Let the base vectors of the

measurement apparatus be $\{|\mu\rangle\}$. The investigated system and the measurement apparatus form a joint system $|\Psi\rangle|\mu\rangle$ together. From an initial product state of the systems the measurement process leads to a coupling between them. After the system evolution the measurement result of $|\Psi\rangle$ can be determined by “reading-out” $|\mu\rangle$. The system’s evolution can be described by an evolution operator $U(\alpha)$, where the parameter α describes the interaction strength. If the initial state of the investigated system is given by $|\Psi_i\rangle$ and that of the measurement apparatus by $|\mu_0\rangle$, the measurement process can be schematically described in the Schrödinger picture as

$$\underbrace{|\Psi_i\rangle|\mu_0\rangle}_{\text{initial state}} \longrightarrow \underbrace{U(\alpha)|\Psi_i\rangle|\mu_0\rangle}_{\text{time evolution}} \longrightarrow \underbrace{|\Psi_f\rangle|\mu_f\rangle}_{\text{final state}}. \quad (1.19)$$

The measurement outcome can be inferred from the measurement apparatus’ final state $|\mu_f\rangle$.

In 1964 Aharonov, Bergmann and Lebowitz (ABL) considered a measurement procedure that explicitly involves both initial and final state, $|\Psi_i\rangle$ and $|\Psi_f\rangle$, of the investigated system [Aharonov et al., 1964]. If the system’s preselected state is given by $|\Psi_i\rangle$ the probability of successfully postselecting the state $|\Psi_f\rangle$ is given by $\mathcal{P} = |\langle\Psi_f|\Psi_i\rangle|^2$. If a measurement is performed between the events of pre and post selection, the initial state gets altered by a system evolution during the measurement and the probability changes to $\mathcal{P} = |\langle\Psi_f|U(\alpha)|\Psi_i\rangle|^2$.

In 1988 Aharonov, Albert and Vaidman (AAV) considered the case in which the influence of the intermediate measurement is made small or weak and introduced the weak value $\langle\hat{A}\rangle_w$ as the parameter for the relevant observable for a system between the events of pre and postselection and weak couplings [Aharonov et al., 1988, Duck et al., 1989]. The weak value is defined as

$$\langle\hat{A}\rangle_w = \frac{\langle\Psi_f|\hat{A}|\Psi_i\rangle}{\langle\Psi_f|\Psi_i\rangle}. \quad (1.20)$$

It depends on both the initial and the final state. In general it is a complex number, so it has a real and an imaginary part. The weak value’s real part is the shift that the pointer system (the measurement apparatus) experiences according to the system evolution during the measurement. As an operational definition, the weak value can be characterized as the relative correction to a detection probability $|\langle\Psi_f|\Psi_i\rangle|^2$ due to a small intermediate perturbation $U(\alpha)$ resulting in a modified detection probability $|\langle\Psi_f|U(\alpha)|\Psi_i\rangle|^2$ [Dressel et al., 2014].

The weak value is extracted in a procedure which is referred to as weak measurement. In the standard scheme the weak measurement is performed in three steps: First the quantum ensemble is created and the system is preselected in the initial state. Then the measurement apparatus is coupled weakly to the quantum system of interest in a way so that the system is only minimally disturbed and the overlap between the initial state $|\Psi_i\rangle$ and the evolved state $|\Psi'\rangle$ is kept large. As a final step the quantum system is measured strongly: It is postselected into a final state. The weak value can then be inferred from the pointer shift of the measurement apparatus^a

It is important to note that the weak value, extracted using weak measurements, does not refer to the property of single particle events, but that of a quantum ensemble. Similar to the standard expectation value it cannot be determined by a measurement performed on one single particle (with the exception of eigenstates). Also there is a tradeoff in the precision with which the weak value can be obtained through a weak measurement. To determine $\langle \hat{A} \rangle_w$ accurately the pointer shift should be large enough to be distinguished from the uncertainty of the pointer. This corresponds to the case where the initial and the final state of the measurement apparatus are precisely defined. However, this is the case for standard von Neumann measurement. The disturbance on the measured system is large and the overlap between the initial state $|\Psi_i\rangle$ and the evolved state $|\Psi'\rangle$ is small. Weak measurements in the contrary are performed in a way so that the pointer shift of the measurement apparatus small. But then less information is obtained. The error of a weak measurement typically scales with \sqrt{N} where N is the number of events the measurement is performed on [Aharonov et al., 2010]. The weak value $\langle \hat{A} \rangle_w$ can then be determined precisely by repeating the measurement on a large number of events as the uncertainty reduces with $1/\sqrt{N}$.

Due to the weakness of the interaction the preselected state is only minimally disturbed, so that the system can evolve (almost) unchanged into the final state. This also means that if a system is in a superposition state, it will not collapse into one possible eigenstate if a weak measurement is performed. It is furthermore (in theory) possible to perform simultaneous weak measurements of incompatible observables. In an actual experiment each weak measurement will add some disturbance to the system, so that the actual amount of measurements that can be performed at the same time is limited [Piacentini et al., 2015].

After its introduction the debate about the interpretation of weak values imme-

^aIn chapter 3 it will be discussed in detail how the weak value of a two-level quantum system can be fully determined.

diately sprung up [Leggett, 1989, Aharonov and Vaidman, 1989]. The argument about the weak value’s physical content still lasts till today [Svensson, 2013, Sokolovski, 2015, Dressel, 2015]. The discussion goes so far, it is even debated if the weak value is a purely quantum mechanical property or if it is also observed in classical systems [Ferrie and Combes, 2014a, Romito et al., 2016]. Besides the above arguments, the weak value is found to be very useful in three experimental circumstances [Dressel et al., 2014]:

1. The weak value can be used to amplify detector signals below practical limitations, which makes it possible to measure small parameters in an experiment.
2. The weak value is a complex number that can be linked to the quantum wave function, which among others makes it possible to perform quantum state reconstructions.
3. The weak value is a conditioned average of observables’ eigenvalues and its real part can be used to investigate so called pre and postselection paradoxes.

In the following sections the three experimental applications of the weak value are explained by listing several key experiments.

1.3.1 Weak measurements of photonic systems

In their original paper AAV proposed a Stern-Gerlach like apparatus to demonstrate the physical validity of weak values and weak measurements: A beam of spin- $1/2$ particles is prepared in a certain preselected spin state and sent through a “weak” magnet in the Stern-Gerlach apparatus. Due to the weakness of the apparatus the two sub beams corresponding to the two spin components are not completely separated, but have a large overlap. Nevertheless a coupling between the particle’s spin and momentum is created. Subsequently the two sub beams pass an ideal (strong) magnet in the Stern-Gerlach apparatus and are then recorded by a position sensitive detector. The detector records a certain distribution, which depends on the momentum of the particles. More precisely the distribution will be shifted in the measurement direction of the weak magnet, with the shift being proportional to the weak value.

Due to the small coherence volume of massive particles, the experimental realization of this kind of experiment turned out to be infeasible and the first experimental determination of a weak value was performed in a photonic setup [Ritchie et al., 1991]. The experiment is a purely optical analogon to the proposed experiment of AAV:

Instead of the spin, the polarization of visible light is the system of interest in this experiment. The Stern-Gerlach magnets are replaced by optically birefringent crystals. A laser beam is prepared with a certain polarization and subsequently a birefringent-crystalline quartz plate spatially separates the beams of the two orthogonal polarizations. By making the beam separation δ small, the condition of a weak measurement is fulfilled. After the postselection, performed by a simple polarizer, the light is detected by a position sensitive detector. The observed intensity pattern is Gaussian with its peak being centered around the position of the polarization operator's weak value. The observed Gaussian pattern is actually a result of a constructive addition of two Gaussian distributions separated by a distance much less than the Gaussian beam waist. The postselection direction can be tuned by rotating the final polarizer. For nearly orthogonal states a large shift of the Gaussian is observed, which corresponds to large weak values. An interesting effect is observed for orthogonal pre and postselected states. Not one but two separate Gaussians are recorded with very low intensities. But the peak separation is two orders of magnitude larger than the beam separation δ caused by the weak measurement. This effect can be used in high precision measurements and is called weak value amplification.

1.3.1.1 Weak value amplification

To understand the weak value amplification scheme, let us reconsider the experimental proposal of AAV. It can be shown that the observed momentum distribution is in first order linear proportional to the imaginary part of the polarization operator's weak value, which we want to denote with $\langle S \rangle_w$, times the interaction parameter, which we want to denote with α [Dressel et al., 2014].:

$$\int p \mathcal{P} dp \propto \text{Im} [\langle S \rangle_w] \alpha. \quad (1.21)$$

Here p is the particles momentum and \mathcal{P} is given by $\mathcal{P} = |\langle \Psi_f | U(\alpha) | \Psi_i \rangle|^2$. If one wants to determine the parameter α even though it is very small, the weak value's imaginary part can be made big by choosing nearly orthogonal pre and postselected states. However, one has to pay a price for the amplification. Due to the orthogonality between pre and postselected states, \mathcal{P} becomes small and therefore the detected intensity is very low, so that this experimental technique is suboptimal for certain situations [Ferrie and Combes, 2014b].

In contrast, in some cases the loss of intensity is not an essential factor and one

can gain an advantage from the weak value amplification scheme. What if the goal of the original AAV experiment were not to determine the weak value, but the amount of beam separation caused by the first “weak” Stern-Gerlach magnet? Due to the weakness in the coupling, the beam separation is small. At the same time the position sensitive detector has a certain pixel size. If the separation is below the pixel size of the detector it cannot be resolved in the experiment even if plenty intensity is available. Tuning the pre and postselected states to be (nearly) orthogonal, amplifies the separation so that it can be resolved with the given pixel size, i.e. the resolution of the detector, at the cost of intensity. Furthermore the weak value amplification scheme is shown to be very robust against certain types of noise [Jordan et al., 2014].

Despite the discussions about the usefulness of the weak value amplification scheme, this effect is confirmed in lots of experiments: One of the most notable ones is the observation of the spin Hall effect of light, where beam displacements of approximately 1 \AA , which cannot be resolved in a conventional setup, were successfully determined [Hosten and Kwiat, 2008]. In another optical experiment implementing the weak value amplification in an interferometric scheme, beam deflections as small as 400 frad were observed [Dixon et al., 2009].

1.3.1.2 The weak value as a measurable complex value

As seen from the weak values definition given by Eq. (1.20), the weak value is in general a complex number. In the publication [Lundeen et al., 2011] it is shown that the weak value can be connected to the preselected state’s wave function which in turn makes a “direct” state characterization possible. *By “direct” it is meant that a value proportional to the wave function appears straight on the measurement apparatus itself without further complicated calculations or fitting* as is explained in [Lundeen and Bamber, 2012]. The “direct” state characterization procedure has been extended to two-level quantum systems [Salvail et al., 2013] and has turned out to be useful in many experimental situations [Wu, 2013, Malik et al., 2014, Mirhosseini et al., 2014].

The term “direct” is controversial [Gross et al., 2015]: It is used here to refer to the state characterization via weak values for clarity and to be in accordance with the literature. A point of criticism of the experimental method is the weakness of the measurement. It has been shown that it is possible to determine weak values without weak interactions [Johansen, 2007, Kedem and Vaidman, 2010, Cormann et al., 2016] and recently it was pointed out theoretically that the weakness of the interaction

is also not a necessary condition to perform a state characterization via weak values [Vallone and Dequal, 2016, Zhang et al., 2016]. Determining weak values with strong interactions preserves the experimental advantages of the direct state characterization and gets rid of its downsides like excessive noise. This topic is also discussed in further detail in chapter 5.

1.3.1.3 The weak value as a conditioned average and quantum paradoxes

Let us consider the so called the three box problem [Aharonov and Rohrlich, 2008], in which a particle is travelling through an interferometer, which offers three possible paths. The particle's state vector in such a situation is given by

$$|\Psi_i\rangle = \frac{1}{\sqrt{3}} (|I\rangle + |II\rangle + |III\rangle). \quad (1.22)$$

Let the particle exit the interferometer so that its postselected state is given by

$$|\Psi_f\rangle = \frac{1}{\sqrt{3}} (|I\rangle + |II\rangle - |III\rangle). \quad (1.23)$$

We now want to ask the question along which path the particle travelled during the time of pre and postselection. This is equivalent to evaluating the projection operators of the individual path eigenstates $\hat{\Pi}_j^P = |j\rangle\langle j|$ with $j = I, II, III$. To calculate the probabilities of finding the particle along one of the paths during the time of pre and postselection we can use the formula proposed by ABL [Aharonov et al., 1964]. The probability \mathcal{P} that a measurements yields the outcome c_j if it is performed at the time t between pre and postselection is

$$\mathcal{P}(c_j, \Psi_i, \Psi_f) = \frac{|\langle\Psi_f|U(t_f, t)|c_j\rangle\langle c_j|U(t, t_i)|\Psi_i\rangle|^2}{\sum_i |\langle\Psi_f|U(t_f, t)|c_i\rangle\langle c_i|U(t, t_i)|\Psi_i\rangle|^2} \quad (1.24)$$

with the pre and postselected states $|\Psi_i\rangle$ and $|\Psi_f\rangle$. The operators $U(t, t_i)$ represent the evolution the state from the the initial time t_i to the intermediate time t . Similar $U(t_f, t)$ causes an evolution from the intermediate to the final time.

If the ABL rule is applied to the three path situation, we find that the particle will travel with probability one along path I . But we also find that it will travel with probability 1 along path II [Aharonov and Rohrlich, 2008]. We found a seemingly paradoxical situation, which is known as the so called three box paradox [Aharonov and Vaidman, 1991]. The paradox can easily be resolved by pointing out that the reason is counterfactual [Kastner, 1999]. If the particle is detected along one of the interferometer's paths, its wave function collapses into one of the three

states and postselection in a superposition state is not possible.

The situation that seems paradoxical at the level of an individual particle can also be analyzed at the level of ensembles using weak values. The weak value's real part acts as an ensemble average of an observable conditioned on pre and postselection [Dressel et al., 2014]. This means that any meter that couples weakly to a system will in average be affected as if the weak value's real part were the actual system property. Also as was already state earlier, weak measurements can in principle be performed simultaneously and only minimally disturb the system making an evolution from the preselected to the postselected state possible. Hence the coexistence of several weak values is permitted and their reasoning is not counterfactual.

If the relevant weak values for the three box problem are calculated, interesting properties can be revealed. For the projection operators along path *I* and *II* one finds $\langle \hat{\Pi}_I^P \rangle_w = \langle \hat{\Pi}_{II}^P \rangle_w = 1$, which is expected from the ABL formula. Interestingly enough one also finds $\langle \hat{\Pi}_{III}^P \rangle_w = -1$. The weak values tell us that an ensemble that is successfully pre and postselected in the states given above will in average behave as if particles were travelling along both paths *I* and *II*. But what is the meaning of the negative weak value of path *III*? The system will in average behave as if a negative particle probability were there. Suppose for example that the experiment were performed with particles that carry a positive charge. If one would then weakly measure the particles by detecting their charges along the way, one would register positive charges along path *I* and *II*, but a negative one in path *III*. The considerations performed above are no mere gedankenexperiment. In 2004 the three box paradox was realized in a photonic setup [Resch et al., 2004]. Another possible interpretation of the negative weak value is that the weak value only exists as an “effective influence” in the measurement. This is similar to effective positive and negative charges in solid state physics [Kittel, 2004].

Treating the weak value's real part as a conditioned average other seemingly counterfactual quantum mechanical situations have been addressed. One example for such a situation is Hardy's paradox [Hardy, 1992]. It was initially designed as a gedankenexperiment, in which an electron and a positron interact with each other without annihilating. While the experimental situation in Hardy's paradox was also dismissed as counterfactual, it can be understood in terms of weak values [Aharonov et al., 2002]. Consequently it was also demonstrated experimentally by two independent groups, both using photonic setups [Lundeen and Steinberg, 2009, Yokota et al., 2009].

Other examples for quantum paradoxes that can be addressed using the weak value formalism are the quantum Cheshire cat, where a particle seems to be spatially sep-

arated from one of its properties [Aharonov et al., 2013b] and the quantum pigeon hole effect, where three pigeons are put into two boxes yet no two pigeons ever seem to occupy the same box [Waegell and Tollaksen, 2015, Aharonov et al., 2016]^b

In general anomalous weak values, i.e. weak values that lie outside the eigenvalue spectrum of an operator, indicate that the system cannot be understood in a classical way and as an ensemble average they provide a physically meaningful interpretation of seemingly paradoxical experiments. Such situations can only happen for postselected sub-ensembles of a quantum system. It has also been shown that anomalous weak values can be connected to violations of generalized Leggett-Garg inequalities [Williams and Jordan, 2008, Goggin et al., 2011] and that they are proof of contextuality [Pusey, 2014].

In a double slit experiment weak measurements have been used to record the weak value of photons' momentum, which made it possible to reconstruct the average photon trajectories throughout the interference experiment [Kocsis et al., 2011]. The weak value as an ensemble average of an observable (for this special case the momentum) gives a meaningful interpretation of the experimentally observed behavior.

1.3.2 Weak values in massive quantum systems

The weak value formalism as proposed by AAV is formulated in a non relativistic framework. Still, due to the small coherence volume of massive particles, the first experimental realization of a weak measurement was performed in a purely optical setup. Most of the experimental work involving weak measurements and weak values can be explained using a semiclassical wave theory [Bliokh et al., 2013] without the need of quantum mechanics. Albeit there are experiments that can only be understood in terms of a nonclassical theory [Pryde et al., 2005], the experimental observation of a weak value of a single massive system has been lacking for a long time.

Neutron interferometry has been successfully used several times to demonstrate purely quantum mechanical effects. The aim of this thesis is to develop an experimental scheme to determine weak values using massive particles and to implement the scheme in an neutron interferometric setup. In the following chapters it is shown how weak measurements using neutrons are achieved. The alignment of the setup and experimental data together with the theory are presented, demonstrating the successful weak value determination.

^bBoth paradoxes will be subject of later chapters.

CHAPTER 2

Neutron optical setup and components

In this chapter several key components for neutron optical experiments are described. At neutron sources and ionization counter tube neutron detectors are briefly explained. It is followed by a description of spin-manipulating components. Finally interferometric components are explained. The working principle behind those neutron optical devices is shortly laid out. As was explained in chapter 1 the neutron's path degree of freedom and its spin degree of freedom can be described as two-level quantum system. Here it is shown how the presented neutron optical components can be used to manipulate the state vectors of each degree of freedom.

2.1 Neutron sources and detectors

To perform neutron optical experiments it is essential to get neutrons from a suitable source and to subsequently detect them. Here important neutron sources and detectors are briefly presented.

2.1.1 Neutron sources

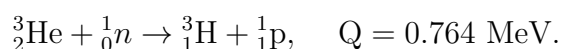
One of the most widely used neutron sources in large scale research facilities are nuclear reactors. In a nuclear reactor, neutrons are produced by nuclear fission. As compared to a commercial powerplants, the aim of a research reactor is to produce a high flux neutron beams, where the released fission energy is only a byproduct.

Research reactors provide a steady neutron beam, with a whole spectrum of wavelengths.

The two most important research reactors for neutron optical experiments, which we carried out and describe here, are the TRIGA reactor of the Institute of Atomic and Subatomic Physics (Atominstitut) operated by the TU Wien and the high flux research reactor of the Institut Laue-Langevin (ILL) in Grenoble, France. TRIGA is an acronym for **T**rainig **R**esearch **I**sotope production **G**enerl **A**tomics. The design of the reactor done by General Atomics allows for a wide range of applications in research. The Vienna reactor operates at a thermal power of 250 kW and offers a neutron flux of 1×10^{13} neutrons per square centimeter and second (in continuous mode). Practically this flux can only be sustained in the core. The observed count rate in polarimetric and interferometric experiments is orders of magnitude lower (typically $\sim 1 \times 10^2 \text{ cm}^{-1}\text{s}^{-1}$ and $\sim 1 \times 10^1 \text{ cm}^{-1}\text{s}^{-1}$ at the final counters respectively). While the available intensity is high enough for polarimetric experiments, neutron interferometric experiments with polarized neutrons are not feasible in Vienna. The ILL research reactor produces a thermal power of 58 MW with one highly enriched fuel element. Consequently its peak flux of $1.5 \times 10^{15} \text{ cm}^{-1}\text{s}^{-1}$ is considerably higher than in Vienna and also the highest flux available from a continuous source worldwide. The typical intensity in neutron interferometric setup with polarized beams are $\sim 1 \times 10^2 \text{ cm}^{-1}\text{s}^{-1}$, which makes actual experiments feasible.

2.1.2 Counter tubes

To detect thermal, i.e. slow neutrons gaseous ionization counter tubes are generally. The neutron is electrically neutral and therefore it does not produce any charge when passing through. However it is possible to fill a counter tube with nuclei that have a large neutron absorption cross section and that emit an electrically charged particle after absorbing a neutron. The charged particle then produces an ionization and the absorbed neutron can be indirectly detected. A schematic depiction of a neutron detector and its radiation shield is shown in Fig. 2.1. A suitable gas for a neutron detector is Helium-3 (^3He). Helium-3 counter tubes utilize the nuclear reaction



When a ^3He nucleus absorbs a neutron, it decays into a triton (^3_1H) and a proton (^1_1p). The energy of 0.764 MeV that is released due to the decay, gets distributed on

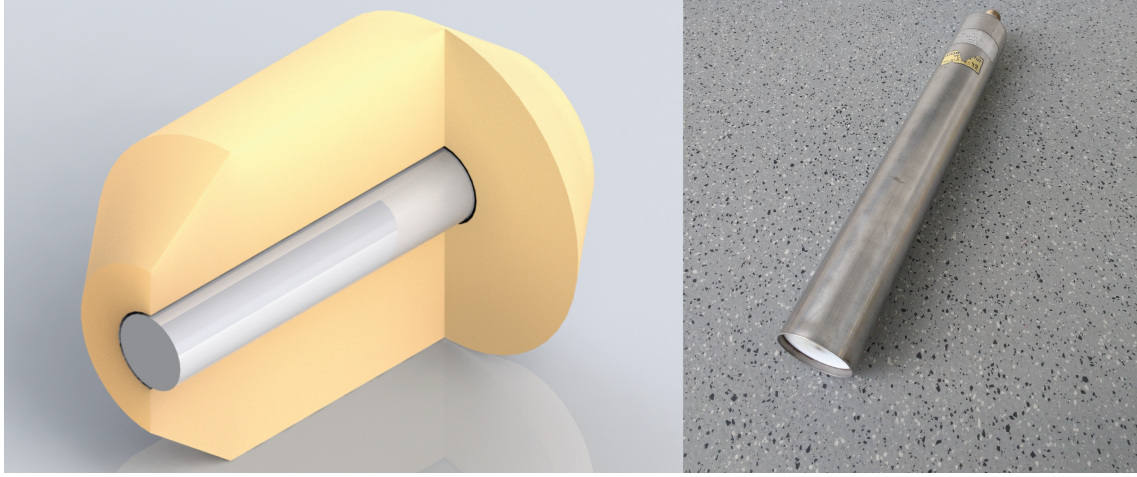
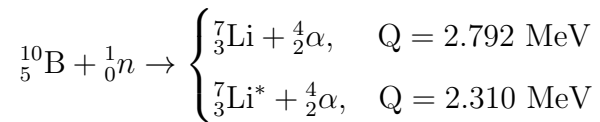


Figure 2.1: Artistic depiction of a neutron detector and its radiation shield (left) and picture of a counter tube (right): To reduce the background counts from scattered neutrons, which are irrelevant to the experiment, the counter tubes (gray; at the center) are usually encased in a neutron absorbing radiation shield (yellow; cut open to make counter tube visible).

the decay products. Since the thermal neutron's energy (~ 20 meV) is much smaller than Q , it is not possible to resolve the energy of the absorbed neutrons. ^3He has a very large absorption cross section and is at the same time insensitive to gamma rays, making it a perfect gas for neutron detectors. At the moment the supply of Helium-3 is limited, which makes it very expensive.

A possible alternative gas is boron trifluoride BF_3 , which makes use of the following nuclear reaction:



If the boron nucleus absorbs a neutron it decays into a Lithium nucleus and an α particle. Boron can either decay into an excited state of Lithium (${}^7_3\text{Li}^*$) or into a non excited one (${}^7_3\text{Li}$). For both cases the released energy Q is much larger than the neutron's energy. BF_3 offers a high neutron absorption cross section. In addition there is a high abundance of boron available. Nevertheless, boron trifluoride has the disadvantage of being highly toxic [Knoll, 2010].

2.2 Neutron interferometer and associated components

In addition to the perfect crystal neutron interferometer itself, interferometric components are used in those parts of the experimental setup, which manipulated the neutron's path degree of freedom, i.e. they tune the state vector moving it on the path Bloch sphere.

If the incident beam hits the interferometer under the angle θ_B , it is split coherently by amplitude division upon the first beam splitter plate (BS). All three plates work as 50:50 beam splitters. Because of that two sub beams leave the interferometer loop at the middle plate (M). Those beams are usually not of interest in our experiment. Upon the third analyzer plate (A) the beams are recombined. A slab can be inserted across both beam paths to introduce a phase shift.

The phase shift is caused by a slab of certain materials, which alters the optical path lengths of the two beams, due to the fact that, the neutron behaves according to a refraction index n , which depends on the material. It is given by

$$n^2 = 1 - \frac{V}{E}, \quad (2.1)$$

where E is the neutron's kinetic energy and V represents the height of the Fermi pseudo potential of the material. It is given by

$$V = \frac{2\pi\hbar^2}{m_n} N b_c, \quad (2.2)$$

where m_n is the neutron's mass, N is the density of nuclei, b_c is the nuclear scattering length and \hbar is the reduced Planck's constant ($\hbar/2\pi$). The neutron refraction index depends on the neutron's energy and therefore on the neutron wavelength λ [Utsuro and Ignatovich, 2010]. The potential V does not necessarily need to be produced by material. It can be also introduced by external magnetic fields [Werner et al., 1975, Rauch et al., 1975] or by gravity [Colella et al., 1975].

If $V \ll E$, the refraction index n is simply given by the approximation

$$n = \sqrt{1 - \frac{V}{E}} \approx 1 - \frac{V}{2E} = 1 - \frac{\lambda^2 N b_c}{2\pi} \quad (2.3)$$

for non magnetic materials. For magnetic materials the potential has to be extended and the refraction index is then given by

$$n = 1 - \lambda^2 \left(\frac{Nb_c}{2\pi} \mp \frac{\mu m_n B}{h} \right), \quad (2.4)$$

with the saturation induction B and the neutron's magnetic moment μ .

In neutron interferometry, the interfering beam leaving the interferometer in forward direction is called O-beam and the beam leaving in reflected direction is called H-beam. We now proceed to calculate the intensities of both beams. The incident wave function is given by a plane wave in the form

$$|\Psi_i\rangle = A_i e^{i\vec{k}\cdot\vec{r}} \quad (2.5)$$

with the wave's momentum vector \vec{k} and its position vector \vec{r} . After the interferometer's first plate a transmitted and a reflected wave appear. Their wave functions are given by

$$|\Psi_t\rangle = t e^{i\vec{k}\cdot\vec{r}} \quad (2.6a)$$

$$|\Psi_r\rangle = r e^{i\vec{k}'\cdot\vec{r}} \quad (2.6b)$$

with the reflected wave vector \vec{k}' and the normalized amplitudes $t = A_t/A_i$ and $r = A_r/A_i$. Using dynamical diffraction theory the intensities of the reflected and transmitted beams relative to the incident beam are calculated and they are given by

$$T = |t|^2 = \frac{\sin^2(B\sqrt{1+y^2})}{1+y^2} \quad (2.7a)$$

$$R = |r|^2 = 1 - \frac{\sin^2(B\sqrt{1+y^2})}{1+y^2} \quad (2.7b)$$

where the parameter B is a function of the thickness of the plate and y takes into account a possible deviation of the incident beam from the exact Bragg angle (see [Suda, 2005] for details). Note that $R + T = 1$. Furthermore in the case of a symmetric beam splitter the transmitted and the reflected waves are phase shifted by $\pi/2$ [Zeilinger, 1981].

Repeating the steps performed above for the interferometer's remaining two plates one obtains the wave function for the O- and the H-beam. The relations given by Eqs. (2.7a) already consider a deviation from the exact Bragg angle. For simplicity,

here we assume that the incident beam is monoenergetic and perfectly collimated, so that Bragg's law is satisfied exactly. Using these assumptions the parameter y becomes zero and we find

$$|\Psi_O\rangle = (rrt + trr e^{i\chi}) e^{i\vec{k}\cdot\vec{r}} \quad (2.8a)$$

$$|\Psi_H\rangle = (trt + rrr e^{i\chi}) e^{i\vec{k}'\cdot\vec{r}} \quad (2.8b)$$

The factor $e^{i\chi}$ is a phase shift typically caused by a sample, i.e the phase shifter, in the beam. The intensities of the beams are then given by

$$I_O = 2R^2T [1 + \cos(\chi)] \quad (2.9a)$$

$$I_H = R(R^2 + T^2) - 2R^2T \cos(\chi) \quad (2.9b)$$

Taking Eq. (1.7) and using the method of equating coefficients one finds relations for an ideal situation so that $\bar{I}_O = 2R^2T$, $C_O = 1$ and $\omega_O = 0$ as well as $\bar{I}_H = R(R^2 + T^2)$, $C_H = 2RT/(R^2 + T^2)$ and $\omega_H = \pi$.

This calculation shows that the O-beam has perfect contrast, where C_H can only become one if $R = T = 1/2$. A more general calculation, which includes possible deviations of the incident beam from the Bragg angle shows that only the forward beam can show a perfect contrast of 100% [Rauch and Suda, 1974] and that the reflected beam can not even in theory reach $C_H = 1$. This is simply because the neutrons detected at the O detector get reflected twice and transmitted once, if they take the lower beam path and also if they take the upper beam path. In comparison to that the number of reflections and transmissions is different for the lower and upper beam path for neutrons detected at the H-detector. Whereas the neutrons travelling along the lower beam path get reflected only once and transmitted twice, they are reflected three times along the upper beam path. While having a lower contrast than the O-detector, the H-detector offers a higher average intensity, due to the single reflected beam [Sears, 1989b].

2.2.1 The neutron's path degree of freedom

The description of the neutron interferometer using dynamical theory of diffraction is undoubtedly very powerful. However, its formulation is complicated. A much simpler description of the neutron interferometer is obtained by treating it as a two-level quantum system [Basu et al., 2001, Allen and Eberly, 2012].

A two-level quantum system is one of the most simplest systems of quantum me-

chanics. As its name already suggests, the system only consists of two states $|+\rangle$ and $|-\rangle$. The quantum system can either be in one of the two possible eigenstates or in a superposition of them. Examples for two-level quantum systems are the spin of a spin- $1/2$ particle or the energy levels of an atom (ground and excited state). Mathematically a two-level quantum system is described by a complex two dimensional Hilbert space and follows the $SU(2)$ formalism. The two states of the system span a basis and any other state can be represented by a linear combination of those two base vectors.

$$|\Psi\rangle = c_+ |+\rangle + c_- |-\rangle = c_+ \begin{pmatrix} 1 \\ 0 \end{pmatrix} + c_- \begin{pmatrix} 0 \\ 1 \end{pmatrix}. \quad (2.10)$$

Since the state vectors have to be normalized, the relation $|c_+|^2 + |c_-|^2 = 1$ holds. In the standard representation the $|+\rangle$ state defines the positive z -axis and the $|-\rangle$ state the negative one. It is therefore convenient to introduce the following notation: The two base states of the two level system Ψ shall be notated as $|\Psi_z; +\rangle$ and $|\Psi_z; -\rangle$, i.e. $|\Psi_z; +\rangle \equiv |+\rangle$ and $|\Psi_z; -\rangle \equiv |-\rangle$. A superposition can then be expressed by a linear combination of both states. In particular we define the x - and y -states as

$$|\Psi_x; \pm\rangle = \frac{1}{\sqrt{2}} (|\Psi_z; +\rangle \pm |\Psi_z; -\rangle) \quad (2.11)$$

and

$$|\Psi_y; \pm\rangle = \frac{1}{\sqrt{2}} (|\Psi_z; +\rangle \pm i |\Psi_z; -\rangle). \quad (2.12)$$

Note that the x , y and z directions of the Hilbert space do not necessarily coincide with the directions in real space! All possible states can be depicted as points on the surface of the so called Bloch sphere. The $|\Psi_z; +\rangle$ points towards the upper pole of the sphere and $|\Psi_z; -\rangle$ to the lower one. Points on the equator of the sphere are in a superposition of those states with the same relative weighting for both base states. Examples for equatorial states are $|\Psi_x; \pm\rangle$ and $|\Psi_y; \pm\rangle$. If the azimuth and polar angles of the sphere are given by ϕ and θ , the Bloch vector

$$|\Psi\rangle = \cos\left(\frac{\theta}{2}\right) |\Psi_z; +\rangle + e^{i\phi} \sin\left(\frac{\theta}{2}\right) |\Psi_z; -\rangle \quad (2.13)$$

can be used to reach any point on the Bloch sphere.

The relevant observables of a two-level quantum system are the Pauli matrices. They

are the three traceless Hermitian 2×2 matrices given by

$$\sigma_x = |\Psi_x; +\rangle \langle \Psi_x; -| - |\Psi_x; -\rangle \langle \Psi_x; +| = \begin{pmatrix} 0 & 1 \\ 1 & 0 \end{pmatrix} \quad (2.14a)$$

$$\sigma_y = i(|\Psi_y; -\rangle \langle \Psi_y; +| - |\Psi_y; +\rangle \langle \Psi_y; -|) = \begin{pmatrix} 0 & -i \\ i & 0 \end{pmatrix} \quad (2.14b)$$

$$\sigma_z = |\Psi_z; +\rangle \langle \Psi_z; +| - |\Psi_z; -\rangle \langle \Psi_z; -| = \begin{pmatrix} 1 & 0 \\ 0 & -1 \end{pmatrix} \quad (2.14c)$$

The vectors $|\Psi_x; \pm\rangle$, $|\Psi_y; \pm\rangle$ and $|\Psi_z; \pm\rangle$ are the eigenvectors of the corresponding Pauli matrices. Together with the identity matrix, the Pauli matrices form a basis for the vector space of all 2×2 matrices [Cohen-Tannoudji et al., 1977].

2.2.2 The neutron's path degree of freedom as a two-level quantum system

We apply the formalism from the previous section to the neutron interferometer [Yurke et al., 1986]. Inside the interferometer the neutron travels along two possible paths, I and II . Those two paths of the interferometer form the basis of the neutron path degree of freedom two-level quantum system. The eigenvectors are denoted as $|\mathbf{P}_z; +\rangle \equiv |I\rangle$ and $|\mathbf{P}_z; -\rangle \equiv |II\rangle$.

In an ideal interferometer the first plate is a perfect 50:50 beam splitter. The neutron is reflected or transmitted with equal probability. In terms of the two-level quantum system, the beam splitter brings the neutron in a superposition state of path I and II , i.e. it is in the $|\Psi_x; +\rangle = 1/\sqrt{2}(|\Psi_z; +\rangle + |\Psi_z; -\rangle)$ state after passing the first plate. Any additional phase χ that is introduced inside the interferometer, does not change the fact that the neutron stays in a superposition of the two path states, but it moves the state around on the equator of the Bloch sphere. Figure 2.2 depicts the path degree of freedom on the Bloch sphere. The $|\Psi_x; +\rangle$ state vector, prepared by the first beam splitter, is depicted as a blue arrow.

Here will now show the way the two-level formalism is used, to understand the evolution of the path two-level system. For this we start with the initial system state given by

$$|\Psi_i\rangle = |\mathbf{P}_x; +\rangle = \frac{1}{\sqrt{2}}(|\mathbf{P}_z; +\rangle + |\mathbf{P}_z; -\rangle). \quad (2.15)$$

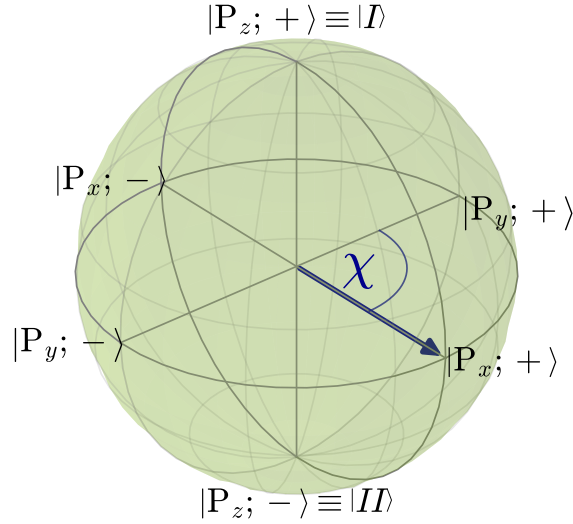


Figure 2.2: Representation of the path degree of freedom on the Bloch sphere: After the interferometer's first plate, the neutron is found in either path I or II with equal probabilities. It is therefore in a superposition of the two path eigenstates which is indicated by the blue vector. χ represents the relative phase between the two path eigenstates.

As discussed above a slab of non absorbing material can be put into the path to introduce a phase shift. This manifests itself in an additional phase factor in the state vector

$$|\Psi(\chi)\rangle = \frac{1}{\sqrt{2}} (|P_z; +\rangle + e^{i\chi} |P_z; -\rangle). \quad (2.16)$$

The beams are recombined at the interferometer's third plate. Mathematically this is represented by a projection onto a specific state. The projectors for O- and H-beam are given by $\hat{\Pi}_{x\pm}^p = |P_x; \pm\rangle \langle P_x; \pm|$ with the projection on the positive x state corresponding to the O- and the one on the negative corresponding to the H-beam. After the projection the state vectors of the two exiting beams can be written as

$$|\Psi_O\rangle = \frac{1}{2} (1 + e^{i\chi}) |P_x; +\rangle \quad (2.17a)$$

$$|\Psi_H\rangle = \frac{1}{2} (1 - e^{i\chi}) |P_x; -\rangle, \quad (2.17b)$$

so that we find the intensities

$$I_O = |\langle \Psi_O | \Psi_O \rangle|^2 = \frac{1}{2} [1 + \cos(\chi)] \quad (2.18a)$$

$$I_H = |\langle \Psi_H | \Psi_H \rangle|^2 = \frac{1}{2} [1 - \cos(\chi)]. \quad (2.18b)$$

The neutron interferometer's path form a two-level system. Using the phase shifter and absorbers it is possible to manipulate and access this degree of freedom experimentally in the interferometer. The neutron offers another two level system that can be used experimentally: The spin degree of freedom, which will be subject of a later section.

2.2.3 Phase shifters

A typical phase shifter is a parallel-sided slab of thickness D_0 , which is inserted across both beam paths of the neutron interferometer, the optical path length difference $\Delta D(\delta)$ of the neutron passing through the phase shifter on the lower beam path minus the one on the upper beam path is given by

$$\Delta D(\delta) = \left[\frac{1}{\cos(\Theta_B + \delta)} - \frac{1}{\cos(\Theta_B - \delta)} \right] D_0, \quad (2.19)$$

where Θ_B is the interferometer's Bragg angle and δ is the rotation angle of the phase shifter. For small δ the phase shift is nearly linear and consequently an interferogram is sinusoidal in δ . The zero phase position is given by the parallel position of the phase shifter [Rauch and Werner, 2015]. A sketch of this phase shifter configuration is depicted in Fig. 2.3. In a material of thickness D_0 and with an refraction index

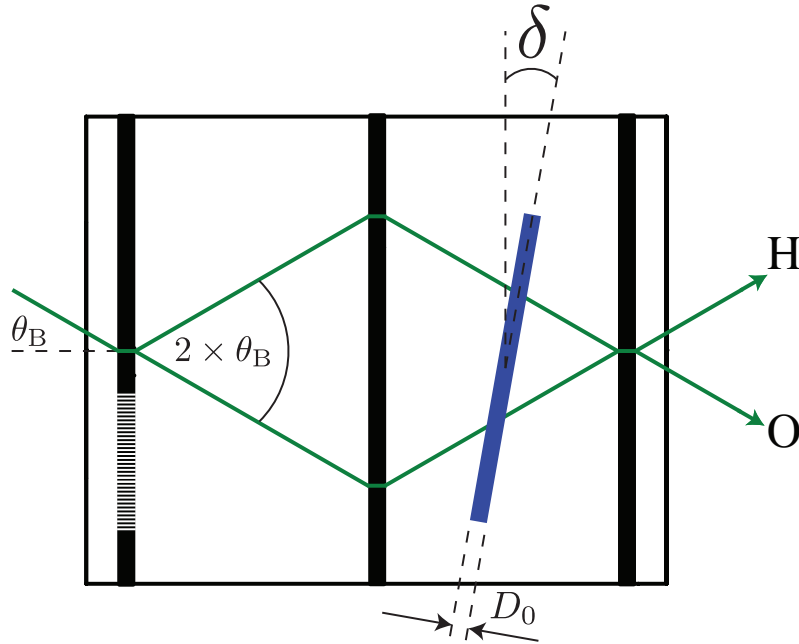


Figure 2.3: Sketch of a phase shifter rotated in both beam paths in a triple Laue interferometer.

n , the magnitude of the phase shift for neutrons with a wave vector k is given by

$$\Delta\chi = (n - 1)kD_0 = -Nb_c\lambda D_0, \quad (2.20)$$

where N is the atomic density of the material, b_c is the materials nuclear scattering length and λ is the neutron wave length. Materials used for a phase shifter should have a high neutron transmission. Frequently used materials are aluminum, silicon and sapphire.

2.2.4 Absorbers

Phase shifters manipulate the path state vector along longitudinal circles of the Bloch sphere. For the latitudinal manipulation, absorbers are used. They move the path state away from the equatorial plane towards the poles of the path Bloch sphere. If either one of the interferometer's paths is completely blocked, the state vector points at a pole.

The transmissivity T , and thus also the absorption coefficient A , of neutrons by a plane slab can be phenomenologically described by the Beer-Lambert Law: The transmissivity of a slab of thickness D is defined by

$$T = \frac{J_t}{J_i} = e^{-\mu D}, \quad (2.21)$$

where J_t is the neutron flux transmitted by the material and J_i is the incoming one. The absorption coefficient μ can be stated in terms of the absorption cross section σ_a

$$\mu = \rho\sigma_a, \quad (2.22)$$

where ρ is the average number of atoms per unit volume. Eq. (2.22) assumes that there is no diffuse scattering inside the material, but only absorption. In reality this is not the case and μ has to be modified so that it is given by $\mu = \rho\sigma_t$, where $\sigma_t = \sigma_a + \sigma_d$ is the total collision cross section, which includes the absorption cross section as well as the scattering cross section [Sears, 1989c].

For interferometric experiments it is essential to find materials that have a high σ_a and a low σ_d to keep a high contrast of the interferogram. Reasonable choices are gold and indium. For the former the absorption and scattering cross sections are $\sigma_a = 98.65(9)$ and $\sigma_d = 7.75(13)$ barn. For the latter they are $\sigma_a = 193.8(1.5)$ and $\sigma_d = 2.62(11)$ barn [Hainbuchner and Jericha, 2001].

2.3 Neutron polarimeter and associated components

The neutron has a magnetic moment $\vec{\mu}$ with a magnitude of $|\vec{\mu}| = 9.66 \times 10^{-27} \text{ J/T}$, which is directly related to the neutron spin by

$$\vec{\mu} = \gamma \vec{S}, \quad (2.23)$$

where γ is the so called gyromagnetic ratio. It is equal to $\gamma = -1.8301 \times 10^8 \text{ s}^{-1}\text{T}^{-1}$ [Abele, 2008].

The neutron spin vector itself is given by

$$\vec{S} = \frac{\hbar}{2} \begin{pmatrix} \langle \hat{\sigma}_x^s \rangle \\ \langle \hat{\sigma}_y^s \rangle \\ \langle \hat{\sigma}_z^s \rangle \end{pmatrix}, \quad (2.24)$$

where \hbar is the reduced Planck constant and $\langle \hat{\sigma}_j^s \rangle$ are the expectation values of the Pauli spin operators [Mezei, 1972]. Note the factor $1/2$ in the above equation. The neutron is a fermion and therefore a spin- $1/2$ particle.

The equation of motion of the spin vector in an externally applied magnetic field \vec{B} is given by

$$\frac{d\vec{S}}{dt} = -\gamma \vec{S} \times \vec{B} = \vec{S} \times \vec{\omega}_L, \quad (2.25)$$

where $\vec{\omega}_L = -\gamma \vec{B}$ is the so called Larmor frequency. The change of \vec{S} in time is normal to both \vec{S} and \vec{B} . Because of that that \vec{S} precesses around the external field \vec{B} .

In a white beam produced by a neutron source the neutrons' spin direction is randomly distributed. If a measurement along a quantization axis is performed, one will find that half of the neutrons are aligned parallel and the other half anti-parallel to the direction of measurement. Such a neutron beam is called unpolarized. To quantify the polarization the so called degree of polarization P is used. It is defined as

$$P = \frac{|N_+ - N_-|}{N_+ + N_-}, \quad (2.26)$$

where N_{\pm} are the number of neutrons found to be aligned parallel (+) or anti-parallel (-) to the direction of measurement. The degree of polarization can vary between

zero and one. For one it describes a completely polarized beam with a polarization parallel to an externally defined axis, for zero the beam is completely unpolarized. For $0 < P < 1$ the beam is partially polarized.

In order to create a polarized neutron beam, so called polarizers are necessary. All of them work by simply removing either the plus or the minus spin component from the beam by various means. A polarizer frequently used in neutron optical experiments is the so called supermirror, which is explained in the a subsequent subsection.

Once the neutron beam is polarized a guide field pointing in the same direction as the neutron spin has to be applied to prevent depolarization. If the direction of the external guide field changes, the neutron spin will follow the change if it is happening slowly on a time scale compared to the spin's Larmor precession (adiabatic case). If the guide field changes abruptly, then the neutron spins stays unaffected (non-adiabatic case) [Schärpf, 1980].

2.3.1 The neutron's spin degree of freedom as a two-level quantum system

The spin of a spin- $1/2$ particle is the one of the best known examples of a two-level quantum system. If a measurement of the spin is performed it will always be found in one of two possible eigenstates. For the neutron spin the base states are given by $|S_z; +\rangle$ and $|S_z; -\rangle$. The $\pm z$ direction can be set by an external magnetic field.

The neutron spin can be depicted on a Bloch sphere, as is shown in Fig. 2.4. Neutron polarizers usually align the neutron spin along the positive z -axis, which is represented by the blue state vector in the above figure. As was already discussed earlier, magnetic fields can be used to coherently manipulate the neutron spin.

2.3.2 Polarizing supermirrors

Historically so called Heusler crystals were used as polarizers, which utilize a spin dependent Bragg reflection. However, Heusler alloys have two experimental disadvantages: Their reflectivity and degree of polarization is low (typically $\sim 30\%$ and $\sim 95\%$ respectively).

An alternative element for a polarizer to Heusler crystals is a so called polarizing supermirror, which offers a higher degree of polarization ($> 99\%$) and are also suitable for neutrons with a higher energy (small wavelengths down to $\lambda \sim 1.7 \text{ \AA}$). Let us first consider a multilayer structure of two different materials A and B as depicted in Fig. 2.5 When a monochromatic neutron beam hits the multilayer under the angle

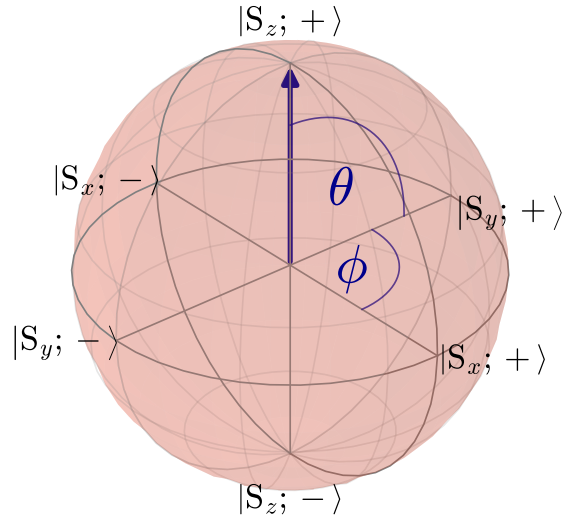


Figure 2.4: Representation of the neutron's spin degree of freedom on the Bloch sphere: Polarizers usually align the spin state along the positive z -axis, as is represented by the blue state vector. The sphere's azimuth and polar angle are given by ϕ and θ from the equator respectively as depicted.

θ it is partially reflected and refracted at each interface, so that due to interference effects the amount of reflected intensity will be high for some angles θ and low for others. This behavior can be understood in terms of Bragg reflection: The multilayer forms an artificial one dimensional pseudo periodic structure with the period a . The reflected intensity is maximum when the Bragg's condition $n\lambda = 2a \sin(\theta)$ (with the order of reflection n) is fulfilled [Sears, 1989d].

If the multilayer is constructed so that the bilayer thickness a increases with the thinnest bilayers on the surface, the Bragg peaks of the individual multilayers overlap. Using such a construction the critical angle θ_c , until which a total reflection

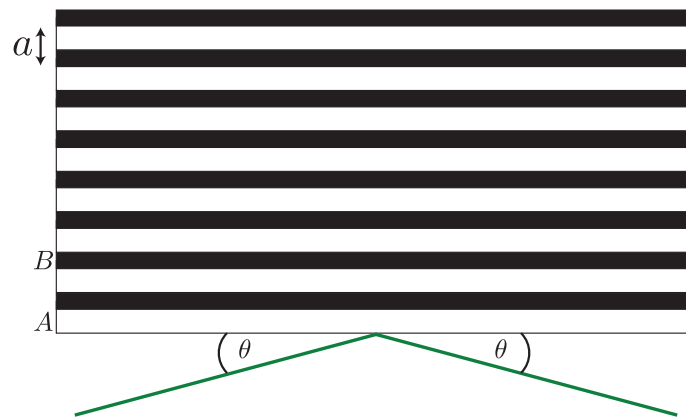


Figure 2.5: Multilayer structure: A multilayer consists of two materials A (white) and B (black) deposited on a smooth surface. The thickness of one double layer is a .

occurs is extendable by a factor of ~ 5 . A multilayer with gradually increasing values of a is called a supermirror [Mezei, 1976]. A structure in a polarizing supermirror is depicted in Fig. 2.6. A supermirror simply reflects the beam, while a polariz-

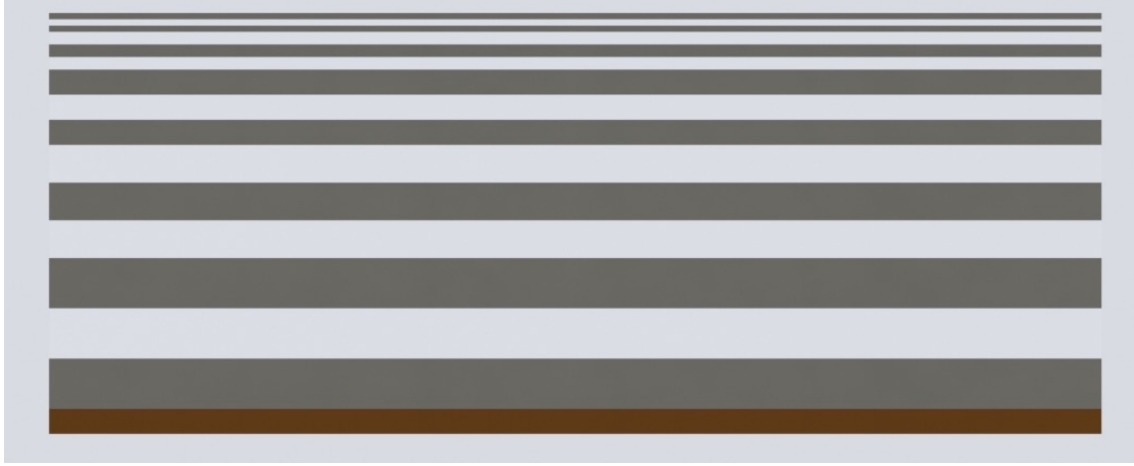


Figure 2.6: Multilayer structure in a supermirror polarizer: A supermirror consists of many layers which form an artificial structure at which reflection can occur. By making the layers thickest on the surface the critical angle θ_c can be extended by a factor of ~ 5 . Neutrons which do not get reflected are filtered out by an absorbing layer on the bottom (bronze).

ing supermirror only reflects one spin component and thereby polarizes the neutron beam. This special kind of spin dependent reflectivity is achieved by making one of the materials in the bilayer structure ferromagnetic: Suppose material A is non magnetic, while material B is ferromagnetic. For the former material the refraction index is given by Eq. (2.3), while for the latter one the scattering length has to be extended by a magnetic part given by Eq. (2.4). The magnetization of the materials has to be tuned in a way that the refraction index becomes the same for both materials for one spin component, but different for the other. Then the neutrons with a spin component for which the refraction index is different for both layers, “see” the layer structure and are reflected. Those with the other spin component the boundaries between the layers vanish and they go straight through the structure and are eventually filtered out by a neutron absorbing layer on the bottom.

The polarizer prepares the spin state on the spin Bloch sphere, so that it is aligned along one direction with unit length.

2.3.3 DC coils as spin rotators

The easiest way to perform a spin rotation is by the use of stationary magnetic fields. When the neutron enters a DC coil, which generates a static magnetic field and it experiences a non-adiabatic field change the, it starts to rotate around the magnetic field vector generated by the coil due to Larmor precession. In order to achieve a spin flip, the time for the neutron spent inside the coil has to correspond to one full Larmor precession which gives us the flip condition

$$d = \frac{v\pi}{\omega_L} = \frac{v\pi}{|\gamma\vec{B}_r|}, \quad (2.27)$$

where d is the width of the coil, v is the neutron speed and \vec{B}_r is the resulting vector of the fields produced by the DC coil and the externally applied guide field. For a given coil width one can adjust the magnetic fields by applying different currents in order to perform the desired spin rotation. Note that DC coils are used only for monochromatic beams, because they can only flip the spin of neutrons with one specific wavelength [Mezei, 1972].

In practice a DC coil is a spin turning device that consists of two coils wound perpendicular to each other: The inner coil is wound in a way that a static magnetic field in the positive y -direction is generated ($\vec{B}_y = (0, B_y, 0)$) when a current is applied. On top of this coil a second one is wound, which generates a static magnetic field in the negative z -direction ($\vec{B}_z = (0, 0, B_z)$). The outer coil is also called compensation coil, because it is used to compensate the externally applied guide field. An artistic depiction of a DC coil is shown in Fig. 2.7. Inside a guide field a DC coil in combination with a translation stage can be used to move the spin vector around in any direction on the Bloch sphere one desires.

2.3.4 Helmholtz coils producing homogenous magnetic Fields

Ideal Helmholtz coils consist of a pair of circular coils with radius R separated by a distance d , which equals the radius. The coils are supplied with a current so that the current flows in the same direction in both of them.

If the origin of the coordinate system is put in the center between the two circular coils and if they are placed with a distance $d = R$ between them, it can be shown that the magnetic field along the symmetric axis (z -axis) at the center is approximated

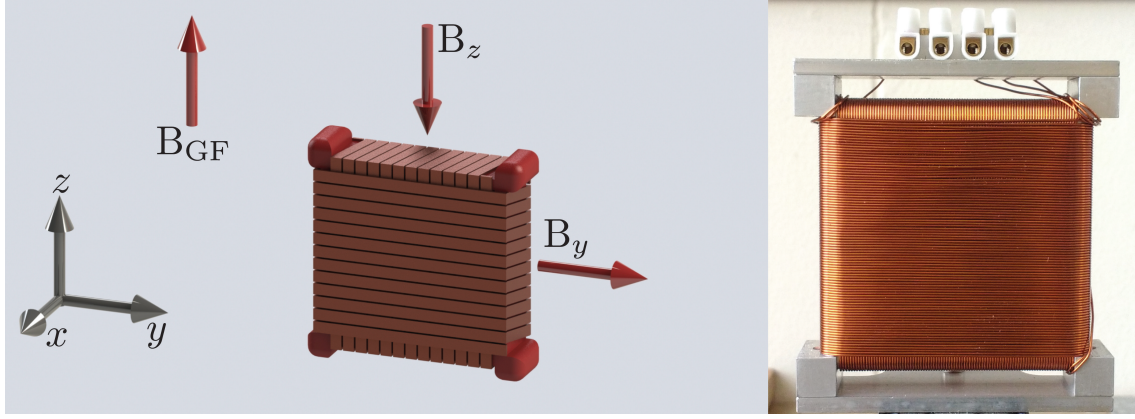


Figure 2.7: Artistic depiction of a DC coil (left) and a picture of a polarimeter DC coil (right): Two layers of wires are wound perpendicular to each other, so that magnetic fields in the z - and y -directions can be created. A combination of both fields makes it possible to flip the neutron spin.

by

$$B(z) \approx \frac{\mu_0 I}{(5/4)^{3/2} R} \left(1 - \frac{144z^4}{125R^4} \right), \quad (2.28)$$

where I is the current applied to the coils and μ_0 is the permeability of free space [Demtröder, 2013]. Around the center of the coil ($z=0$) the field is almost to constant.

This property is convenient for two experimental applications. As discussed above an external guide field is necessary in order to prevent depolarization. For this the geometry of the Helmholtz coils is altered in a way that they are not circular but rather rectangular and bent up at the end, as is shown schematically in Fig. 2.8. The modification at the entrance and exit of the beam is to avoid magnetic fields pointing in the opposite direction of the field one wants to create. Using this geometry a uniform magnetic field pointing in the $\pm z$ direction depending on the sign of the applied current can be generated. The field is homogenous along the longer center line of the coils. If the center line coincides with the neutron path of flight the neutrons are travelling along a uniform guide field and do not lose their polarization. Helmholtz coils can also be used to manipulate the neutron spin. If the spin vector is lying in the xy -plane and an external magnetic field is applied along the z -axis parallel to the guide field, the spin's equation of motion given by Eq. (2.25) tells us that the spin vector will precess in the xy -plane. Again in terms of the vector on the Bloch sphere, Helmholtz coils can be used to shift the spin state around on the

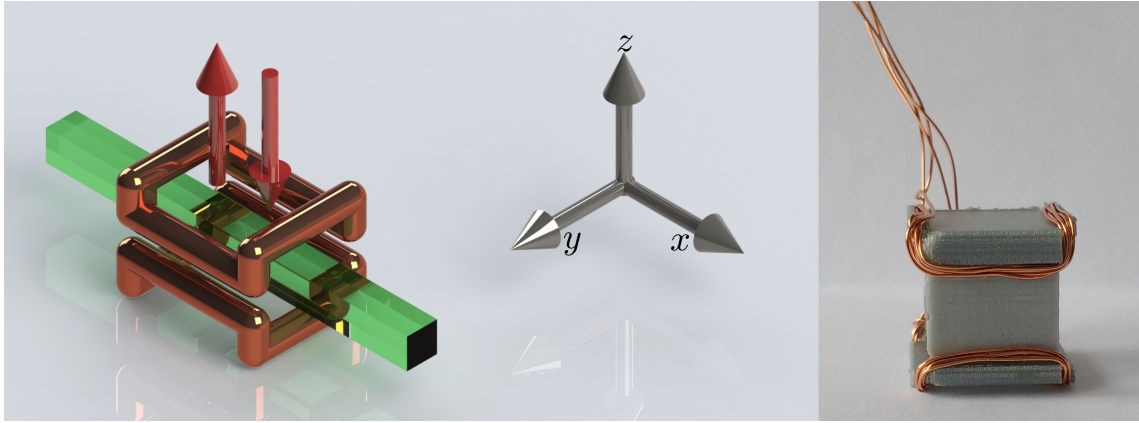


Figure 2.8: Artistic depiction of an altered Helmholtz coil pair with the beam (green) at the center (left) and photograph of an actual coil pair on a 3D printed frame (right): For experimental reasons the geometry is changed from circular to rectangular. Coils shaped that way produce a homogenous magnetic field along the beam trajectory with the field's direction depending on the sign of the applied current.

equator. If the coils are sized down accordingly they can be put inside the interferometer, where they can be used to perform path dependent spin manipulations. To avoid thermal stress from the coils heat waste the coils that are put inside the interferometer are flooded with temperature controlled water [Geppert et al., 2014].

CHAPTER 3

Weak values of two-level quantum systems

In this chapter it is shown how it is possible to determine the real and imaginary part as well as the modulus of weak values of two-level quantum systems. In particular measurement schemes are presented, which make it possible to extract the weak value of Pauli operators and those of projection operators using weak and strong interactions.

3.1 Weak values of Pauli operators

Let us assume that we have full coherent control over two two-level quantum systems \mathcal{H}_A and \mathcal{H}_B . Each of the two quantum systems is described by a two dimensional Hilbert space, which commute with each other. Let us denote states aligned along the $\pm j$ -direction as $|A_j; \pm\rangle$ and $|B_j; \pm\rangle$ respectively. The state vectors $|A_z; \pm\rangle$ and $|B_z; \pm\rangle$ span a basis of the respective Hilbert spaces and any other vector can be represented as a linear combination of them, e.g. $|A_x; +\rangle = 1/\sqrt{2}(|A_z; +\rangle + |A_z; -\rangle)$ or $|B_y; +\rangle = 1/\sqrt{2}(|B_z; +\rangle + i|B_z; -\rangle)$. At this moment we do not want to restrict our considerations to specific two-level systems, like the spin of a spin-1/2 particle, but keep them completely general.

To determine weak values of either one of the quantum systems, relations between experimentally accessible quantities, namely intensities, and operator's weak values have to be derived. For all our considerations A shall be the investigated quantum system, whose weak value should be determined and B shall serve as a meter system. As the first step we concentrate on the weak value of $\hat{\sigma}_z^a$, i.e. the weak value of the

Pauli operator given by

$$\hat{\sigma}_z^a = |A_z; +\rangle \langle A_z; +| - |A_z; -\rangle \langle A_z; -| = \begin{pmatrix} 1 & 0 \\ 0 & -1 \end{pmatrix} \quad (3.1)$$

and on weak interactions. We then proceed to extend our analysis to strong interactions and other operators.

3.1.1 Weak interactions

In the standard weak measurement scheme [Aharonov et al., 1988] three steps have to be taken to determine the weak value of $\hat{\sigma}_z^a$:

- i) Preselection: A certain initial state of the composite system $|\Psi_i\rangle = |A_i\rangle |B_i\rangle$ has to be prepared.
- ii) Interaction: A coupling between A and B has to be created.
- iii) Postselection: Only certain final states $|A_f\rangle$ and $|B_f\rangle$ must be selected.

Let us assume that the initial state of our composite system is prepared to be given by

$$|\Psi_i\rangle = |A_i\rangle |B_i\rangle = |A_x; +\rangle |B_x; +\rangle = \sqrt{\frac{1}{2}} (|A_z; +\rangle + |A_z; -\rangle) \sqrt{\frac{1}{2}} (|B_z; +\rangle + |B_z; -\rangle). \quad (3.2)$$

The quantum ensemble is preselected in a way that the states of both subsystems A and B are aligned along the positive x -axis^a. Note that the state vector of the composite system is given by a completely separable state. There is no coupling between them. As a next step a coupling is created by letting the interaction Hamiltonian \hat{H}_{int} act upon the initial state vector given by Eq. (3.2). Let this Hamiltonian be of the form

$$\hat{H}_{\text{int}} = \frac{\alpha \hat{\sigma}_z^a \hat{\sigma}_z^b}{2}. \quad (3.3)$$

This interaction can be understood as a rotation of the state vector $|A_i\rangle$ around the z -axis of Hilbert space \mathcal{H}_A by the angle α conditioned on the state in the Hilbert space of \mathcal{H}_B . The condition for a weak measurement is fulfilled by making α sufficiently

^aAt this stage the choice for the initial state might seem arbitrary. However, there are important experimental reasons why it was chosen exactly that way. We will come back to this point at a later stage.

small.

The interaction Hamiltonian given by Eq. (3.3) causes an evolution of the system state vector from an initial state $|\Psi_i\rangle$ to the evolved state $|\Psi'\rangle$.

$$\begin{aligned}
|\Psi'\rangle &= e^{-i\alpha\hat{\sigma}_z^a\hat{\sigma}_z^b/2} |\Psi_i\rangle \approx \left(1 - i\alpha\hat{\sigma}_z^a\hat{\sigma}_z^b/2\right) |\Psi_i\rangle = \left(1 - i\alpha\hat{\sigma}_z^a\hat{\sigma}_z^b/2\right) |A_i\rangle |B_i\rangle \\
&= |A_x; +\rangle |B_x; +\rangle - \frac{i\alpha}{2} \hat{\sigma}_z^a |A_x; +\rangle \hat{\sigma}_z^b |B_x; +\rangle \\
&= |A_x; +\rangle |B_x; +\rangle - \frac{i\alpha}{2} \hat{\sigma}_z^a |A_x; +\rangle (|B_z; +\rangle \langle B_z; +| - |B_z; -\rangle \langle B_z; -|) |B_x; +\rangle \\
&= |A_x; +\rangle |B_x; +\rangle - \frac{i\alpha}{2} \hat{\sigma}_z^a |A_x; +\rangle |B_x; -\rangle.
\end{aligned} \tag{3.4}$$

Now the post selection onto a general final state of $|A_f\rangle$

$$|A_f\rangle = \cos\left(\frac{\theta}{2}\right) |A_z; +\rangle + \sin\left(\frac{\theta}{2}\right) e^{i\phi} |A_z; -\rangle \tag{3.5}$$

with ϕ and θ denoting azimuth and polar angle on the Bloch sphere of \mathcal{H}_A respectively, is performed. Then the final state of the composite system is given by

$$\begin{aligned}
|\Psi_f\rangle &= |A_f\rangle \langle A_f | \Psi' \rangle = |A_f\rangle \left(\langle A_f | A_i \rangle |B_x; +\rangle - \frac{i\alpha}{2} \langle A_f | \hat{\sigma}_z^a | A_i \rangle |B_x; -\rangle \right) \\
&= |A_f\rangle \langle A_f | A_i \rangle \left(|B_x; +\rangle - \frac{i\alpha}{2} \underbrace{\frac{\langle A_f | \hat{\sigma}_z^a | A_i \rangle}{\langle A_f | A_i \rangle}}_{\equiv \langle \hat{\sigma}_z^a \rangle_w} |B_x; -\rangle \right) \\
&= |A_f\rangle \frac{\langle A_f | A_i \rangle}{\sqrt{2}} \left[(|B_z; +\rangle + |B_z; -\rangle) - \frac{i\alpha}{2} \langle \hat{\sigma}_z^a \rangle_w (|B_z; +\rangle - |B_z; -\rangle) \right] \\
&= |A_f\rangle \frac{\langle A_f | A_i \rangle}{\sqrt{2}} \left[\left(1 - \frac{i\alpha}{2} \langle \hat{\sigma}_z^a \rangle_w\right) |B_z; +\rangle + \left(1 + \frac{i\alpha}{2} \langle \hat{\sigma}_z^a \rangle_w\right) |B_z; -\rangle \right] \\
&\approx |A_f\rangle \frac{\langle A_f | A_i \rangle}{\sqrt{2}} \left[e^{-i\alpha \langle \hat{\sigma}_z^a \rangle_w / 2} |B_z; +\rangle + e^{i\alpha \langle \hat{\sigma}_z^a \rangle_w / 2} |B_z; -\rangle \right].
\end{aligned} \tag{3.6}$$

With Eq. (3.6), which is obtained for $\alpha \ll 1$, we arrived at a very important result. Recalling that in general the weak value is a complex quantity, i.e.

$$\langle \hat{\sigma}_z^a \rangle_w = \text{Re}[\langle \hat{\sigma}_z^a \rangle_w] + i \text{Im}[\langle \hat{\sigma}_z^a \rangle_w], \tag{3.7}$$

we see that the weak value of $\hat{\sigma}_z^a$ gets “encoded” in the system in \mathcal{H}_B : The real part of the Pauli operator’s weak value acts as an additional phase shift, i.e. a longitudinal move, of the state vector, whereas the imaginary part causes a change in the weight, i.e. a latitudinal shift. This situation is shown in Fig 3.1, which depicts

the evolution of the state on the Bloch sphere for \mathcal{H}_B . $\text{Re}[\langle\hat{\sigma}_z^a\rangle_w]$ rotates the system's

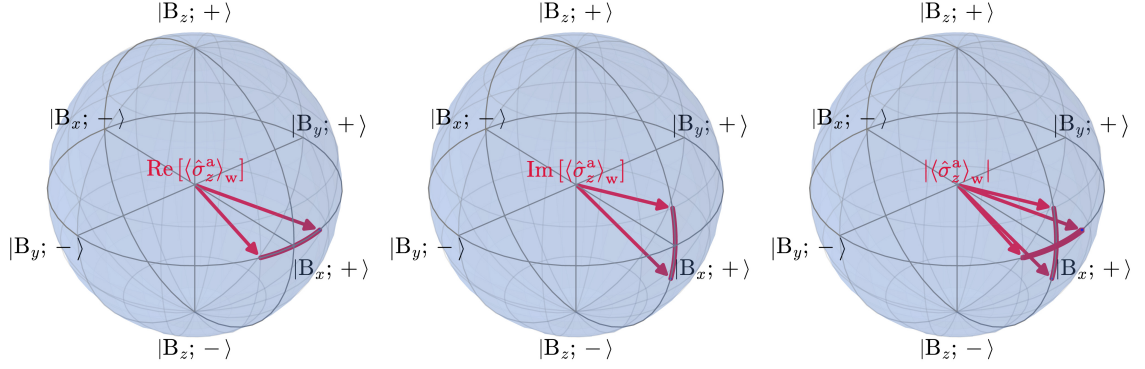


Figure 3.1: Effect of $\langle\hat{\sigma}_z^a\rangle_w$ on the state vector of the system B, depicted on the Bloch sphere: $\text{Re}[\langle\hat{\sigma}_z^a\rangle_w]$ rotates the state vector in the xy -plane (left); $\text{Im}[\langle\hat{\sigma}_z^a\rangle_w]$ moves the state vector out of the xy -plane towards the poles (middle); the modulus is simply a combination of both (right).

state around the z -axis in the xy -plane. In comparison $\text{Im}[\langle\hat{\sigma}_z^a\rangle_w]$ moves the state out of that plane towards the poles of the Bloch sphere. The weak value's modulus is then a combination of both movements on the sphere, just as the modulus of a general complex number consists of a combination of its real and imaginary part. It is also instructive to note that the weak value's modulus only appears with α^2 . It is a second order effect.

The real and imaginary part as well as the modulus of the weak value of the Pauli operator $\hat{\sigma}_z^s$ can now be extracted by evaluating the expectation values of the three Pauli operators of B, namely $\hat{\sigma}_x^b$, $\hat{\sigma}_y^b$ and $\hat{\sigma}_z^b$. Hence the six intensities $I_{x\pm}$, $I_{y\pm}$ and $I_{z\pm}$ have to be used. Basic algebra leads to the result^b.

$$\begin{aligned}
 I_{x+} &= |\langle B_x; + | \Psi_f \rangle|^2 \\
 &= \frac{|\langle A_f | A_i \rangle|^2}{4} [e^{i\alpha(u-iv)/2} + e^{-i\alpha(u-iv)/2}] [e^{-i\alpha(u+iv)/2} + e^{i\alpha(u+iv)/2}] \\
 &= \frac{|\langle A_f | A_i \rangle|^2}{2} \{ \cosh(\alpha \text{Im}[\langle\hat{\sigma}_z^a\rangle_w]) + \cos(\alpha \text{Re}[\langle\hat{\sigma}_z^a\rangle_w]) \}, \tag{3.8}
 \end{aligned}$$

^bFor simplicity's sake the short notation

$$\langle\hat{\sigma}_z^a\rangle_w = \text{Re}[\langle\hat{\sigma}_z^a\rangle_w] + i \text{Im}[\langle\hat{\sigma}_z^a\rangle_w] \equiv u + iv$$

was introduced in the above equations.

$$\begin{aligned}
I_{x-} &= |\langle B_x; - | \Psi_f \rangle|^2 \\
&= \frac{|\langle A_f | A_i \rangle|^2}{4} \left[e^{i\alpha(u-iv)/2} - e^{-i\alpha(u-iv)/2} \right] \left[e^{-i\alpha(u+iv)/2} - e^{i\alpha(u+iv)/2} \right] \\
&= \frac{|\langle A_f | A_i \rangle|^2}{2} \left\{ \cosh(\alpha \operatorname{Im} [\langle \hat{\sigma}_z^a \rangle_w]) - \cos(\alpha \operatorname{Re} [\langle \hat{\sigma}_z^a \rangle_w]) \right\}, \tag{3.9}
\end{aligned}$$

$$\begin{aligned}
I_{y+} &= |\langle B_y; + | \Psi_f \rangle|^2 \\
&= \frac{|\langle A_f | A_i \rangle|^2}{4} \left[e^{i\alpha(u-iv)/2} + i e^{-i\alpha(u-iv)/2} \right] \left[e^{-i\alpha(u+iv)/2} - i e^{i\alpha(u+iv)/2} \right] \\
&= \frac{|\langle A_f | A_i \rangle|^2}{2} \left\{ \cosh(\alpha \operatorname{Im} [\langle \hat{\sigma}_z^a \rangle_w]) + \sin(\alpha \operatorname{Re} [\langle \hat{\sigma}_z^a \rangle_w]) \right\}, \tag{3.10}
\end{aligned}$$

$$\begin{aligned}
I_{y-} &= |\langle B_y; - | \Psi_f \rangle|^2 \\
&= \frac{|\langle A_f | A_i \rangle|^2}{4} \left[e^{i\alpha(u-iv)/2} - i e^{-i\alpha(u-iv)/2} \right] \left[e^{-i\alpha(u+iv)/2} + i e^{i\alpha(u+iv)/2} \right] \\
&= \frac{|\langle A_f | A_i \rangle|^2}{2} \left\{ \cosh(\alpha \operatorname{Im} [\langle \hat{\sigma}_z^a \rangle_w]) - \sin(\alpha \operatorname{Re} [\langle \hat{\sigma}_z^a \rangle_w]) \right\}, \tag{3.11}
\end{aligned}$$

$$\begin{aligned}
I_{z+} &= |\langle B_z; + | \Psi_f \rangle|^2 = \frac{|\langle A_f | A_i \rangle|^2}{2} e^{-i\alpha(u+iv)/2} e^{i\alpha(u-iv)/2} \\
&= \frac{|\langle A_f | A_i \rangle|^2}{2} e^{\alpha \operatorname{Im} [\langle \hat{\sigma}_z^a \rangle_w]} \tag{3.12}
\end{aligned}$$

and

$$\begin{aligned}
I_{z-} &= |\langle B_z; - | \Psi_f \rangle|^2 = \frac{|\langle A_f | A_i \rangle|^2}{2} e^{i\alpha(u+iv)/2} e^{-i\alpha(u-iv)/2} \\
&= \frac{|\langle A_f | A_i \rangle|^2}{2} e^{-\alpha \operatorname{Im} [\langle \hat{\sigma}_z^a \rangle_w]}. \tag{3.13}
\end{aligned}$$

Combining the results for the intensities, all components of the weak value of the Pauli matrix are explicitly obtained as

$$\langle \hat{\sigma}_x^b \rangle = \frac{I_{x+} - I_{x-}}{I_{x+} + I_{x-}} = \frac{\cos(\alpha \operatorname{Re} [\langle \hat{\sigma}_z^a \rangle_w])}{\cosh(\alpha \operatorname{Im} [\langle \hat{\sigma}_z^a \rangle_w])} \tag{3.14a}$$

$$\langle \hat{\sigma}_y^b \rangle = \frac{I_{y+} - I_{y-}}{I_{y+} + I_{y-}} = \frac{\sin(\alpha \operatorname{Re} [\langle \hat{\sigma}_z^a \rangle_w])}{\cosh(\alpha \operatorname{Im} [\langle \hat{\sigma}_z^a \rangle_w])} \tag{3.14b}$$

$$\langle \hat{\sigma}_z^b \rangle = \frac{I_{z+} - I_{z-}}{I_{z+} + I_{z-}} = \tanh(\alpha \operatorname{Im} [\langle \hat{\sigma}_z^a \rangle_w]) \tag{3.14c}$$

In Eq. (3.4) the evolution operator was already expanded, considering only terms up to the first order in α . To arrive at a direct relation between experimentally observable quantities and the real as well as the imaginary part of the Pauli operator's weak value we expand Eqs. (3.14a) and (3.14b) once again around α . We get

$$\begin{aligned}\langle \hat{\sigma}_x^b \rangle &= \frac{\cos(\alpha \operatorname{Re}[\langle \hat{\sigma}_z^a \rangle_w])}{\cosh(\alpha \operatorname{Im}[\langle \hat{\sigma}_z^a \rangle_w])} = 1 - \frac{1}{2}\alpha^2 (\operatorname{Re}[\langle \hat{\sigma}_z^a \rangle_w]^2 + \operatorname{Im}[\langle \hat{\sigma}_z^a \rangle_w]^2) + \mathcal{O}(\alpha^4) \\ &\approx \cos(\alpha |\langle \hat{\sigma}_z^a \rangle_w|)\end{aligned}\quad (3.15a)$$

and

$$\begin{aligned}\langle \hat{\sigma}_y^b \rangle &= \frac{\sin(\alpha \operatorname{Re}[\langle \hat{\sigma}_z^a \rangle_w])}{\cosh(\alpha \operatorname{Im}[\langle \hat{\sigma}_z^a \rangle_w])} \\ &= \alpha \operatorname{Re}[\langle \hat{\sigma}_z^a \rangle_w] - \frac{\alpha^3 \operatorname{Re}[\langle \hat{\sigma}_z^a \rangle_w]^3}{3!} - \frac{\alpha^3 \operatorname{Re}[\langle \hat{\sigma}_z^a \rangle_w] \operatorname{Im}[\langle \hat{\sigma}_z^a \rangle_w]^2}{2} + \mathcal{O}(\alpha^5) \\ &= \alpha \operatorname{Re}[\langle \hat{\sigma}_z^a \rangle_w] - \frac{\alpha^3 \operatorname{Re}[\langle \hat{\sigma}_z^a \rangle_w]^3}{3!} \left[1 - \frac{3 \operatorname{Im}[\langle \hat{\sigma}_z^a \rangle_w]^2}{\operatorname{Re}[\langle \hat{\sigma}_z^a \rangle_w]^2} \right] + \mathcal{O}(\alpha^5) \\ &\approx \sin(\alpha \operatorname{Re}[\langle \hat{\sigma}_z^a \rangle_w]).\end{aligned}\quad (3.15b)$$

Eqs. (3.14c), (3.15a) and (3.15b) are a very important result, since they allow us to directly relate real and imaginary part as well as the modulus of $\langle \hat{\sigma}_z^a \rangle_w$ to expectation values of the two-level quantum system \mathcal{H}_B , i.e. to intensities obtained in an experiment. The relations

$$\operatorname{Re}[\langle \hat{\sigma}_z^a \rangle_w] = \frac{1}{\alpha} \arcsin(\langle \hat{\sigma}_y^b \rangle) = \frac{1}{\alpha} \arcsin\left(\frac{I_{y+} - I_{y-}}{I_{y+} + I_{y-}}\right) \quad (3.16a)$$

$$\operatorname{Im}[\langle \hat{\sigma}_z^a \rangle_w] = \frac{1}{\alpha} \operatorname{artanh}(\langle \hat{\sigma}_z^b \rangle) = \frac{1}{\alpha} \operatorname{artanh}\left(\frac{I_{z+} - I_{z-}}{I_{z+} + I_{z-}}\right) \quad (3.16b)$$

$$|\langle \hat{\sigma}_z^a \rangle_w| = \frac{1}{\alpha} \arccos(\langle \hat{\sigma}_x^b \rangle) = \frac{1}{\alpha} \arccos\left(\frac{I_{x+} - I_{x-}}{I_{x+} + I_{x-}}\right) \quad (3.16c)$$

hold up to the first order in α . Note that they not only link all components of the weak value to experimentally accessible quantities, but also hint at essential properties of the weak value. In general the weak value gives no meaningful information about a single event, but only about the ensemble average [Johansen, 2004, Dressel et al., 2014]. This property is evident in Eqs. (3.16), since they cannot be evaluated using a measurement of a single particle. The measurements needs to be repeated many times and therefore the knowledge about the whole ensemble is necessary to determine the expectation values of the $\hat{\sigma}_j^b$ operators.

It should be emphasized here that, given the intensities in Eqs. (3.8) to (3.13), we

can derive other relations in order to extract components of the Pauli operator's weak value. For example the imaginary part of $\langle \hat{\sigma}_z^a \rangle_w$ can be expressed by the sum of I_{x+} and I_{x-} or I_{y+} and I_{y-} as

$$\text{Im} [\langle \hat{\sigma}_z^a \rangle_w] = \frac{1}{\alpha} \text{arccosh} \left(\frac{I_{y+} + I_{y-}}{|\langle A_f | A_i \rangle|^2} \right), \quad (3.17)$$

where $|\langle A_f | A_i \rangle|^2$ acts as a normalization factor. However, Eq. (3.17) is obviously plain wrong! For an arbitrary postselected state the imaginary part of $\langle \hat{\sigma}_z^a \rangle_w$ can be negative. This means that the arccosh-function in Eq. (3.17) has to yield a negative number somehow. This is only possible if the function's argument becomes negative. In Eq. (3.17) the top of the fraction is a sum of two count rates, which is always positive. At the bottom of the fraction is a quantity's absolute square, which can never become negative by definition. Thus the argument in Eq. (3.17) will never become negative and it will never yield the imaginary part of the complex weak value.

Where did we go wrong? In Eq. (3.4) we expanded the evolution operator and neglected all terms but the linear one. In Eq. (3.6) we re-exponentiated, even though we only had terms of linear order in α . By using the exponential we made an approximation, which is afflicted with an error. This ultimately lead to the incorrect relation in Eq. (3.17). Then the question arises how we can be sure that the other relations we derived will hold? Fortunately the coupling between our two two-level systems can be solved analytically and the intensities expected in the experiment can be calculated.

3.1.2 Expected intensities for ideal situations

The intensities I_{x+} , I_{x-} , I_{y+} , I_{y-} , I_{z+} and I_{z-} are calculated analytically by taking the system's initial wave function given by Eq. (3.2) and letting the coupling Hamiltonian act on it.

$$\begin{aligned} |\Psi'\rangle &= e^{-i\alpha\hat{\sigma}_z^b\hat{\sigma}_z^a/2} \left[\sqrt{\frac{1}{2}} (|B_z; +\rangle + |B_z; -\rangle) \sqrt{\frac{1}{2}} (|A_z; +\rangle + |A_z; -\rangle) \right] \\ &= e^{-i\alpha\hat{\sigma}_z^b\hat{\sigma}_z^a/2} \frac{1}{2} (|B_z; +\rangle |A_z; +\rangle + |B_z; +\rangle |A_z; -\rangle + |B_z; -\rangle |A_z; +\rangle + |B_z; -\rangle |A_z; -\rangle) \\ &= \frac{1}{2} (e^{-i\alpha/2} |B_z; +\rangle |A_z; +\rangle + e^{i\alpha/2} |B_z; +\rangle |A_z; -\rangle + \\ &\quad + e^{i\alpha/2} |B_z; -\rangle |A_z; +\rangle + e^{-i\alpha/2} |B_z; -\rangle |A_z; -\rangle) \end{aligned} \quad (3.18)$$

Now we postselect on the final state to get $|\Psi_f\rangle = |A_f\rangle \langle A_f | \Psi'\rangle$

$$\begin{aligned}
|\Psi_f\rangle &= |A_f\rangle \left[\cos\left(\frac{\theta}{2}\right) \langle A_z; + | + \sin\left(\frac{\theta}{2}\right) e^{-i\phi} \langle A_z; - | \right] \times \\
&\quad \times \frac{1}{2} \left[e^{-i\alpha/2} |B_z; +\rangle |A_z; +\rangle + e^{i\alpha/2} |B_z; +\rangle |A_z; -\rangle + \right. \\
&\quad \left. + e^{i\alpha/2} |B_z; -\rangle |A_z; +\rangle + e^{-i\alpha/2} |B_z; -\rangle |A_z; -\rangle \right] \\
&= |A_f\rangle \frac{1}{2} \left[\cos\left(\frac{\theta}{2}\right) e^{-i\alpha/2} |B_z; +\rangle + \cos\left(\frac{\theta}{2}\right) e^{i\alpha/2} |B_z; -\rangle + \right. \\
&\quad \left. + \sin\left(\frac{\theta}{2}\right) e^{-i\phi} e^{i\alpha/2} |B_z; +\rangle + \sin\left(\frac{\theta}{2}\right) e^{-i\phi} e^{-i\alpha/2} |B_z; -\rangle \right] \\
&= |A_f\rangle \frac{1}{2} \left\{ \left[\cos\left(\frac{\theta}{2}\right) e^{-i\alpha/2} + \sin\left(\frac{\theta}{2}\right) e^{-i\phi} e^{i\alpha/2} \right] |B_z; +\rangle + \right. \\
&\quad \left. + \left[\cos\left(\frac{\theta}{2}\right) e^{i\alpha/2} + \sin\left(\frac{\theta}{2}\right) e^{-i\phi} e^{-i\alpha/2} \right] |B_z; -\rangle \right\} \quad (3.19)
\end{aligned}$$

Using Eq.(3.19) the intensities I_{x+} , I_{x-} , I_{y+} , I_{y-} , I_{z+} and I_{z-} are found to be

$$I_{x+} = |\langle B_x; + | \Psi_f \rangle|^2 = \frac{1}{2} \cos\left(\frac{\alpha}{2}\right)^2 [1 + \cos(\phi) \sin(\theta)], \quad (3.20)$$

$$I_{x-} = |\langle B_x; - | \Psi_f \rangle|^2 = \frac{1}{2} \sin\left(\frac{\alpha}{2}\right)^2 [1 - \cos(\phi) \sin(\theta)], \quad (3.21)$$

$$I_{y+} = |\langle B_y; + | \Psi_f \rangle|^2 = \frac{1}{4} [1 + \cos(\theta) \sin(\alpha) + \cos(\alpha) \cos(\phi) \sin(\theta)], \quad (3.22)$$

$$I_{y-} = |\langle B_y; - | \Psi_f \rangle|^2 = \frac{1}{4} [1 - \cos(\theta) \sin(\alpha) + \cos(\alpha) \cos(\phi) \sin(\theta)], \quad (3.23)$$

$$I_{z+} = |\langle B_z; + | \Psi_f \rangle|^2 = \frac{1}{4} [1 + \cos(\alpha - \phi) \sin(\theta)] \quad (3.24)$$

and

$$I_{z-} = |\langle B_z; - | \Psi_f \rangle|^2 = \frac{1}{4} [1 + \cos(\alpha + \phi) \sin(\theta)]. \quad (3.25)$$

Putting the intensities given above, into Eqs. (3.16a), (3.16b) and (3.16c), we get

$$\operatorname{Re} [\langle \hat{\sigma}_z^a \rangle_w] = \frac{1}{\alpha} \arcsin \left[\frac{1}{\csc(\alpha) \sec(\theta) + \cos(\phi) \cot(\alpha) \tan(\theta)} \right]. \quad (3.26a)$$

$$\operatorname{Im} [\langle \hat{\sigma}_z^a \rangle_w] = \frac{1}{\alpha} \operatorname{artanh} \left[\frac{\sin(\alpha) \sin(\phi)}{\cos(\alpha) \cos(\phi) + \csc(\theta)} \right] \quad (3.26b)$$

$$|\langle \hat{\sigma}_z^a \rangle_w| = \frac{1}{\alpha} \arccos \left[\frac{\cos(\alpha) + \cos(\phi) \sin(\theta)}{1 + \cos(\alpha) \cos(\phi) \sin(\theta)} \right] \quad (3.26c)$$

The analytic solution of the weak value is given by

$$\begin{aligned} \langle \hat{\sigma}_z^a \rangle_w &= \frac{\langle A_f | \hat{\sigma}_z^a | A_i \rangle}{\langle A_f | A_i \rangle} = \frac{\cos(\frac{\theta}{2}) - \sin(\frac{\theta}{2}) e^{-i\phi}}{\cos(\frac{\theta}{2}) + \sin(\frac{\theta}{2}) e^{-i\phi}} \\ &= \frac{\cos(\theta)}{1 + \sin(\theta) \cos(\phi)} - i \frac{\sin(\phi) \sin(\theta)}{1 + \sin(\theta) \cos(\phi)} \end{aligned} \quad (3.27)$$

The analytic solution of $\langle \hat{\sigma}_z^a \rangle_w$ can now be compared to an experimentally expected outcome for ideal measurements, which is given by the Eqs. (3.26a) to (3.26c). The result of such a comparison is depicted in Fig. 3.2, where Eqs. (3.26a) to (3.26c) are plotted in dashed red and the real and imaginary part of the weak value's analytic solution as well as its modulus are plotted in solid blue. For fixed parameters of $\phi = 60^\circ$ and $\alpha = 15^\circ$ a perfect agreement between the experimentally expected outcome and the analytic solution is found. This leads to the conclusion that Eqs. (3.16a) to (3.16c) can indeed be used to extract $\langle \hat{\sigma}_z^a \rangle_w$ from our measurement data.

3.1.3 Interactions with arbitrary strengths

For a deeper understanding we show here how relations between experimentally observable intensities and the weak value are derived without approximations. The derived relations can be used for measurements with arbitrary interaction strengths. Again the system's preselected state vector given by Eq.(3.2) is the starting point of the calculation. The evolution operator containing the interaction Hamiltonian acts upon it, but now instead of performing a series expansion around α the exact formula

$$\exp(-i\alpha \hat{\sigma}_z^a \hat{\sigma}_z^b / 2) = \cos(\alpha/2) - i \hat{\sigma}_z^a \hat{\sigma}_z^b \sin(\alpha/2) \quad (3.28)$$

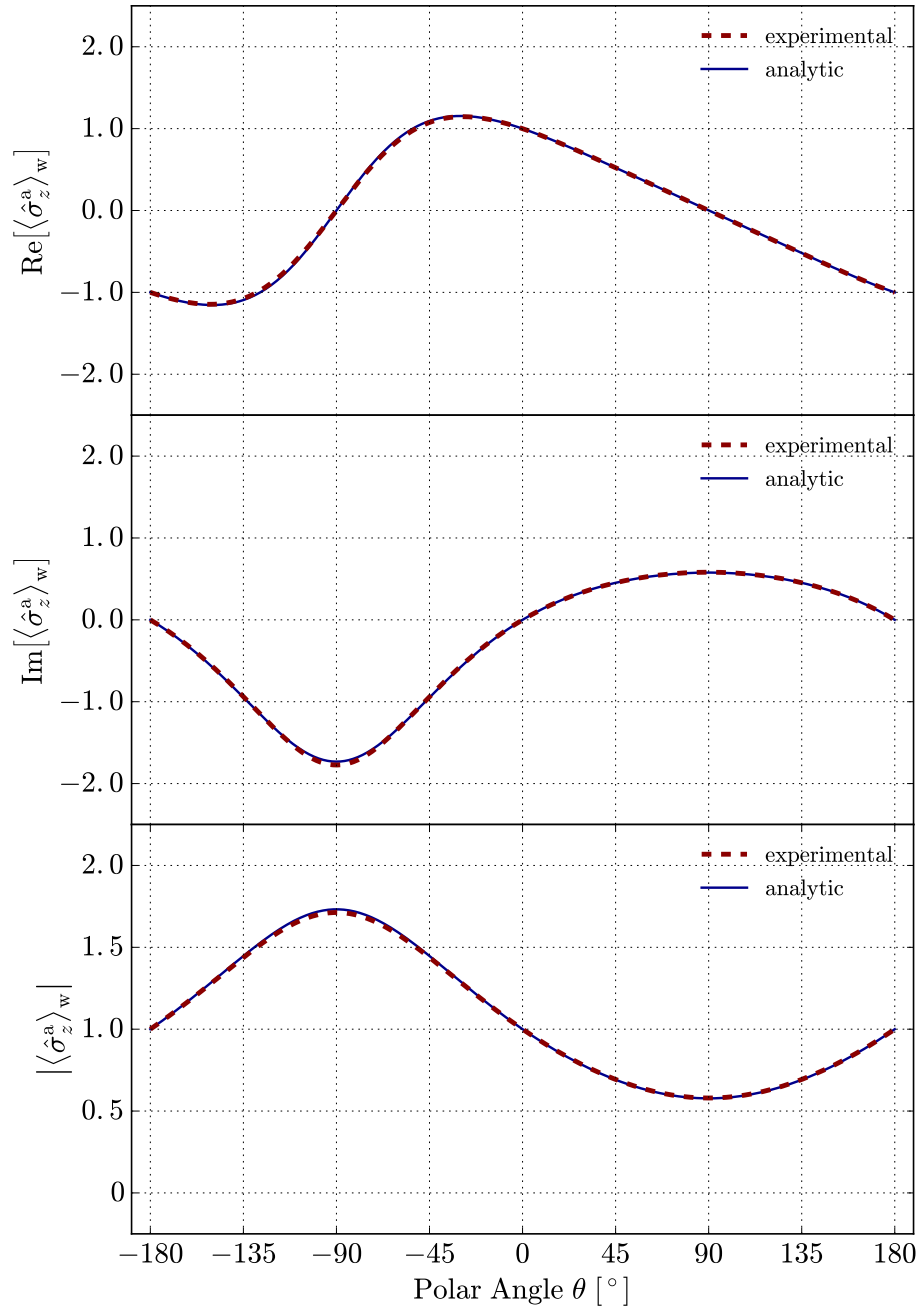


Figure 3.2: Comparison of the analytic solution and the experimentally expected outcome: The experimentally expected outcome [Eqs. (3.26a) to (3.26c)] is plotted in dashed red. The real and imaginary part of the weak value's analytic solution (top and middle) as well as its modulus (bottom) are plotted in solid blue. The analytic solution is given by Eq.(3.27). The parameters for the plot are $\phi = 60^\circ$ and $\alpha = 15^\circ$.

is used [Sakurai and Napolitano, 2011]. This is equivalent to taking all orders of α into account. The action of the evolution operator is then given by

$$\begin{aligned}
 |\Psi'\rangle &= e^{-i\alpha\hat{\sigma}_z^a\hat{\sigma}_z^b/2} |\Psi_i\rangle = \left[\cos\left(\frac{\alpha}{2}\right) - i\hat{\sigma}_z^a\hat{\sigma}_z^b \sin\left(\frac{\alpha}{2}\right) \right] |B_x; +\rangle |A_x; +\rangle \\
 &= \cos\left(\frac{\alpha}{2}\right) |B_x; +\rangle |A_x; +\rangle - i\hat{\sigma}_z^a\hat{\sigma}_z^b \sin\left(\frac{\alpha}{2}\right) |B_x; +\rangle |A_x; +\rangle \\
 &= \cos\left(\frac{\alpha}{2}\right) |B_x; +\rangle |A_x; +\rangle - i\hat{\sigma}_z^a \sin\left(\frac{\alpha}{2}\right) |B_x; -\rangle |A_x; +\rangle, \tag{3.29}
 \end{aligned}$$

Now the postselection on the the final state $|A_f\rangle$ is performed, leading to

$$\begin{aligned}
 |\Psi_f\rangle &= |A_f\rangle \left[\cos\left(\frac{\alpha}{2}\right) \langle A_f | A_i \rangle |B_x; +\rangle - i \sin\left(\frac{\alpha}{2}\right) |B_x; -\rangle \langle A_f | \hat{\sigma}_z^a | A_i \rangle \right] \\
 &= |A_f\rangle \langle A_f | A_i \rangle \left[\cos\left(\frac{\alpha}{2}\right) |B_x; +\rangle - i \sin\left(\frac{\alpha}{2}\right) \langle \hat{\sigma}_z^a \rangle_w |B_x; -\rangle \right] \\
 &= |A_f\rangle \langle A_f | A_i \rangle \left[\cos\left(\frac{\alpha}{2}\right) |B_x; +\rangle - i \sin\left(\frac{\alpha}{2}\right) (u + iv) |B_x; -\rangle \right] \\
 &= |A_f\rangle \frac{\langle A_f | A_i \rangle}{\sqrt{2}} \left\{ \left[\cos\left(\frac{\alpha}{2}\right) - i \sin\left(\frac{\alpha}{2}\right) (u + iv) \right] |B_z; +\rangle + \right. \\
 &\quad \left. + \left[\cos\left(\frac{\alpha}{2}\right) + i \sin\left(\frac{\alpha}{2}\right) (u + iv) \right] |B_z; -\rangle \right\}. \tag{3.30}
 \end{aligned}$$

Again the six intensities $I_{x\pm}$, $I_{y\pm}$ and $I_{z\pm}$ are of interest. They are given by

$$I_{x+} = |\langle B_x; + | \Psi_f \rangle|^2 = |\langle A_f | A_i \rangle|^2 \cos^2\left(\frac{\alpha}{2}\right), \tag{3.31}$$

$$\begin{aligned}
 I_{x-} &= |\langle B_x; - | \Psi_f \rangle|^2 = |\langle A_f | A_i \rangle|^2 \sin^2\left(\frac{\alpha}{2}\right) (v - iu)(v + iu) \\
 &= |\langle A_f | A_i \rangle|^2 \sin^2\left(\frac{\alpha}{2}\right) (u^2 + v^2) \\
 &= |\langle A_f | A_i \rangle|^2 \sin^2\left(\frac{\alpha}{2}\right) |\langle \hat{\sigma}_z^a \rangle_w|^2, \tag{3.32}
 \end{aligned}$$

$$\begin{aligned}
 I_{y+} &= |\langle B_y; + | \Psi_f \rangle|^2 \\
 &= \frac{|\langle A_f | A_i \rangle|^2}{4} \left[\cos\left(\frac{\alpha}{2}\right) (1 - i) - \sin\left(\frac{\alpha}{2}\right) (iu - v - u - iv) \right] \times \\
 &\quad \times \left[\cos\left(\frac{\alpha}{2}\right) (1 + i) - \sin\left(\frac{\alpha}{2}\right) (-iu - v - u + iv) \right] \\
 &= \frac{|\langle A_f | A_i \rangle|^2}{4} \left\{ 1 + [u^2 + v^2] + [1 - (u^2 + v^2)] \cos(\alpha) + 2u \sin(\alpha) \right\} \\
 &= \frac{|\langle A_f | A_i \rangle|^2}{4} \left\{ 1 + \cos(\alpha) + [1 - \cos(\alpha)] |\langle \hat{\sigma}_z^a \rangle_w|^2 + 2 \operatorname{Re} [\langle \hat{\sigma}_z^a \rangle_w] \sin(\alpha) \right\}, \tag{3.33}
 \end{aligned}$$

$$\begin{aligned}
I_{y-} &= |\langle B_y; - | \Psi_f \rangle|^2 \\
&= \frac{|\langle A_f | A_i \rangle|^2}{4} \left[\cos\left(\frac{\alpha}{2}\right) (1+i) - \sin\left(\frac{\alpha}{2}\right) (iu - v + u + iv) \right] \times \\
&\quad \times \left[\cos\left(\frac{\alpha}{2}\right) (1-i) - \sin\left(\frac{\alpha}{2}\right) (-iu - v + u - iv) \right] \\
&= \frac{|\langle A_f | A_i \rangle|^2}{4} \{ 1 + [u^2 + v^2] + [1 - (u^2 + v^2)] \cos(\alpha) - 2u \sin(\alpha) \} \\
&= \frac{|\langle A_f | A_i \rangle|^2}{4} \{ 1 + \cos(\alpha) + [1 - \cos(\alpha)] |\langle \hat{\sigma}_z^a \rangle_w|^2 - 2 \operatorname{Re} [\langle \hat{\sigma}_z^a \rangle_w] \sin(\alpha) \}, \tag{3.34}
\end{aligned}$$

$$\begin{aligned}
I_{z+} &= |\langle B_z; + | \Psi_f \rangle|^2 \\
&= \frac{|\langle A_f | A_i \rangle|^2}{2} \left[\cos\left(\frac{\alpha}{2}\right) - i \sin\left(\frac{\alpha}{2}\right) (u + iv) \right] \left[\cos\left(\frac{\alpha}{2}\right) + i \sin\left(\frac{\alpha}{2}\right) (u - iv) \right] \\
&= \frac{|\langle A_f | A_i \rangle|^2}{4} [1 + u^2 + v^2 - (u^2 + v^2 - 1) \cos(\alpha) + 2v \sin(\alpha)] \\
&= \frac{|\langle A_f | A_i \rangle|^2}{4} \{ 1 + \cos(\alpha) - [\cos(\alpha) - 1] |\langle \hat{\sigma}_z^a \rangle_w|^2 + 2 \operatorname{Im} [\langle \hat{\sigma}_z^a \rangle_w] \sin(\alpha) \} \tag{3.35}
\end{aligned}$$

and

$$\begin{aligned}
I_{z-} &= |\langle B_z; + | \Psi_f \rangle|^2 \\
&= \frac{|\langle A_f | A_i \rangle|^2}{2} \left[\cos\left(\frac{\alpha}{2}\right) + i \sin\left(\frac{\alpha}{2}\right) (u + iv) \right] \left[\cos\left(\frac{\alpha}{2}\right) - i \sin\left(\frac{\alpha}{2}\right) (u - iv) \right] \\
&= \frac{|\langle A_f | A_i \rangle|^2}{4} [1 + u^2 + v^2 - (u^2 + v^2 - 1) \cos(\alpha) - 2v \sin(\alpha)] \\
&= \frac{|\langle A_f | A_i \rangle|^2}{4} \{ 1 + \cos(\alpha) - [\cos(\alpha) - 1] |\langle \hat{\sigma}_z^a \rangle_w|^2 - 2 \operatorname{Im} [\langle \hat{\sigma}_z^a \rangle_w] \sin(\alpha) \}. \tag{3.36}
\end{aligned}$$

At this point one easily sees why the relation given by Eq. (3.17) fails to yield the imaginary part of the weak value. If an exact calculation using no approximations is performed, the imaginary part does not appear independently in the intensities I_{x+} , I_{x-} , I_{y+} and I_{y-} . The imaginary part of $\langle \hat{\sigma}_z^a \rangle_w$ appears nowhere on its own. It is always squared and always in combination with $\operatorname{Re} [\langle \hat{\sigma}_z^a \rangle_w]$. This means that the only information obtained from these intensities about the imaginary part is somehow extracted from the weak value's modulus. We can only extract the imaginary part's modulus. That is why one needs the intensities I_{z+} and I_{z-} to determine the imaginary part. Again we calculate the expectation $\langle \hat{\sigma}_x^b \rangle$, $\langle \hat{\sigma}_y^b \rangle$ and $\langle \hat{\sigma}_z^b \rangle$, to see whether they give the information needed to determine the weak value. Starting

with $\langle \hat{\sigma}_x^b \rangle$ we find

$$\langle \hat{\sigma}_x^b \rangle = \frac{I_{x+} - I_{x-}}{I_{x+} + I_{x-}} = \frac{\cos\left(\frac{\alpha}{2}\right)^2 - |\langle \hat{\sigma}_z^a \rangle_w|^2 \sin\left(\frac{\alpha}{2}\right)^2}{\cos\left(\frac{\alpha}{2}\right)^2 + |\langle \hat{\sigma}_z^a \rangle_w|^2 \sin\left(\frac{\alpha}{2}\right)^2}, \quad (3.37)$$

some basic mathematical simplifications show that the modulus of the Pauli operator's weak value can be determined by

$$|\langle \hat{\sigma}_z^a \rangle_w| = \cot\left(\frac{\alpha}{2}\right) \sqrt{\frac{I_{x-}}{I_{x+}}}. \quad (3.38)$$

Note that Eq. (3.38) is exact. No approximations are made during its derivation. The expectation value of $\hat{\sigma}_y^b$ becomes

$$\langle \hat{\sigma}_y^b \rangle = \frac{I_{y+} - I_{y-}}{I_{y+} + I_{y-}} = \frac{2 \operatorname{Re} [\langle \hat{\sigma}_z^a \rangle_w] \sin(\alpha)}{1 + |\langle \hat{\sigma}_z^a \rangle_w|^2 + (1 - |\langle \hat{\sigma}_z^a \rangle_w|^2) \cos(\alpha)}. \quad (3.39)$$

Similarly we find for the expectation value of $\hat{\sigma}_z^b$

$$\langle \hat{\sigma}_z^b \rangle = \frac{I_{z+} - I_{z-}}{I_{z+} + I_{z-}} = \frac{2 \operatorname{Im} [\langle \hat{\sigma}_z^a \rangle_w] \sin(\alpha)}{1 + |\langle \hat{\sigma}_z^a \rangle_w|^2 + (1 - |\langle \hat{\sigma}_z^a \rangle_w|^2) \cos(\alpha)}. \quad (3.40)$$

Note that the expectation values given by Eqs. (3.39) and (3.40) have no direct relations between the weak value and experimentally observable intensities, which make it possible to extract the real and imaginary part of the weak value respectively. Nevertheless it can be shown that they are equivalent to relations (3.16a) and (3.16b) up to the first order of α :

$$\begin{aligned} \langle \hat{\sigma}_y^b \rangle &= \frac{2 \operatorname{Re} [\langle \hat{\sigma}_z^a \rangle_w] \sin(\alpha)}{1 + |\langle \hat{\sigma}_z^a \rangle_w|^2 + (1 - |\langle \hat{\sigma}_z^a \rangle_w|^2) \cos(\alpha)} \\ &\approx \operatorname{Re} [\langle \hat{\sigma}_z^a \rangle_w] + \mathcal{O}(\alpha^2), \end{aligned} \quad (3.41a)$$

$$\begin{aligned} \langle \hat{\sigma}_z^b \rangle &= \frac{2 \operatorname{Im} [\langle \hat{\sigma}_z^a \rangle_w] \sin(\alpha)}{1 + |\langle \hat{\sigma}_z^a \rangle_w|^2 + (1 - |\langle \hat{\sigma}_z^a \rangle_w|^2) \cos(\alpha)} \\ &\approx \operatorname{Im} [\langle \hat{\sigma}_z^a \rangle_w] + \mathcal{O}(\alpha^2). \end{aligned} \quad (3.41b)$$

Making the same expansions for Eqs. (3.14c) and (3.15b) one finds the equivalency with the approximation $\alpha \ll 1$.

The direct relations between the components of the weak value and experimentally

observable quantities are given by.

$$I_{x+} - I_{x-} = |\langle A_f | A_i \rangle|^2 \left[\cos\left(\frac{\alpha}{2}\right)^2 - |\langle \hat{\sigma}_z^a \rangle_w|^2 \sin\left(\frac{\alpha}{2}\right)^2 \right], \quad (3.42a)$$

$$I_{x+} + I_{x-} = |\langle A_f | A_i \rangle|^2 \left[\cos\left(\frac{\alpha}{2}\right)^2 + |\langle \hat{\sigma}_z^a \rangle_w|^2 \sin\left(\frac{\alpha}{2}\right)^2 \right], \quad (3.42b)$$

$$I_{y+} - I_{y-} = |\langle A_f | A_i \rangle|^2 \operatorname{Re} [\langle \hat{\sigma}_z^a \rangle_w] \sin(\alpha), \quad (3.42c)$$

$$I_{y+} + I_{y-} = \frac{|\langle A_f | A_i \rangle|^2}{2} \{1 + \cos(\alpha) - [\cos(\alpha) - 1] |\langle \hat{\sigma}_z^a \rangle_w|^2\}, \quad (3.42d)$$

$$I_{z+} - I_{z-} = |\langle A_f | A_i \rangle|^2 \operatorname{Im} [\langle \hat{\sigma}_z^a \rangle_w] \sin(\alpha), \quad (3.42e)$$

$$I_{z+} + I_{z-} = \frac{|\langle A_f | A_i \rangle|^2}{2} \{1 + \cos(\alpha) - [\cos(\alpha) - 1] |\langle \hat{\sigma}_z^a \rangle_w|^2\}. \quad (3.42f)$$

The relations

$$\operatorname{Re} [\langle \hat{\sigma}_z^a \rangle_w] = \frac{1}{2} \cot\left(\frac{\alpha}{2}\right) \frac{I_{y+} - I_{y-}}{I_{x+}} \quad (3.43)$$

and

$$\operatorname{Im} [\langle \hat{\sigma}_z^a \rangle_w] = \frac{1}{2} \cot\left(\frac{\alpha}{2}\right) \frac{I_{z+} - I_{z-}}{I_{x+}} \quad (3.44)$$

allow to extract the real and the imaginary part of the Pauli operator's weak value, without using any approximations or dealing with any normalization factors. As an incidental remark we now want to show how it is possible to use the system \mathcal{H}_B to strongly measure the $|A_x; +\rangle$ state of \mathcal{H}_A in an ideal Stern-Gerlach sense. This means that only maximum interaction strengths ($\alpha = \pi/2$) are considered and that the the initial state $|A_x; +\rangle$ should be separated into its eigenstates, i.e. the measurement should allow to select the state vectors $|A_z; +\rangle$ and $|A_z; -\rangle$.

We start with the system's preselected sate vector given by Eq.(3.2)

$$|\Psi_i\rangle = |A_i\rangle |B_i\rangle = |A_x; +\rangle |B_x; +\rangle = \frac{1}{\sqrt{2}} (|B_z; +\rangle + |B_z; -\rangle) |A_x; +\rangle. \quad (3.45)$$

and let the the evolution operator with the interaction Hamiltonian act on the state vector:

$$\begin{aligned} |\Psi'\rangle &= e^{-i\alpha \hat{\sigma}_z^a \hat{\sigma}_z^b / 2} |\psi\rangle = e^{-i\alpha \hat{\sigma}_z^a \hat{\sigma}_z^b / 2} |B_x; +\rangle |A_x; +\rangle \\ &= \left[\cos\left(\frac{\alpha}{2}\right) - i \hat{\sigma}_z^a \hat{\sigma}_z^b \sin\left(\frac{\alpha}{2}\right) \right] |B_x; +\rangle |A_x; +\rangle \end{aligned} \quad (3.46)$$

We set $\alpha = \pi/2$ and get

$$\begin{aligned}
|\Psi'\rangle(\pi/2) &= \frac{1}{\sqrt{2}} |A_x; +\rangle |B_x; +\rangle - \frac{i}{\sqrt{2}} |A_x; -\rangle |B_x; -\rangle \\
&= \frac{1}{\sqrt{8}} [|B_z; +\rangle |A_z; +\rangle + |B_z; +\rangle |A_z; -\rangle + |B_z; -\rangle |A_z; +\rangle + |B_z; -\rangle |A_z; -\rangle - \\
&\quad -i(|B_z; +\rangle |A_z; +\rangle - |B_z; +\rangle |A_z; -\rangle - |B_z; -\rangle |A_z; +\rangle + |B_z; -\rangle |A_z; -\rangle)] \\
&= \frac{1}{\sqrt{8}} \{[(1-i)|A_z; +\rangle + (1+i)|A_z; -\rangle] |B_z; +\rangle + \\
&\quad + [(1+i)|A_z; +\rangle + (1-i)|A_z; -\rangle] |B_z; -\rangle\} \tag{3.47}
\end{aligned}$$

Finally we add an additional phase shift of $\exp(i\pi/4) = 1+i/\sqrt{2}$ to the state $|B_z; +\rangle$ and one of $\exp(-i\pi/4) = 1-i/\sqrt{2}$ to $|B_z; -\rangle$.

$$\begin{aligned}
|\Psi''\rangle &= \frac{1}{\sqrt{16}} \{(1+i)[(1-i)|A_z; +\rangle + (1+i)|A_z; -\rangle] |B_z; +\rangle + \\
&\quad + (1-i)[(1+i)|A_z; +\rangle + (1-i)|A_z; -\rangle] |B_z; -\rangle\} \\
&= \frac{1}{2} \{[|A_z; +\rangle + i|A_z; -\rangle] |B_z; +\rangle + [|A_z; +\rangle - i|A_z; -\rangle] |B_z; -\rangle\} \tag{3.48}
\end{aligned}$$

To select either the $|A_z; +\rangle$ or the $|A_z; -\rangle$ states of the initial superposition state $|A_x; +\rangle$ one needs to postselect on either $|B_x; +\rangle$ or $|B_x; -\rangle$ respectively. Then one can select the $|A_z; +\rangle$ state

$$\begin{aligned}
|\Psi_f\rangle_{x+} &= |B_x; -\rangle \langle B_x; - | \Psi''\rangle \\
&= \frac{1}{\sqrt{32}} \{2|A_z; +\rangle - 2i|A_z; -\rangle + 2|A_z; +\rangle + 2i|A_z; -\rangle\} |B_x; +\rangle \\
&= \frac{1}{\sqrt{2}} |A_z; +\rangle |B_x; +\rangle \tag{3.49}
\end{aligned}$$

or the $|A_z; -\rangle$ state

$$\begin{aligned}
|\Psi_f\rangle_{x-} &= |B_x; -\rangle \langle B_x; - | \Psi''\rangle \\
&= \frac{1}{\sqrt{32}} \{2|A_z; +\rangle - 2i|A_z; -\rangle - 2|A_z; +\rangle - 2i|A_z; -\rangle\} |B_x; -\rangle \\
&= \frac{-i}{\sqrt{2}} |A_z; -\rangle |B_x; -\rangle. \tag{3.50}
\end{aligned}$$

We see that two two-level quantum systems can be used to build a Stern-Gerlach like apparatus, which separates the $|A_z; +\rangle$ and $|A_z; -\rangle$ states of an initial state $|A_x; +\rangle$ up to an irrelevant phase.

3.2 Weak values of projection operators

In this section we show how to completely determine the weak value of projection operators using two two-level quantum systems. As in the previous section we want to measure operators of system \mathcal{H}_A using \mathcal{H}_B as a meter system.

Let $\langle \hat{\Pi}_{z\pm}^a \rangle_w$ be the projection operator onto the states $|A_z; \pm\rangle$. If one relies on the completeness of two-level system, i.e. if one uses the relations

$$\langle \hat{\sigma}_z^a \rangle_w = \langle \hat{\Pi}_{z+}^a \rangle_w - \langle \hat{\Pi}_{z-}^a \rangle_w \quad (3.51a)$$

$$1 = \langle \hat{\Pi}_{z+}^a \rangle_w + \langle \hat{\Pi}_{z-}^a \rangle_w \quad (3.51b)$$

the measurement of the Pauli operator $\hat{\sigma}_z^a$ also yields the projection operators' weak values $\langle \hat{\Pi}_{z+}^a \rangle_w$ and $\langle \hat{\Pi}_{z-}^a \rangle_w$. Here we show a more direct way, which does not rely on the assumption of linearity and completeness.

3.2.1 Weak interaction

Again we want to use the same preselected state as in the last section, which was given by Eq. (3.2). Then, in order to measure $\langle \hat{\Pi}_{z\pm}^a \rangle_w$ we have to change the interaction Hamiltonian accordingly. We modify the Hamiltonian from Eq. (3.3) to

$$\hat{H}_{\text{int}} = \frac{\alpha \hat{\Pi}_{z\pm}^a \hat{\sigma}_z^b}{2}. \quad (3.52)$$

Instead of coupling two Pauli operators to each other the interaction Hamiltonian now couples projection operators of system A to the meter system B. The action of the Hamiltonian can still be understood as a rotation of the state vector $|A_i\rangle$ around the z -axis of Hilbert space A by the angle α conditioned on the Hilbert space of B. While in Eq. (3.3) the conditioning was symmetric on the states $|B_z; \pm\rangle$, it is now asymmetric on either $|B_z; +\rangle$ or $|B_z; -\rangle$.

First we make the standard weak measurement approach, in which we series expand an evolution operator and then neglect all terms higher than the linear order.

$$|\Psi'\rangle = e^{-i\alpha \hat{\Pi}_{z\pm}^a \hat{\sigma}_z^b/2} |\Psi_i\rangle \approx (1 - i\alpha \hat{\Pi}_{z\pm}^a \hat{\sigma}_z^b/2) |\Psi_i\rangle = (1 - i\alpha \hat{\Pi}_{z\pm}^a \hat{\sigma}_z^b/2) |B_i\rangle |A_i\rangle \quad (3.53)$$

It is trivial to show that Eqs. (3.16a) to (3.16c) will hold for the case of projection operators as well. We can extract all parts of $\langle \hat{\Pi}_{z\pm}^a \rangle_w$ using

$$\operatorname{Re} \left[\left\langle \hat{\Pi}_{z\pm}^a \right\rangle_w \right] = \frac{1}{\alpha} \arcsin (\langle \hat{\sigma}_y^b \rangle) \quad (3.54a)$$

$$\operatorname{Im} \left[\left\langle \hat{\Pi}_{z\pm}^a \right\rangle_w \right] = \frac{1}{\alpha} \operatorname{artanh} (\langle \hat{\sigma}_z^b \rangle) \quad (3.54b)$$

$$\left| \left\langle \hat{\Pi}_{z\pm}^a \right\rangle_w \right| = \frac{1}{\alpha} \arccos (\langle \hat{\sigma}_x^b \rangle). \quad (3.54c)$$

3.2.2 Strong interactions

Here we now want to proceed with the case of strong interactions. For this we have to take a closer look at the evolution operator $U(\alpha) = \exp(-i\alpha\hat{\Pi}_{z\pm}^a\hat{\sigma}_z^b/2)$. The exact formula we used in subsection 3.1.3 does not hold any more since $(\hat{\Pi}_{z\pm}^a)^2 \neq \mathbb{1}$. However, we can use the idempotence of projection operators to find a different analytic solution for the evolution operator.

$$\begin{aligned} U(\alpha) &= e^{-i\alpha\hat{\Pi}_{z\pm}^a\hat{\sigma}_z^b/2} \\ &= 1 - \frac{i}{2}\alpha\hat{\Pi}_{z\pm}^a\hat{\sigma}_z^b - \frac{1}{8}\alpha^2(\hat{\Pi}_{z\pm}^a)^2(\hat{\sigma}_z^b)^2 + \frac{i}{48}\alpha^3(\hat{\sigma}_z^b)^3(\hat{\Pi}_{z\pm}^a)^3 + \mathcal{O}(\alpha^4) \\ &= 1 - \frac{i}{2}\alpha\hat{\Pi}_{z\pm}^a\hat{\sigma}_z^b - \frac{1}{8}\alpha^2\hat{\Pi}_{z\pm}^a + \frac{i}{48}\alpha^3\hat{\sigma}_z^b\hat{\Pi}_{z\pm}^a + \dots \\ &= 1 - \hat{\Pi}_{z\pm}^a \left(\frac{i}{2}\alpha\hat{\sigma}_z^b + \frac{1}{8}\alpha^2 - \frac{i}{48}\alpha^3\hat{\sigma}_z^b + \dots \right) \\ &= 1 - \hat{\Pi}_{z\pm}^a \left\{ i \left[\frac{1}{2}\alpha\hat{\sigma}_z^b - \frac{(\hat{\sigma}_z^b)^3}{3!} \left(\frac{\alpha}{2} \right)^3 + \dots \right] + \left[\frac{1}{2!} \left(\frac{\alpha}{2} \right)^2 - \frac{1}{4!} \left(\frac{\alpha}{4} \right)^2 + \dots \right] \right\} \\ &= 1 - \hat{\Pi}_{z\pm}^a \left[i\hat{\sigma}_z^b \sin\left(\frac{\alpha}{2}\right) + 2 \sin\left(\frac{\alpha}{4}\right)^2 \right] \end{aligned} \quad (3.55)$$

Equation. (3.55) is exact [Vallone and Dequal, 2016]. No approximations are made and it is valid for any angle α . As in the previous section we can now let the evolution operator act upon our system's state vector:

$$\begin{aligned} |\Psi'\rangle &= e^{-i\alpha\hat{\sigma}_z^b\hat{\Pi}_{z\pm}^a/2} |\Psi_i\rangle = e^{-i\alpha\hat{\sigma}_z^b\hat{\Pi}_{z\pm}^a/2} |A_i\rangle |B_i\rangle \\ &= \left\{ 1 - \hat{\Pi}_{z\pm}^a \left[i\hat{\sigma}_z^b \sin\left(\frac{\alpha}{2}\right) + 2 \sin\left(\frac{\alpha}{4}\right)^2 \right] \right\} |A_i\rangle |B_x; +\rangle \\ &= |B_x; +\rangle |A_i\rangle - \hat{\Pi}_{z\pm}^a |A_i\rangle \left[i\hat{\sigma}_z^b \sin\left(\frac{\alpha}{2}\right) + 2 \sin\left(\frac{\alpha}{4}\right)^2 \right] |B_x; +\rangle \\ &= |B_x; +\rangle |A_i\rangle - \hat{\Pi}_{z\pm}^a |A_i\rangle \left[i \sin\left(\frac{\alpha}{2}\right) |B_x; -\rangle + 2 \sin\left(\frac{\alpha}{4}\right)^2 |B_x; +\rangle \right]. \end{aligned} \quad (3.56)$$

Now postselection on some final state $|A_f\rangle$ is carried out.

$$\begin{aligned}
|\Psi_f\rangle &= |A_f\rangle \langle A_f | \Psi' \rangle \\
&= |A_f\rangle \langle A_f | A_i \rangle |B_x; +\rangle - \langle A_f | \hat{\Pi}_{z\pm}^a | A_i \rangle \left[i \sin\left(\frac{\alpha}{2}\right) |B_x; -\rangle + 2 \sin\left(\frac{\alpha}{4}\right)^2 |B_x; +\rangle \right] \\
&= |A_f\rangle \langle A_f | A_i \rangle \left\{ |B_x; +\rangle - \langle \hat{\Pi}_{z\pm}^a \rangle_w \left[i \sin\left(\frac{\alpha}{2}\right) |B_x; -\rangle + 2 \sin\left(\frac{\alpha}{4}\right)^2 |B_x; +\rangle \right] \right\} \\
&= |A_f\rangle \frac{\langle A_f | A_i \rangle}{\sqrt{2}} \left\{ \left[1 - i \sin\left(\frac{\alpha}{2}\right) \langle \hat{\Pi}_{z\pm}^a \rangle_w - 2 \sin\left(\frac{\alpha}{4}\right)^2 \langle \hat{\Pi}_{z\pm}^a \rangle_w \right] |B_z; +\rangle + \right. \\
&\quad \left. + \left[1 + i \sin\left(\frac{\alpha}{2}\right) \langle \hat{\Pi}_{z\pm}^a \rangle_w - 2 \sin\left(\frac{\alpha}{4}\right)^2 \langle \hat{\Pi}_{z\pm}^a \rangle_w \right] |B_z; -\rangle \right\} \tag{3.57}
\end{aligned}$$

Similar to the treatment of weak values of Pauli operators, the weak value of projection operator $\hat{\Pi}_{z\pm}^a$ gets “encoded” on the two-level quantum system B. In the limiting case of zero interaction, i.e. $\alpha = 0$, the weak value vanishes. To read out the the real and imaginary part of the weak value, as well as its modulus the meter system B has to be evaluated. For this we perform strong projective measurements along the six directions $|B_x; \pm\rangle$, $|B_y; \pm\rangle$ and $|B_z; \pm\rangle$. We find the six intensities corresponding to the projective spin measurements to be

$$\begin{aligned}
I_{x+} &= |\langle B_x; + | \Psi_f \rangle|^2 \\
&= |\langle A_f | A_i \rangle|^2 \left\{ 1 - 4 \operatorname{Re} \left[\langle \hat{\Pi}_{z\pm}^a \rangle_w \right] \sin\left(\frac{\alpha}{4}\right)^2 + 4 \left| \langle \hat{\Pi}_{z\pm}^a \rangle_w \right|^2 \sin\left(\frac{\alpha}{4}\right)^4 \right\}, \tag{3.58}
\end{aligned}$$

$$\begin{aligned}
I_{x-} &= |\langle B_x; - | \Psi_f \rangle|^2 \\
&= |\langle A_f | A_i \rangle|^2 \left| \langle \hat{\Pi}_{z\pm}^a \rangle_w \right|^2 \sin\left(\frac{\alpha}{2}\right)^2, \tag{3.59}
\end{aligned}$$

$$\begin{aligned}
I_{y+} &= |\langle B_y; + | \Psi_f \rangle|^2 \\
&= \frac{|\langle A_f | A_i \rangle|^2}{2} \left\{ 1 + \left| \langle \hat{\Pi}_{z\pm}^a \rangle_w \right|^2 [2 + \sin(\alpha)] - 2 \operatorname{Re} \left[\langle \hat{\Pi}_{z\pm}^a \rangle_w \right] - \right. \\
&\quad \left. - 2 \left[\cos\left(\frac{\alpha}{2}\right) + \sin\left(\frac{\alpha}{2}\right) \right] \left[\left| \langle \hat{\Pi}_{z\pm}^a \rangle_w \right|^2 - \operatorname{Re} \left[\langle \hat{\Pi}_{z\pm}^a \rangle_w \right] \right] \right\}, \tag{3.60}
\end{aligned}$$

$$\begin{aligned}
I_{y-} &= |\langle B_y; - | \Psi_f \rangle|^2 \\
&= \frac{|\langle A_f | A_i \rangle|^2}{2} \left\{ 1 + \left| \langle \hat{\Pi}_{z\pm}^a \rangle_w \right|^2 [2 - \sin(\alpha)] - 2 \operatorname{Re} \left[\langle \hat{\Pi}_{z\pm}^a \rangle_w \right] - \right. \\
&\quad \left. - 2 \left[\cos\left(\frac{\alpha}{2}\right) - \sin\left(\frac{\alpha}{2}\right) \right] \left[\left| \langle \hat{\Pi}_{z\pm}^a \rangle_w \right|^2 - \operatorname{Re} \left[\langle \hat{\Pi}_{z\pm}^a \rangle_w \right] \right] \right\}, \tag{3.61}
\end{aligned}$$

$$\begin{aligned}
I_{z+} &= |\langle B_z; + | \Psi_f \rangle|^2 \\
&= \frac{|\langle A_f | A_i \rangle|^2}{2} \left\{ 1 + 2 \left| \langle \hat{\Pi}_{z\pm}^a \rangle_w \right|^2 - 2 \operatorname{Re} \left[\langle \hat{\Pi}_{z\pm}^a \rangle_w \right] + 2 \sin\left(\frac{\alpha}{2}\right) \operatorname{Im} \left[\langle \hat{\Pi}_{z\pm}^a \rangle_w \right] - \right. \\
&\quad \left. - 2 \cos\left(\frac{\alpha}{2}\right) \left[\left| \langle \hat{\Pi}_{z\pm}^a \rangle_w \right|^2 - \operatorname{Re} \left[\langle \hat{\Pi}_{z\pm}^a \rangle_w \right] \right] \right\}, \tag{3.62}
\end{aligned}$$

and

$$\begin{aligned}
I_{z-} &= |\langle B_z; - | \Psi_f \rangle|^2 \\
&= \frac{|\langle A_f | A_i \rangle|^2}{2} \left\{ 1 + 2 \left| \langle \hat{\Pi}_{z\pm}^a \rangle_w \right|^2 - 2 \operatorname{Re} \left[\langle \hat{\Pi}_{z\pm}^a \rangle_w \right] - 2 \sin\left(\frac{\alpha}{2}\right) \operatorname{Im} \left[\langle \hat{\Pi}_{z\pm}^a \rangle_w \right] - \right. \\
&\quad \left. - 2 \cos\left(\frac{\alpha}{2}\right) \left[\left| \langle \hat{\Pi}_{z\pm}^a \rangle_w \right|^2 - \operatorname{Re} \left[\langle \hat{\Pi}_{z\pm}^a \rangle_w \right] \right] \right\}, \tag{3.63}
\end{aligned}$$

These rather complicated expressions can be dramatically simplified, if we only consider the special case of a measurement with maximum strength, i.e. if $\alpha = -\pi$. In this case we get

$$I_{x+} = |\langle A_f | A_i \rangle|^2 \left\{ 1 - 2 \operatorname{Re} \left[\langle \hat{\Pi}_{z\pm}^a \rangle_w \right] + \left| \langle \hat{\Pi}_{z\pm}^a \rangle_w \right|^2 \right\}, \tag{3.64a}$$

$$I_{x-} = |\langle A_f | A_i \rangle|^2 \left| \langle \hat{\Pi}_{z\pm}^a \rangle_w \right|^2, \tag{3.64b}$$

$$I_{y+} = \frac{|\langle A_f | A_i \rangle|^2}{2} \left\{ 1 - 4 \operatorname{Re} \left[\langle \hat{\Pi}_{z\pm}^a \rangle_w \right] + 4 \left| \langle \hat{\Pi}_{z\pm}^a \rangle_w \right|^2 \right\}, \tag{3.64c}$$

$$I_{y-} = \frac{|\langle A_f | A_i \rangle|^2}{2}, \tag{3.64d}$$

$$I_{z+} = \frac{|\langle A_f | A_i \rangle|^2}{2} \left\{ 1 + 2 \left| \langle \hat{\Pi}_{z\pm}^a \rangle_w \right|^2 - 2 \operatorname{Re} \left[\langle \hat{\Pi}_{z\pm}^a \rangle_w \right] - 2 \operatorname{Im} \left[\langle \hat{\Pi}_{z\pm}^a \rangle_w \right] \right\}, \tag{3.64e}$$

$$I_{z-} = \frac{|\langle A_f | A_i \rangle|^2}{2} \left\{ 1 + 2 \left| \langle \hat{\Pi}_{z\pm}^a \rangle_w \right|^2 - 2 \operatorname{Re} \left[\langle \hat{\Pi}_{z\pm}^a \rangle_w \right] + 2 \operatorname{Im} \left[\langle \hat{\Pi}_{z\pm}^a \rangle_w \right] \right\}. \tag{3.64f}$$

Using Eqs. (3.64a) to (3.64f) it is easy to find relations to extract the real and imaginary part of A's projection operator as well as its modulus.

$$\operatorname{Re} \left[\left\langle \hat{\Pi}_{z\pm}^a \right\rangle_w \right] = \frac{2 I_{x-} + I_{y-} - I_{y+}}{4 I_{y-}}, \quad (3.65a)$$

$$\operatorname{Im} \left[\left\langle \hat{\Pi}_{z\pm}^a \right\rangle_w \right] = \frac{I_{z-} - I_{z+}}{4 I_{y-}}, \quad (3.65b)$$

$$\left| \left\langle \hat{\Pi}_{z\pm}^a \right\rangle_w \right| = \sqrt{\frac{I_{x-}}{2 I_{y-}}}. \quad (3.65c)$$

These relations can be used to completely determine a projection operator's using maximum strength interactions.

3.3 Summary

In this chapter measurement protocols were presented, to determine the weak value of the Pauli operator $\hat{\sigma}_z^a$ and that of the projection operator $\hat{\Pi}_{z\pm}^a$ using weak and strong interactions. For all schemes the initial state of both the investigated and the meter system were assumed to be aligned along the positive x -direction. While this choice seems arbitrary in the theoretical context of chapter 3, the directions are carefully selected bearing in mind the experimental conditions of neutron interferometry. In the next chapters the reason for this choice is shown. The analysis of this chapter is restricted to the z -component of the Pauli and the projection operator. However, it is straightforward to change the measurement scheme in order to measure operators along other directions. To do so the interaction Hamiltonian has to be changed accordingly. Again the choice for z -component seems arbitrary, but has solid experimental reasons.

CHAPTER 4

Spin weak values

In this chapter neutron interferometric experiments are presented, in which the weak value of the Pauli spin operator $\hat{\sigma}_z^s$ is determined. In the experiments the measurement scheme described in chapter 3, is implemented. The system of interest is the neutron spin degree of freedom S and the neutron path degree of freedom P serves as a meter system.

Parts of the results are published in [Sponar et al., 2015] and [Sponar et al., 2016].

4.1 Background and motivation of the experiment

To determine the Pauli operator's weak value, the neutron spin is weakly coupled to the neutron's path degree of freedom. The way to achieve this in an actual experiment using neutron optical components is depicted schematically in Fig. 4.1.

The experiment starts with a polarized neutron beam, so that the neutron's spin state is given by $|S_z; +\rangle$. Before the neutron enters the interferometer the spin is turned by $\frac{\pi}{2}$ around the y -axis, leading to the initial spin state $|S_i\rangle \equiv |S_x; +\rangle$. As soon as the neutron enters the interferometer, its state vector has to be extended by a path dependent part:

$$|\Psi_i\rangle = |P_i\rangle |S_i\rangle = \sqrt{\frac{1}{2}} (|P_z; +\rangle + e^{i\chi} |P_z; -\rangle) |S_x; +\rangle, \quad (4.1)$$

where the states $|P_z; +\rangle$ and $|P_z; -\rangle$ are the eigenstates of the path I and II respectively. The parameter χ describes the relative phase between the paths. For

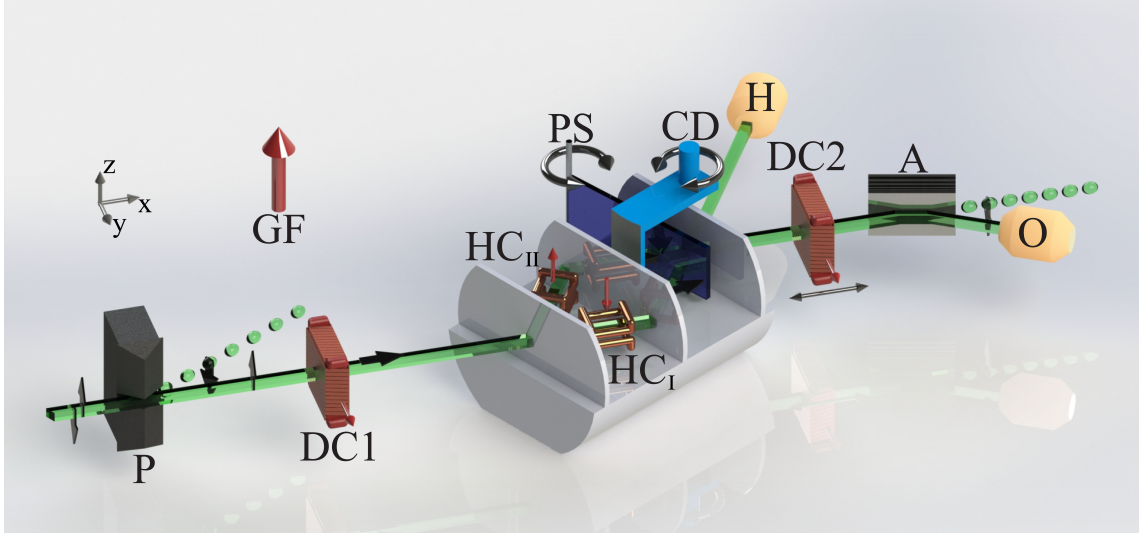


Figure 4.1: Artistic depiction of the experimental setup: The neutron beam passes through polarizing magnetic prisms (P). To prevent depolarization a magnetic guide field (GF) is applied around the whole setup (not depicted). Before the neutrons enter the interferometer a DC coil (DC1) prepares the initial spin state $|S_i\rangle$. At the interferometer's first plate the neutron beam gets split into path I and II , preparing $|P_i\rangle$. In each beam path small coils in Helmholtz configuration (HC_j in path j) allow the manipulation of the neutron spin in the xy -plane. A cadmium holder (CD) can be rotated inside the interferometer to block either one of the beam paths. The phase shifter (PS) tunes the relative phase χ between I and II and therefore the selection of the state $|P_f\rangle$. The postselection on the spin state $|S_f\rangle$ is performed using a second DC coil (DC2) on a translation stage (TS) in combination with a CoTi supermirror analyzer (A). Of the two outgoing beams of the interferometer, only the O-beam is spin analyzed (O). Both detectors (O & H) are ^3He counter tubes.

simplicity's sake, we assume that the phase shifter is in the position $\chi = 0$, leading to

$$|\Psi_i\rangle = |P_i\rangle |S_i\rangle = \sqrt{\frac{1}{2}} (|P_z; +\rangle + |P_z; -\rangle) \sqrt{\frac{1}{2}} (|S_z; +\rangle + |S_z; -\rangle). \quad (4.2)$$

After the preselection the state vector of both degrees of freedom is aligned along the positive x -direction, as proposed in the measurement protocol presented in chapter 3. This is an experimentally convenient situation. The spin state can be produced using a combination of a polarizer and a simple spin rotator. The path state $|P_x; +\rangle$ is automatically set by the neutron interferometer's first plate, which acts as a 50:50 beam splitter for the incoming beam by amplitude division. At the interferometer's first plate the preselection is accomplished.

Recalling our measurement scheme a coupling between the two degrees of freedom

is created. This is done by performing path-dependent spin rotations. To be precise the spin is rotated by a certain angle α around the z -axis in the xy -plane. In addition the spin rotation is positive (clockwise) in path I and negative (counter clockwise) in path II . The interaction Hamiltonian for such a measurement is given by

$$\hat{H}_{\text{int}} = -\vec{\mu} \cdot \vec{B} \hat{\Pi}_{z+}^{\text{p}} + \vec{\mu} \cdot \vec{B} \hat{\Pi}_{z-}^{\text{p}}, \quad (4.3)$$

where $\vec{\mu}$ is the neutron's magnetic moment, $\vec{B} = (0, 0, B_z)$ an externally applied magnetic field and $\hat{\Pi}_{z\pm}^{\text{p}}$ are the projection operators on the path eigenstates $|P_z; +\rangle$ and $|P_z; -\rangle$ respectively. Just like the choice for the initial state, the rotational axis is also chosen in a very convenient manner from an experimental point of view. The spin rotation is performed with coils in Helmholtz configuration, placing no material in the neutron beam and thus avoiding decoherence.

If an evolution operator is given by an interaction Hamiltonian its effect upon the initial state of the composite system is written in the form

$$|\Psi'\rangle = e^{-i/\hbar \int \hat{H}_{\text{int}} dt} |\Psi_i\rangle = e^{-i\alpha \hat{\sigma}_z^{\text{s}} \hat{\sigma}_z^{\text{p}}/2} |\Psi_i\rangle. \quad (4.4)$$

The parameter α describes an angle of rotation and therefore represents the interaction strength of the measurement. It is given by $-2\mu B_z \tau / \hbar$, where τ is the neutron's time of flight in the magnetic field. $\hat{\sigma}_z^{\text{s}}$ is the spin operator, that describes the rotation around the z -axis. $\hat{\sigma}_z^{\text{p}}$ is a linear combination of the path projection operators. It is given by a Pauli matrix as $\hat{\sigma}_z^{\text{p}} = |P_z; +\rangle \langle P_z; +| - |P_z; -\rangle \langle P_z; -|$ in consideration of the fact that the spin rotation is positive along path I and negative along path II . The condition for a weak measurement is fulfilled by making α small.

At the interferometer's third plate the beams are recombined and the final path state $|P_f\rangle$ is postselected. Subsequently a combination of a coil mounted on a translation stage and a CoTi super mirror carries out the postselection onto a general spin state

$$|S_f\rangle = \cos\left(\frac{\theta}{2}\right) |S_z; +\rangle + \sin\left(\frac{\theta}{2}\right) e^{i\phi} |S_z; -\rangle \quad (4.5)$$

parameterized with ϕ and θ denoting azimuth and polar angle on the spin Bloch sphere respectively. This neutron interferometric setup permits all procedures necessary to complete each step of the weak value measurement protocol of chapter 3.

4.2 Experimental realizations of spin weak measurements

To experimentally realize the measurement of $\langle \hat{\sigma}_z^s \rangle_w$ the neutron's spin and path degree of freedom should be well manipulated. To control the neutron spin, magnetic fields are well suited, which utilize the spin's Larmor precession. In our experiment the control of the path degree of freedom is achieved by inserting a phase shifter and beam blocks into the interferometer. The phase shifter makes it possible to tune the relative phase χ between beam path *I* and *II*, making among others the states $|P_x; \pm\rangle$ and $|P_y; \pm\rangle$ accessible. By performing phase shifter scans, during which the spin manipulation inside the interferometer is turned on and off alternately, two interferograms are recorded together, which then allow one to extract the phase of the empty interferogram and evaluate the expectation values of $\hat{\sigma}_x^p$ and $\hat{\sigma}_y^p$.

To evaluate $\hat{\sigma}_z^p$ the eigenstates of path *I* and *II* have to be accessed. This is done by measuring intensities with blocking one beam path at a time. If either one of the beam paths is blocked, no interference effects appear and one ends up with a purely neutron polarimetric setup, needed to determine $I_{z\pm}$. This has the advantage of much higher experimental stability, such as resistance against temperature fluctuations and vibrations. Consequently $\text{Im}[\langle \hat{\sigma}_z^s \rangle_w]$ was determined with two different approaches. One was performed using the neutron interferometric setup with alternatively blocked beam paths at the S18 beam line at the research reactor of the Institute Laue Langevin (ILL) [Kroupa et al., 2000, Geppert et al., 2014]. A schematic drawing of the interferometric setup at ILL was already depicted in Fig. 4.1. The measurements were performed during reactor cycle 169 in April/May in 2013. For the experiment a triple Laue interferometer (the so called Kaiser interferometer) was used. Another experiment was carried out at the TRIGA Mark II research reactor at Institute of Atomic and Subatomic Physics of the Vienna University of Technology in 2014^a. Such a polarimetric setup is depicted in Fig. 4.2. The two experimental approaches are now explained in more detail.

4.2.1 Interferometer experiment

The experiment can be divided into three main parts. Here a short overview of each component is given, followed by a detail descriptions of their adjustment in the

^aOne might object to the approach that modulus and real part were measured using a different setup than for the measurement of the imaginary part. To counter this criticism the imaginary part of $\langle \hat{\sigma}_z^s \rangle_w$ was measured using the interferometer setup at a later point during reactor cycle 177 in December 2015.

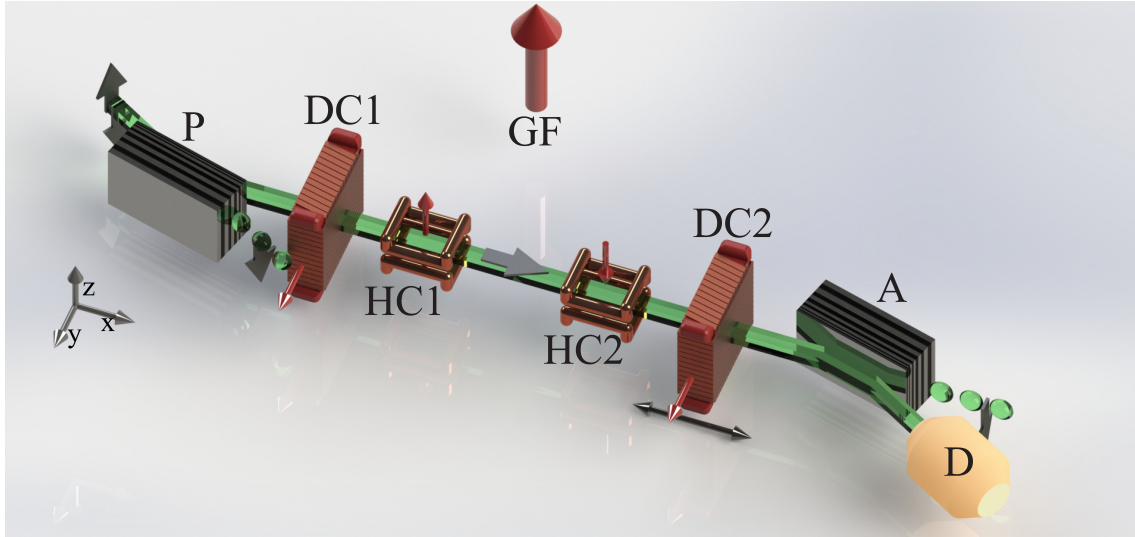


Figure 4.2: Artistic depiction of the polarimetric setup at the Institute of Atomic and Subatomic Physics: A monochromatic neutron beam passes a CoTi supermirror polarizer (P). To prevent depolarization a magnetic guide field (GF) is applied around the whole setup (not depicted). Subsequently a DC coil (DC1) generates the initial spin state $|S_i\rangle$. Along the polarimetric beam line two spin rotators in Helmholtz configuration (HC1 & HC2) allow to either increase or decrease the neutron spin's Larmor precession by creating magnetic fields along the z -axis. Similar to the interferometric setup the spin postselection is performed using a second DC coil (DC2) mounted on a translation stage (TS) in combination with a second CoTi supermirror analyzer (A). The neutrons are detected by a BF_3 counter (D). In comparison to the interferometer the polarimeter offers much higher stability and resistance against vibrations and temperature fluctuations.

subsequent subsection.

- i) Preselection: A monochromatic neutron beam of wavelength $\lambda_0 = 1.91 \text{ \AA}$ ($\lambda/\lambda_0 \sim 0.02$) and a cross section of $5 \times 5 \text{ mm}^2$ passes two magnetic prisms which deflect spin down component. Due to this deflection only neutrons with a spin component aligned along the positive z -axis, fulfill Bragg's law and get reflected at the first plate of the interferometer. Neutrons with a spin component along the negative z -axis pass through the first plate and do not contribute to the experiment. This leads to a polarization of the neutron beam along the positive z -axis. A DC coil turns the neutron spin by $\pi/2$ so that it is aligned along the positive x -axis. After the first plate of the interferometer the system's state vector is given by Eq. (4.2).
- ii) Interaction: Inside the interferometer one coil in Helmholtz configuration in each beam path perform the path conditioned spin rotations that lead to a coupling between the path and spin degree of freedom. The coils produce addi-

tional magnetic fields in the $\pm z$ -direction that cause the neutron spin's Larmor precession to decrease or increase respectively. The strength of the magnetic field determines the magnitude of the rotation angle α and is related to the coupling parameter in Eq. (4.4) and . In the experiment the angle of rotation was fixed at $\alpha = 15^\circ$. To reduce the thermal stress on the interferometer the coils are water cooled.

- iii) Postselection: A sapphire slab is inserted between the second and the third plate of the interferometer, to tune the relative phase χ . In a χ -scan, the path system is systematically investigated on the equator of the Bloch sphere. One phase shifter scan is enough to access the states $|P_x; \pm\rangle$ and $|P_y; \pm\rangle$. A cadmium slab mounted on a rotational stage can be used to block either one of the beam paths. After the interferometer the spin postselection is performed by a second DC coil mounted on a translation stage. By positioning the coil at different points along the neutrons' flight path, the neutrons' Larmor precession within the guide field is utilized to tune the azimuth angle ϕ . By applying different currents, the polar angle θ can be adjusted. Subsequently a CoTi supermirror array filters out all neutrons but those with a spin aligned along (ϕ, θ) -direction beforehand. Finally the neutrons are detected by a ^3He detector.

4.2.1.1 Adjustment

To obtain sound results it is essential to have a well adjusted experimental setup. In this section the most important steps of the setup adjustment, are described in detail. To build up and tune the whole experiment it takes two to three experimentalists and 100 to 200 hours of work.

First of all the monochromator crystal that feeds the neutrons from the beam guide to the experimental box, was oriented. A single-cut triple-bounce silicon crystal is used. It has the advantage of a very good monochromatization resulting in a very narrow rocking curve. It is shown later how a high monochromatization is crucial for the increase of the initial degree of polarization.

Next the interferometer itself can be placed in the beam and it has to be rotated around the z -axis so that the incoming neutron beam fulfills the Bragg condition at the first plate. A Piezo drive is used to adjust the interferometer with an accuracy of one ten thousandth of a degree. For the final adjustment the ρ -axis (a tilting axis)

has to be adjusted^b, to obtain the narrowest and highest peak possible. In Fig. 4.3 a typical rocking curve is depicted. Subsequently a phase shifter has to be inserted

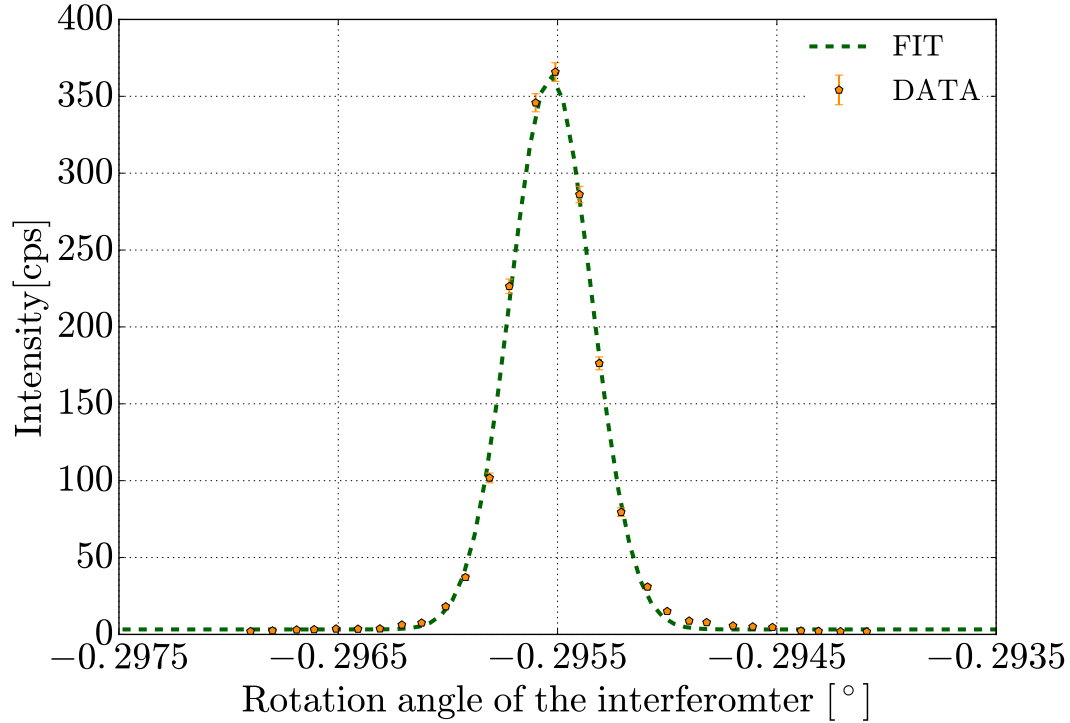


Figure 4.3: Rocking curve of the interferometer: After the interferometer is adjusted correctly in the beam a rocking peak with a full width at half maximum (FWHM) of less than one thousandth of a degree is obtained (typically $\approx 0.5''$ or 2×10^{-6} rad. The fit to the data was performed with a single Gaussian of the form $y_0 + A * \exp [(-x-x_0/\Delta)^2]$.

into interferometer setup to obtain interference fringes. For all experiments present in this thesis phase plates made out of sapphire (Al_2O_3) are used. By rotating the phase shifter by a few degrees, an optical path difference is introduced and sinusoidal intensity modulation is observed. A typical interference fringe is plotted in Fig. 4.4.

If a phase shifter is put into the interferometer and rotated, as depicted in Fig. 4.1, sinusoidal interference patterns are observed, as described in section 2.2.3. A χ^2 -fit to the recorded data points is performed, in the form

$$g(x) = y_0 + A \cos(p x + f) \quad (4.6)$$

^bThis adjustment tilts the interferometer relative to the xy -plane, so that its base is parallel to the incoming neutron beam.

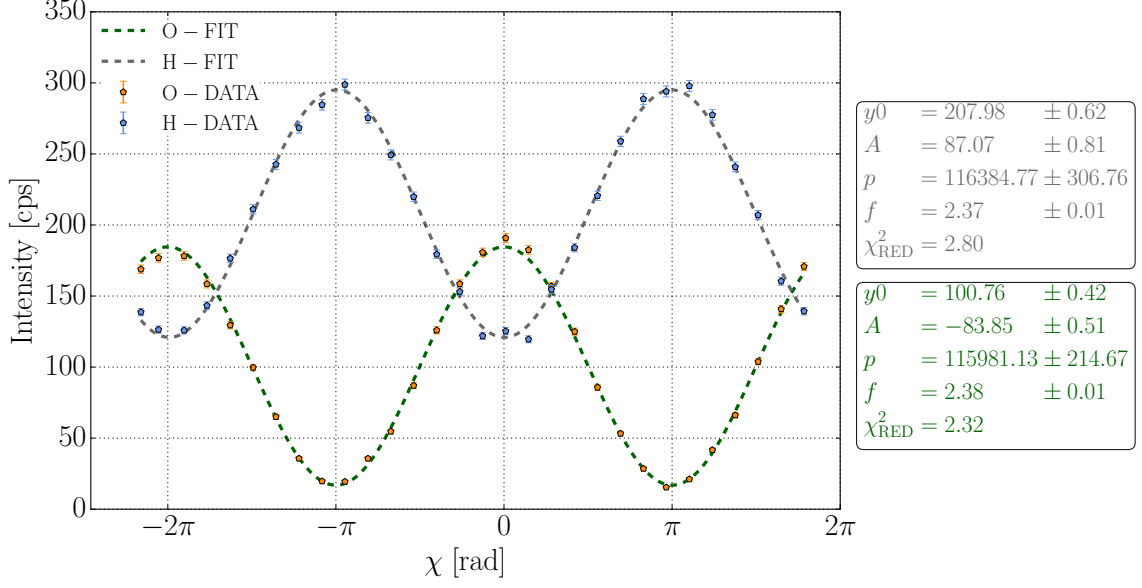


Figure 4.4: Typical interference fringes of the unpolarized setup: The contrast of the O-detector is over 80%, whereas the H-detector contrast is over 40%.

where the parameters y_0 , A , p and f represent the mean intensity, amplitude, period and phase of the oscillation respectively. Using these fit parameters one can calculate the contrast C of the interference fringes by $C = A/y_0$. Note that the contrast of the O-beam (forward direction) is always higher than that for the H-beam (reflected direction): it is over 80% for the O-beam and over 40% for the H-beam for the interferograms depicted in 4.4.

The interferometer has certain spots on its plates, where it will work better. To find those “sweetspots” it is helpful to perform a raster scan with the aperture. During such a scan the aperture is moved systematically in x and y direction and for every xy pair a phase shifter scan is performed. The results of such a scan are depicted in Fig. 4.5. For the Kaiser interferometer, which is used to determine the spin weak values, it has repeatedly been observed that the obtained contrast is highest closest to the base. The best experimental conditions are given when the spot of highest contrast coincides with the spot of highest intensity.

To determine the spin operator’s weak value it is necessary to manipulate the spin degree of freedom. First the neutron beam needs to be polarized, by using magnetic prisms [Badurek et al., 1979, Badurek et al., 2000]. The permanent magnetic field of those prisms leads to a deflection of the neutron beam depending on whether the neutrons’ spin component is aligned parallel (up) or anti-parallel (down) to the z -axis. Although the deflection of the spin down component is below $8''$, this is suf-

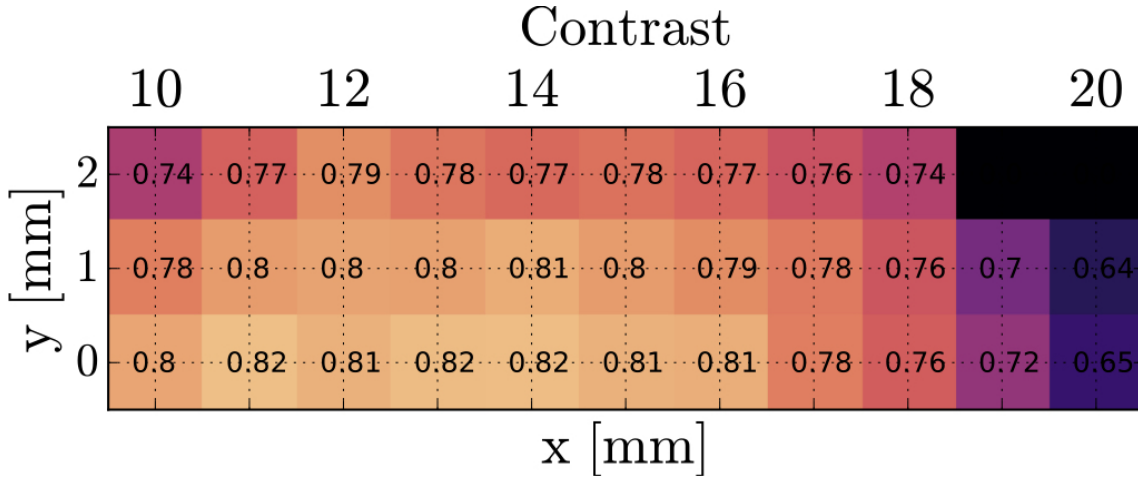


Figure 4.5: Results of a scan of the apertures position: for every xy value a phase shifter scan is performed and the obtained contrast is recorded. The spot of highest contrast is found for $(x, y)=(0, 12)$.

ficiently large to clearly distinguish two separate peaks in the rocking curve of the interferometer. A typical rocking curve with two peaks obtained during the setup adjustment is depicted in Fig. 4.6.

If the interferometer is now turned at the left peak, only neutrons with a spin state given by $|S_z; +\rangle$ get reflected at the first plate. Neutrons with a spin aligned anti-parallel to the z -axis do not fulfill the Bragg conditions any more, due to the deflection caused by the prisms and therefore do not contribute to the experiment after the interferometer's first plate. A good collimation of the incoming beam is important to achieve a high degree of polarization. This is because a good collimation leads to a narrow rocking peak. A narrow rocking peak in turn leads to a large peak separation of the spin up and spin down component when the prisms are inserted before the interferometer. Finally the large peak separation prevents neutrons with a spin down component to be reflected at the first plate, which guarantees a high degree of initial polarization. When the triple bounce monochromator is used, a neutron beam with a degree of polarization above 99% is achieved. To prevent a depolarization of the neutron beam, a guide field pointing in the positive z -direction is applied around the whole setup. The guide field strength was set to ~ 13 G. At this point the polarizing supermirror is put into the setup. It acts as a filter that lets only neutrons with a $|S_z; +\rangle$ spin state pass, as is described in chapter 2. The supermirror is put directly in front of the O-detector and dramatically reduces the count rate, due to its small window of acceptance. Neutrons have to hit the supermirror with the correct angle (within $\sim 1^\circ$ of accuracy) so that they fulfill Bragg's

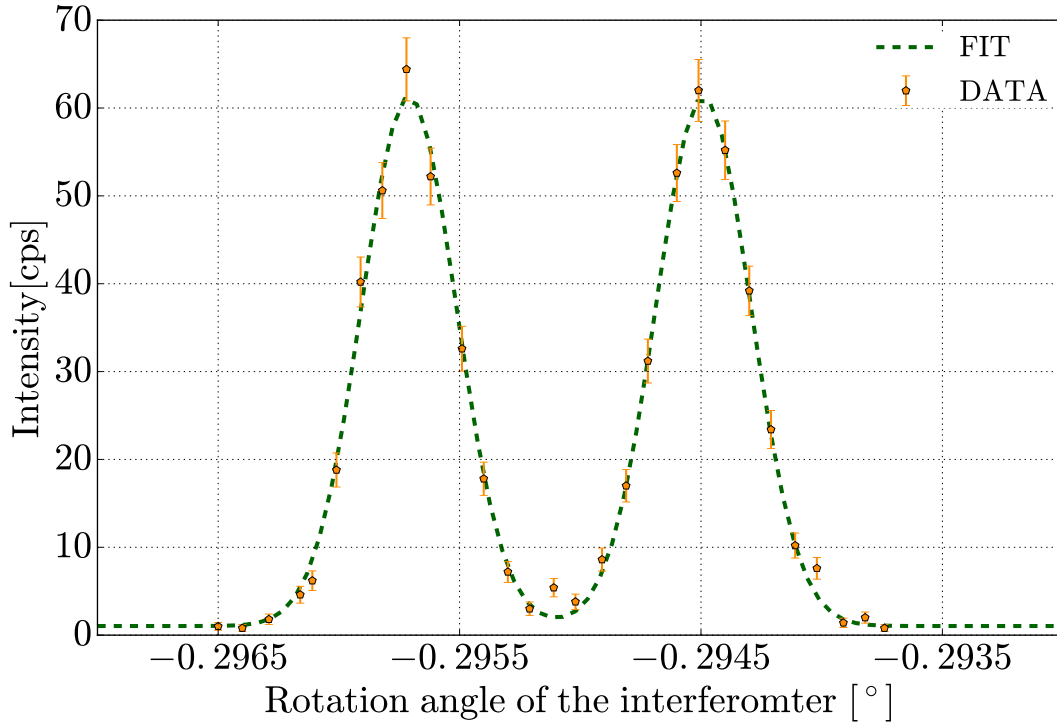


Figure 4.6: Rocking curve of the interferometer with a beam deflection by the polarizing magnetic prisms: After the polarizing prisms are introduced into the setup two rocking peaks appear. If the interferometer is turned into the left peak only neutrons with a spin state given by $|S_z; +\rangle$ get reflected at the first plate. The fit to the data was performed with a single Gaussian of the form $y_0 + A * \exp [(-x-x_1/\Delta)^2] + A * \exp [(-x-x_2/\Delta)^2]$.

condition at its many layers. Its position is adjusted so that the count rate at the O-detector becomes maximum. This ensures that the beam hits it in the center of the aperture window and also under the correct angle.

Although the prisms polarize the neutron beam, they are not enough to prepare an arbitrary initial spin state. The neutron's spin wave function is only set to the state $|S_z; +\rangle$. To prepare $|S_x; +\rangle$, the initial spin state needed to measure the spin operator's weak value, a spin rotator, made of a so called DC coil, as described in chapter 2 is used. By shifting a DC coil positioned between the polarizing prisms and the interferometer it is possible to generate arbitrary initial spin states.

The adjustment of a DC coil requires three steps. First of all a current is applied only to the inner coil, generating a magnetic field in the $\pm y$ -direction. This results in an intensity modulation in dependence of the applied current, as can be seen in Fig. 4.7. A χ^2 -fit to the data points, using a fit function of the same form as Eq. (4.6), is performed.

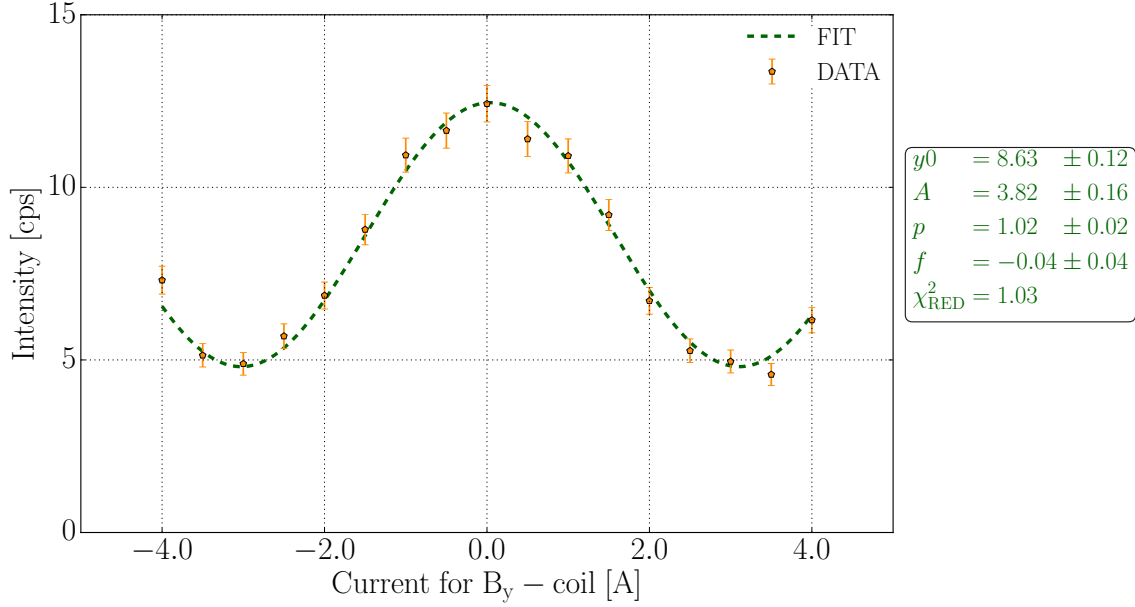


Figure 4.7: B_y -scan of DC1 (not compensated): If a current is applied to the DC coil sinusoidal intensity oscillations are observed. As long as the compensation field is not adjusted the contrast of the oscillation is very poor and hence only low flipping ratios can be achieved.

As long as the compensation field in z -direction is not suitably adjusted the contrast of the oscillation is very poor and hence only low flipping ratios can be achieved. This is of course due to the fact that the guide field applied around the whole setup tilts the magnetic field vector generated by the inner coil away from the $\pm y$ -direction and consequently a π -flip of the neutron's spin state is never achieved. Therefore in a second step the current of the compensations coil has to be adjusted. To do that again a current is applied to the inner coil so that it a magnetic field B_y is generated. The current to produce B_y is adjusted so that a minimum in count rate is observed. In the case of DC1 this was around ± 3 A, as can be seen in Fig. 4.7. Subsequently the outer coil is applied with a current. With increasing current the guide field gets compensated more and more until a minimum in count rate appears and the external guide field is completely cancelled. After this point the count rate starts to increase again due to an overcompensation of the guide field. A current scan of DC1's compensation coil (B_z) is plotted in Fig. 4.8.

Again a χ^2 -fit to the data points is performed, but now the fit function is a second order polynomial function in the form

$$g(x) = a + b x + c x^2. \quad (4.7)$$

The correct current for the compensation coil is given by the local minimum of the fit function in the scanned current range.

Finally the first step has to be repeated with the correct current applied to the compensation coil so that a B_z is generated. Again a sinusoidal intensity oscillation is observed. Now the contrast and the flipping ratio are much higher. From the fit function additional information about the coil can be gained. If the coil is tilted in the yz -plane, the field vectors of the guide field and B_z in the DC coil are not normal to each other. This misalignment will manifest itself in the parameter f (a phase shift). More precisely f will not equal 0° within the error of the fit function. Hence, the coil has to be tilted and the current scan has to be repeated till a value sufficiently close to $f = 0^\circ$ is obtained in the data fit. The final plot of the DC1 adjustment is seen in Fig. 4.9.

After the final adjustment, the DC1 coil showed a flipping ratio (defined as $I_{\text{MAX}}/I_{\text{MIN}}$) of ~ 70 , a contrast of $\sim 97\%$ and a phase of $f = -0.009$ rad (all without a background correction). In our experimental circumstances this is considered excellent. There are several limiting factors for the adjustment of the coil: First and most importantly we mention the inhomogeneity of the external guide field, which leads to a suboptimal field distribution within the DC coil. This problem is made worse by the

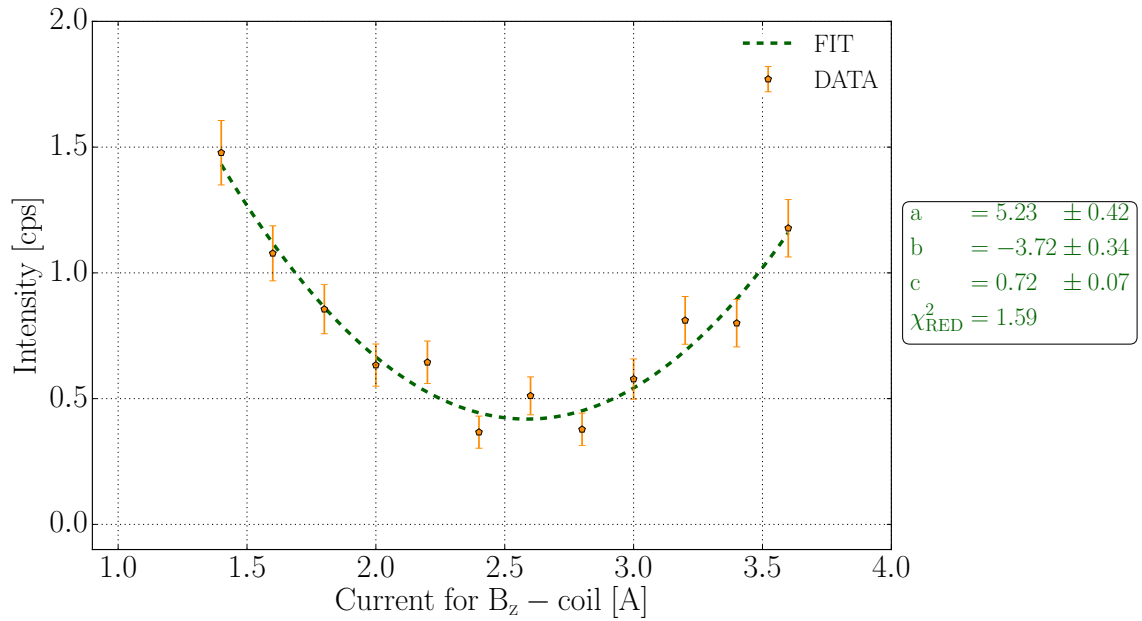


Figure 4.8: B_z -scan of DC1 (compensation field): Inside the coil the guide field gets compensated more and more with increasing current until a minimum in count rate is observed, until it is completely cancelled. After this point the count rate starts to increase again due to an overcompensation of the guide field.

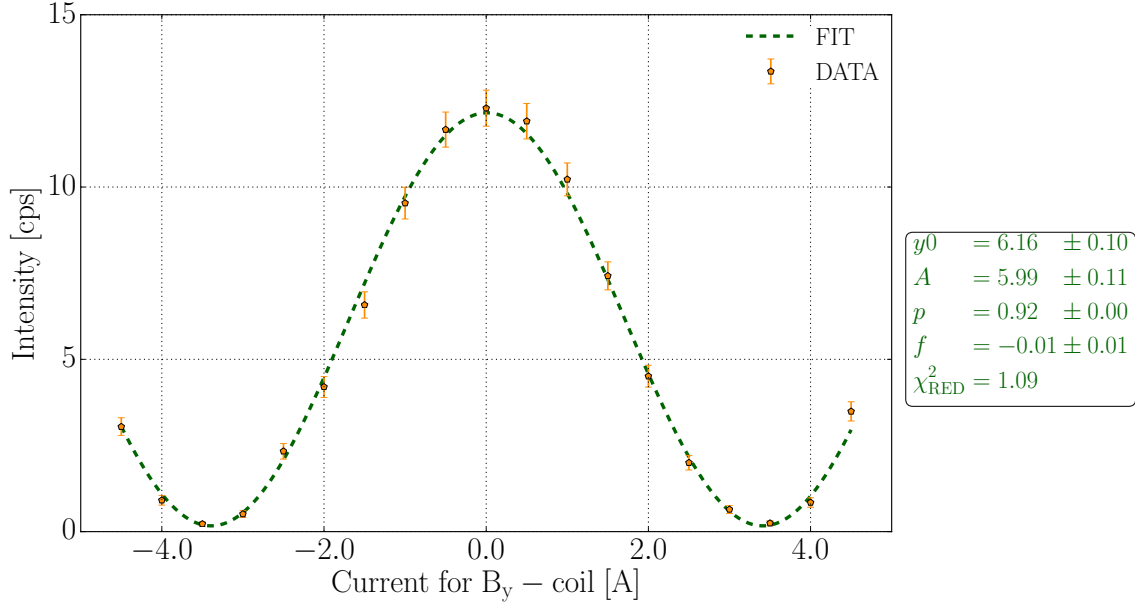


Figure 4.9: B_y -scan of DC1 obtained with a suitable compensation field B_z : After the final adjustment, the DC1 coil showed a flipping ratio of ~ 70 , a contrast of $\sim 97\%$ and a phase of $f = -0.009$ rad (without background correction).

strong stray fields emerging from the polarizing prisms. In addition the tilting of the coil during its adjustment is done manually using a micrometer rocker. Coils at the TRIGA Mark II research reactor at Institute of Atomic and Subatomic Physics used to be adjusted with manual rockers as well. After switching to motorized rockers the Vienna coils doubled their flipping ratio. Switching to motorized rockers can lead to the same performance increase in Grenoble. Figure 4.10 shows a picture of part of the experimental setup including the interferometer, the aperture, the guide field and DC1 and its micrometer rocker.

Note that the coils of the guide field are very close to the interferometer, which decreases the field homogeneity along the neutron's path through the interferometer. The small guide field coils also have the disadvantage, that make the setup crammed together not leaving a lot of space to work with. In a more recent version of the setup the guide field coils are replaced by bigger ones. The results of this modification is described in chapter 5.

To postselect an arbitrary final spin state $|S_f\rangle$ the same problem as with the preselection arises: The polarizing supermirror is a passive element. It acts as a filter that lets only $|S_z; +\rangle$ spin states pass so that arbitrary spin states cannot be simply selected. Therefore the second DC coil (DC2), has to be mounted on a motorized stage between the interferometer and the supermirror. This second coil turns the

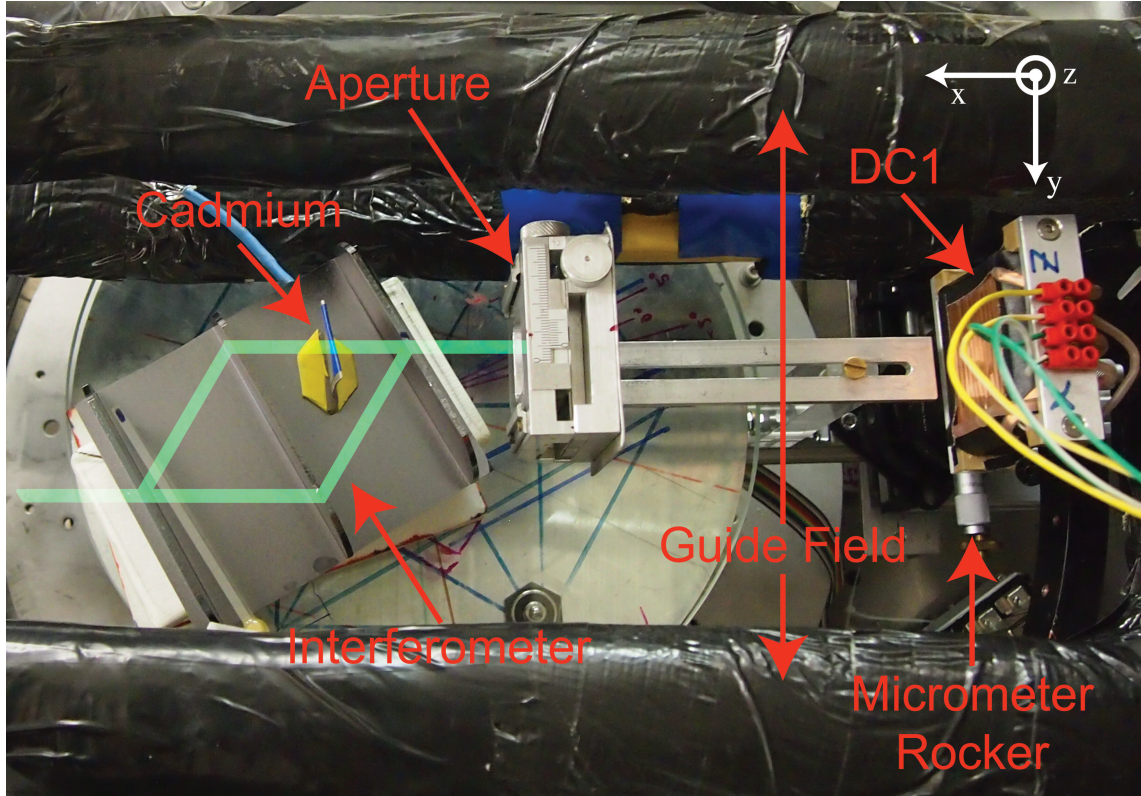


Figure 4.10: Picture of parts of the experimental setup: The interferometer sits at the center enclosed by the coils of the guide field. The aperture is placed between the interferometer and the DC1 coil, which sits on a micrometer rocker. A cadmium slab is placed in the interferometer to block one beam path for setup adjustment. To guide the eye a schematic drawing of the beam path has been added to the picture (green).

spin into the positive z -direction. By tuning the current to DC2 any polar angle θ can be selected. By moving the coil on the translation stage along the x -axis any azimuth angle ϕ is adjusted, by utilizing the neutrons Larmor precession in the guide field. Thus, a combination of the correct position and current can realize an arbitrary postselected spin state.

The adjustment of DC2 is performed in the same way as DC1's. First current has to be applied to the inner coil to generate B_y and to find a minimum in the count rate of the B_y -scan, then the compensation field B_z is adjusted as described above and finally the current scan of B_y is repeated till the correct tilt of the coil is found. Unfortunately this procedure has to be repeated for every motor position, i.e. for different azimuth angles ϕ . This is due to inhomogeneities in the magnetic guide field. In Fig. 4.11 the final adjustment of the DC2 coil at a midway position of the translation stage is plotted.

At this position the B_y -scan of DC2 coil showed a flipping ratio of ~ 60 , a contrast

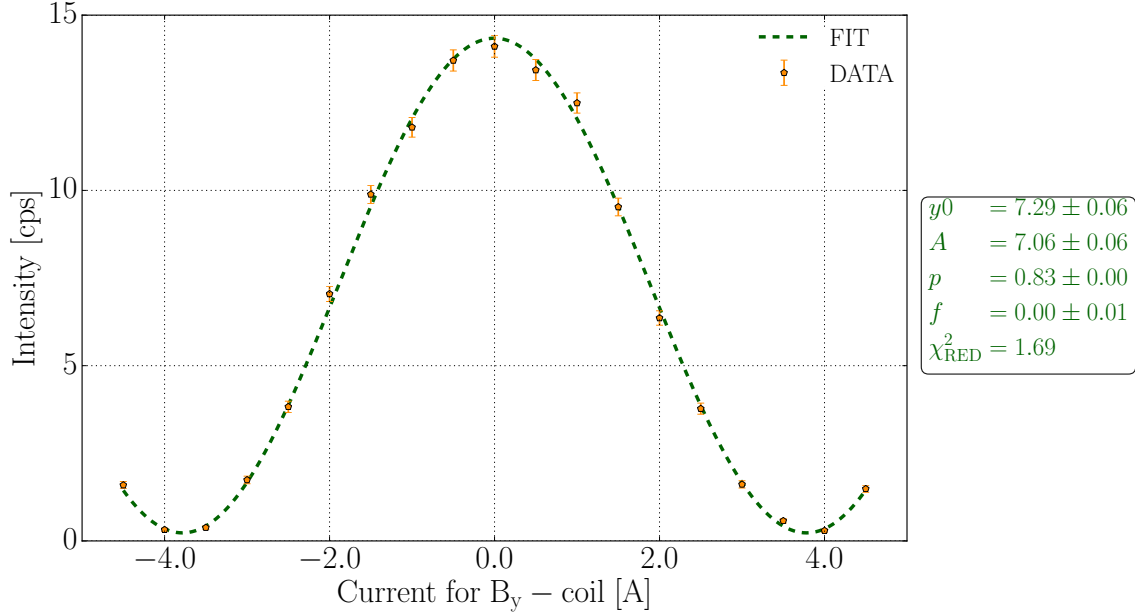


Figure 4.11: B_y -scan of DC2 obtained with a suitable compensation field B_z : After the final adjustment, the DC2 coil showed a flipping ratio of ~ 60 , a contrast of $\sim 97\%$ and a phase of $\phi = 0.001$ rad (without background correction).

of $\sim 97\%$ and a phase of $\phi = 0.001$ rad (all without background correction). While the stray field of the polarizing prisms does not cause serious any problems at the position of the DC2 coil, the supermirror analyzer behind DC2 produces a strong magnetic field as well, which causes inhomogeneities in the guide field. For both DC coils the efficiency is basically limited by those stray fields. Since the stray fields of the polarizer and analyzer cannot be shielded, we could have put the coils farther away from the prisms and supermirror at most. Sometimes, this was not actually possible with the available setup, since the coils of the guide field are a practical boundary, limiting the usable space. To increase the precision of the experiment it is necessary to construct new guide field Helmholtz coils, which are larger and can offer more space. Figure 4.12 shows a picture of a larger part of the setup also including DC2 on its translation stage.

Once DC1 and DC2 are adjusted, the spin manipulating Helmholtz coils are inserted into the interferometer [Geppert et al., 2014]. During the whole process of setting up the experiment, this is the most difficult task and great care has to be taken, in order to position them correctly and not to damage the interferometer during the adjustment. To test the spin manipulators, DC1 is adjusted to prepare the initial spin state $|S_x; +\rangle$, i.e. after the prisms the spin gets turned by $\pi/2$ around the y -axis and is aligned along the direction of neutron flight. The current applied

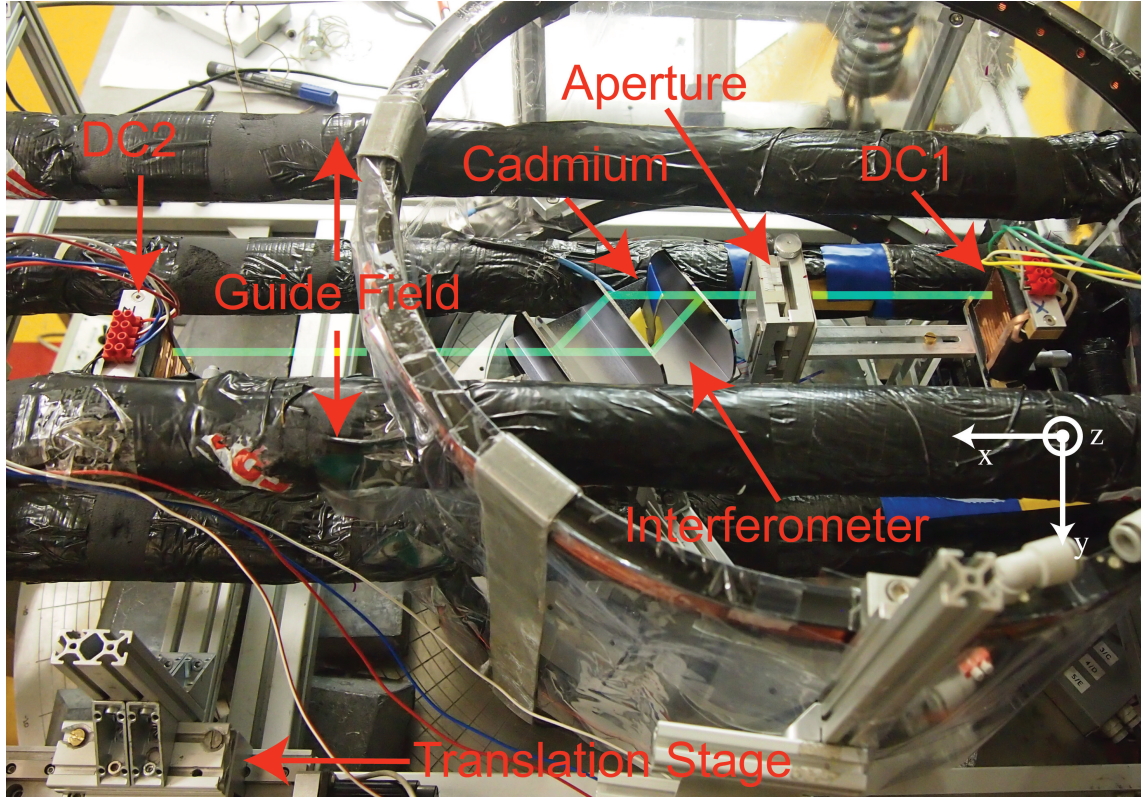


Figure 4.12: Picture of parts of the experimental setup: In addition to the interferometer, DC1 and the aperture, DC2 and its translation stage are also visible in this picture. Note that the whole setup is enclosed by the guide field coils. To guide the eye a schematic drawing of the beam path has been added to the picture (green).

to DC2 is then set so that the polar angle $\theta = \pi/2$ is selected. That is, for an azimuth angle of $\phi = 0$ a maximum is expected in the intensity, while for $\phi = \pi$ the intensity is minimum, because the incident beam is prepared in the spin state $|S_x; +\rangle$. As already mentioned above, ϕ is tuned by the position of DC2 along the x -axis. For fixed currents, so that a $\pi/2$ spin rotation is performed by both DC1 and DC2 a full intensity oscillation in dependence of the position of DC2 is expected. To test and configure the spin manipulators, two scans of DC2's position with fixed current values are done. For the first scan a slab of Cadmium is put into path *II* of the interferometer, for the second scan the Cadmium slab is put into path *I*. The results of both scans are combined in Fig. 4.13 and tell us two important facts.

First there is a notable difference in the count rate, depending on whether path *I* or *II* of the interferometer is blocked. This can be caused by the spin manipulators that are not correctly positioned in the beam. If this is the case the neutron beam hit material along one of the two possible paths inside the interferometer and neutrons get absorbed or scattered. To get rid of this problem the intensity is mon-

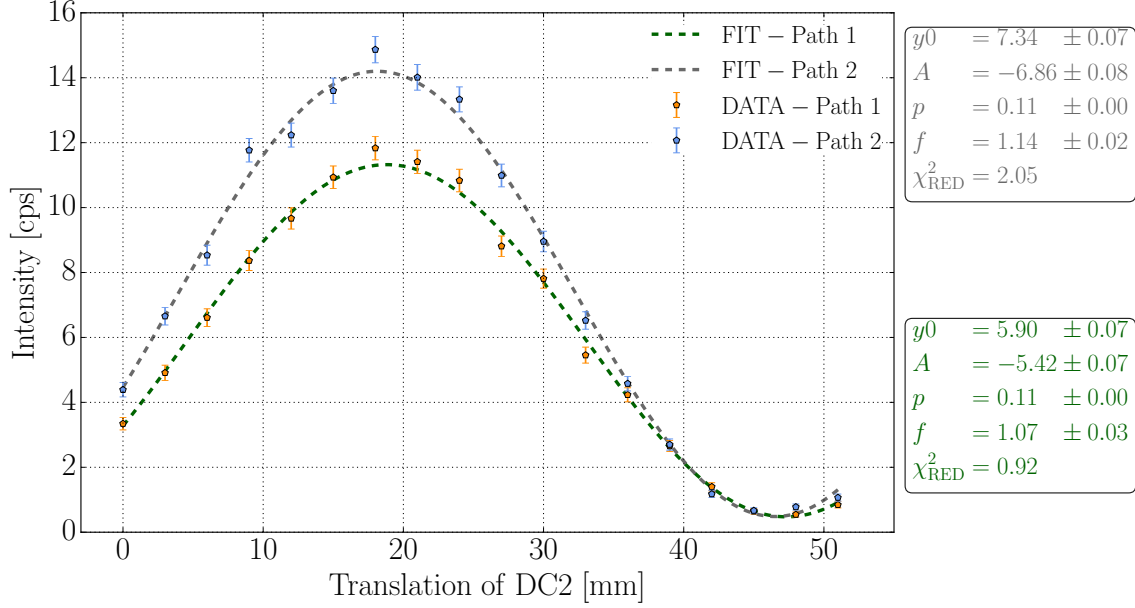


Figure 4.13: Position scan of DC2 with misaligned Helmholtz coils inside the interferometer: The count rates depend on whether path *I* or *II* is blocked. In addition to that the intensity oscillations are phase shifted by several degrees.

itored while the coils are moved diagonally through the interferometer with one of the paths blocked at a time. In addition to that a similar scan is performed with the coils being rotated instead of translated. This ensures that the coils are parallel to the neutron beam and that it does not hit them anywhere.

The difference in count rate can also occur if the interferometer's crystal is disturbed by temperature fluctuations. Then, due to a shift of the pendellösung oscillation of each of the three beam splitters, the ratio between reflection and transmission can vary, which also leads to a count rate difference. To increase thermal stability of the whole setup, the guide field coils are water cooled. The temperature of the cooling water can be adjusted with an external pump. One can now perform phase shifter scans at different cooling water temperatures until a maximum in observable contrast is found. Figure 4.14 shows the measurement results of a systematic change in guide field temperature. The highest contrast is observed for a guide field temperature of 23.6° C. Note that for any temperature the contrast is poor (below 60%). Similar to the guide field coils, the small Helmholtz coil spin manipulators inside the interferometer are flooded with temperature controlled water. The scan of the guide field temperature is performed at an earlier point in time, then the scan of the spin manipulator temperature. Since the spin manipulators are placed inside the interferometer, their temperature has much more effect on observable

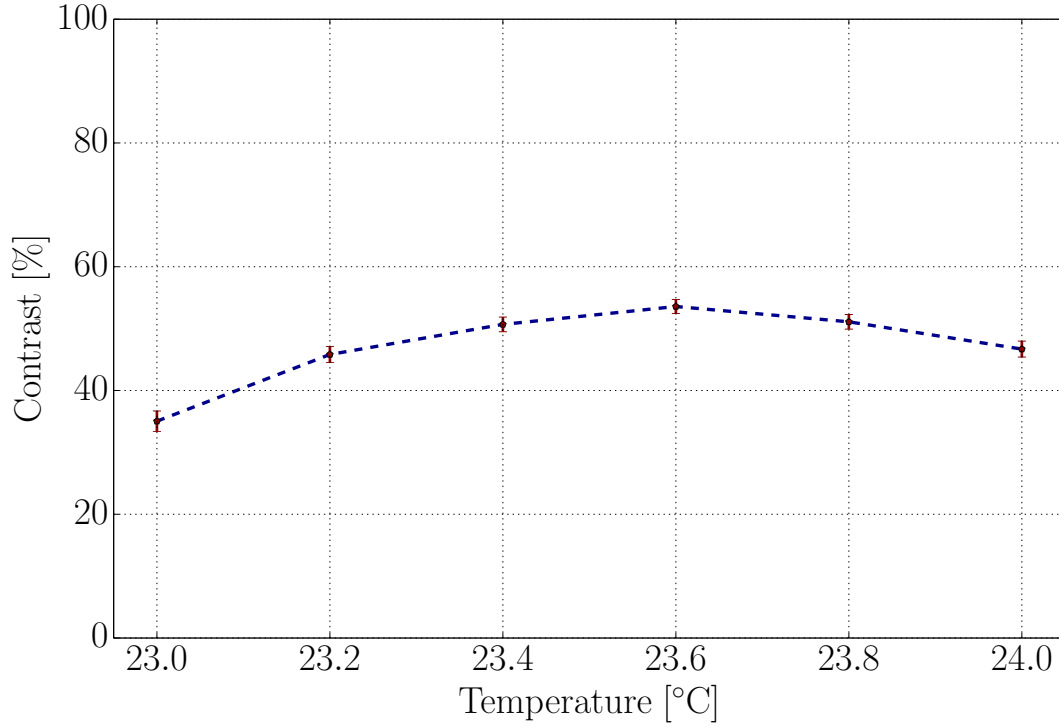


Figure 4.14: Observed contrast as a function of the guide field temperature: The temperature of the guide field's cooling water is changed and subsequently phase shifter scans are performed. The highest value in contrast indicates the correct optimum temperature.

contrast. A detuned temperature of the Helmholtz coils inside the interferometer is the reason for the poor contrast during the guide field scan. However, once the correct guide field temperature is found the temperature of the spin manipulators can also be changed systematically while doing contrast scans. Again the correct temperature is found, when the contrast of the recorded interference fringes is the highest. Figure 4.15 shows the results of a scan of the spin manipulator's temperature. The maximum in contrast is now over 80%. It is observed for a temperature of 23.4° C. To increase thermal stability the interferometer has to be insulated from the environment as well as possible by putting it inside an extra box.

Once thermal stabilization is achieved the second problem visible, in Fig. 4.13, should be solved. Namely, when the data is fitted using a function of the same form as Eq. (4.6), a phase shift of several degrees is visible between the two curves. Even though the current applied at DC1 and DC2 is the same for the scans for path *I* and path *II* the phase of the Larmor precession depends on the path in the interferometer. This is a consequence of the guide field inhomogeneities. During its

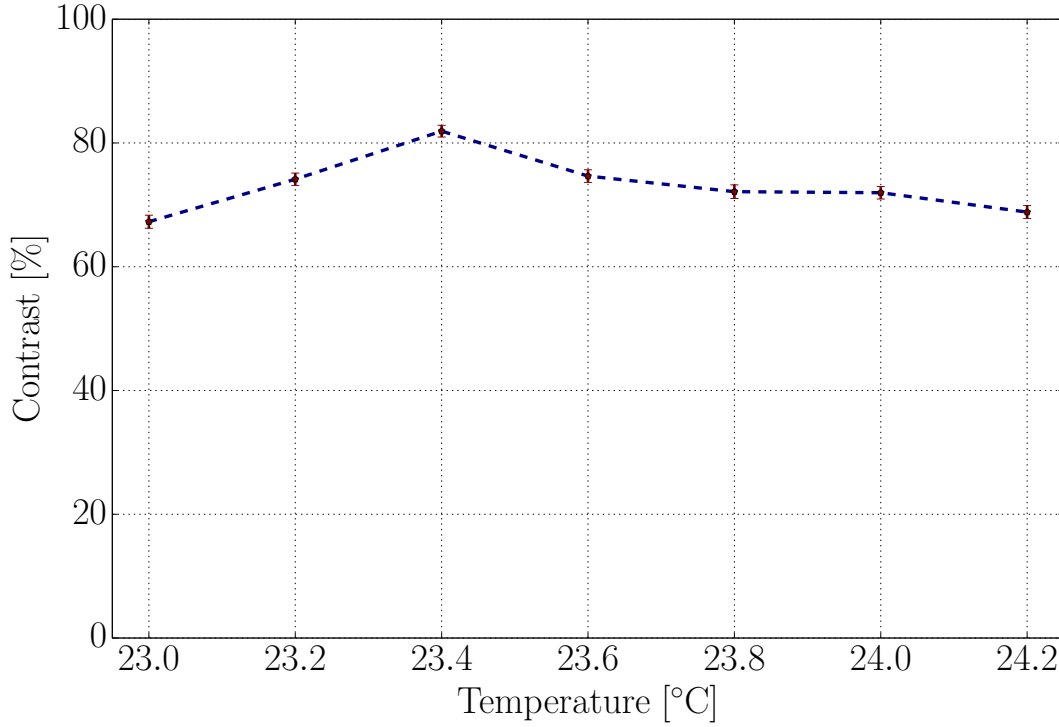


Figure 4.15: Observed contrast as a function of the spin manipulator temperature: The temperature of the spin manipulator's cooling water is changed and subsequently phase shifter scans are performed. The highest value in contrast indicates the correct optimum temperature.

Larmor precession in the xy -plane the neutron picks up a path dependent phase for up and down spin eigenstates.

It is very important that the accumulated phase between path I and II is the same in order to be able to control the neutron spin manipulation within a accuracy of one degree in the setup. To compensate the different phases between the paths a so called zero point calibration of the spin manipulators has to be done. As with the position scan of DC2, DC1 is set so that the preselected spin state is given by $|S_x; +\rangle$. The current supplied to DC2 is chosen so that the polar angle is posts-elected on $\theta = \pi/2$. Instead of moving DC2 along the x -axis the current of the spin manipulators inside the interferometer is varied. Since they are two small coils in Helmholtz configuration, they create an additional field pointing in the positive z -direction, when a positive current is applied, and in the negative one for negative current. This additional field accelerates or decelerates the neutron's Larmor precession in the xy -plane during its passing through the coils. As with the position scan this equals a change of the azimuth angle; this time the variation in ϕ is not

due to the position change of DC2 but due to the current supplied to the Helmholtz coils inside the interferometer. The result of the current scan of the Helmholtz coils in path *I* and *II* are plotted in Fig. 4.16

The first thing one may notice is the difference of count rate in Fig. 4.16. Within the

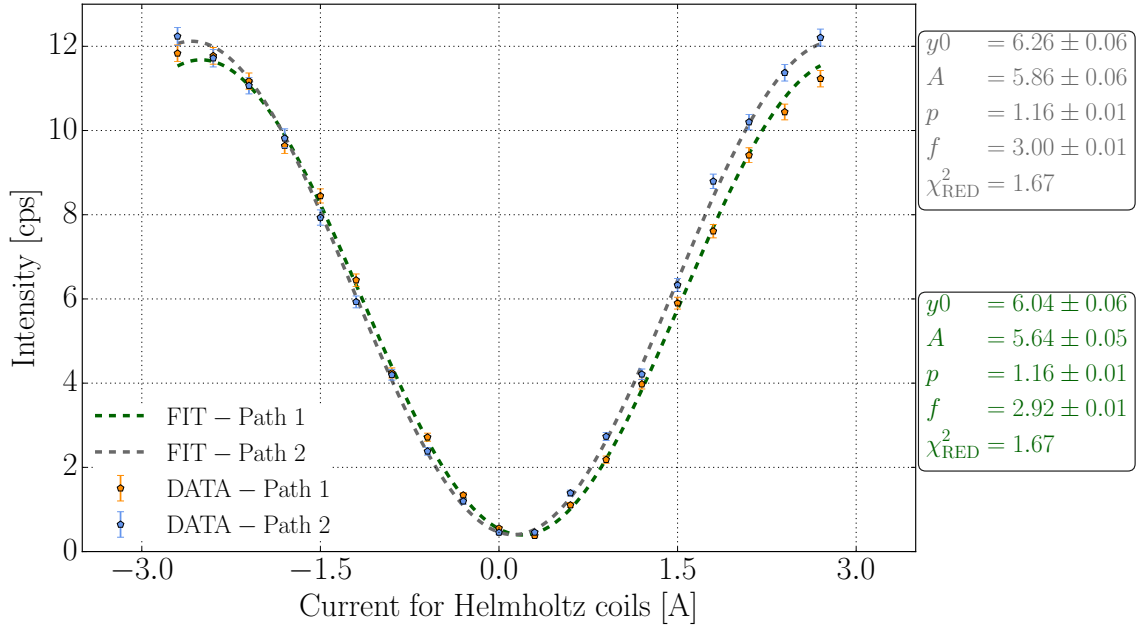


Figure 4.16: Current scan of the spin manipulators inside the interferometer: If a current is applied to the Helmholtz coils inside the interferometer they cause an additional Larmor precession of the neutron's spin in the xy -plane leading to an effective change of the azimuth angle ϕ and a sinusoidal intensity oscillation appears after the spin postselection.

error it is now equal in both paths with a maximum intensity of about 12 counts per second. The Helmholtz coils are now positioned correctly in the interferometer and that thermal stability is achieved. We also find a phase difference of $\sim 5^\circ$ between the data fits in the upper and the lower plot. This is hardly noticeable to the naked eye, but very important for the configuration of the experiment. From the current scans of both Helmholtz coils though, we do know how much phase shift we obtain per applied ampere and so we can set the phase between path *I* and *II* to be zero. By applying a small constant current “offset” to one of the two spin manipulators a zero point calibration is achieved. Furthermore the data fits in Fig. 4.16 allows us to calculate a flipping ratio as well as a contrast for each spin manipulator in the interferometer. Both Helmholtz coils have a flipping ratio of ~ 30 and a contrast of $\sim 94\%$. The Helmholtz coils used in the weak spin experiment are the components that cause the largest imprecision in the experiment.

Once the phase difference between path *I* and *II* is corrected by a current offset

at one of the two Helmholtz coils inside the interferometer, the position scan with DC2, as it was described above, is repeated. The result of two such position scans with compensated and correctly aligned spin manipulators is plotted in Fig. 4.17. Finally the problems described at an earlier stage are now obviously solved. The

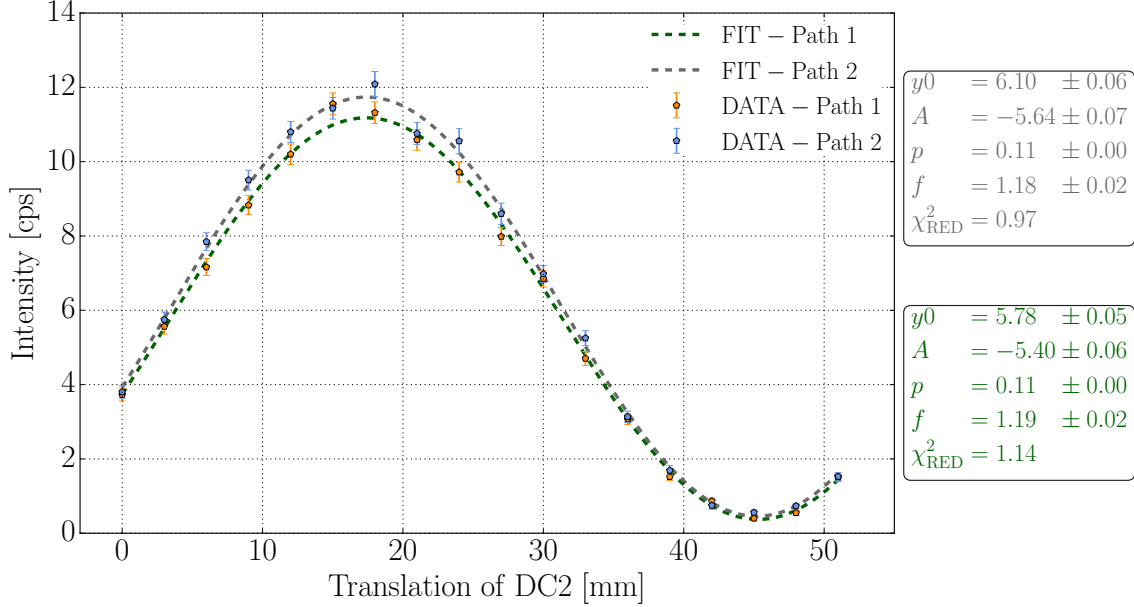


Figure 4.17: Position scan of DC2 with compensated and correctly aligned spin manipulators: After the position of the spin manipulators inside the interferometer has been adjusted and a current offset is applied to one of the Helmholtz coils inside the interferometer, the data fits for HC_I and HC_I show no more count rate and phase difference within the error of the fit. The contrast of the position scans is $\sim 93\%$, their flipping ratio is ~ 28 . The phase shift between path I and II is reduced to $\sim 0.003\text{rad}$.

phase shift between path I and II is reduced to $\sim 0.003\text{rad}$. Also the count rate is now equal no matter which path of the interferometer is blocked. The contrast of the position scans is $\sim 93\%$, their flipping ratio is ~ 28 .

The calibration of the Helmholtz coils inside the interferometer ends the adjustment of the experimental components. In general it is true that the best results will be obtained, when the whole experimental system is put in thermodynamic equilibrium and no stress acts upon it due to temperature gradients. To achieve this thermal equilibrium once the correct guide field and Helmholtz temperature are found as described above, we simply have to wait. During the calibration of the experimental setup it was also observed that the contrast improved, when the setup was left undisturbed for longer periods of time, i.e. when no one came close to it and the experiment was operated via remote control.

A high contrast interference fringe of the completely adjusted setup after the po-

larimeter's adjustment, is depicted in Fig. 4.18.

Fig. 4.18 shows that even though the count rate of the O-detector is reduced dra-

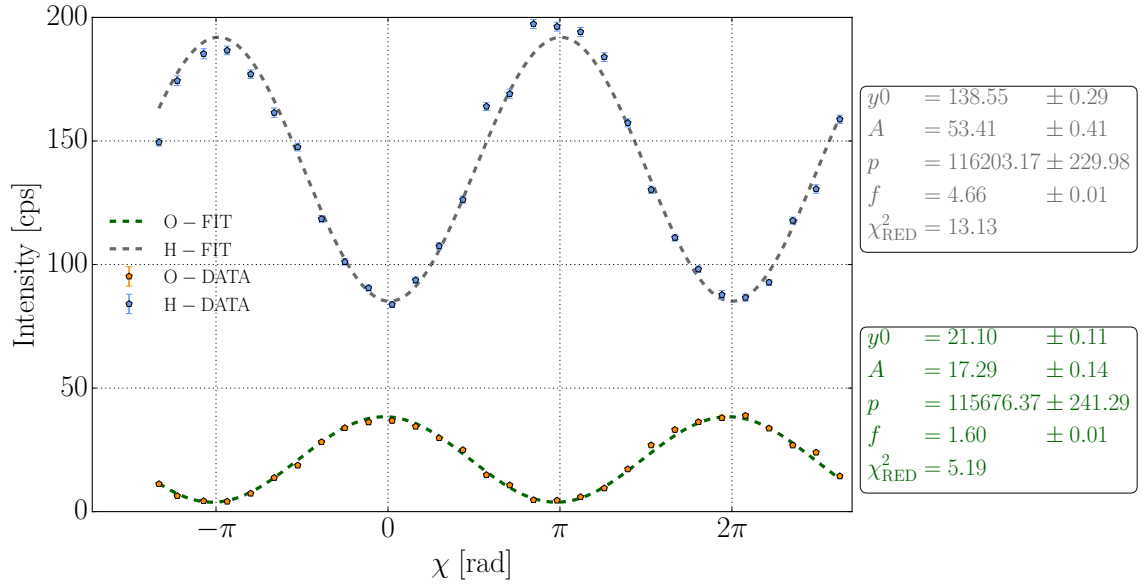


Figure 4.18: Interference fringes of the polarized setup: Even though the count rate is reduced dramatically, the contrast of the O-detector is still over 80%. The H-detector contrast is also still at $\sim 40\%$.

matically, its contrast is still over 80% and that the H-detector contrast is also still at $\sim 40\%$, showing that the setup is excellently calibrated.

4.2.1.2 Optimizing the measurement strength

The question of how weak the interaction of the measurement should be comes naturally to the mind of the experimentalist, in dealing with weak measurements. The theoretical considerations of chapter 3 tell us that the relations to extract the weak value for weak interactions, i.e. Eq. (3.16a) to (3.16c), will give a more accurate result if the interaction strength is decreased. At the same time experimental circumstances, including noise, demand to determine an interaction strength that can be used in practice.

To find an experimentally suitable magnitude for α , two interference fringes are recorded for different values of α . One without any spin manipulation between pre and postselection, the OUT curve, and one with a spin rotation of α in each path, the IN curve. In particular the postselection direction $\phi = 0^\circ$ and $\theta = 0^\circ$ is regarded. For this direction the spin manipulation inside the interferometer manifests itself in a phase shift of α between the IN and the OUT curve. Fig. 4.19 shows the IN and

OUT interferogram for an interaction strength of $\alpha = 10^\circ$. The phase shift between

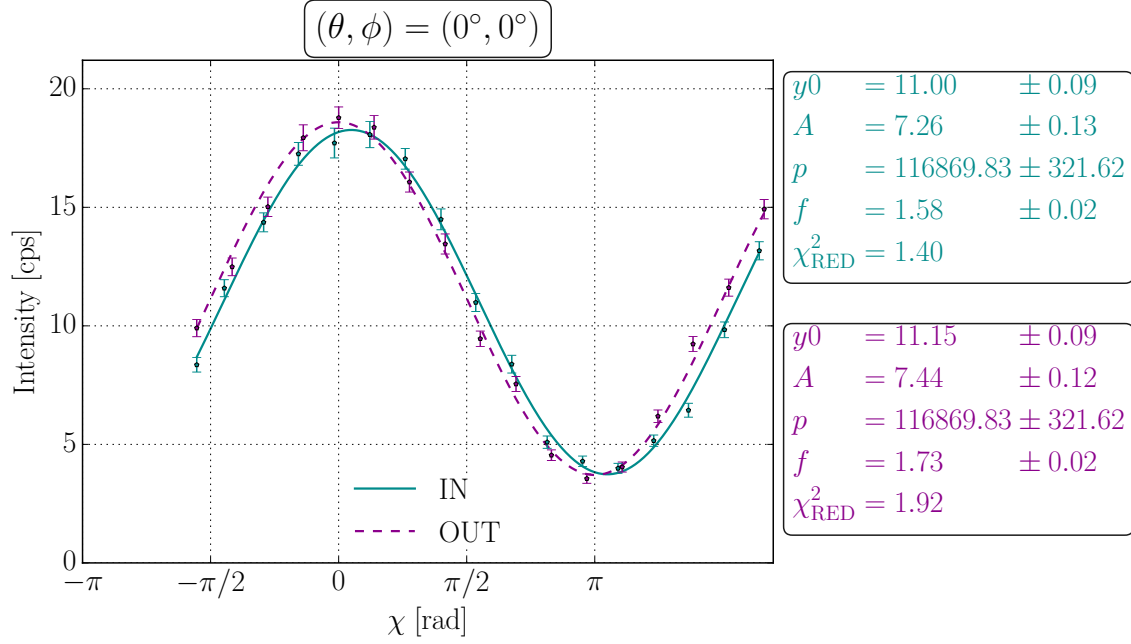


Figure 4.19: IN and OUT curve for an interaction parameter $\alpha = 10^\circ$. A phase shift of $8.6^\circ \pm 1.6^\circ$ between the IN and the OUT curve is observed (without a phase correction from the H-beam).

the two curves can be determined from the data fit. It is given by $8.6^\circ \pm 1.6^\circ$. Figure 4.20 shows the same measurement results for an interaction strength of $\alpha = 15^\circ$. The phase shift between the IN and the OUT curve is now noticeable larger. From the fit parameters a phase shift of $12.1^\circ \pm 1.6^\circ$ is obtained. Systematic phase fluctuations between the IN and the OUT curve can be taken into account using the H-detector interference fringes as a reference. If this is done the obtained value improves to $16.5^\circ \pm 1.6^\circ$ so that it is in accordance with the theoretical prediction of $\alpha = 15^\circ$.

We see that reasonable results are already obtained for interaction strengths as small as $\alpha = 10^\circ$ and we expect the experiment to yield accurate results for the weak value for such small interactions. However, in general it is true that every extra increase in the interaction strength makes the experiment easier to perform^c.

Using the correlation function defined as [Sakurai and Napolitano, 2011]

$$C(t) = \langle \psi(t) \psi(0) \rangle, \quad (4.8)$$

^cThe advantages of larger interaction strengths are also discussed in chapter 5.

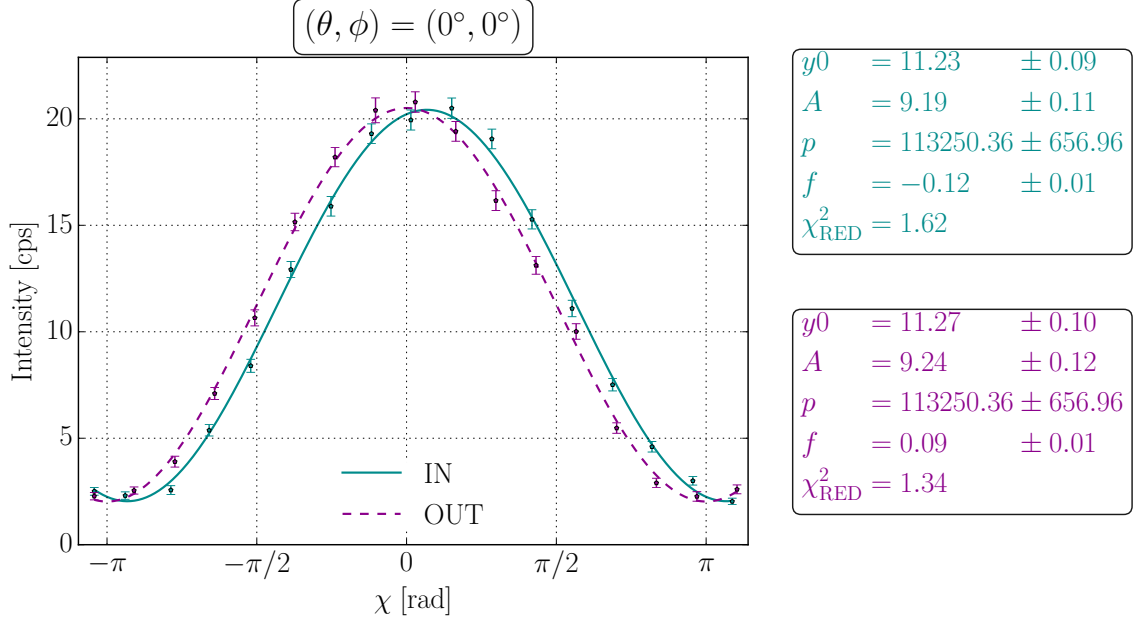


Figure 4.20: IN and OUT curve for an interaction parameter $\alpha = 15^\circ$. A phase shift of $12.1^\circ \pm 1.6^\circ$ between the IN and the OUT curve is observed (without a phase correction from the H-beam).

one can calculate the wave function overlap between the preselected state and the evolved state spin state, i.e. the state after the spin rotation of α . For $\alpha = 15^\circ$ it is still over 98% and consequently $\alpha = 15^\circ$ is chosen for the interaction strength for the actual experiment.

To illustrate the experimental advantages of larger interaction strengths, the results of a measurement with $\alpha = 90^\circ$, i.e. with maximum interactions strength, are depicted in Fig. 4.21. For the maximum interaction strength a phase shift of $\alpha = 90^\circ$ between the IN and the OUT curve is expected. A phase shift of $90.5^\circ \pm 1.3^\circ$ is experimentally observed^d.

4.2.1.3 Data acquisition

The experiment to determine the spin weak value was carried out for different post-selected spin states $|S_f\rangle$. For each experimental run the azimuth angle is held fixed. As explained in the previous section this is equivalent to fixing the position of DC2. Then the polar angle is varied, i.e. the current applied to DC2 is tuned. Four different azimuth angles changed to $\phi = 0^\circ$, $\phi = 30^\circ$, $\phi = 60^\circ$ and $\phi = 90^\circ$ are investigated. For each ϕ -direction the weak value of thirteen different polar angles

^dThe interferogram was obtained during cycle 175 in June 2015 with a very similar setup.

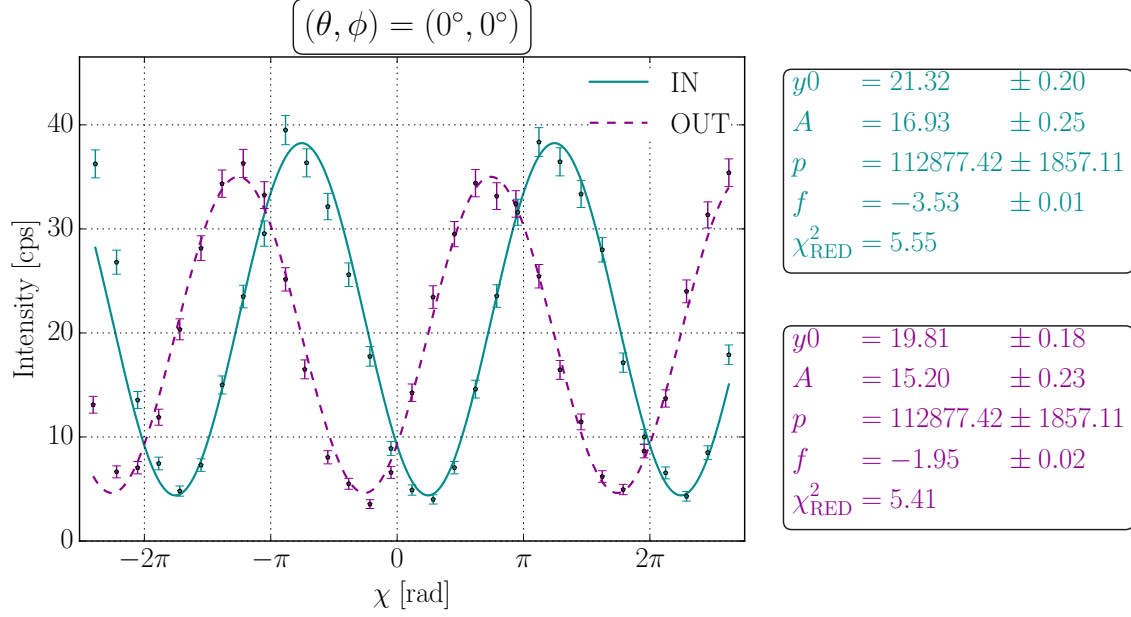


Figure 4.21: IN and OUT curve for an interaction parameter $\alpha = 90^\circ$. A phase shift of $90.5^\circ \pm 1.3^\circ$ between the IN and the OUT curve is observed (without a phase correction from the H-beam).

from $\theta = -180^\circ$ to $\theta = +180^\circ$ in 30 degree steps is evaluated. A total of 52 interferograms are recorded through which the real part as well as the modulus of the spin operator's weak value $\langle \hat{\sigma}_z^s \rangle_w$ are determined.

The angle of spin rotation inside the interferometer is set $\alpha = \pm 15^\circ$ in each path. This corresponds to a relative interaction strength^e of $\sim 17\%$. One additional test measurement was performed for a lower interaction strength of $\alpha = \pm 10^\circ$.

All measurements are performed in the IN/OUT style, i.e. the spin rotation is turned on, then the intensity is recorded for a fixed phase shifter position. After that the spin rotation is turned off and again the intensity is measured for the same phase shifter position. This style makes it possible to determine the phase χ of the “empty” interferometer. With scan the whole path qubit is scanned in the xy -plane by using the phase shifter. Therefore it is possible to extract all necessary data to obtain the real part, as well as the modulus of the spin operator's weak value from one such phase shifter scan. The H-beam is not spin analyzed. Therefore it is not used to extract the weak value. Nevertheless it can be used to determine the period of the interference measurements (also those of the O-beam) with the advantage of better statistics due to a higher intensity. The H-beam can also be used as a monitor

^eThe maximum measurement strength is $\alpha = 90^\circ$ which corresponds to a relative interaction strength of 100%. $\alpha = 45^\circ$ corresponds to a relative interaction strength of 50%, etc.

to correct phase fluctuations.

As already mentioned before the imaginary part was not determined during reactor cycle 169 in April/May 2013. To counter criticism against the experimental approach, the experiment was built up for a second time during reactor cycle 177 December in 2015 and $\text{Im}[\langle \hat{\sigma}_z^s \rangle_w]$ was determined for a spin postselection direction of $\phi = 90^\circ$ using the interferometric setup at ILL. Both the results for $\text{Im}[\langle \hat{\sigma}_z^s \rangle_w]$ obtained in Vienna and in Grenoble at a later stage, will be subject of the following sections.

All measurements are fitted with a function of the form of Eq. (4.6). The period of the measurement is extracted from the H-beam results and then used to fit the O-beam. Therefore the error of the period for the O-beam fits is per definition zero. For the estimation of an error for the O-beam fits, a mean error of the period is used to calculate the weak value. The purpose of the OUT measurement, i.e. the one without a spin rotation inside the interferometer, is to find the phase values of $\chi = 0$, $\chi = \pi/2$, $\chi = \pi$ and $\chi = 3\pi/2$ of the empty interferogram. The maximum of the OUT curve corresponds to $\chi = 0$, the minimum to $\chi = \pi$, i.e. $\chi = 0 \hat{=} \chi|_{\text{max(OUT)}}$ and $\chi = \pi \hat{=} \chi|_{\text{min(OUT)}}$. The phase value of $\chi = \pi/2$ is then given by $\chi = \pi/2 \hat{=} \chi|_{\text{max(OUT)}} + [\chi|_{\text{min(OUT)}} - \chi|_{\text{max(OUT)}}]/2$. The phase value of $\chi = 3\pi/2$ is determined by finding the point $\chi = 3\pi/2 \hat{=} \chi|_{\text{min(OUT)}} + [\chi|_{\text{min(OUT)}} - \chi|_{\text{max(OUT)}}]/2$. In order to calculate the intensities corresponding to the states $|P_x; \pm\rangle$ and $|P_y; \pm\rangle$ the phase values obtained from the OUT measurements are inserted into the IN measurement's fit functions. The result of this process is depicted by Fig. 4.22.

We now know how to experimentally record intensities that can be linked to certain pre and post selected states. We also know how to use these intensities to get the real and imaginary part of the weak value. The last thing that needs to be clarified is the way to derive the weak value's error.

Looking again at Eqs. (3.16a) to (3.16c) we see that they are basically functions of three parameters, i.e. $g(\alpha, I_{j+}, I_{j-})$. Each of these three parameters has an error attached to it. Since there is no correlation between the three parameters and the functions to extract the weak values are linear in the region we are interested in, we can use the simple rule for propagation of uncertainty

$$\sigma_{\text{wv}} = \left[\left(\frac{\partial g}{\partial \alpha} \right)^2 (\Delta\alpha)^2 + \left(\frac{\partial g}{\partial I_{j+}} \right)^2 (\Delta I_{j+})^2 + \left(\frac{\partial g}{\partial I_{j-}} \right)^2 (\Delta I_{j-})^2 \right]^{\frac{1}{2}}, \quad (4.9)$$

where Δ_{wv} is the weak value's error of the and $\Delta\alpha$ and $\Delta I_{j\pm}$ are the errors of the quantities that are used to calculate the weak value [Ku, 1966].

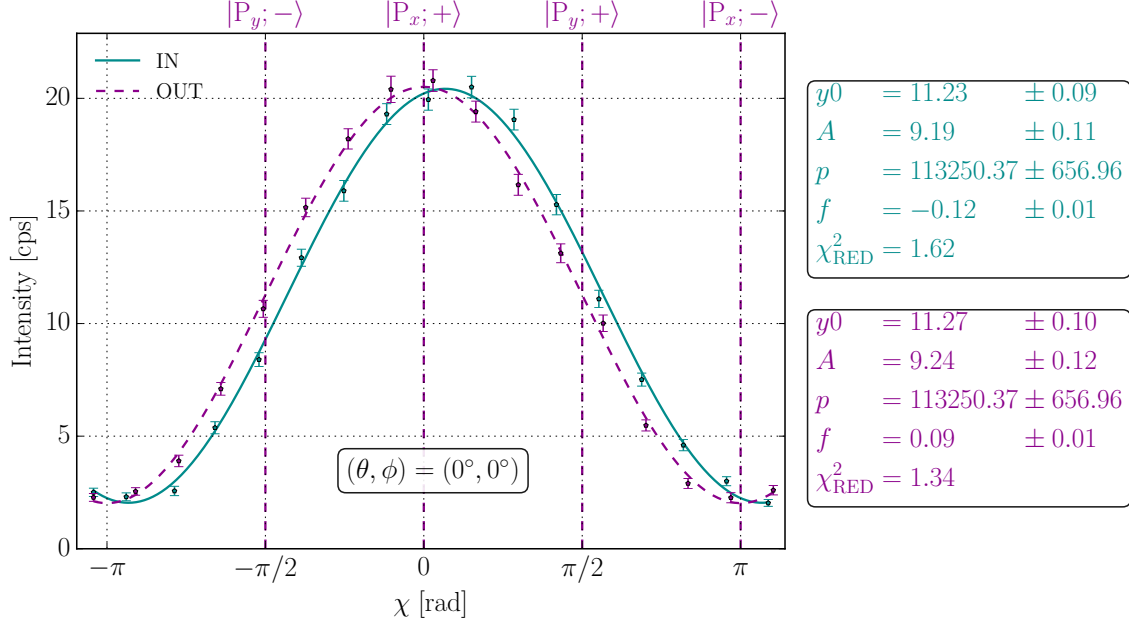


Figure 4.22: O-detector interferogram for a direction of spin postselection of $\phi = 0^\circ$ and $\theta = 0^\circ$. The dashed lines are least-square fits to the data. The error bars represent one standard deviation. The measurements without spin rotation inside the interferometer (OUT-scan in magenta) are used to determine the phase of the empty interferometer and therefore the value of χ for the states $|P_x; \pm\rangle$ and $|P_y; \pm\rangle$. The intensities $I_{x\pm}$ and $I_{y\pm}$ are then taken from the data fit of the measurements with an additional spin rotation inside the interferometer (IN-scan in cyan). Both interference fringes are plotted without background correction.

Finally we have to clarify the sources of the individual errors of these quantities. The error of the rotation angle of the spin in the interferometer α is obtained from the calibration measurement of the spin manipulators inside the interferometers. It can be read off the fit parameter errors in Fig. 4.16. If it is set to $\Delta\alpha = 2^\circ$. This is a conservative upper boundary.

For the imaginary part of the weak value $\sigma_{I_{z\pm}}$ are simply given by the square roots of the single intensities $I_{z\pm}$ due to the Poissonian counting statistics. For the weak value's real part and its modulus the intensities are not directly recorded, but taken from the fit to many recorded data points. Because of that the situation becomes more complicated. The measurements are fitted with a function of the form of Eq. (4.6) using the method of minimizing chi square. For each fitted parameter the fit yields an error, which can be used to calculate the intensities' error. First the OUT measurement has to be fitted to get the phase values of $\chi = 0$, $\chi = \pi/2$, $\chi = \pi$ and $\chi = 3\pi/2$. The phase values are of course defined by the position on the cosine function. However they are still attached by an error, which is given by the phase

error obtained from the OUT fit. In the example given in Fig. 4.22 this error $\Delta\chi$ is given by $\Delta\chi = 0.01$. As was already mentioned the intensities $I_{y\pm}$ and $I_{x\pm}$ are taken from the fit of the IN curve. To get the errors $\Delta I_{y\pm}$ again the rules of propagation of uncertainty can be applied using the errors the fit on the IN data points yields. When the fit function g is given by Eq. (4.6) we get the intensities error

$$\Delta I_{j\pm} = \left[\left(\frac{\partial g}{\partial y_0} \right)^2 (\Delta y_0)^2 + \left(\frac{\partial g}{\partial A} \right)^2 (\Delta A)^2 + \left(\frac{\partial g}{\partial p} \right)^2 (\Delta p)^2 + \left(\frac{\partial g}{\partial x} \right)^2 (\Delta x)^2 + \left(\frac{\partial g}{\partial f} \right)^2 (\Delta f)^2 \right]^{\frac{1}{2}} \quad (4.10)$$

where $\Delta x = \Delta\chi$ is given by the phase error of the OUT fit (0.01 in the example above) and Δy_0 , ΔA , Δp as well as Δf are given by the parameter errors of the IN fit.

The effect of the weak interaction is clearly visible in Fig. 4.22. Compared to the OUT curve, recorded without active spin rotation during the events of pre and post-selection, the IN curve, with active spin rotation, is phase shifted. With the intuitive picture developed in chapter 3 and visualized in Fig. 3.1 we can easily understand this behavior. Let us recall that the real part of the spin operator's weak value acts as an additional phase in the meter system. This additional phase can now be observed in the measurement. The theoretical considerations performed in chapter 3 are fully supported by the experiment. In addition to those at the O-detector two interferograms are also recorded at the H-detector during the measurement of one postselection direction. In Fig. 4.23 the H-detector results for the direction $(\theta, \phi) = (0, 0)$ are plotted.

As was already stated, in contrast to the O-beam, the H-beam is not spin analyzed. This means that the neutrons detected at the H-detector are not subject to any spin postselection and not all effects of the weak interaction are observable. While in Fig. 4.22 the IN curve is shifted to the right of the OUT curve, no systematic phase shift can be seen in the H-detector interferograms. Nevertheless the spin rotation inside the interferometer brings the spin states closer to orthogonality, which manifests itself in a loss of contrast also at the H-beam. This loss in contrast scales with the interaction parameter α and is for $\alpha = \pm 15^\circ$ too small to be observed at the H-beam. Note that the least square fits to the IN and the OUT curve yield slightly different periods. The average of both periods is used to fit the O-detector as described previously.

During the weak spin measurement a total of 52 interferograms were recorded. In

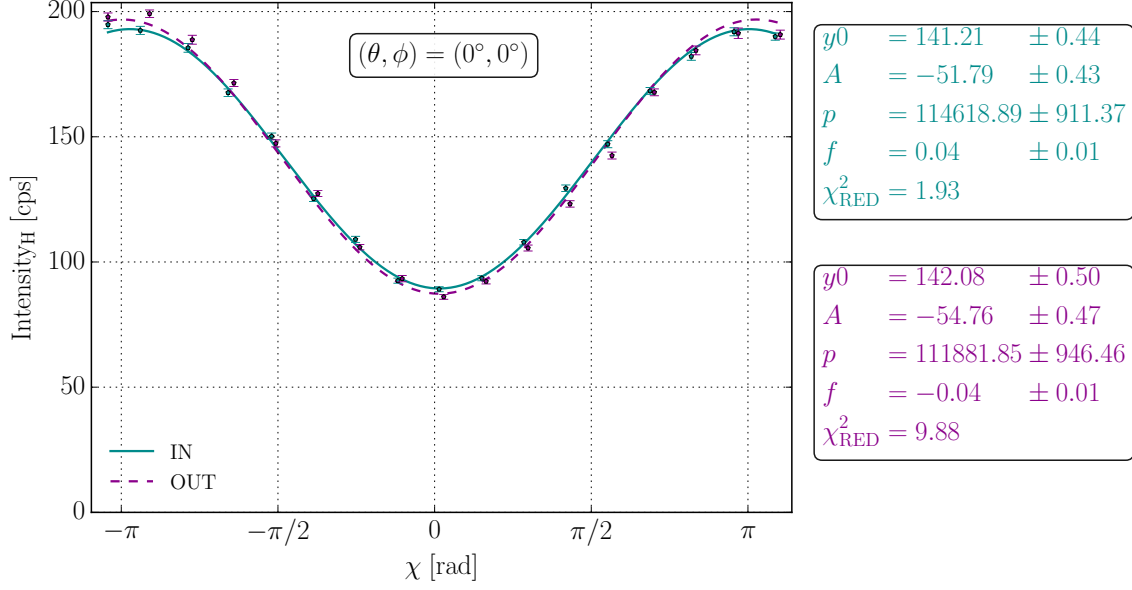


Figure 4.23: H-beam interferogram for a direction of spin postselection of $\phi = 0^\circ$ and $\theta = 0^\circ$. The dashed lines are least-square fits to the data. The error bars represent one standard deviation. Since the H-beam is not spin analyzed, the effects of the weak interaction are not observable. Note that average of both periods is $\bar{p} = 113250$, which was used to fit the O-data. Both interference fringes are without background correction.

the following pages a selection is presented: Fig. 4.24 shows three interferograms for an postselection azimuthal direction of $\phi = 0^\circ$. For clarity Bloch spheres are included besides the interferograms, where the preselected state $|S_i\rangle$ is indicated by a green and the postselected state $|S_f\rangle$ by a blue arrow.

As was already mentioned in the previous chapter the weak value's real part manifests itself in a phase shift in the meter system. This shift is already visible in the interferograms. For the postselection direction $(\theta, \phi) = (0^\circ, 0^\circ)$, $\text{Re}[\langle \hat{\sigma}_z^s \rangle_w]$ is expected to be plus one. Indeed we find that the IN curve is slightly shifted to the right as compared to the OUT curve, when looking at the middle panel of Fig. 4.24. For the postselection directions $(\theta, \phi) = (-150^\circ, 0^\circ)$ and $(\theta, \phi) = (150^\circ, 0^\circ)$ (upper and lower panel of Fig. 4.24, respectively) negative values for the spin operator's weak value are expected and actually we find that for those interferograms the IN curve is shifted to the left, compared to the OUT curve. In addition the magnitude of $\text{Re}[\langle \hat{\sigma}_z^s \rangle_w]$ is bigger for $(\theta, \phi) = (-150^\circ, 0^\circ)$ than it is for $(\theta, \phi) = (150^\circ, 0^\circ)$. Therefore the phase shift between IN and OUT curve is larger in the first case.

Figure 4.25 shows the obtained interference fringes for the postselection directions $(\theta, \phi) = (-150^\circ, 30^\circ)$, $(\theta, \phi) = (0^\circ, 30^\circ)$ and $(\theta, \phi) = (150^\circ, 30^\circ)$.

It is interesting to note that for any azimuthal angle ϕ the postselected spin state

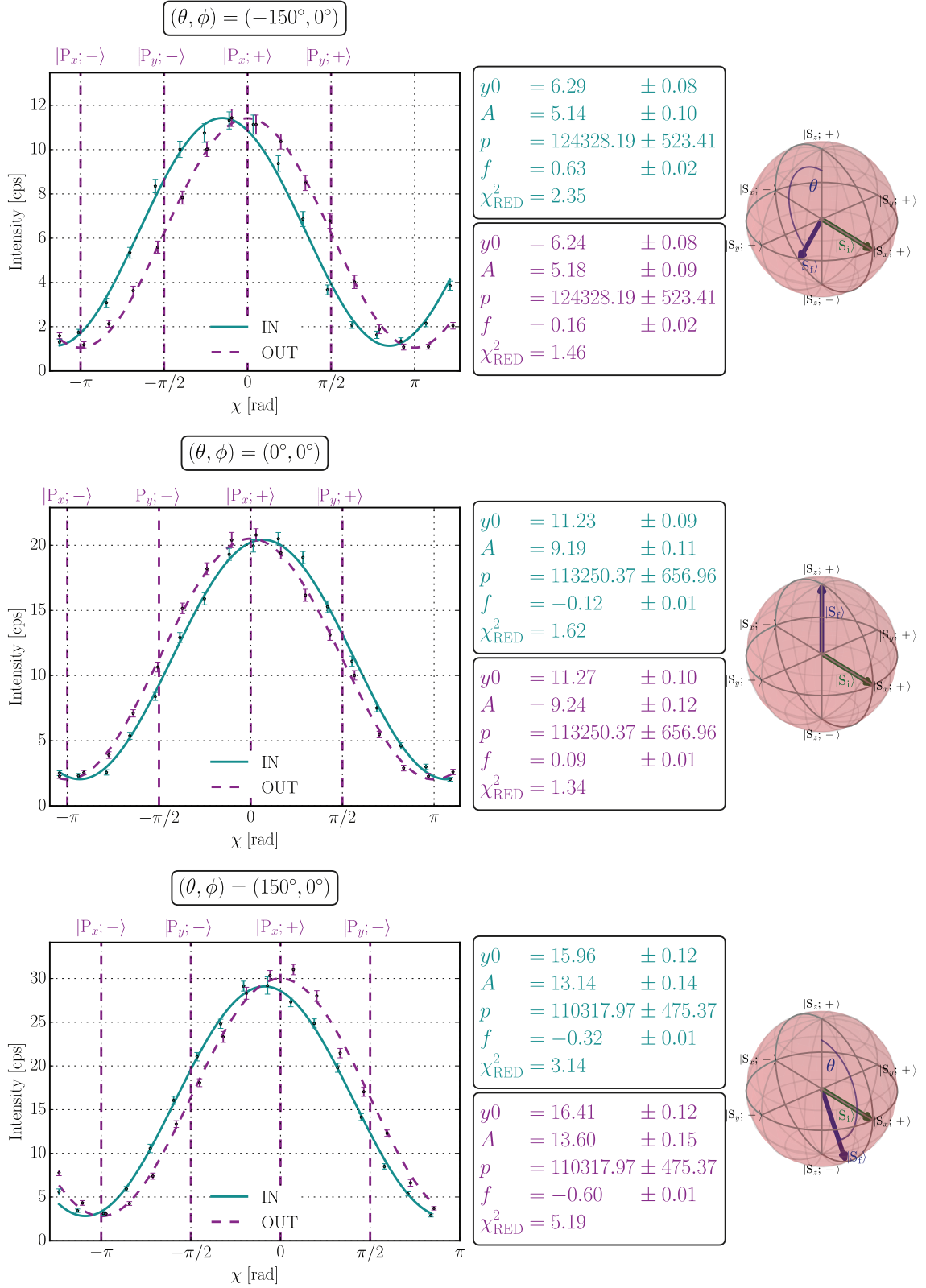


Figure 4.24: O-detector interferograms for the postselection directions $(\theta, \phi) = (-150^\circ, 0^\circ)$, $(\theta, \phi) = (0^\circ, 0^\circ)$ and $(\theta, \phi) = (150^\circ, 0^\circ)$. The lines are a least-square fits to the data. The error bars show one standard deviation.

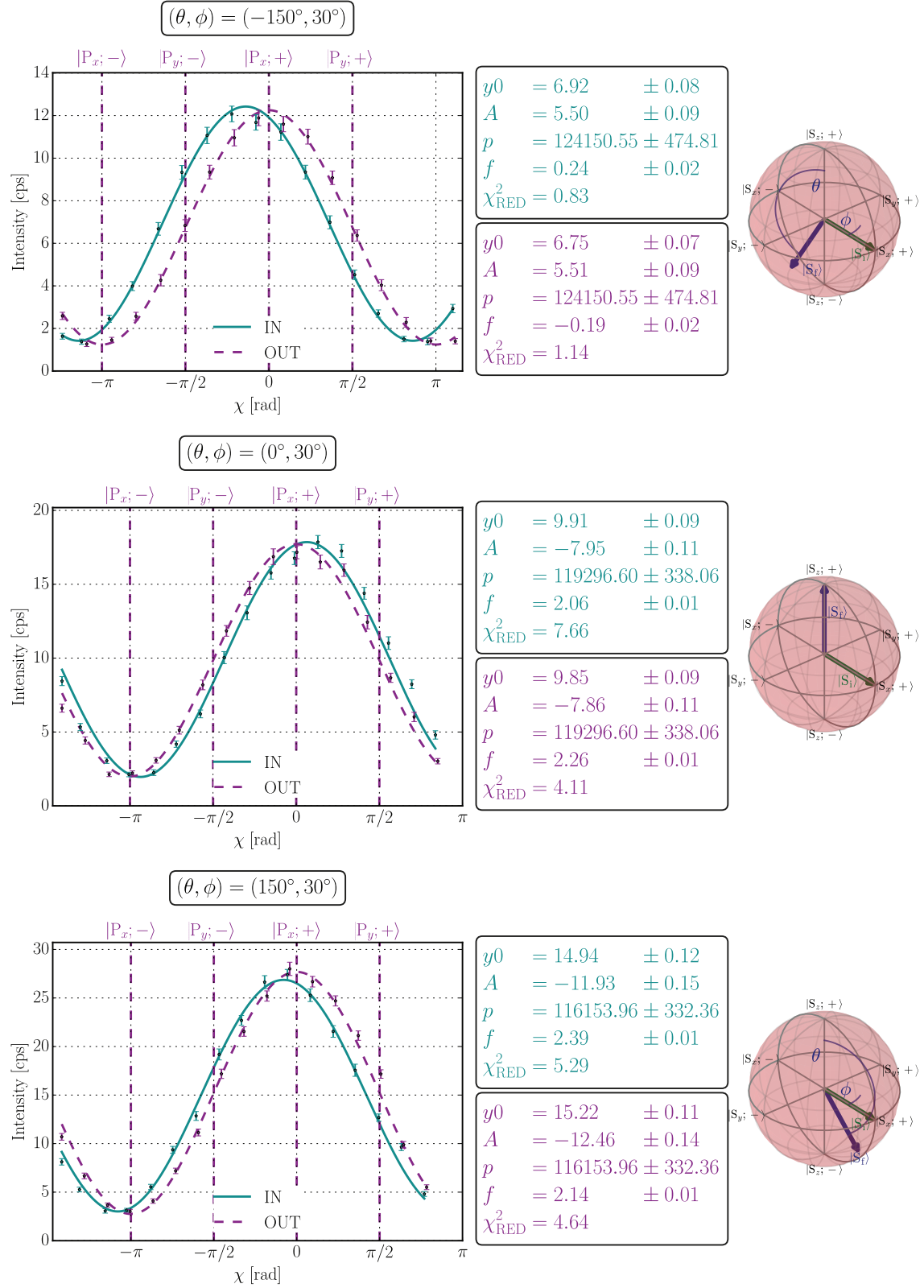


Figure 4.25: O-detector interferograms for the postselection directions $(\theta, \phi) = (-150^\circ, 30^\circ)$, $(\theta, \phi) = (0^\circ, 30^\circ)$ and $(\theta, \phi) = (150^\circ, 30^\circ)$. The lines are a least-square fits to the data. The error bars show one standard deviation.

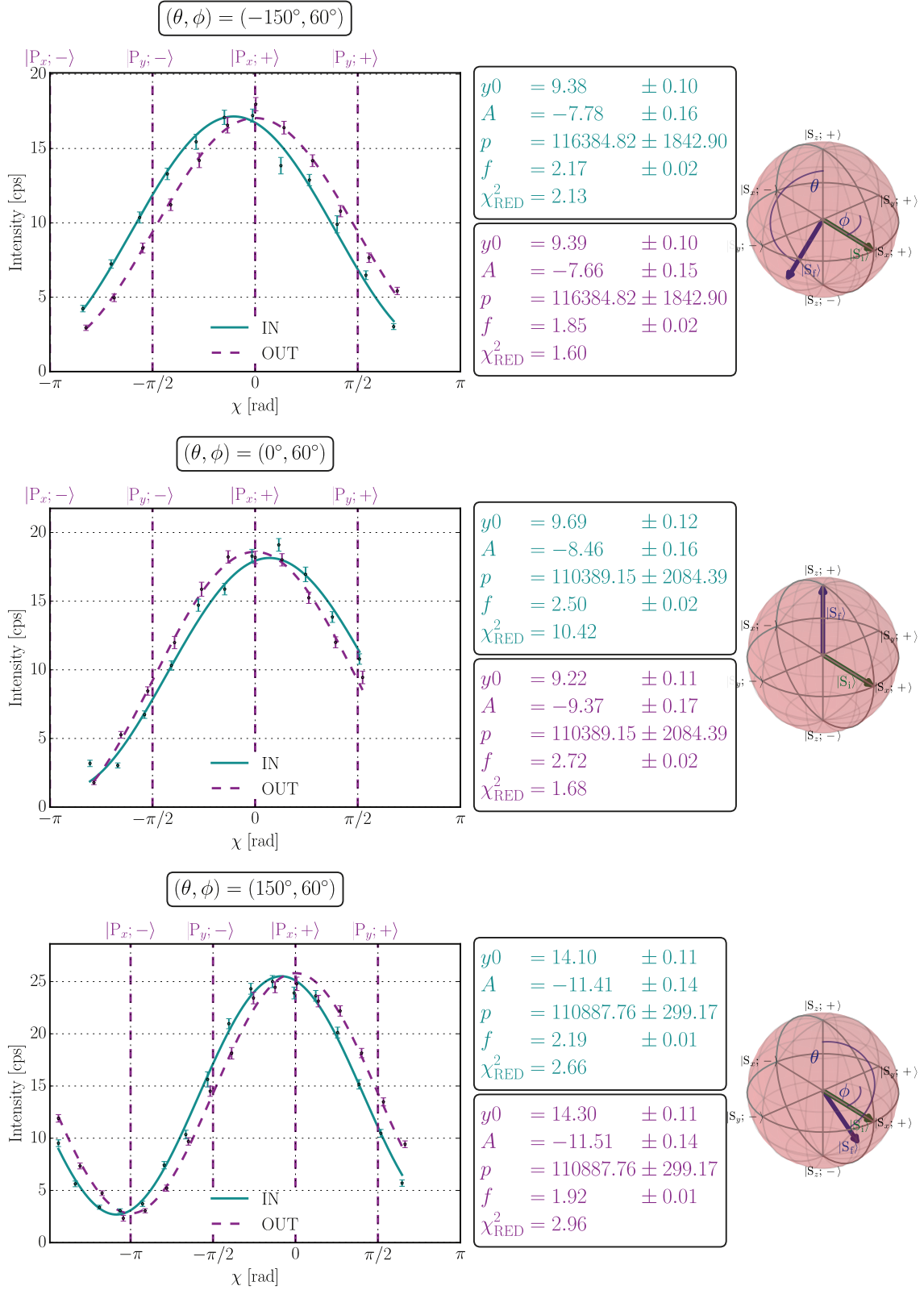


Figure 4.26: O-detector interferograms for the postselection directions $(\theta, \phi) = (-150^\circ, 60^\circ)$, $(\theta, \phi) = (0^\circ, 60^\circ)$ and $(\theta, \phi) = (150^\circ, 60^\circ)$. The lines are a least-square fits to the data. The error bars show one standard deviation.

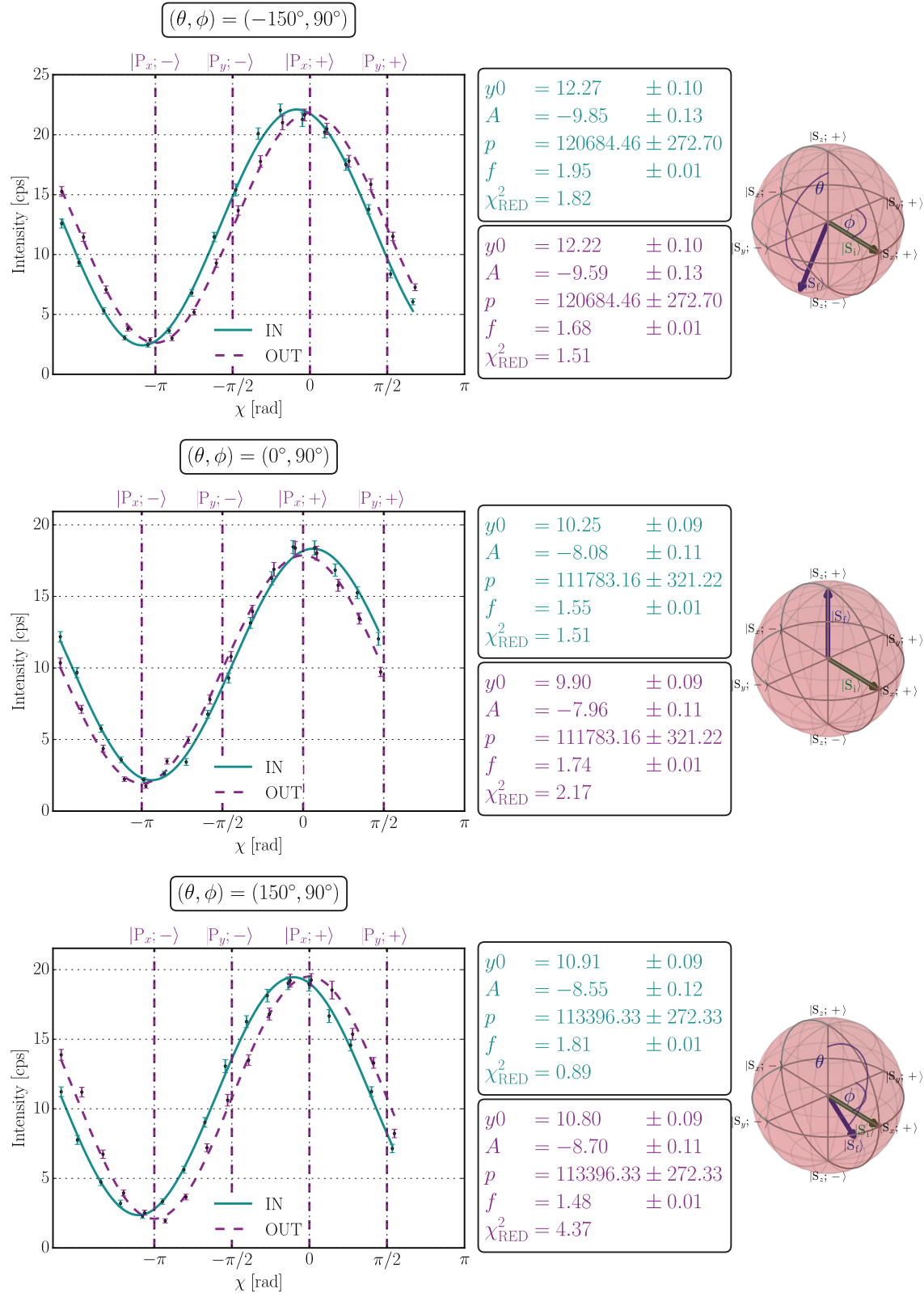


Figure 4.27: O-detector interferograms for the postselection directions $(\theta, \phi) = (-150^\circ, 90^\circ)$, $(\theta, \phi) = (0^\circ, 90^\circ)$ and $(\theta, \phi) = (150^\circ, 90^\circ)$. The lines are a least-square fits to the data. The error bars show one standard deviation.

$|S_f\rangle$ will be $|S_f\rangle \equiv |S_z; +\rangle$ as long as $\theta = 0$. Because of that the weak value's real part will be plus one for all values of ϕ . Consequently all interferograms for this direction are expected to be similar. Looking at Figs. 4.24 to 4.27 one sees that this is indeed the true. All eight interferograms (4 IN and 4 OUT measurements) have roughly the same amplitude A and mean y_0 . The phase shift between IN and OUT curves is also ~ 0.2 rad for all four ϕ postselection directions.

The interferograms in Fig. 4.26 are noteworthy because they demonstrate an experimental problem that arose during the measurements. Due to limited beam time at the S18 interferometer station in Grenoble the points that were recorded for each interferogram were set to a minimum. Only 17 data points were recorded per interference fringe. This guaranteed that a full period was observed for every interferogram, which is needed to get good results for minimizing χ^2 -fit to the data points. However, during the experiment a problem with the setup arose. The phase shifter made unwanted movements rendering parts of the recorded interferogram useless. This is the reason why the interference fringes in the upper two panels of Fig. 4.26 offer less data points than the others. Of course the lack of data does not help to get sound results. Later we will see that in general the theory is in very good agreement with the measurement, but that there are some data points that show a large deviation. The “broken” interferograms are exactly the reason for that. There are even data points missing. This is the case whenever the interferogram was cut into pieces by the experimental problem, rendering it useless, due to the wrong movement of the phase shifter. The interested reader is surely happy to know that the cause of the unwanted phase shifter movements was eventually identified and eliminated. A loose screw allowed the phase shifter to move unwantedly. Fastening the screw tight solved the problem.

Finally Fig. 4.27 shows the interference fringes for the azimuthal postselection direction $\phi = 90^\circ$. For this postselection direction the weak value's real part is symmetric in θ around zero. Because of that the interference fringes of $\theta = -150^\circ$ and $\theta = 150^\circ$ are very similar. As we will see in the next section they will yield an identical weak value.

4.2.1.4 Background and contrast corrections

The aim of weak measurements is to perform quantum measurements only with minimal disturbance of the quantum system. While this brings the advantage that the wave function of the investigated system does not necessarily gets altered much and collapses, it also has the disadvantage that one needs to deal with very low

signals. Therefore it is important to be able to deal with bad signal to noise ratios. First it is important to realize that there are neutrons that are coherent in the spin Hilbert space, but not coherent in the path Hilbert space and vice versa. Both sort of particles reduce the overall contrast of the experiment. This kind of effect has to be taken into account for a detailed analysis.

Let us first consider those particles that are not coherent in the spin space. In general the polarimetric part of the experiment^f offers a higher contrast than the interferometer itself. Taking all components into account one typically achieves a contrast of $\sim 95\%$. Albeit this is very high it still has to be considered, for the treatment of weak interactions and small signals. When pre and postselected states are orthogonal, i.e. $|S_i\rangle \equiv |S_x; +\rangle$ and $|S_f\rangle \equiv |S_x; -\rangle$, one expects to detect no neutrons at all for zero interaction. But due to experimental imperfections of the polarimetric part, this never happens. The recorded interference fringes (IN and OUT curve) for orthogonal pre and postselected states are shown in Fig. 4.28.

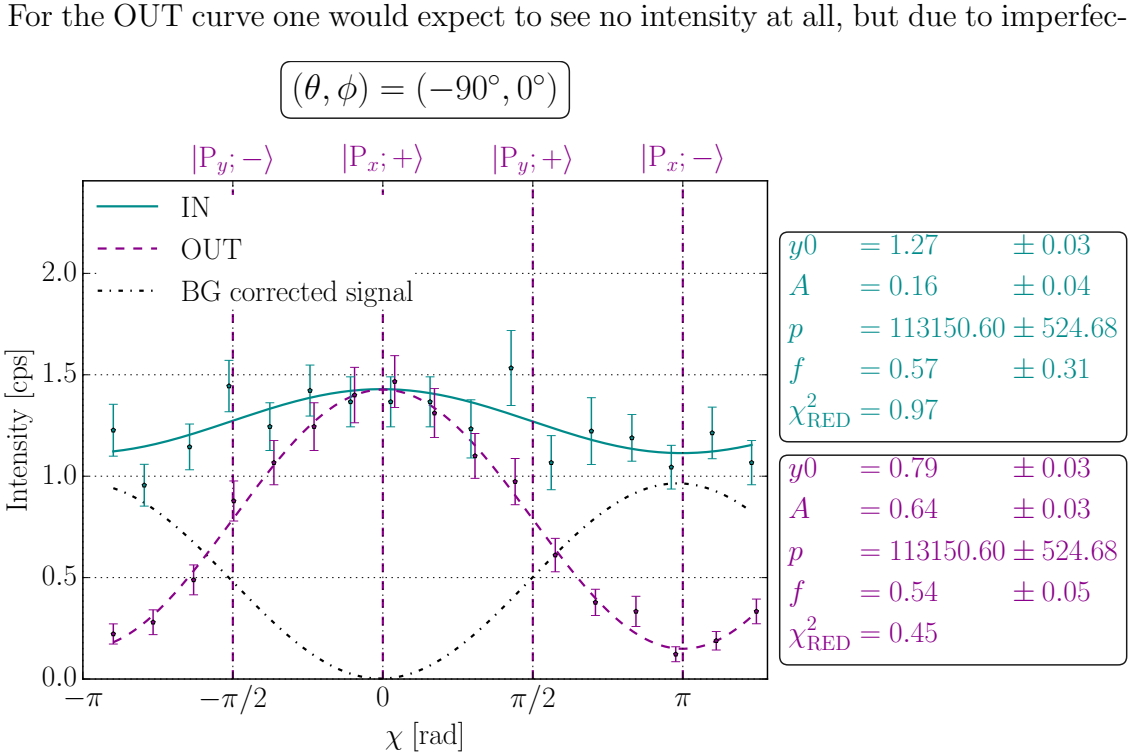


Figure 4.28: Interference fringes of the O-beam for orthogonal pre and postselected states: For the OUT curve one would expect no intensity at all. When the OUT curve's fit is subtracted from the IN curve, the correct signal is observed.

tions in the experimental setup, there is a “leak” intensity. Instead an interference

^fThe polarimetric part of the experiment are all components that manipulate the neutron spin, such as polarizer, analyzer, coils and so on.

fringe with very little intensity is observed. Note that the contrast of the interference is $\sim 80\%$, which also corresponds to the contrast of the empty interferometer. Moreover, from the H-detector data it can be inferred, that this interference is in phase with the empty interferogram. The OUT curve is obtained by neutrons that are coherent in the path space, independent of spin. The OUT curve for orthogonal pre and postselected states is an effective background, which also present in the IN signal. The ratio between IN signal and background depends on the direction of spin postselection and is worst for orthogonal pre and postselected states. For this case the IN signal is very low, because of the weakness of the interaction and the signal to noise ration (ratio between IN and OUT curve) is $\sim 1 : 1$. Only when the OUT fit is subtracted from the IN fit the correct IN signal is observed. For $|S_f\rangle \equiv |S_x; -\rangle$ and $\alpha = 15^\circ$ the IN curve is expected to be phase shifted by π compared to the interference fringe of the empty interferometer. We see that the black line in Fig. 4.28 is phase shifted by π as compared to the OUT curve. We can therefore treat the OUT signal for orthogonal states as an effective background and subtract it from any IN curve in the experiment. This takes the background into account and therefore allows to resolve the correct signal also for weak interactions. Note that for the determination of the spin operator's weak value we are only interested in the data fits, not in a point to point comparison. This makes the problem easier to solve, since single outliers can be neglected. If a point to point comparison is needed, the stability of the setup and the alignment of the components has to be improved considerably, so that no single point of the IN curve drops below the OUT curve. This experimental obstacle will be discussed in more detail in chapter 5.

It is true for polarized neutron interferometry in general that the maximally achievable contrast is 90% at most. The reduced contrast is mainly due to incoherent neutrons and not due to background of the detector or the polarimetric part. The calculations performed in chapter 3 assume that the neutron interferometer works perfectly. It is therefore necessary to consider the influences of the interferometer's contrast for the final analysis of the data.

If both the pre and postselected state are the same, i.e. $|S_i\rangle \equiv |S_x; +\rangle$ and $|S_f\rangle \equiv |S_x; +\rangle$, one expects to have a perfect cosine interference fringe for the OUT curve. As Fig. 4.29 shows, this is not the case. The OUT curve in Fig. 4.29 can be used as a reference intensity I_R . If the neutron interferometer worked perfectly this interferogram would show 100% contrast. Therefore the contrast of this interference fringe serves as a reference for all other measurements. Having determined this value a

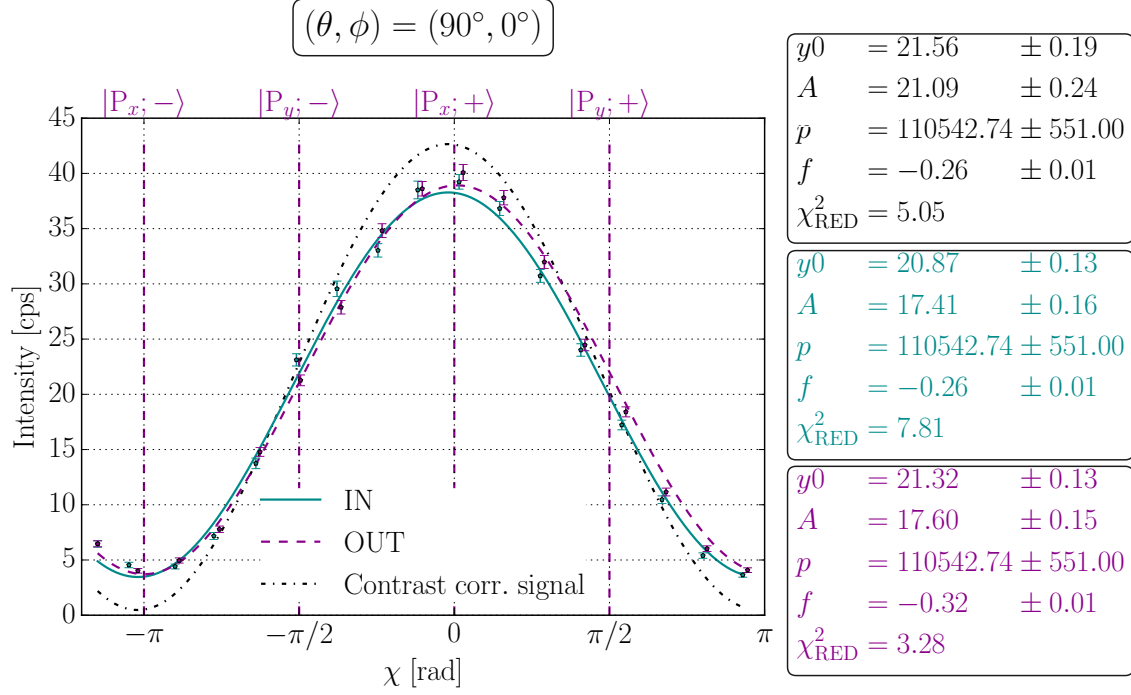


Figure 4.29: Contrast Correction: For identical pre and postselected states a perfect cosine interference fringe is expected. Due to imperfections of the neutron interferometer this is not the case. The contrast of the OUT interferogram can be used to renormalize.

measured intensity I_M can be normalized using the relation

$$I_N = \frac{I_M}{C_R} - \frac{1}{2} \sin(\theta) \cos(\phi) \min[I_R], \quad (4.11)$$

where C_R is the reference contrast, $\min[I_R]$ the minimum of the reference intensity, from which the reference contrast was extracted and θ and ϕ are the polar and azimuthal spin postselection directions respectively. The naive approach would be to simply divide the intensity by the contrast to normalize it. But this leaves the normalized intensity I_N sitting on a large offset, which has to be considered as well. The offset given by the minimum of the reference intensity times a weighting factor, which takes into account the spin postselection direction. The term $\frac{1}{2} \sin(\theta) \cos(\phi)$ scales the offset subtraction according to the expected count rate for each spin direction. In Fig. 4.29 the IN curve was normalized using Eq. (4.11) and the result is given by the black line, which shows $\sim 98\%$ contrast. This is exactly what one would expect for the IN curve of this spin direction, showing that the model we use to normalize the contrast works well. Note that the relative error of y_0 and A of the normalized curve increases. This is a consequence of propagation of uncertainty. Again it has to be remarked, that a more stable experimental setup is needed if a

point to point normalization is performed instead of working with a fit.

As a remark we want to introduce another normalization model, that can be used whenever one wants to normalize two intensities $I_{j\pm}$ that are expected to show full contrast while being phase shifted by π relative to each other. In this case the relation

$$I_{j+N} = \frac{I_{j+} + I_{j-}}{2} + \frac{I_{j+} - I_{j-}}{2C_R} \quad (4.12)$$

leads to a satisfying result. Again C_R is the contrast extracted from the reference measurement with identical pre and postselected spin states and no interaction in the interferometer.

For both operations, the background correction and the contrast normalization, propagation of uncertainty are essential for the data analysis and are taken into account for the final measurement results.

4.2.1.5 Results

The final results of the interferometric part of the weak spin measurement are shown in Figs. 4.30 and 4.31. To illustrate the directions of spin pre and postselection Bloch spheres are included in each graph. While the green arrow represents the pre-selected spin state, one of the postselection directions is implied by the blue arrow. All postselection directions lie on the blue circle. To extract the spin weak value's components from the measured intensities the relations given by Eqs. (3.16a) and (3.16c) are used. An excellent agreement between theory and experiment is found.

For $\phi = 0^\circ$ the modulus of $\langle \hat{\sigma}_z^s \rangle_w$ is simply given by the absolute of the real part, with no contribution from the imaginary part. $|\langle \hat{\sigma}_z^s \rangle_w|$ and $\text{Re}[\langle \hat{\sigma}_z^s \rangle_w]$ have a discontinuity where $|S_i\rangle$ and $|S_f\rangle$ are orthogonal. It is interesting to note that for $\theta = 90^\circ$ initial and final states coincide. For this case the weak value reduces to the expectation value, which is zero (marked by a green circle). Also for the case $\theta = 0^\circ$, $|S_f\rangle$ is an eigenstate of the operator $\hat{\sigma}_z^s$ and the eigenvalue one appears (marked by a green arrow). For $\phi = 30^\circ$ the discontinuities of $|\langle \hat{\sigma}_z^s \rangle_w|$ and $\text{Re}[\langle \hat{\sigma}_z^s \rangle_w]$ disappear, since pre and postselected spin state are nowhere orthogonal. With an increasing postselection azimuth angle the pre and postselected spin state move further away from orthogonality and the magnitude of the weak value's real part as well as that of its modulus becomes smaller as can be seen in the results for $\phi = 60^\circ$. For $\phi = 90^\circ$, $\text{Re}[\langle \hat{\sigma}_z^s \rangle_w]$ oscillates describing a cosine function while $|\langle \hat{\sigma}_z^s \rangle_w|$ is constant.

As is already discussed in chapter 3 the weak value's modulus only appears in the

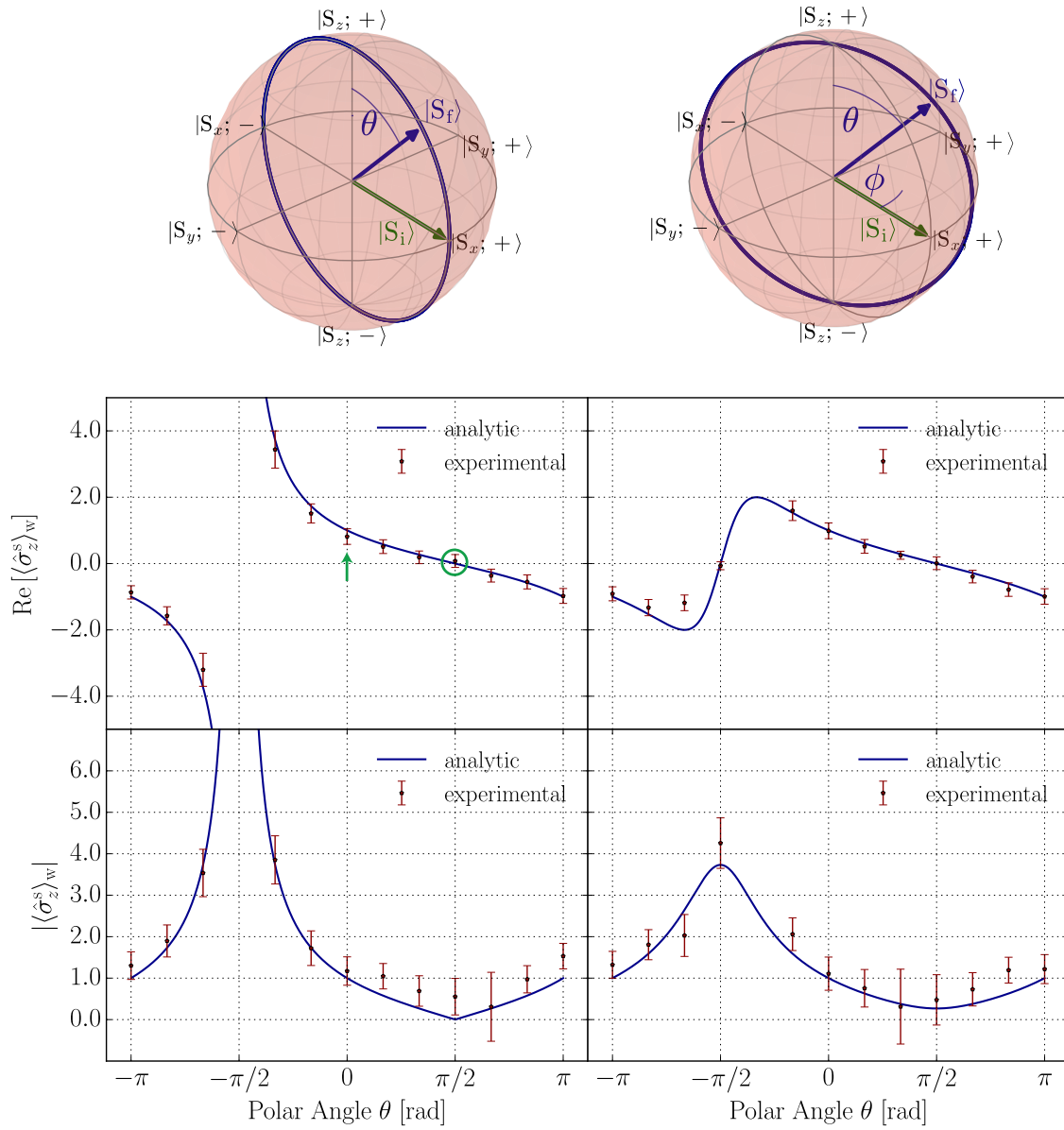


Figure 4.30: Main measurement results (red) together with the theoretical prediction (blue) for the spin operator's weak value. The error bars represent one standard deviation. Pre and postselected states are depicted on the Bloch sphere in green and blue respectively: For $\phi = 0^\circ$ the weak value's real part and its modulus have a discontinuity where $|S_i\rangle$ and $|S_f\rangle$ are orthogonal. For $\theta = 90^\circ$ initial and final states coincide, the weak value reduces to the expectation value, which is zero (marked by a green circle). For the case $\theta = 0^\circ$, $|S_f\rangle$ is an eigenstate of the operator $\hat{\sigma}_z^s$ and the eigenvalue one appears (marked by a green arrow). For $\phi = 30^\circ$ the pre and postselected state are orthogonal nowhere, the discontinuity disappears.

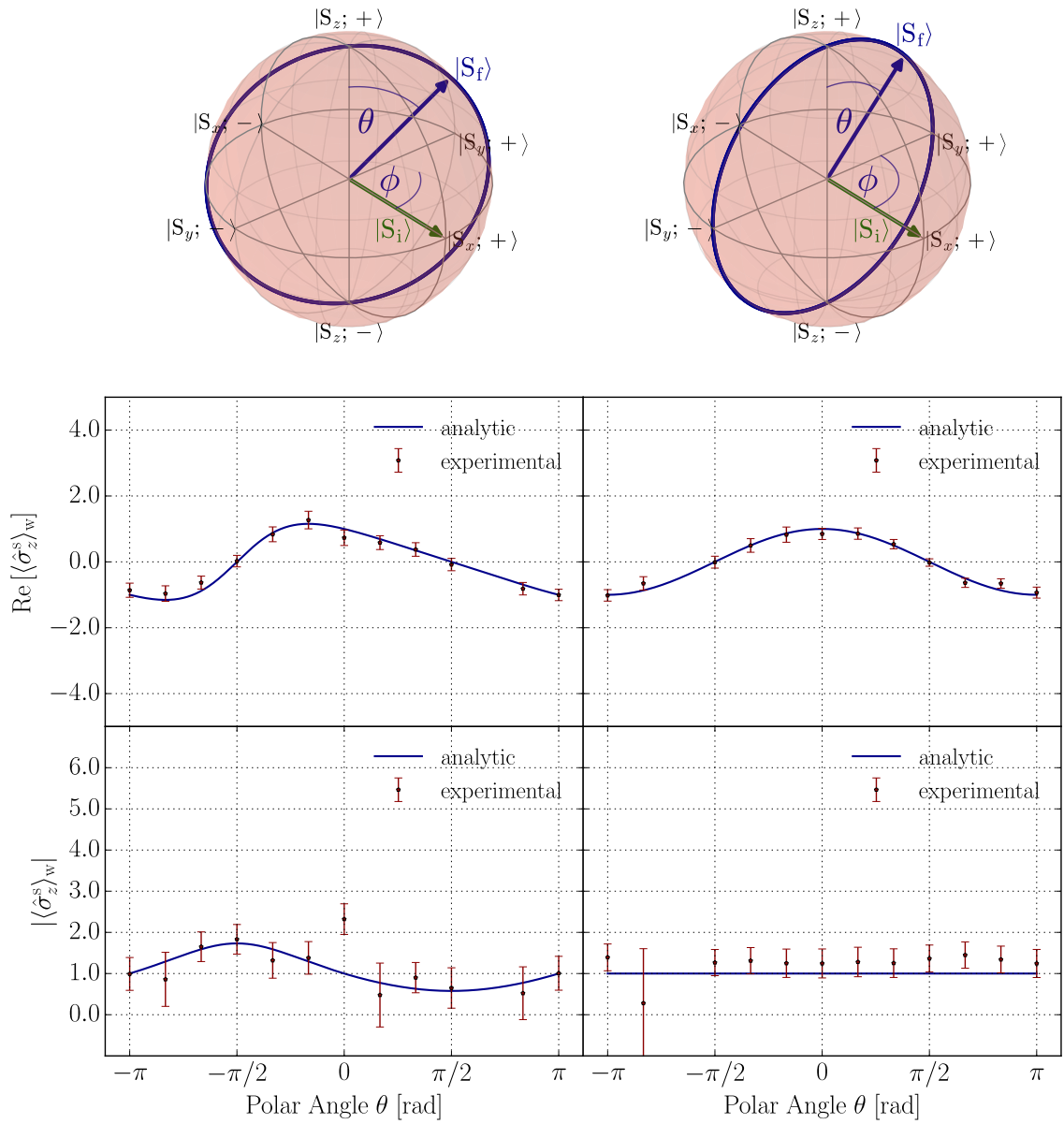


Figure 4.31: Main measurement results (red) together with the theoretical prediction (blue) for the spin operator's weak value. The error bars represent one standard deviation. Pre and postselected states are depicted on the Bloch sphere in green and blue respectively: For $\phi = 60^\circ$ $|S_i\rangle$ and $|S_f\rangle$ are further away from orthogonality and $\text{Re}[\langle \hat{\sigma}_z^s \rangle_w]$ as well as $|\langle \hat{\sigma}_z^s \rangle_w|$ become smaller. For $\phi = 90^\circ$, $\text{Re}[\langle \hat{\sigma}_z^s \rangle_w]$ oscillates describing a cosine function while $|\langle \hat{\sigma}_z^s \rangle_w|$ is constant.

second order of the interaction parameter α . In practice this means $\alpha^2 \approx 0.07$ for our setup, which corresponds to only 2.8% of relative interaction strength. For weak interactions as is the case in this experiment the second order term is hard to resolve. In contrast $\text{Re}[\langle\hat{\sigma}_z^s\rangle_w]$ already appears in the linear order. This is the reason why in general the agreement between theory and experiment is better for the weak value's real part than it is for its modulus.

In the final results the contrast of the interferometer has been taken into account. The average reproducible contrast of all measurements is $C \sim 80\%$. Although this is excellent for neutron interferometry, the influence of the limited contrast has to be considered when the absolute of the weak value is extracted from the measurement data. For the weak value's real part this is not necessary. The reason for this is simple: For $|\langle\hat{\sigma}_z^s\rangle_w|$ the intensities corresponding to the states $|P_x; \pm\rangle$ are investigated. $|P_x; +\rangle$ yields a maximum in intensity, while $|P_x; -\rangle$ gives a minimum, as can be seen in Fig. 4.22. So Eq. (3.16c), the relation to obtain $|\langle\hat{\sigma}_z^s\rangle_w|$ from the measurement data, directly compares a maximum and a minimum to each other. If, due to the reduced contrast of the interferometer, the minimum does not reach zero but a larger value, Eq. (3.16c) will never reproduce the weak value's modulus correctly. In addition a small deviation from zero leads to a large change in the obtained values. Therefore the contrast C of the empty interferogram has to be considered when the data is evaluated. At the same time C is of minor importance when $\text{Re}[\langle\hat{\sigma}_z^s\rangle_w]$ is evaluated, since I_{y+} and I_{y-} are of approximately the same magnitude as can again be seen in Fig. 4.22. The data necessary to evaluate Eq. (3.16a) is taken from the flanks of the sine fit, where C has no significant effect. This is also the reason why the error bars are significantly larger for the weak value's modulus. For all data points background has been subtracted as described in section 4.2.1.4 for the final results (typically ~ 1 cps). Propagation of uncertainty as described above is taken into account when calculating the error of each component of the weak value from the experimentally obtained intensities.

Note that some data points for $|\langle\hat{\sigma}_z^s\rangle_w|$ and $\text{Re}[\langle\hat{\sigma}_z^s\rangle_w]$ are missing in Figs. 4.30 and 4.31 (see for example the direction $[\theta, \phi] = [-120^\circ, 90^\circ]$). This is due to the technical problems with the phase shifter, which have already been mentioned.

As an addition we also want to present the weak values obtained for smaller interaction strengths, i.e. for $\alpha = \pm 10^\circ$. The weak value's real part as well as its modulus were extracted only for the postselection azimuthal direction of $\phi = 0^\circ$. The results are depicted in Fig. 4.32. As anticipated in the previous section concerning the optimization of the interaction parameter α , a good agreement between

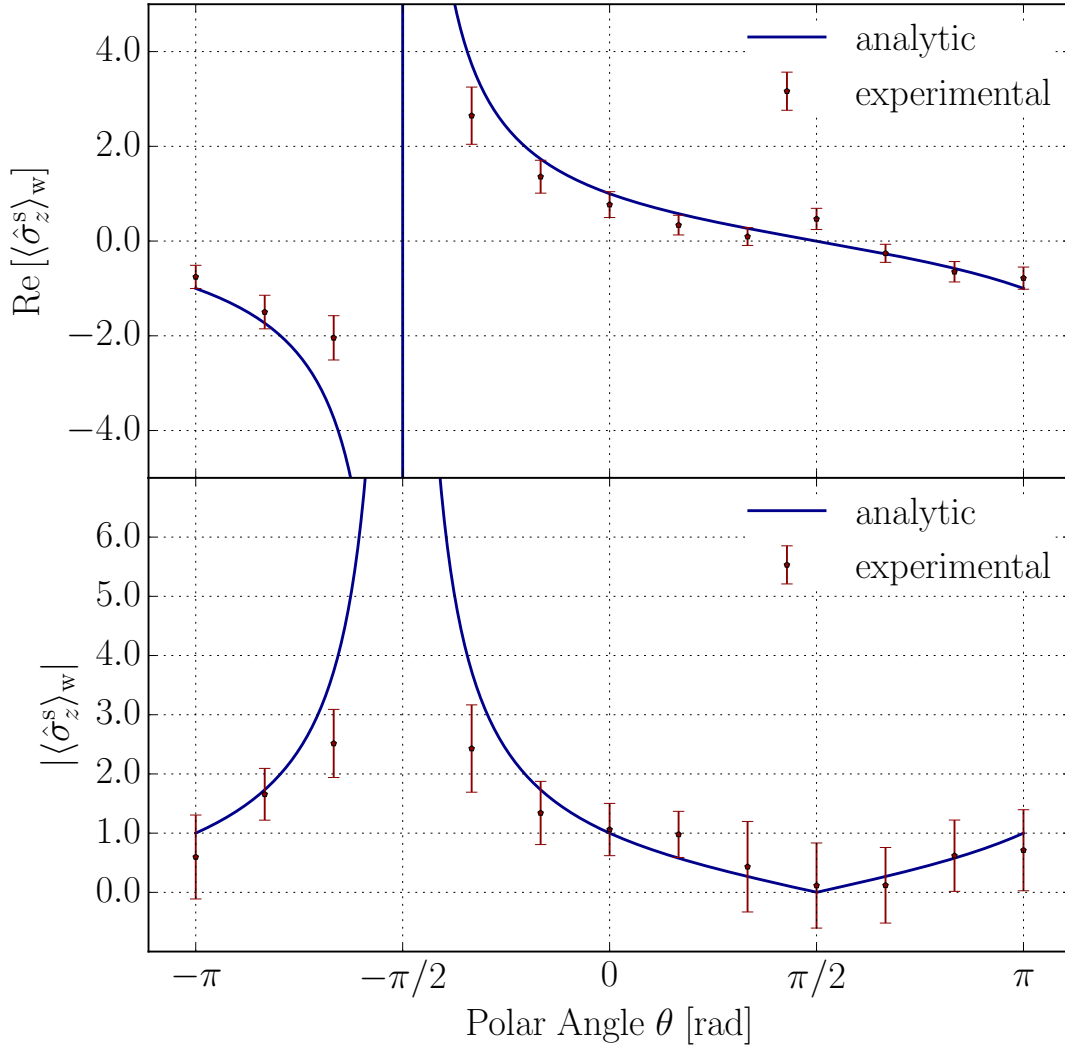


Figure 4.32: Measurement results (red) together with the theoretical prediction (blue) for the spin operator's weak value for an interaction strength of $\alpha = 10^\circ$. The error bars represent one standard deviation.

the theoretical prediction and the measurement is also found for $\alpha = \pm 10^\circ$. When compared to the 15 degree results the most obvious difference are found for weak values bigger then one. While the $\alpha = 15^\circ$ measurement results accurately describe the weak value outside the eigenvalue spectrum of the operator, the $\alpha = 10^\circ$ fail to do so for several measured points. Also the error bars of the individual points are in general larger.

Nevertheless the results let us conclude that weak values of a quantum system can be accurately determined using neutron interferometry using spin manipulations with a magnitude as small as only 10 degrees.

4.2.2 Polarimeter experiment

In comparison to the interferometer experiment, in which the real part of $\langle \hat{\sigma}_z^s \rangle_w$ as well as its modulus are measured, the polarimeter experiment to determine $\text{Im} [\langle \hat{\sigma}_z^s \rangle_w]$ is much simpler. An artistic representation of the experiment is presented in Fig. 4.2. Again it can be divided into three main parts:

- i) Preselection: The wavelength of the monochromatic neutron beam of the polarimeter at the Institute of Atomic and Subatomic Physics in Vienna is $\lambda_0 = 2.02 \text{ \AA}$ ($\lambda/\lambda_0 \sim 0.02$). It is polarized by a CoTi supermirror polarizer which offers a degree of polarization of $\sim 99\%$. To preselect the neutron's spin state a DC coil is used. For the weak spin experiment it is tuned in a way that the neutron spin is turned by $\pi/2$ so that it is aligned along the positive x -axis.
- ii) Interaction: For the polarimetric version of the weak spin experiment the neutron spin has to be first rotated by $+\alpha$ and then by $-\alpha$ in two consecutive experimental runs. For simplicity's sake, no additional coils are used for the spin rotation. Instead the neutron's Larmor precession in the xy -plane, caused by the guide field applied around the whole setup, is exploited. To obtain an effective rotation of $\pm\alpha$ the position of the second DC coil, which also used for the postselection of the spin state, is changed accordingly.
- iii) Postselection: No path postselection is necessary at the polarimeter. The spin postselection is performed in the exact same manner as in the interferometer experiment. A DC coil is mounted on a translation stage. The polar angle θ is tuned by applying different currents to the coil. The azimuth angle ϕ is changed by moving the DC coil along the neutron's direction of flight. After the postselection angles are set by the DC coil a second CoTi supermirror analyzer, which is of identical construction as the polarizer, filters all neutrons but those with a spin aligned along the chosen direction. Finally the neutrons are detected by a BF_3 counter.

4.2.2.1 Adjustment

Throughout the preceding sections it was stated several times that the polarimetric setup is easier to handle and much more robust against external influences such as temperature fluctuations and vibrations than the interferometer. During this section we explain these statements.

First of all the one component most difficult and fragile to adjust is not included in the setup any longer, i.e. the interferometer. The supermirrors used as polarizer and analyzer in the polarimeter, are installed routinely in the setup and do not need to be further adjusted. External guide fields applied around the whole setup are also permanent installations and do not need to be configured either. As with the interferometer experiment the guide field strength is set to ~ 13 G. The first component to be adjusted is the DC1 coil. This is done in exactly the same manner as in the interferometer experiment. The results of the adjustment are plotted in Fig. 4.33.

After the final adjustment DC1 showed a flipping ration of ~ 185 , a contrast of

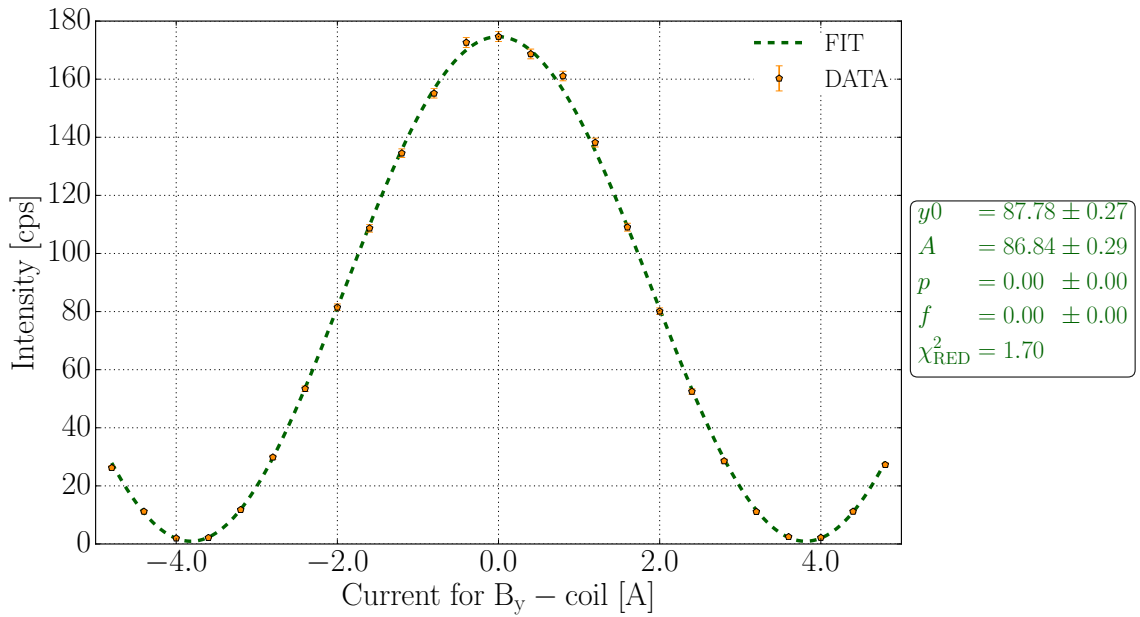


Figure 4.33: B_y -scan of DC1 obtained with a suitable compensation field B_z : After the final adjustment, the DC1 coil at the polarimeter showed a flipping ratio of ~ 185 , a contrast of $\sim 99\%$ and a phase of $\phi = 0.003$ rad (without background correction).

$\sim 99\%$ and a phase of $\phi = 0.003$ rad (all without a background correction). The flipping ratio is more than twice as high as in the interferometric experiment at the ILL. This is due to two reasons: First the guide field at the polarimeter is more spacious and therefore offers a more homogenous field distribution. In addition motorized micrometer rockers are used to adjust the tilt of the coils, which dramatically increases the precision of the positioning of the coil.

The spin postselection is performed in the exact same manner as in the interferometer experiment. Again a second DC coil, also dubbed DC2, is mounted on a translation stage. The motorized translation stage can move the DC2 in the $\pm x$ -

direction, which enables the adjustment of the azimuth angle ϕ . Again the polar angle θ is selected by applying current to the coil. DC2 is adjusted in the conventional manner. The results of the adjustment procedure at a midway position are plotted in Fig. 4.34.

Also with DC2 a very good adjustment has been achieved. A flipping ratio of

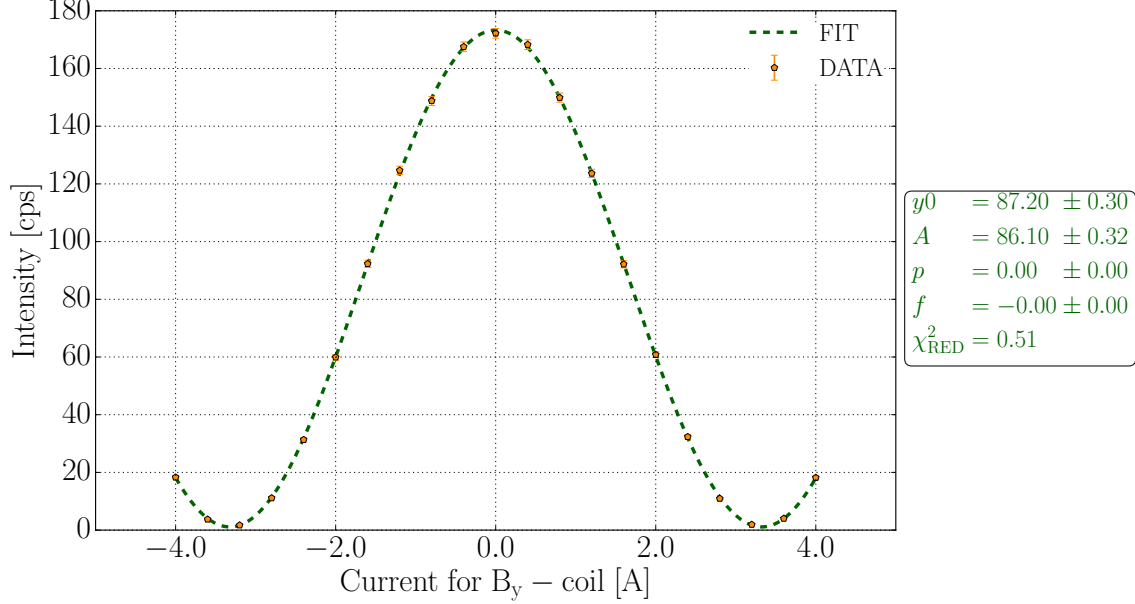


Figure 4.34: B_y -scan of DC2 obtained with a suitable compensation field B_z : After the final adjustment, the DC2 coil at the polarimeter showed a flipping ratio of ~ 160 , a contrast of $\sim 99\%$ and a phase of $\phi = -0.001$ rad (without background correction).

~ 160 , a contrast of $\sim 99\%$ and a phase of $\phi = -0.001$ rad are obtained (all without background correction). The slightly lower flipping ratio than that of DC1 can be explained by the proximity to the supermirror. For any position of the translation stage, DC2 is closer to the analyzer than DC1 is to the polarizer. The stray fields produced by the analyzer cause the reduction of the flipping ratio.

Next the adjustment of the polarimetric setup a position scan with active DC1 and DC2 has to be performed. Again this is very similar to the interferometric experiment. For the position scan DC1 is set in a way that $|S_x; +\rangle$ is preselected. Then a constant current is applied to DC2 so that the a polar angle of $\theta = \pi/2$ is postselected. By changing the position of DC2 the azimuth angle is scanned. Fig. 4.35 shows the result of DC2's position scan at the polarimeter setup.

The contrast of the intensity oscillation that can be observed the motor position is scanned reached $\sim 96\%$. The position scan of DC2 includes all errors of the whole measurement apparatus, since all components are involved during the measurement.

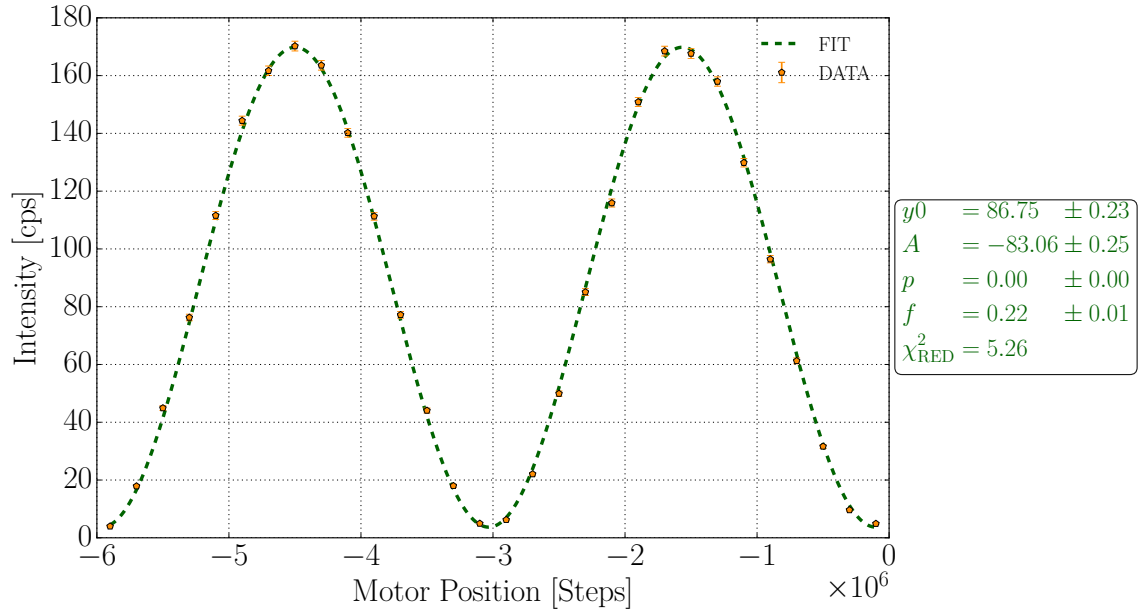


Figure 4.35: DC2 position scan at the polarimeter beam line: Since the neutrons are not separated into two ways at the polarimeter, no fluctuations between the paths has to be taken into account and a single position scan is enough to adjust DC2. The contrast of the intensity oscillations is $\sim 96\%$.

Hence, the polarimeter offers a much higher overall contrast than the interferometer setup. In addition no beam separation exists in the polarimeter. Thus there is no phase fluctuations between different paths and only one position scan is sufficient to adjust the entire spin postselection.

4.2.2.2 Optimizing the measurement strength

In addition to the measurement presented in section 4.2.1.2, the spin weak value's imaginary part has been determined using different interaction strengths at the polarimeter. Measurements performed there are highly precise and the available beam time is quite flexible at the Vienna research reactor. Therefore a more thorough investigation of the optimal magnitude for α can be performed.

For the spin postselection the azimuth angle is held fixed at $\phi = 90^\circ$ and the polar angle θ is varied. This postselection direction is chosen intentionally. In Fig. 4.35 one sees that for this value of ϕ the measurement takes place at the flanks of the sine curve obtained during the adjustment of the azimuth angle. Thus, any deviation from the correct experimental parameters will manifest itself most prominently at this direction. If the measurement yields accurate results for $\phi = 90^\circ$ it will yield accurate results for any other azimuthal direction.

The test has been performed with three different interaction strengths: $\alpha = 6^\circ$, $\alpha = 9^\circ$ and $\alpha = 15^\circ$. The results are depicted in Fig. 4.36.

The upper panel depicts the measurement results for $\alpha = 6^\circ$, which is a relative

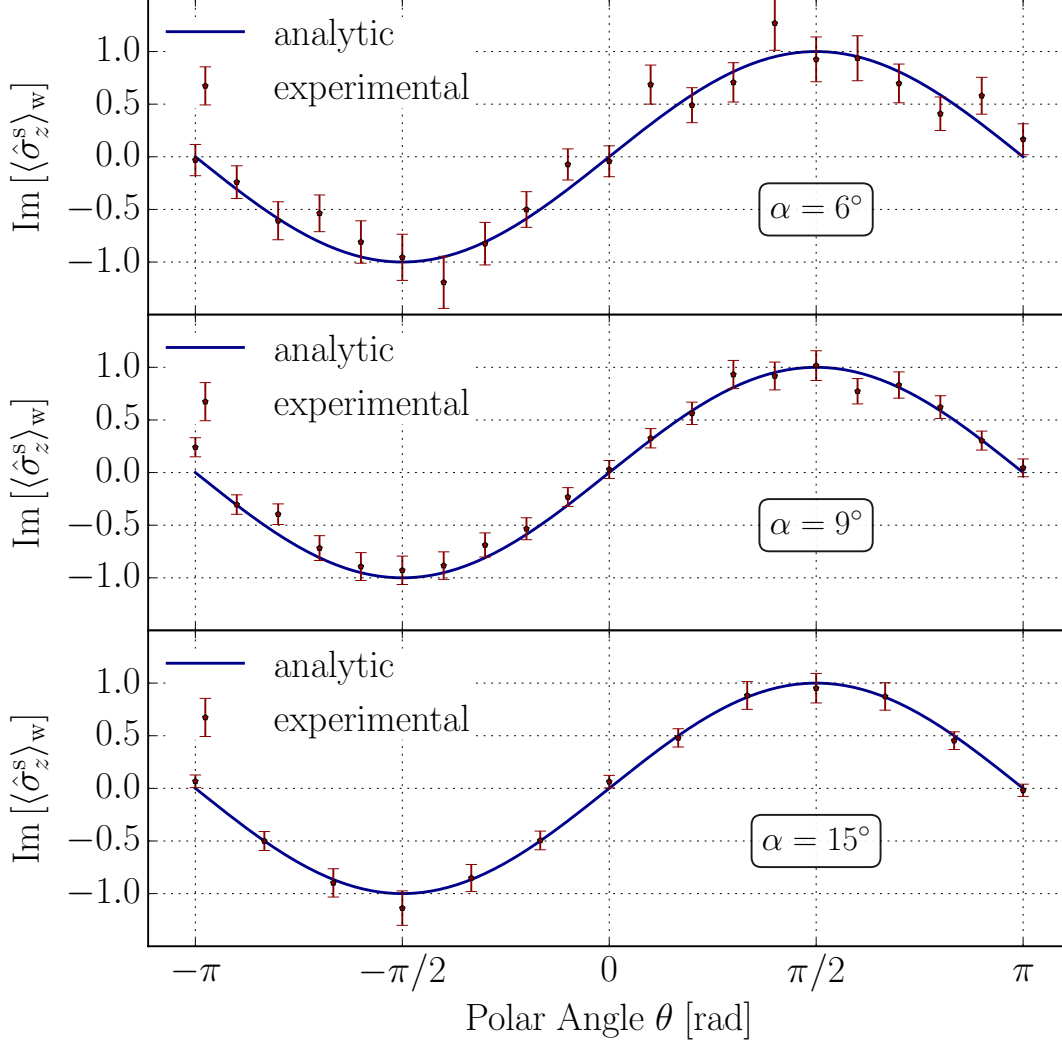


Figure 4.36: Measurement of $\text{Im}[\langle\hat{\sigma}_z^s\rangle_w]$ using different measurement strengths parameterized by α : For $\alpha = 6^\circ$ (upper panel) there are several points that are outside of the theoretical prediction (not even in the limit of error). For $\alpha = 9^\circ$ (middle panel) the agreement becomes better, till for $\alpha = 15^\circ$ (lower panel) all points agree with the theoretical prediction (within the error).

interaction strength of $\sim 7\%$. A noticeable spread of the measurement results, uncertainty, around the theoretical prediction can be observed. Also the individual error bars of each data point are large. In general the measurement results reflect the theoretical prediction of the weak value correctly, albeit being noisy. We conclude that an interaction strength of six degrees is too small from an experimental

point of view.

Next the measurement strength is tuned to $\alpha = 9^\circ$ corresponding a relative interaction strength of 10%. The measurement results are depicted in the middle panel of Fig. 4.36. They are less noisy and the agreement between the theoretical prediction and the measurement results is now much better. There are only a few data points that lie offside the theoretical curve. The interaction strength of $\alpha = 9^\circ$ is sufficiently large to perform experiments. While the $\alpha = 6^\circ$ results would be difficult to reproduce, the $\alpha = 9^\circ$ are good enough to accurately extract the weak value's imaginary part with that interaction strength. The change from six to nine degrees does not seem much, but one has to consider that the three extra degrees increase the interaction strength by 50%!

For comparison the lower panel of Fig. 4.36 shows the measurement results for $\alpha = 15^\circ$, which is the interaction strength used in the interferometer experiment. A perfect agreement between theory and the experimentally determined values can be observed. Within the error all determined weak values touch the theoretical curve.

4.2.2.3 Data acquisition

While for each post selection direction a whole interferogram has to be recorded during the interferometer experiment in order to obtain the real part as well as the modulus of the spin operator's weak value, two simple intensity measurements are sufficient to determine $\text{Im}[\langle \hat{\sigma}_z^s \rangle_w]$. Instead of 52 interferograms only 52 intensity pairs have to be collected. In Fig. 4.37 the recorded intensities for $\alpha = \pm 15^\circ$ for all data points are shown.

For a postselection direction of $(\theta, \phi) = (-\pi \leq \theta \leq \pi, 0)$ the imaginary part of $\langle \hat{\sigma}_z^s \rangle_w$ vanishes. This can already be seen when looking at the measurement data depicted in the upper left panel of Fig. 4.37. The artanh function used to extract $\text{Im}[\langle \hat{\sigma}_z^s \rangle_w]$ becomes zero if its argument is zero. It is given by $I_{z+} - I_{z-} / I_{z+} + I_{z-}$, which becomes (close to) zero when the observed intensities are nearly identical. An alternative understanding of the results can be gained through Fig. 4.35. An azimuth angle of $\phi = 0^\circ$ is equivalent to a maximum in the position scan. To record the intensity I_{z+} the coil has to be positioned 15° to the right of the maximum, for I_{z-} 15° to the left. It is easy to see that in this case the recorded intensities will be the same for any polar angle θ for symmetry reasons. This picture also intuitively explains the intensity differences in the other three panels of Fig. 4.37.

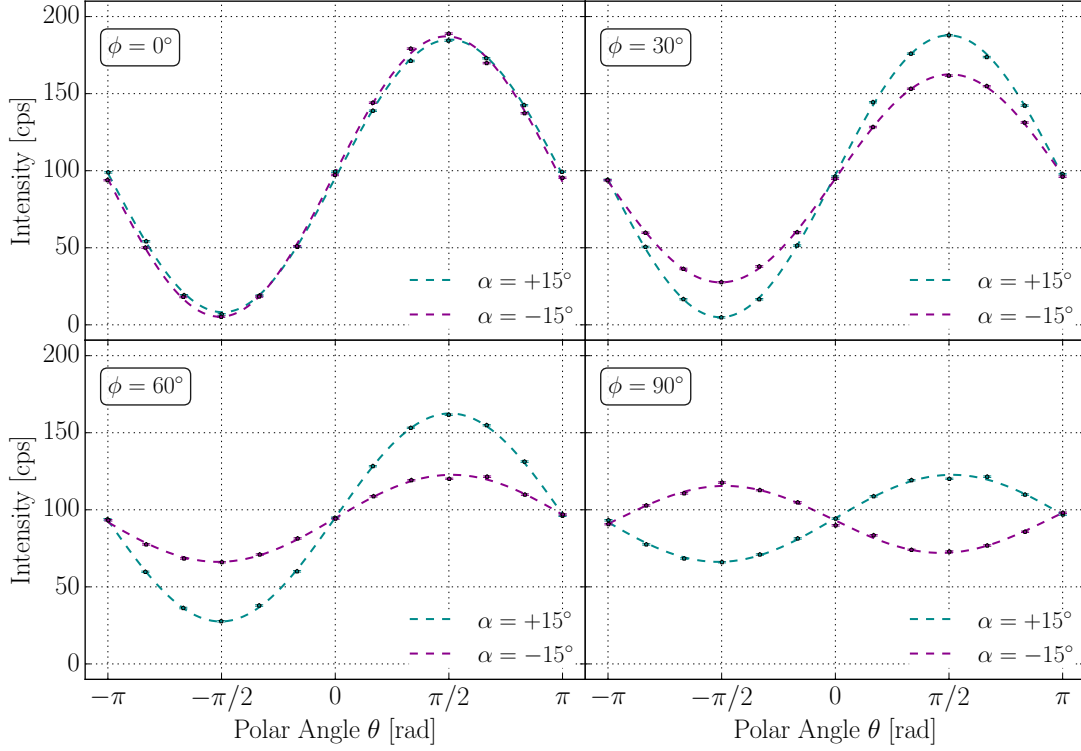


Figure 4.37: Polarimeter intensities for all postselection directions. The error bars represent one standard deviation. The dashed lines are drawn to guide the eye, but do not have any further purpose. Note that at $\phi = 0^\circ$ the intensities for $\pm\alpha$ coincide and $\text{Im}[\langle\hat{\sigma}_z^s\rangle_w]$ vanishes.

4.2.2.4 Results

The polarimeter data presented above makes it possible to extract the imaginary part of the spin operator's weak value with high accuracy for four different azimuth angles ϕ .

The final results of the weak spin experiment at the polarimeter are shown in Fig. 4.38. To extract the spin weak value's components from the measured intensities the relation given by Eq. (3.16b) is used. An excellent agreement between theory and experiment is seen.

For $\phi = 0^\circ$ the imaginary part of $\langle\hat{\sigma}_z^s\rangle_w$ is always zero. This result was already anticipated in the previous sections while looking at the measurement data in Fig. 4.37. The intensities coincided for $\pm\alpha$ which hints at a vanishing imaginary part of the weak value. With increasing azimuthal angle pre and postselected spin states move away from orthogonal positions and the weak value's imaginary part starts to oscillate, describing a sine for $\phi = 90^\circ$. The average contrast of the polarimeter

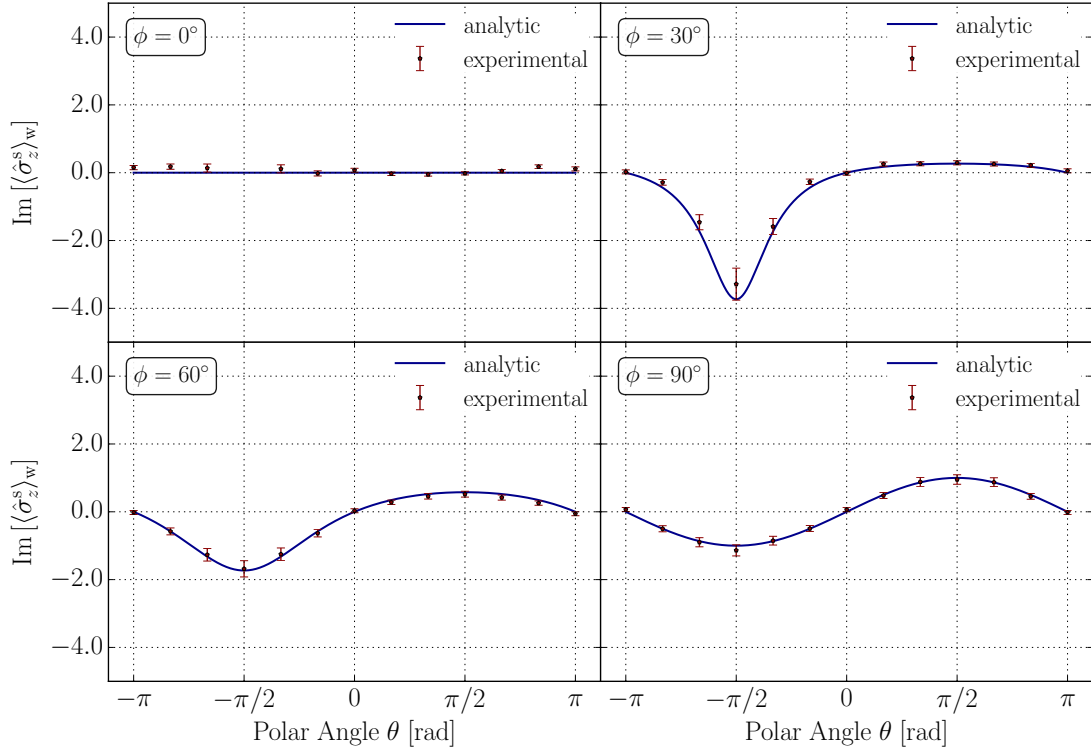


Figure 4.38: Final results of the measurement of $\text{Im} [\langle \hat{\sigma}_z^s \rangle_w]$ for all postselection directions: The measurement results (red) are plotted together with the theoretical prediction (blue). The error bars represent one standard deviation. For $\phi = 0^\circ$ $\text{Im} [\langle \hat{\sigma}_z^s \rangle_w]$ is always zero. With increasing azimuthal angle the weak value's imaginary part starts to oscillate, describing a sine for $\phi = 90^\circ$.

measurements is over 96%. Because of that no contrast corrections as with the interferometer data has to be performed, when the imaginary part of the weak value is extracted from the data. For all measurements the background has been subtracted and propagation of uncertainty is taken into account, when calculating the weak value's error.

As already stated several times the purely polarimetric setup is far more robust than the interferometric one. Therefore the precision that can be achieved is even higher than the one an interferometric setup offers. Also the average intensity available at the polarimeter beam line is higher, which makes the necessary data collection times shorter. Therefore it is possible to tune the angle α , and hence the disturbance of the measurement, to even smaller values. In addition the high stability makes it possible to systematically vary the postselection angles θ and ϕ in small increments: the imaginary part of the spin weak value is scanned on the whole Bloch sphere.

Additional data was collected at the polarimetric setup in which $\text{Im} [\langle \hat{\sigma}_z^s \rangle_w]$ is sys-

tematically investigated: The post selection angle ϕ and θ are varied between $-\pi$ and π with an increment of $\pi/18$ respectively, yielding a total of 441 data points. For all measurements the angle of rotation α is fixed at $\alpha = 9^\circ$. The measurement results are presented in Fig. 4.39, where they are compared to the analytic solution of $\text{Im} [\langle \hat{\sigma}_z^s \rangle_w]$.

Again an excellent agreement between the theoretical prediction on the left and the

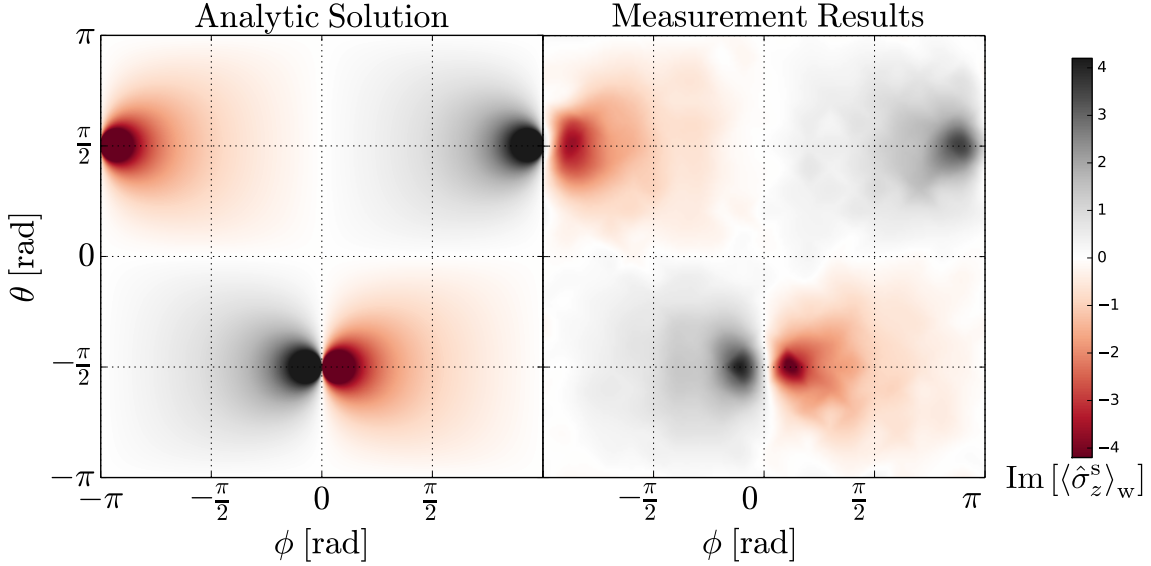


Figure 4.39: Contour plot of $\text{Im} [\langle \hat{\sigma}_z^s \rangle_w]$ (left) in comparison to the measurement results (right) as a function of θ and ϕ : The polarimetric setup made it possible to systematically evaluated $\text{Im} [\langle \hat{\sigma}_z^s \rangle_w]$ on the whole Bloch sphere. The postselection angles ϕ and θ were varied between $-\pi$ and π with a step size of $\pi/18$, yielding a total of 441 data points, which make it possible to interpolate a contour plot of the measurement results. For all measurements α was fixed at $\alpha = 9^\circ$.

actual measurement results on the right can be observed. For $\phi = 0^\circ$ the imaginary part of the weak value is expected to be zero, which is indicated by the white line in the contour plot. This line is perfectly reproduced in the experiment. In addition one expects to find four discontinuous points, wherever pre and postselected spin state become orthogonal. These points are also clearly visible in the measurement data. To obtain the contour plot shown in Fig. 4.39 it is necessary to interpolate between the recorded data points. It is also possible to plot the data in a discretized way so that each pixel on the image represents one data point. The discretized data is depicted in Fig. 4.40.

One may object to the way the measurement data is presented in Fig. 4.39, since no error bar is depicted and so no assertion of the data's quality can be made. However, one can “cut” out slices of Fig. 4.39 for a fixed value of ϕ , as has been done

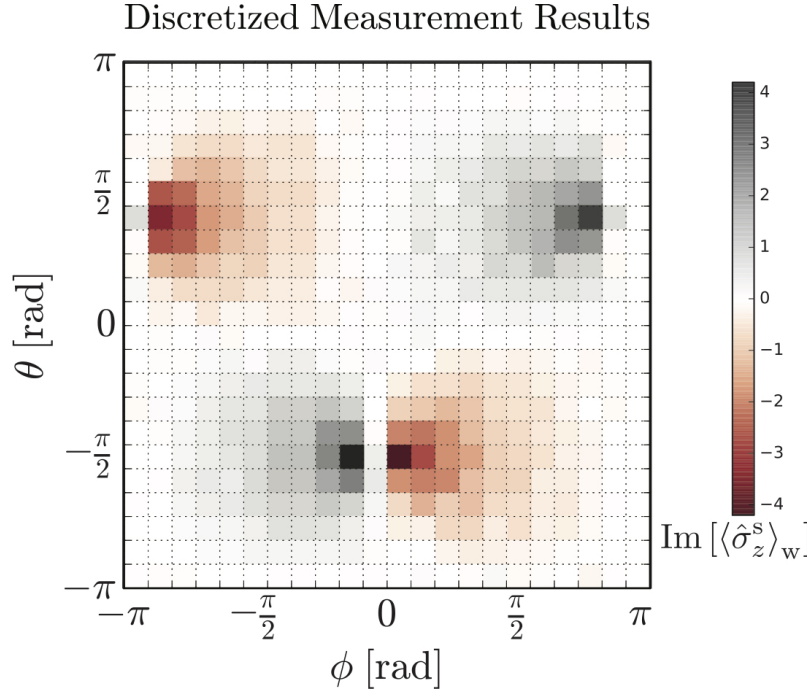


Figure 4.40: Discretized Contour plot of $\text{Im}[\langle\hat{\sigma}_z^s\rangle_w]$: Each of the 441 recorded data points is represented by one square.

in Fig. 4.41, which shows the measurement results for a fixed azimuth postselection angle of $\phi = -144^\circ$.

As can be seen in this Figure the quality of the measurement data is superb, with very little error and in complete agreement with the theoretical predictions.

4.2.3 Measurement of $\text{Im}[\langle\hat{\sigma}_z^s\rangle_w]$ using the interferometric setup

To overcome possible criticism that the imaginary part of $\langle\hat{\sigma}_z^s\rangle_w$ was initially measured using another setup than $\text{Re}[\langle\hat{\sigma}_z^s\rangle_w]$ and $|\langle\hat{\sigma}_z^s\rangle_w|$, the experiment was carried out once more, this time using an updated interferometer setup during reactor cycle 177 at ILL. An important new component is added to the setup, which is worth mentioning. In the first version of the experiment the interferometer's beams had to be blocked by manually putting small cadmium slabs in the beam path. This approach has a big disadvantage: whenever a beam needs to be blocked, someone has to come physically close to the interferometer. The body heat of the experimentalist induces thermal stress and one has to wait for thermal stabilization to be reached again. To avoid this experimental inconvenience and to increase the precision of the experiment a rotational motor stage is introduced in the new setup. A special cad-

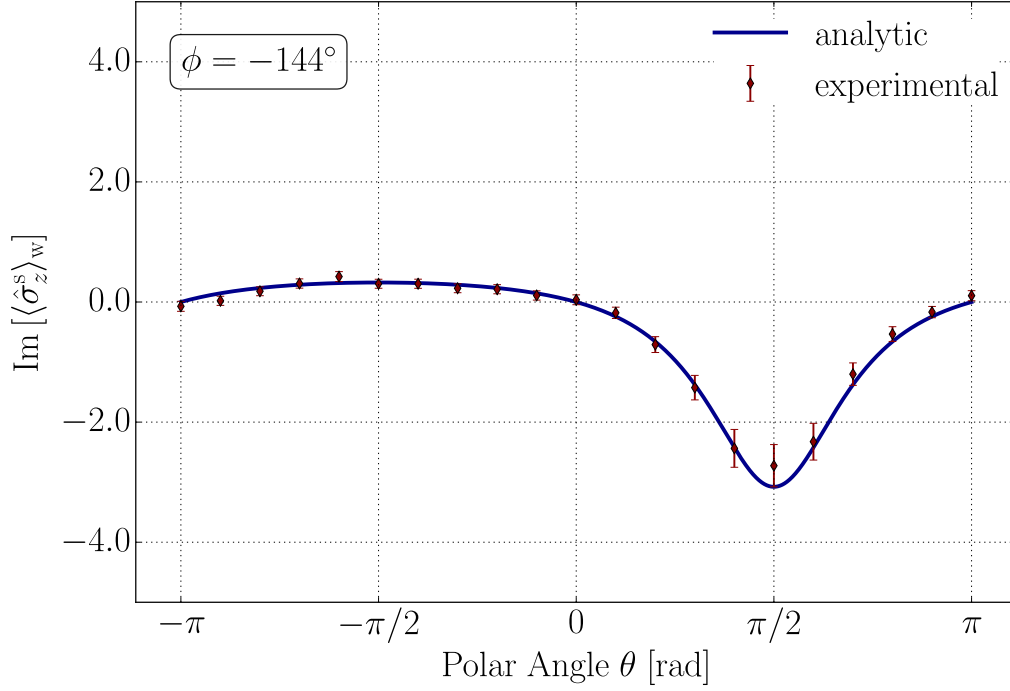


Figure 4.41: Slice of the contour plot of $\text{Im}[\langle\hat{\sigma}_z^s\rangle_w]$ shown in Fig. 4.39 for $\phi = -144^\circ$ as a function of θ . The error bars represent one standard deviation: Measurement data (red) and theoretical prediction (blue) are in excellent agreement. α was fixed at $\alpha = 9^\circ$.

mium holder, which is 3D printed, is rotated through the setup as seen in Fig. 4.42.

If the cadmium holder is in a central position both beams can pass through the interferometer undisturbed. If it is rotated either to the left or to the right, one of the beams gets blocked, so that path eigenstates of the interferometer are accessible. Figure 4.43 shows the results of one position scan of the cadmium rotator.

Looking at the combined count rate of O and H detector it is easy to see that for $\sim 40^\circ$ both beam paths are free, because the full count rate is reached. For $\sim 10^\circ$ and $\sim 70^\circ$ the count rate decreases to halve its initial value, which indicates that either one of the two beam paths is blocked. If the cadmium holder is rotated even further, the count rate goes back up to its maximum. At this point the beam stopper is completely outside of the interferometer. The adjustment of the rest updated setup is very similar to the old one and will not be presented here in detail.

Using the new setup it is possible to reproduce the data of the measurements performed at the polarimeter in Vienna using an interferometric setup. Due to limited beam time only one postselection azimuthal direction is investigated. The imaginary part of the spin operator's weak value is measured for thirteen different postselection directions given by $(-180^\circ \leq \theta \leq 180^\circ, \phi = 90^\circ)$. For this 26 single intensities are recorded and additional background measurements are performed. The results of the experiment are depicted in Fig. 4.44.

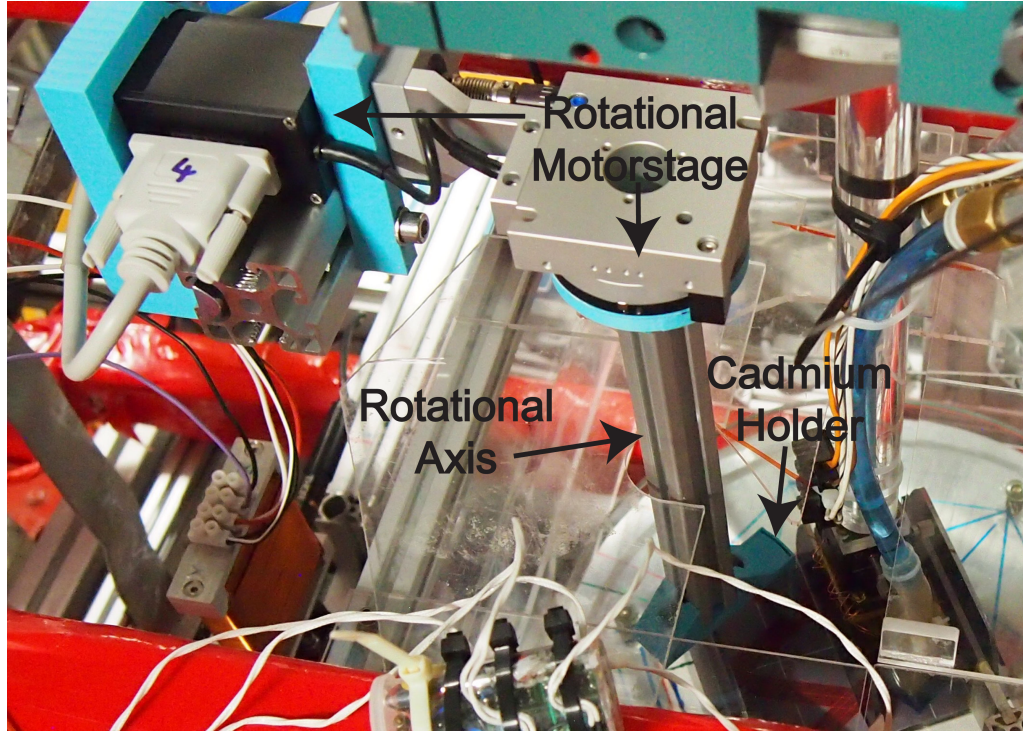


Figure 4.42: Picture of the updated interferometric setup at ILL during reactor cycle 177: To increase the precision of the experiment and for experimental convenience a cadmium holder is inserted into the interferometer.

For the final results presented here the background has been taken into account. The interferometric experiment again fully confirms the results which were obtained with the polarimeter at an earlier point in time. The weak value's imaginary part is determined with high precision and an excellent agreement between theory and experiment is observed.

4.3 The quantum pigeon hole effect

The experiments presented above show that it is possible to determine all components of the neutron spin's weak value with high precision. While the measurement of weak values using massive particles seems to be a purely pedagogic exercise at first, the newly established technique can be used to investigate the foundations of quantum mechanics experimentally.

One example for a test of the foundations of quantum mechanics is the so called quantum pigeon hole effect: The classical pigeon hole principle states that if n pigeons are put into m boxes and if $n > m$, then at least two pigeons end up in the same box [Herstein, 1964]. In 2016 Aharonov *et al.* theoretically proposed the quantum pigeonhole effect [Aharonov et al., 2016], showing that the classical pigeon

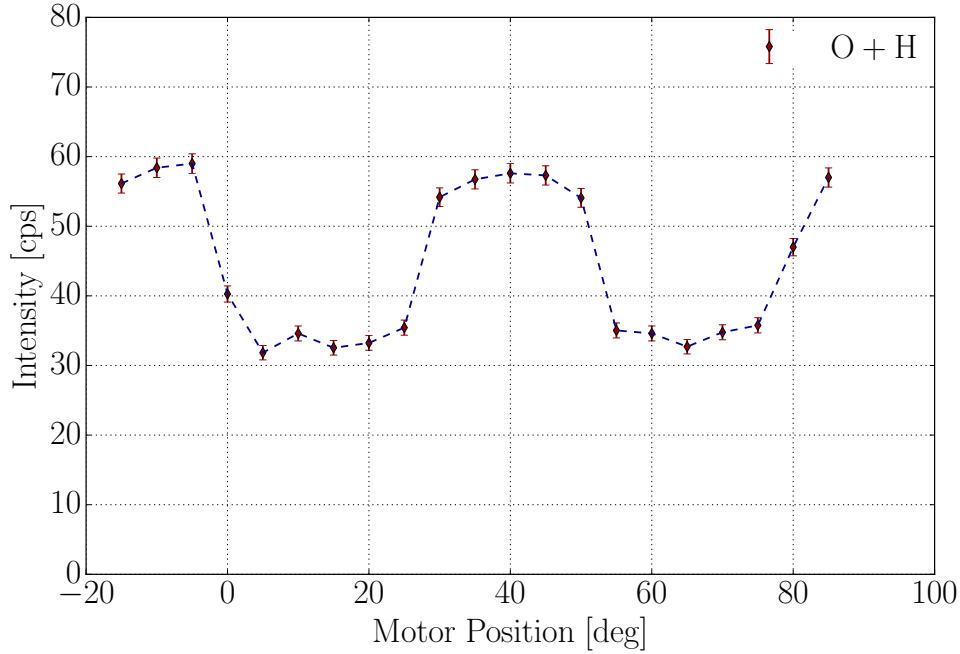


Figure 4.43: Position scan of the cadmium rotator: The combined count rate of both the O and the H detector is plotted versus the rotational angle of the cadmium holder. If it is in a neutral position ($\sim 40^\circ$) both beam paths are free and the full count rate is obtained. When it gets rotated into either one of the beams ($\sim 10^\circ$ and $\sim 70^\circ$) the count rate gets halved due to the block of one of the beams.

hole principle is in general not valid in quantum mechanics and that situations can arise in which three pigeons are put into two boxes and yet no two pigeons seem to be in the same box at a given time.

Since pigeons as macroscopic objects do not obey the laws of quantum mechanics, let us consider quantum particles. The role of the pigeons is taken by the neutrons' spins and the two boxes are replaced by the two spin eigenstates $|S_z; +\rangle$ and $|S_z; -\rangle$. Let all three particles be prepared in a spin state that is aligned along the positive x -axis, so that they are in a superposition $|S_x; +\rangle = 1/\sqrt{2}(|S_z; +\rangle + |S_z; -\rangle)$. The initial state of the three particles is then given by a product state

$$|\Psi_i\rangle = |S_x; +\rangle_1 |S_x; +\rangle_2 |S_x; +\rangle_3. \quad (4.13)$$

We now only consider situations in which the three particles get successfully postselected in the spin state $|S_y; +\rangle = 1/\sqrt{2}(|S_z; +\rangle + i|S_z; -\rangle)$ so that their spin is aligned

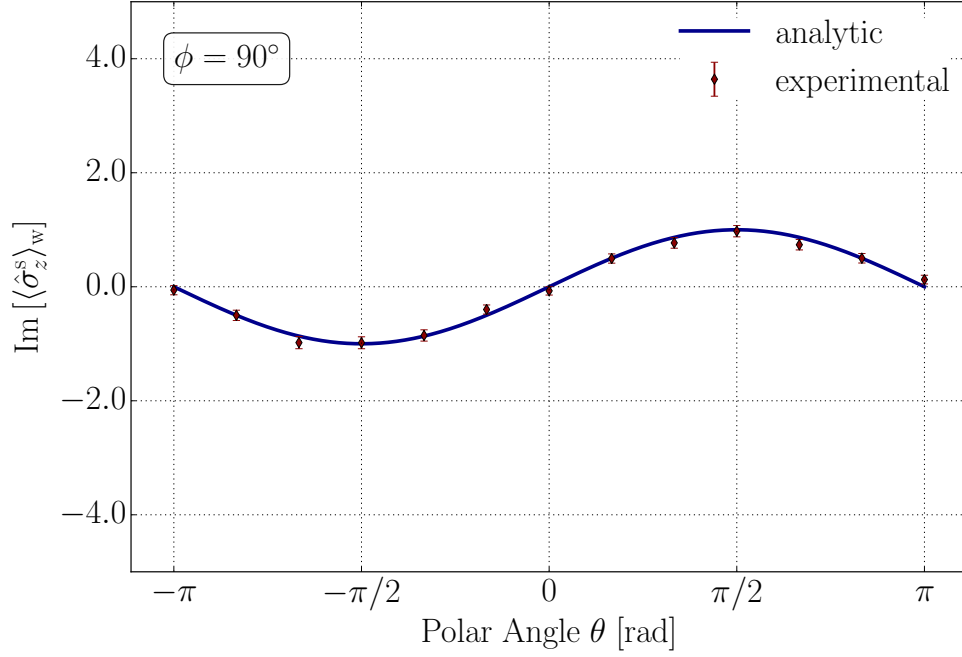


Figure 4.44: Results of the weak spin measurement for $\text{Im}[\langle \hat{\sigma}_z^s \rangle_w]$ for $\phi = 90^\circ$ using the upgraded interferometric setup: Theoretical predictions (blue) and measurement results (red) for the imaginary part of the spin operator's weak value. The error bars represent one standard deviation. The results obtained using the polarimetric setup are reproduced using the interferometric one. A perfect agreement between theory and experiment is observed.

along the positive y -axis. The final product state of the three neutrons is given by

$$|\Psi_f\rangle = |S_y; +\rangle_1 |S_y; +\rangle_2 |S_y; +\rangle_3. \quad (4.14)$$

Let us look at the product of the Pauli spin operator's weak values $\langle \hat{\sigma}_{z_k}^s \rangle_w$ and $\langle \hat{\sigma}_{z_l}^s \rangle_w$ of the k -th and l -th neutron. Due to the choice for the preselected and the postselected spin states the spin weak value of each neutron will be $\langle \hat{\sigma}_z^s \rangle_w = i$ and hence the weak value of the product any of two Pauli operators will equal minus one $\langle \hat{\sigma}_{z_k}^s \hat{\sigma}_{z_l}^s \rangle_w = -1^g$, showing that the two neutron spins are anti correlated. Because the problem is symmetric under permutation the operator product will be minus one for any two out of the three particles, implying that no two spins are ever in the same state.

For a better understanding of the reason why the classical pigeon hole principle is

^gNote that in general the weak value of a product of operators is not equal to the product of weak values of the operators, i.e. $\langle \hat{\sigma}_{z_k}^s \hat{\sigma}_{z_l}^s \rangle_w \neq \langle \hat{\sigma}_{z_k}^s \rangle_w \langle \hat{\sigma}_{z_l}^s \rangle_w$. However, if initial and final states are given by product states, as is the case for the states in Eq. (4.13) and (4.14), the product rule holds, so that $\langle \hat{\sigma}_{z_k}^s \hat{\sigma}_{z_l}^s \rangle_w = \langle \hat{\sigma}_{z_k}^s \rangle_w \langle \hat{\sigma}_{z_l}^s \rangle_w$ is true.

violated by that, the product operator $\hat{\sigma}_{z_k}^s \hat{\sigma}_{z_l}^s$ is decomposed into projection operators so that $\hat{\sigma}_{z_k}^s \hat{\sigma}_{z_l}^s = (+1) \hat{\Pi}_e^s + (-1) \hat{\Pi}_o^s$ with

$$\hat{\Pi}_e^s = |S_z; +\rangle_k |S_z; +\rangle_l \langle S_z; +|_k \langle S_z; +|_l + |S_z; -\rangle_k |S_z; -\rangle_l \langle S_z; -|_k \langle S_z; -|_l, \quad (4.15a)$$

$$\hat{\Pi}_o^s = |S_z; +\rangle_k |S_z; -\rangle_l \langle S_z; +|_k \langle S_z; -|_l + |S_z; -\rangle_k |S_z; +\rangle_l \langle S_z; -|_k \langle S_z; +|_l. \quad (4.15b)$$

The even and odd projection operators $\hat{\Pi}_e^s$ and $\hat{\Pi}_o^s$ tell us how many neutron spins are in one state. If the spins of both the k th and the l th neutron are in the same state, the weak value of the even projection operator $\hat{\Pi}_e^s$ equals one. If they are in different states the odd projection operator $\hat{\Pi}_o^s$ equals one. Given the pre and postselected states of Eq. (4.13) and (4.14) we find that $\hat{\Pi}_e^s = 0$ and $\hat{\Pi}_o^s = 1$. The spin of the k th and the l th neutron are always in different states. Because the initial and final states are symmetric, no two spins ever seem to be in the same state, but at the same time we have only two states for three spins, leading to a violation of the classical pigeon hole principle.

4.3.1 Experimental realization

In the paper by Aharonov *et. al* [Aharonov et al., 2016] an experiment in which three particles are simultaneously sent through a Mach-Zehnder type interferometer is proposed. The two boxes are then given by the two paths of the interferometer. Would such an experiment be feasible with neutrons? The answer to this question is no. Any neutron interferometric experiment is a single particle experiment and it is impossible to inject three particles into the interferometer at the same time. Nevertheless there is still hope for an experimental investigation of the effect using neutrons. The nature of the quantum pigeon hole principle is such that each particle is prepared and postselected individually. It is a widely accepted assumption that any non-classical correlation between particles must be due to the fact that the particles are in an entangled state, which requires them to be near each other during preparation. However, in the alternative correlation concept considered in [Aharonov et al., 2016], the particles could have been prepared at arbitrary separations. They are in a product state and there does not appear to be any entanglement or interaction involved. Nevertheless, any pair with purely imaginary weak values would exhibit non-classical correlations. We therefore use the neutron interferometer and the experimental technique described in the sections above to prepare different ensembles in time. Note that for all pairs of spins the operator product $\hat{\sigma}_{z_k}^s \hat{\sigma}_{z_l}^s$ will equal minus one, which implies a nonclassical correlation.

During reactor cycle 177 in December 2015 the technique presented above was implemented in a neutron interferometric experiment^h. To measure the weak value of the Pauli spin operator $\hat{\sigma}_z^s$ the spin degree of freedom is weakly coupled to the path degree of freedom. As described above the weak value's real part is then inferred from a interference fringe, while two single intensity measurements are necessary to determine the weak value's imaginary part. For the quantum pigeon hole effect the weak value's modulus is not of interest and is not extracted during the experiment. To determine $\text{Re}[\langle\hat{\sigma}_z^s\rangle_w]$ three interference fringes are recorded:

1. The OUT curve without any interaction, to evaluate the phase of the empty interferogram.
2. The IN curve with a weak spin rotation of $\alpha = 15^\circ$ in each of the interferometer's arms.
3. One interference fringe with orthogonal pre and postselected states, which is then subtracted from the IN/OUT curve as an effective background as described in section 4.2.1.4ⁱ.

Additionally two single intensities with alternately closed beam paths as described in section 4.2.3 are recorded. Also for those two intensities a background measurement with orthogonal pre and postselected states are performed. The recorded background intensities are then subtracted from the signal.

Altogether the beam time of 14 days at S18 was enough to measure the spin weak value of 19 different ensembles. Figure 4.45 shows typical IN and OUT curves of one experimental run.

Using the intuitive geometric picture of the weak value on the Bloch sphere developed in Fig. 3.1 of chapter 3 the results of the weak value determination are obvious. There is no phase shift between the IN and the OUT interference fringes leading to a vanishing real part of the weak value. Looking at the recorded intensities $I_{z\pm}$ shows that the relative amplitudes of the path eigenstates are not equal. This is because $\text{Im}[\langle\hat{\sigma}_z^s\rangle_w]$ shifts the pointer state away from the equatorial plane, towards the poles of the path Bloch sphere.

The measured intensities are inserted into the relations given by Eqs. (3.16a) and (3.16b) to determine the real and imaginary part of the weak value. We repeated the measurement to study 19 individual ensembles. The results for each ensemble are listed in Tab. 4.1. In general a very good agreement between the theory and

^hThe aperture cross section was reduced to $4 \times 4 \text{ mm}^2$ in the pigeon hole experiment

ⁱA correction of the neutron interferometer's contrast was not needed, since only the spin operator's real and imaginary part is of interest.

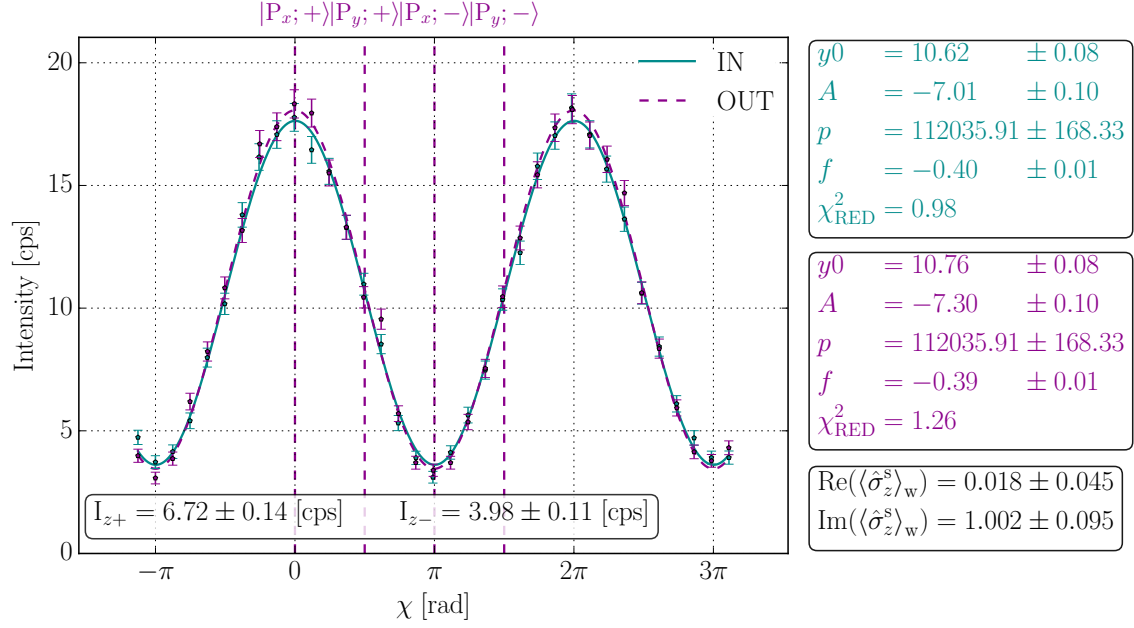


Figure 4.45: Obtained interferogram for one quantum ensemble: Since the weak value's real part is zero no phase shift is observable between the IN and the OUT curve. $I_{z\pm}$ are obtained by two single intensity measurements. Background has been taken into account.

Set Number	$\text{Re} [\langle \hat{\sigma}_z^s \rangle_w]$	$\text{Im} [\langle \hat{\sigma}_z^s \rangle_w]$
# 1	0.002 ± 0.049	0.912 ± 0.099
# 2	-0.041 ± 0.049	0.985 ± 0.102
# 3	0.101 ± 0.051	0.920 ± 0.099
# 4	-0.020 ± 0.050	0.931 ± 0.099
# 5	0.022 ± 0.050	1.037 ± 0.104
# 6	0.056 ± 0.049	1.301 ± 0.129
# 7	-0.070 ± 0.049	0.874 ± 0.095
# 8	0.011 ± 0.049	0.790 ± 0.092
# 9	0.062 ± 0.050	0.910 ± 0.096
# 10	-0.084 ± 0.051	1.039 ± 0.105
# 11	-0.121 ± 0.052	0.973 ± 0.103
# 12	-0.079 ± 0.050	1.003 ± 0.103
# 13	0.022 ± 0.043	0.889 ± 0.090
# 14	-0.024 ± 0.044	0.970 ± 0.094
# 15	-0.005 ± 0.044	1.050 ± 0.098
# 16	0.018 ± 0.045	1.002 ± 0.095
# 17	-0.103 ± 0.045	0.925 ± 0.092
# 18	-0.032 ± 0.044	0.979 ± 0.094
# 19	-0.097 ± 0.045	1.024 ± 0.096

Table 4.1: Experimentally determined weak values for 19 different ensembles.

the experiment is found. Nonetheless, there is one set that lies outside the expected range. For set number six $\text{Im} [\langle \hat{\sigma}_z^s \rangle_w] = 1.301$ is determined, which is almost three sigmas away from the expected value. Log files of the experiment show that the large deviation from the expected value is caused by a defect in one of the setup's coils.

It is also noteworthy that the errors of set 13 to 19 are smaller than the others. This is due to a change in reactor power. While the first twelve interferograms were recorded at a power of $\sim 43\text{MW}$, for the last seven a power of $\sim 58\text{MW}$ was available^j. The increase in reactor power leads to an increase in neutron flux. A higher count rate offers better statistics and reduces the uncertainty of the recorded values.

4.3.2 The quantum pigeon hole effect and contextuality

The idea of the quantum pigeon hole effect is further investigated in the theoretical paper [Waegell and Tollaksen, 2015], where a structural connections between the Kochen-Specker theorem and the observed anomalous weak values is analyzed, showing that the quantum pigeon hole effect is strongly related to contextuality.

Quantum mechanics is contextual, meaning that for a given observable the measurement outcome depends in which “context”, i.e. the setup, the combination of observables, etc. the measurement is performed at. Also quantum mechanics is non deterministic, meaning that in general it does not predict the outcome of any measurement with certainty. It only predicts the probabilities that a certain outcome will be observed. This inability to predict the outcome of a measurement with certainty motivated the development of so called hidden variable theories. In those theories the properties of a quantum system are predefined and fixed. This simple classical extension leads to the fact that the measurement outcome for any commuting observable will be the same regardless of the measurement context. Such theories are often called non-contextual hidden variable theories (NCHVT).

If a NCHVT exists, the standard interpretation of quantum mechanics would be an incomplete description of nature. A NCHVT would then be a more fundamental theory than quantum mechanics. However, as Kochen and Specker showed, no NCHVT can reconstruct the correct measurement outcome for certain sets of observables [Kochen and Specker, 1967]. In other words, it is impossible for hidden variable assignments to agree with the predictions made by quantum mechanics.

An example for such a set of observables are the tensor products of Pauli matri-

^jThere are different operational powers of the reactor at ILL, two of them being $\sim 43\text{MW}$ and $\sim 58\text{MW}$

ces of three spins and the identity matrix. They are mutually commuting and can be simultaneously measured. Nine such observables can be arranged in a square [Mermin, 1990]. A modified Mermin square for such a three spin system is shown in Fig. 4.46.

The possible eigenvalues of the observables are plus and minus one. According

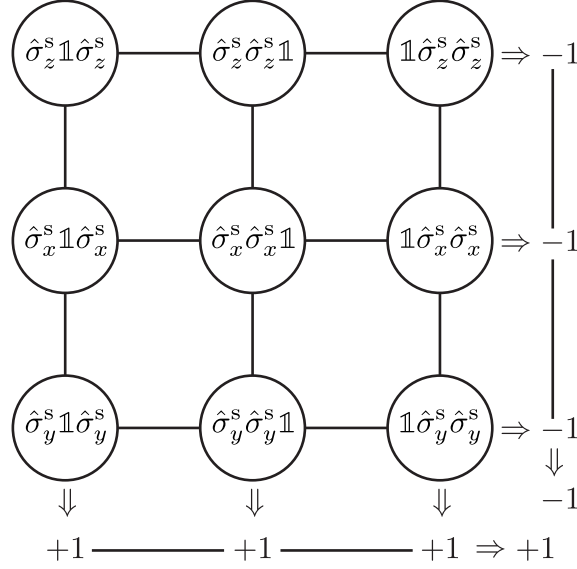


Figure 4.46: Mermin square used to illustrate the set of three spins demonstrating the Kochen-Specker theorem: The product of the three observables is minus one in each column and plus one in each row.

to quantum mechanics the eigenvalues of each observable must obey the product rule in each basis they are being measured. In Fig. 4.46 the product of the three observables is minus one in each column and plus one in each row. Consequently the products from the columns is plus one and the product of the rows is minus one, which is a contradiction.

We now want to consider the case discussed above, where the spins are pre and post-selected with the initial state given by Eq. (4.13) and final one by Eq. (4.14). Any predictions made by a NCHVT must be consistent with the boundary conditions given the pre and postselection. This constrains the results of products of the x and y direction in Fig. 4.46 to plus one. As was shown above the product of any two spin operators can be spectrally decomposed [Eqs. (4.15a) and (4.15b)]. Using this decomposition for the given pre and postselection the measurement outcome will be minus one for any pair of spins involving the z basis, i.e. $\hat{\sigma}_z^s \hat{\sigma}_z^s = -1$. Consequently all observable of the uppermost row in Fig. 4.46 have an eigenvalue of minus one, but no NCHVT can satisfy this result by assigning plus and minus one to each spin independently. The quantum pigeon hole effect is strongly related to contextuality.

4.4 Summary and perspective

In chapter 3 a theoretical treatment of a weak measurement scheme is presented, which can be used to completely determine the weak value of one two-level quantum system using another two-level quantum system as a meter. This is applied to different experimental situations in which the neutron's spin degree of freedom is investigated by coupling it weakly to the neutron's path degree of freedom. In this chapter the raw data of the experimental realization is described along with a detailed explanation of the way to reach such high quality data despite bad signal to noise ratios caused by the weakness of the interaction. From the experimental data the theoretical prediction is confirmed. Also the intuitive picture developed within the theoretical section, is fully justified by the experiment and helps to gain a deeper understanding of the involved physics.

For the spin operator's real part, weak values ranging from -3.2 to 3.4 are obtained, which is clearly outside the eigenvalue range of the spin operator. For its modulus, a value well above 3 is obtained. The imaginary part of $\langle \hat{\sigma}_z^s \rangle_w$ is determined using two slightly different experimental approaches, one with a purely polarimetric and one with an interferometric setup. Additionally $\text{Im} [\langle \hat{\sigma}_z^s \rangle_w] = 1.301$ is mapped out in several hundred measurements in a minimally disturbing polarimetric experiment.

For the special situation in which the preselected spin state is given by $|S_i\rangle = |S_x; +\rangle$ and the postselected one by $|S_f\rangle = |S_y; +\rangle$ 19 quantum ensembles were created in a sequence of time, which have a purely imaginary weak value of $\langle \hat{\sigma}_z^s \rangle_w = i$. These ensembles are used for the test of the quantum pigeon hole principle. The experiment showed that the weak value of each ensemble is indeed purely imaginary with a vanishing real contribution. Consequently any two of the 19 ensembles will show non-classical correlations in the sense of Aharonov *et. al.*.

It has to be stressed that all measurement results are of a purely quantum mechanical nature, since the neutron is modeled with a matter wave following the Schrödinger equation. No classical theory can describe the results. In addition the obtained results establish a way to determine weak values of massive particles with high accuracy. This establishes a new measurement technique that allows to test quantum mechanics at a fundamental level.

The measurement scheme presented in chapter 3 is in fact completely general and can be extended easily to a coupling between any two two-level systems. Therefore it can be used to not only investigate the spin degree of freedom, but also the path degree of freedom. In the following chapter a neutron interferometric experiment will be presented in which the role of spin and path are swapped. Then the spin

degree of freedom serves as a meter system to measure $\langle \hat{\sigma}_z^p \rangle_w$ and $\langle \hat{\Pi}_{z\pm}^p \rangle_w$.

Furthermore the measurement scheme can be easily extended to higher level quantum systems. An example for such a system would be a four plate interferometer. In such an interferometer, the neutron can travel along three different paths. It is a three level quantum system. Another example for a higher dimensional system is the neutron energy degree of freedom, which is a n -dimensional system. If the energy degree of freedom established as a meter, which can be used to completely determine all components of the spin operator's weak value, novel experimental schemes are possible. For example the energy degree of freedom could play the role of the path at a purely polarimetric experiment. Also the n -dimensional nature of the energy degree of freedom would open up the possibility to perform simultaneous weak measurements of incompatible observables.

CHAPTER 5

Path weak values

In this chapter a neutron interferometric experiment is presented, in which the weak value of the Pauli path operator $\hat{\sigma}_z^p$ is fully determined using both weak and strong interactions. Due to the completeness of two-level quantum systems this also yields the weak values of the operators $\hat{\Pi}_{z\pm}^p$, i.e. of the projection operators on the path eigenstates $|P_z; +\rangle$ and $|P_z; -\rangle$. Additionally measurements are presented in which $\langle \hat{\Pi}_{z\pm}^p \rangle_w$ are directly determined using maximum strength measurements not relying on the completeness of the system. The determined weak values can be used for a “direct” state characterization [Lundeen et al., 2011, Salvail et al., 2013] in the Mach-Zehnder interferometer. Precision and accuracy of weak and strong interaction approach are compared, showing that strong interactions outperform weak ones.

For the determination of $\langle \hat{\sigma}_z^p \rangle_w$ and $\langle \hat{\Pi}_{z\pm}^p \rangle_w$ individual intensity points on different interference fringes have to be compared to each other. This makes it necessary to record up to 16 interferograms at the same time. To perform this experimental task the stability of the setup has to be improved. Additionally a new supermirror with a larger window of acceptance is installed in the setup, doubling the count rate and thus halving the measurement time.

At first a short summary of the underlying experimental idea is presented. The improvements in the setup including their effects on the alignment of the components are demonstrated. Subsequently the experimental raw data are shown and the measurement results of $\langle \hat{\sigma}_z^p \rangle_w$ and $\langle \hat{\Pi}_{z\pm}^p \rangle_w$ are shown. Finally a “direct” state characterization of the neutron interferometer’s path degree of freedom is performed.

The results of a weak and strong interaction approach for such are compared to each other.

5.1 Underlying experimental idea

To determine $\langle \hat{\sigma}_z^P \rangle_w$ and $\langle \hat{\Pi}_{z\pm}^P \rangle_w$ the roles of the path and the spin degree of freedom are switched as compared to the experiments described in chapter 4. Experimentally this is achieved by minimally modifying the setup. Figure 5.1 shows an artistic depiction of the experimental setup. It is not necessary any more to access the

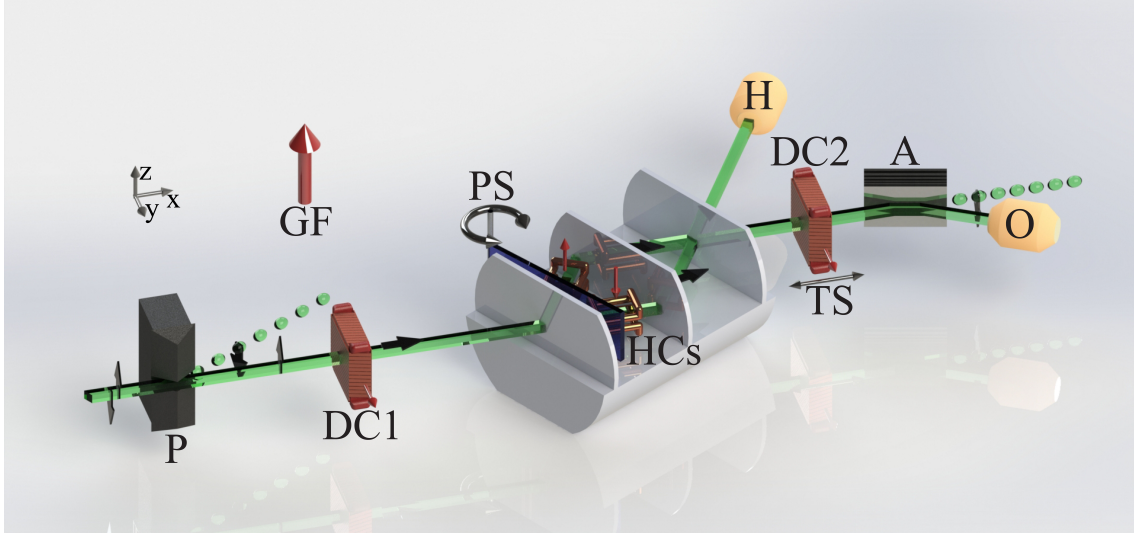


Figure 5.1: Artistic depiction of the experimental setup: The neutron beam passes magnetic prisms (P) that polarize it. To prevent depolarization a magnetic guide field (GF) is applied around the whole setup. Before the neutrons enter the interferometer a DC coil (DC1) prepares the initial spin state $|S_i\rangle$. At the interferometer's first plate the neutron beam gets separated into path *I* and *II*. The phase shifter (PS) placed between the first and the second plate of the interferometer prepares the initial path state $|P_i\rangle$. In each beam path small coils in Helmholtz configuration (HCs) allow the manipulation of the neutron spin in the xy -plane, making the measurement of $\langle \hat{\sigma}_z^P \rangle_w$ and $\langle \hat{\Pi}_{z\pm}^P \rangle_w$ possible. At the interferometer's third plate the final path state $|P_f\rangle$ gets postselected. The projective measurement of the meter system $|S_f\rangle$ is performed using a second DC coil (DC2) mounted on a translation stage (TS) in combination with a CoTi supermirror analyzer (A). Of the two outgoing beams of the interferometer, only the O-beam is spin analyzed (O). Both detectors (O & H) are ^3He counter tubes.

interferometer's path eigenstates. Therefore a cadmium beam block inside the interferometer is not needed. Also for clarity we want to change the preselected path state $|P_i\rangle$ and keep the postselected one $|P_f\rangle$ fixed. Therefore the phase shifter is moved between the first and the second plate of the interferometer.

Again the experiment starts with a polarized neutron beam, so that the neutron's spin state is given by $|S_z; +\rangle$. Before the neutron enters the interferometer the spin is turned by $\frac{\pi}{2}$ around the y -axis, leading to the initial spin state $|S_i\rangle \equiv |S_x; +\rangle$, which is exactly the same as in chapter 4. After the interferometer's first plate the neutron's state vector is extended by a path dependent component:

$$|\Psi\rangle = |P_i\rangle |S_i\rangle = (c_+ |P_z; +\rangle + c_- |P_z; -\rangle) |S_x; +\rangle, \quad (5.1)$$

where the states $|P_z; +\rangle$ and $|P_z; -\rangle$ are the eigenstates of the path I and II respectively, with the corresponding probability amplitudes c_+ and c_- .^a After the phase shifter the ensemble's preselection is complete. Again the coupling between the two degrees of freedom is created by performing small path dependent spin rotations. If $\langle \hat{\sigma}_z^p \rangle_w$ is measured, the spin is rotated by a certain angle α around the z -axis in the xy -plane with a positive (clockwise) rotation in path I and negative (counter clockwise) one in path II . The same interaction Hamiltonian is given for the measurement of the spin weak value:

$$\hat{H}_{\text{int}} = -\vec{\mu} \cdot \vec{B} \hat{\Pi}_{z+}^p + \vec{\mu} \cdot \vec{B} \hat{\Pi}_{z-}^p, \quad (5.3)$$

where $\vec{\mu}$ is the neutron's magnetic moment, $\vec{B} = (0, 0, B_z)$ an externally applied magnetic field. If $\hat{\Pi}_{z\pm}^p$ is the observable of interest, the spin rotation is set to take place only in one beam path and the interaction Hamiltonian is simplified to

$$\hat{H}'_{\text{int}} = -\vec{\mu} \cdot \vec{B} \hat{\Pi}_{z\pm}^p. \quad (5.4)$$

The Hamiltonian of either Eq. (5.3) or (5.4) can be realized as an evolution operator to obtain the evolved state vector. For the measurement of $\langle \hat{\sigma}_z^p \rangle_w$ exactly the same spin evolution as in Eq. (4.4) of the spin measurements is carried out. If the projection operators are of interest, the evolved state is given by

$$|\Psi'\rangle = e^{-i/\hbar \int \hat{H}_{\text{int}} dt} |\Psi_i\rangle = e^{-i\alpha \hat{\Pi}_{z\pm}^p \hat{\sigma}_z^s/2} |\Psi_i\rangle \quad (5.5)$$

^aFor a 50:50 beam splitter as is the case in a Mach-Zehnder type interferometer the probability amplitudes are $c_+ = c_- = 1/\sqrt{2}$, so that the initial path state is given by

$$|P_i\rangle = \frac{1}{\sqrt{2}} (|P_z; +\rangle + e^{i\chi} |P_z; -\rangle), \quad (5.2)$$

with some relative phase χ between the path eigenstates.

Again the parameter α describes an angle of rotation and therefore the interaction strength of the measurement. It is given by $-2\mu B_z \tau / \hbar$, where τ is the neutron's time of flight in the externally applied magnetic field. $\hat{\sigma}_z^s$ is the Pauli spin operator, that describes the rotation around the z -axis.

At the interferometer's third plate the beams are recombined and the final path state

$$|P_f\rangle = \frac{1}{\sqrt{2}} (|P_z; +\rangle + |P_z; -\rangle) \quad (5.6)$$

is postselected. Subsequently a combination of a coil mounted on a translation stage and a CoTi super mirror is used to evaluate the pointer system. This is done by projective measurements along the six spin directions $\pm x$, $\pm y$ and $\pm z$, which yields the six intensities $I_{j\pm} = |\langle S_j; \pm | \Psi_f \rangle|$ with $j = x, y, z$. The relations derived in chapter 3 can then be used to extract the path weak values from the recorded intensities.

5.2 Experimental realization

The setup used for the measurement of $\langle \hat{\sigma}_z^p \rangle_w$ and $\langle \hat{\Pi}_{z\pm}^p \rangle_w$ is very similar to that described in section 4.2.1, but for the determination of path weak values a higher stability is necessary since at least six intensities, corresponding to the six spin postselection directions, have to be recorded in a combined measurement. In practice twelve interference fringes are recorded for the measurement of $\langle \hat{\sigma}_z^p \rangle_w$ (one with and one without a spin rotation for each spin direction) in one experimental run. For the direct determination of $\langle \hat{\Pi}_{z\pm}^p \rangle_w$ 16 interferograms are recorded in a combined measurement (one measurement with a spin rotation for each beam path and spin direction plus one without a spin rotation for each spin postselection direction). Since the data points of the individual interferograms should be directly compared to each other it is not possible to rely on the data fits and perform phase corrections as was the case in the measurement of the spin weak value. It is necessary to have a highly stable setup.

To increase the stability of the setup, the old Helmholtz coils of the guide field are replaced by larger ones, which create a more homogenous magnetic field than the old coils. At the same time make a larger experimental space available, so that the interferometer itself can be placed in an extra box insulating it from the environment. Also during the cycles 174 and 175 (April to July 2015) a thermal stabilization system is installed at the instrument S18, which minimizes the thermal fluctuations of the experimental area.

In addition the efficiency of the polarimetric part of the setup is further improved by installing motorized micrometer rockers to adjust the DC coils. Furthermore a new supermirror with a larger window of acceptance is used as an analyzer, doubling the count rate without losing any sensitivity and degree of polarization. Finally simple line lasers are used to align all components correctly. Figure 5.2 shows a picture of the renewed setup (upper panel) and one of the alignment using the line laser (lower panel). In the experimental setup the aperture serves as an original starting point along which all other setup components are aligned.

5.2.1 Adjustment

The adjustment procedure of the setup is quite similar to that presented in section 4.2.1.1 and therefore a detailed description of its procedure is not repeated here. Only the final adjustment results of several components are presented, because they serve as a reference for future experimentalists.

All results presented in this chapter were recorded during reactor cycles 174 and 175 (April to July 2015) at ILL during which a reactor power of 53MW was available. The aperture used in the experiments has a cross section of $6 \times 4 \text{ mm}^2$, which offers almost the same cross section as a $5 \times 5 \text{ mm}^2$ aperture. This aperture size is chosen, because the entrance of the spin manipulation devices inside the interferometer are narrow and every extra millimeter in width helps to install them correctly. The change of aperture size has no significant effect on the count rate. In general great care is taken to maximize the count rate for the experiment. At the early stages of the experiment the monochromator adjusted several times. The higher count rate is of importance because it reduces the necessary time for each experimental run and consequently also the time during which the setup has to be kept stable. It is worth noting that during all measurements a triple Laue interferometer, the so called Kaiser interferometer, was used. This is exactly the same interferometer that was already used during the measurement of the spin operator's weak value. The Kaiser interferometer is a symmetric three plate Mach-Zehnder type interferometer. It has the "FRONT" and "BACK" carved into the faces of its base. While during the previous experiment the "FRONT" side was facing the polarizing prisms, it is now facing the detector. The interferometer is turned by 180 degree as compared to the previous experiments. In theory this should not change anything, since the interferometer is symmetric. The observed contrast during the measurements of the path degree of freedom's weak values was lower than during the experiments concerning the spin weak values (an average of 75% as compared to an average of

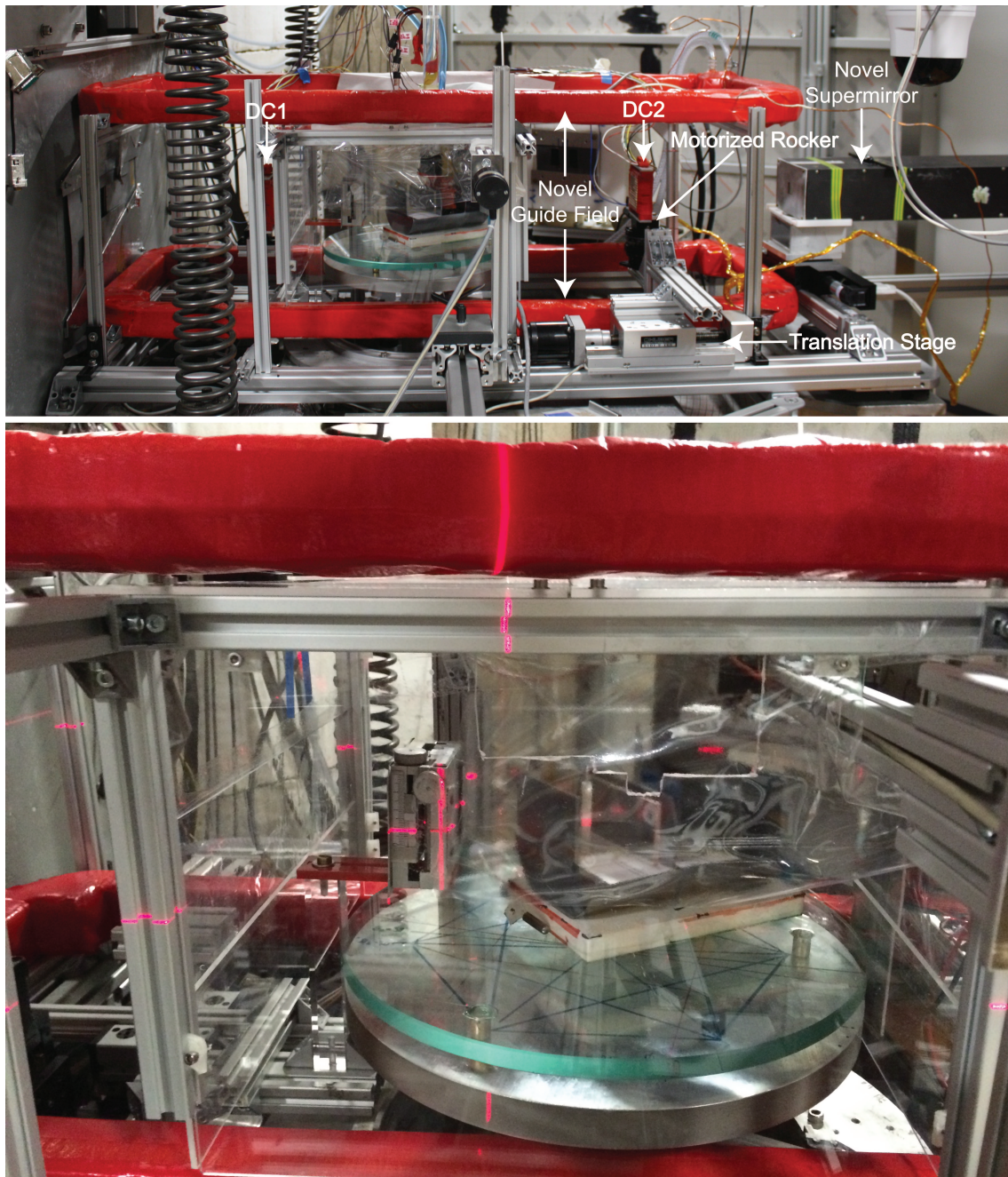


Figure 5.2: Picture of the experimental setup during cycles 174 and 175 (April to July 2015): The newly installed guide field coils (red) offer more space, making it possible to put a small box around the interferometer. The DC coils are put onto motorized rockers and a novel supermirror with a larger window of acceptance is used (all upper panel). The aperture serves as an original starting point along which all other setup components are aligned using linear lasers. Note that this picture shows a four plate interferometer, which was also tested during these cycles but was not in use for the actual experiment described here (lower panel).

80% in the previous experiment). Whether the decrease in contrast is due to the

positioning of the interferometer is only speculation. Due to the complexity of the system it can also have a number of other reasons. For future experiments it can be noted that it is certainly not a mistake to position the Kaiser interferometer with the carving “FRONT” facing the polarizing prisms.

As in the previous experiment the monochromator is adjusted first and subsequently the interferometer is set correctly in the beam, so that its region of maximum contrast coincides with the beam’s spot of maximum intensity. After that polarizer and analyzer are put into the setup, so that the adjustment of the spin manipulating devices can be done.

The DC coils used in this experiment are of the same design as in the previous experiment, which are especially built for the experiment. A new manufacturing technique using 3D printing, allows us to make the coils thinner and more precisely wound. Also a thinner copper band is used to minimize neutron absorption in the coil. The result of the final adjustment of the DC1 coil is shown in Fig. 5.3 After the

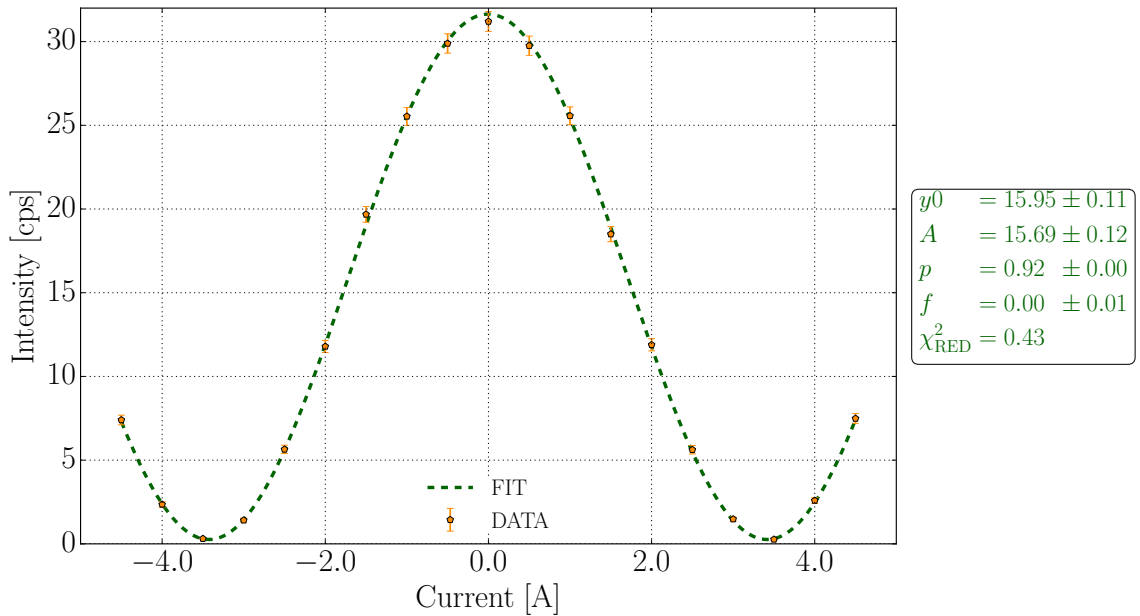


Figure 5.3: B_y -scan of DC2 obtained with a suitable compensation field B_z : After the final adjustment, the DC1 coil showed a flipping ratio of ~ 85 , a contrast of $\sim 98\%$ and a phase shift of $f = 0.004$ rad (without background correction).

final adjustment, the DC1 coil showed a flipping ratio of ~ 85 , a contrast of $\sim 98\%$ and a phase shift of $f = 0.004$ rad. The flipping ratio is already better than the results obtained in previous experiments, but it is still bounded by the stray fields of the polarizing prisms.

The DC2 coil is adjusted in the same manner. During the experiment investigating

the spin operator's weak value the coil had to be readjusted for every azimuthal angle, i.e. for different translation stage positions in the setup. Now this is not the case any more, because the new guide field is far more homogenous. Once the correct settings are found they can be used for any translation stage position. Figure 5.4 shows the final adjustment results of DC2. After the final adjustment, the DC2 coil

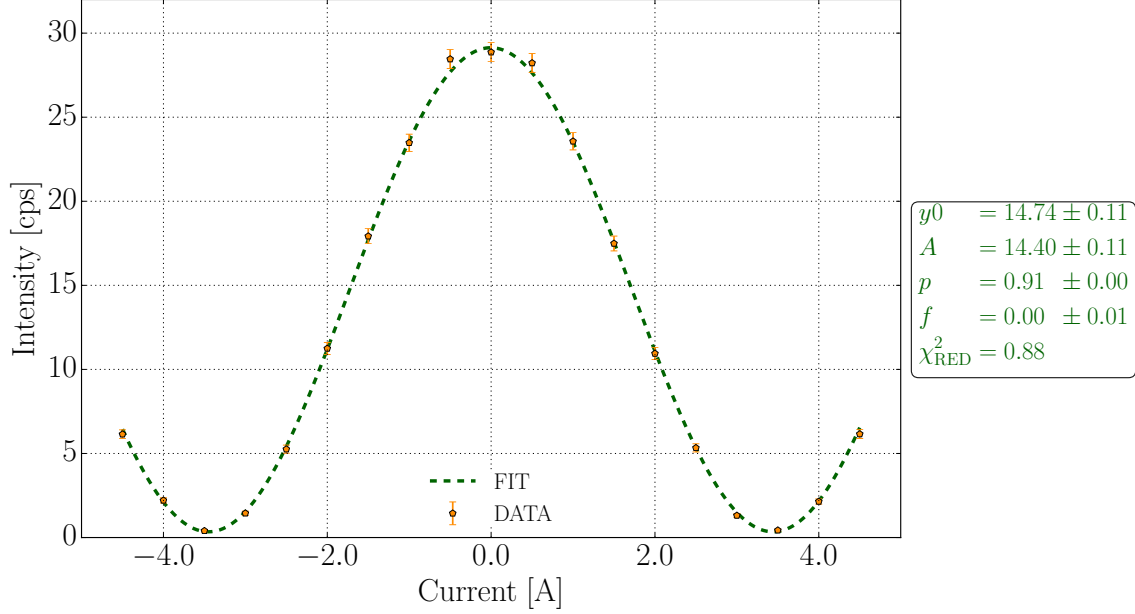


Figure 5.4: B_y -scan of DC2 obtained with a suitable compensation field B_z : After the final adjustment, the DC1 coil showed a flipping ratio of ~ 121 , a contrast of $\sim 98\%$ and a phase shift of $f = 0.005$ rad (without background correction).

showed a flipping ratio of ~ 121 , a contrast of $\sim 98\%$ and a phase of $f = 0.005^\circ$. Note that the count rate is slightly lower than during the adjustment of DC1. This is due to neutron absorption in the coils copper band. The flipping ratio is higher, more then doubling the results of the previous experiment. This is owing to the motorized rockers, the new guide field and an increased distance to the supermirror analyzer.

The results of the adjustment of the other components (position scan with DC2, current scan of the spin manipulators, etc.) are, aside from the higher count rate, very similar to previous results and will not be shown here in detail. In Fig. 5.5 a direct comparison between the old and the new data of adjustment measurements of DC1 is shown. Note that the count rate more than doubled in the new experimental setup. This is mostly the consequence of the new analyzer and its larger window of acceptance. At a first glance a doubling in count rate might not contribute a lot, but for an experimentalist this is very exciting news since it will open up new

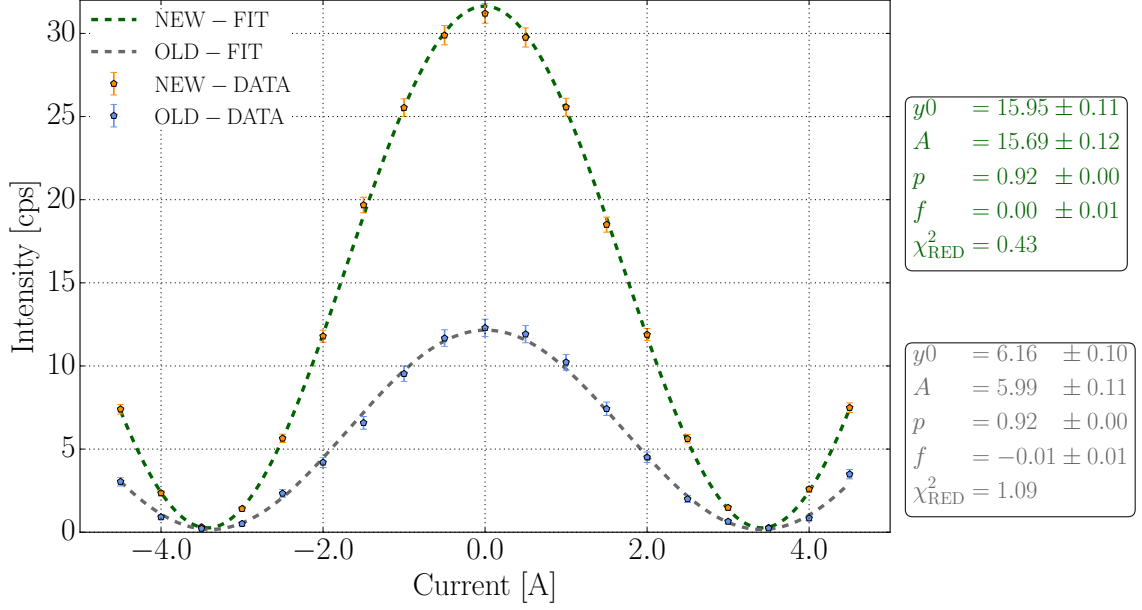


Figure 5.5: Comparison between DC adjustment with old and new analyzer. Note the dramatically increased count rate in the new data.

possibilities for experiments. To put the number in perspective one has to consider that a typical beam time last six weeks. Doubling the count rate equals a doubling of beam time to 12 weeks. Or one can also think the other way around: The results which previously took six weeks to accomplish can now be done in only three weeks!

5.2.2 Measurement of Pauli operators

One of the goals of the beam times of reactor cycles 174 and 175 (April to July 2015) was to determine the weak value of the Pauli path operator $\hat{\sigma}_z^p$. In this section the recorded intensities as well as the results of the weak value determination are presented.

A general preselected path state is given by

$$|P_i\rangle = \cos\left(\frac{\kappa}{2}\right) |P_z; +\rangle + \sin\left(\frac{\kappa}{2}\right) e^{i\rho} |P_z; -\rangle, \quad (5.7)$$

where κ and ρ are the polar and azimuth angles on the path Bloch sphere respectively. The azimuthal angle ρ describes the relative phase between the path eigenstates $|P_z; +\rangle$ and $|P_z; -\rangle$. In the experiment it is controlled by the phase shifter. If one assumes that $\kappa = \pi/2$ as is the case for a 50:50 beam splitter realized in a Mach-Zehnder type neutron interferometer and if the postselected path state is

given by Eq. (5.6), the weak value of the Pauli path operator $\hat{\sigma}_z^p$ is expected to be

$$\langle \hat{\sigma}_z^p \rangle_w = \frac{\langle P_f | \hat{\sigma}_z^p | P_i \rangle}{\langle P_f | P_i \rangle} = \frac{1 - e^{i\rho}}{1 + e^{i\rho}} = -i \tan \frac{\rho}{2}. \quad (5.8)$$

The weak value $\langle \hat{\sigma}_z^p \rangle_w$ has no real part. It is purely imaginary with $\text{Im} [\langle \hat{\sigma}_z^p \rangle_w]$ given by the negative tangent oscillating with a period of double the phase. The tangent has points of discontinuity for multiples of $\pm\pi/2$. For these phase values, i.e. for $\rho = \pm\pi$ pre and postselected path states become orthogonal.

In the experiment, $\langle \hat{\sigma}_z^p \rangle_w$ is determined using two different interaction strengths. To perform measurements in the weak regime α is set to $\alpha = 15^\circ$. For strong interactions the maximum value is set for α , i.e. it is given by $\alpha = 90^\circ$. All components of the Pauli path operator's weak value are extracted from the experimentally recorded intensities using the relations given by Eqs. (3.38), (3.43) and (3.44). Since they are valid for arbitrary angles of α they can be equally applied for both the weak and the strong interaction case and allow for a comparison of both experimental approaches.

5.2.2.1 Data

To fully determine the path operator's weak value the meter system, i.e. the neutron spin degree of freedom, has to be projectively measured along the six directions $\pm x$, $\pm y$ and $\pm z$ which yields the six intensities $I_{j\pm} = |\langle S_j; \pm | \Psi_f \rangle|^2$ with $j = x, y, z$. Given the preselected system state of Eq. (5.1), the evolution operator of Eq. (5.3) and the postselected path state of Eq. (5.6) it is possible to analytically calculate those intensities for ideal circumstances. They are given by

$$I_{x+} = \cos^2 \left(\frac{\alpha}{2} \right) \cos^2 \left(\frac{\chi}{2} \right) \quad (5.9a)$$

$$I_{x-} = \sin^2 \left(\frac{\alpha}{2} \right) \sin^2 \left(\frac{\chi}{2} \right) \quad (5.9b)$$

$$I_{y+} = \frac{1}{4} [1 + \cos(\alpha) \cos(\chi)] \quad (5.9c)$$

$$I_{y-} = \frac{1}{4} [1 + \cos(\alpha) \cos(\chi)] \quad (5.9d)$$

$$I_{z+} = \frac{1}{4} [1 + \cos(\alpha + \chi)] \quad (5.9e)$$

$$I_{z-} = \frac{1}{4} [1 + \cos(\alpha - \chi)] \quad (5.9f)$$

If the initial and final spin states are the same, the intensity I_{x+} is obtained. It comes as no surprise that in this case an interference fringe with full intensity and full contrast is expected to be observed, as long as there is no interaction, i.e. as

long as $\alpha = 0^\circ$. At the same time initial and final spin states are orthogonal for the I_{x-} measurement. Thus null intensity is expected for zero interaction. Also I_{x+} and I_{x-} are expected to be phase shifted by π for χ . For $\alpha = 90^\circ$ the intensities are expected to have equal average intensity.

The intensities $I_{y\pm}$ are expected to be equal with in average half of the maximum intensity. With increasing measurement strength the contrasts are expected to be reduced, so that they show zero contrast for $\alpha = 90^\circ$. This is because the spin rotation inside the interferometer brings the spin state towards orthogonality with increasing α .

For $I_{z\pm}$ a phase shift is expected to be observed with I_{z+} being shifted by α to the left and I_{z-} to the right in the χ -scan. In the maximum interaction case, the intensity modulations are supposed to be phase shifted by π , which is two times the angle α . Figure 5.6 shows the intensity modulations of the weak interaction case. The recorded intensities are exactly what one would expect: Maximum and minimum average count rates are observed for I_{x+} and I_{x-} respectively. Within error I_{y+} and I_{y-} are equal. I_{z+} and I_{z-} are phase shifted by $\sim 2\alpha$. It is true that the neutron interferometer - just like any other quantum system - cannot exhibit an ideal behavior as assumed in the intensity calculations. Therefore I_{x+} does not show full contrast: the average contrast of the recorded interference fringes is $\sim 75\%$, which is taken into account in the final weak value determination as described in chapter 4.

In Fig. 5.6 six intensities are plotted, one for each spin postselection direction of interest with an interaction strength of $\alpha = 15^\circ$ for each (IN measurements). In the actual experiment also six additional interference fringes with zero interaction, $\alpha = 0$, (OUT measurements) are recorded. In total twelve interferograms are recorded in a combined measurement at the O-detector. Additionally there are also twelve intensity curves measured at the H-detector. They are not spin analyzed, but the H-detector's OUT measurements can be used to accurately determine the period of the empty interferometer. This is done by fitting the H-detector data with a function of the same form as Eq. (4.6), where the period of the fit is initially set as a free parameter. The average of all obtained periods is then used to fit the O-detector data. The curves in Fig. 5.6 are minimizing χ^2 -fits to the data. For the determination of the Pauli path operator's weak value they are of minor importance, since the intensities are compared point by point. Only for the determination of the weak value's phase, the phase of the intensity I_{x+} is used, which is extracted from the data fit.

Figure 5.7 shows the intensity modulations for the strong interaction case. Again

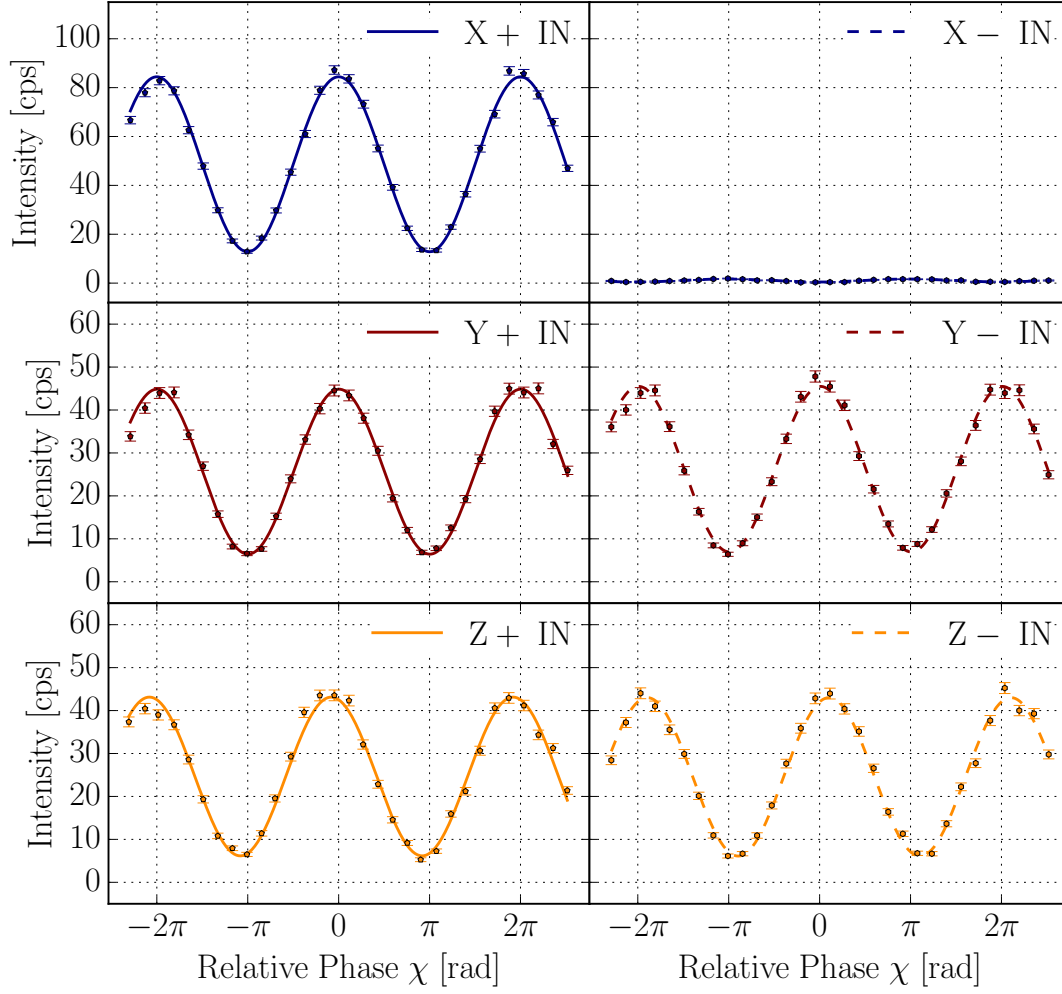


Figure 5.6: Intensity modulations obtained in the χ -scan for the weak interaction case: maximum and minimum average count rates are observed for $I_{x\pm}$ respectively. Within error $I_{y\pm}$ are equal. $I_{z\pm}$ are phase shifted by $\sim 2\alpha$. The lines represent minimizing χ^2 -fits to the data. The error bars show one standard deviation. Background has been subtracted for all measurements.

they confirm what one would expect to see. The intensities $I_{x\pm}$ are phase shifted by $\sim \pi$ with the same average count rate. $I_{y\pm}$ show only negligible little contrast. $I_{z\pm}$ are phase shifted by $\sim 2\alpha$. Again the interferometer does not show 100% contrast, which has to be considered in the final weak value determination. Again additional OUT intensities are recorded in the experiment, which are not shown here.

Looking at the intensities plotted in Figs. 5.6 and 5.7 one can already make assertions about the weak value using the intuitive picture of the weak value's action in the meter system presented in chapter 3: The weak value's modulus can only be determined in second order of the interaction parameter. Therefore we see that the

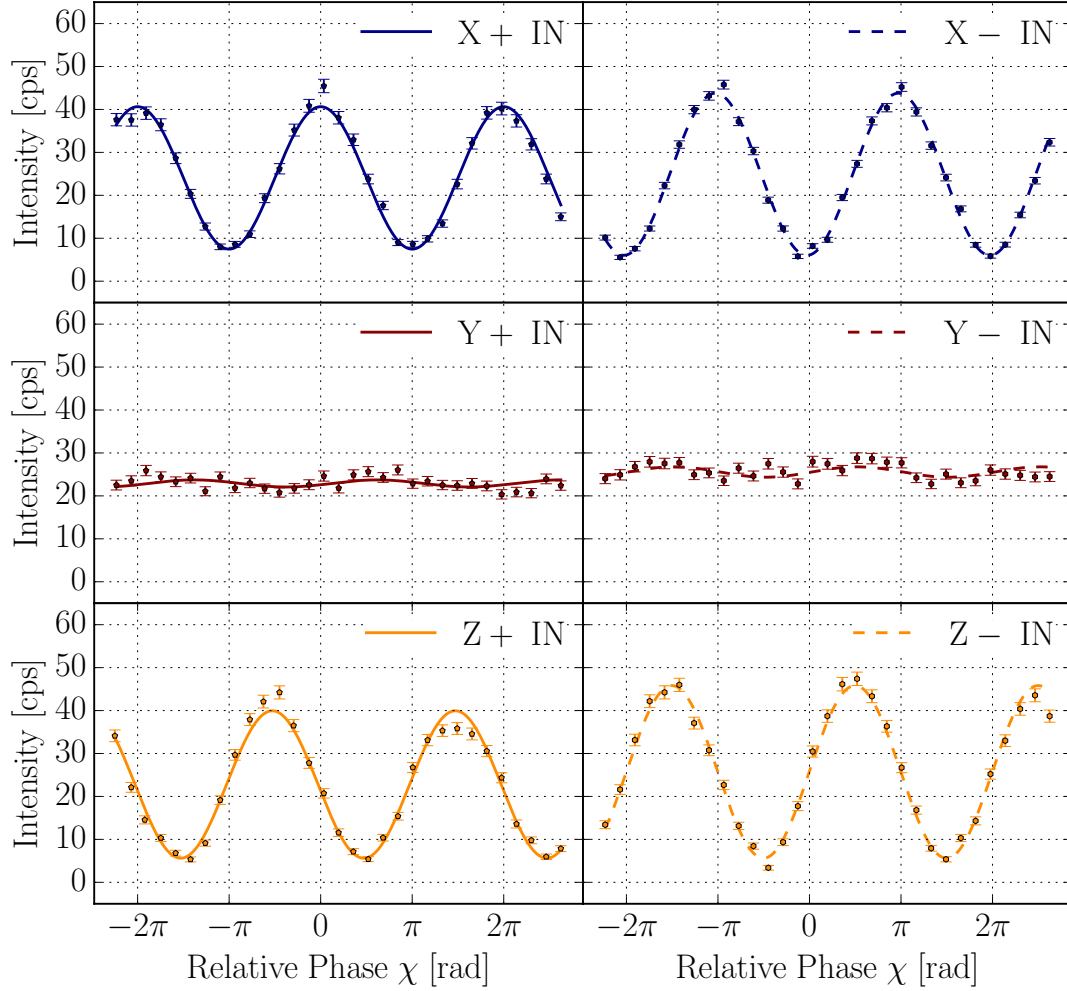


Figure 5.7: Intensity modulations obtained in the χ -scan for the strong interaction case: the intensities $I_{x\pm}$ are phase shifted by $\sim \pi$ with the same average count rate. $I_{y\pm}$ show only negligible little contrast. $I_{z\pm}$ are phase shifted by $\sim 2\alpha$. The lines represent minimizing χ^2 -fits to the data. The error bars show one standard deviation. Background has been subtracted for all measurements.

intensity I_{x-} , which is crucial to determine, also scales with the second order of α . In the weak interaction approach the huge signal I_{x+} has to be compared to the tiny signal I_{x-} to determine $|\langle \hat{\sigma}_z^p \rangle_w|$. For the strong interaction measurement this is not the case any more, since $I_{x\pm}$ have an intensity in the same order. This already suggests qualitatively that the strong interaction approach can be favorable for the determination of weak values.

The weak value's real part is extracted from the intensities $I_{y\pm}$ and expected to be zero. $I_{y\pm}$ are nearly identical: there is no significant difference in the intensities that would lead to a non zero result when they are inserted into Eq. (3.43) and

consequently $\text{Re} [\langle \hat{\sigma}_z^p \rangle_w]$ is close to zero.

In the geometric picture presented in chapter 3 $\text{Im} [\langle \hat{\sigma}_z^p \rangle_w]$ tilts the state vector of the meter system away from the equator towards the poles of the Bloch sphere. In the case of the measurements of the Pauli path operator this manifests itself in a phase shift of the interference fringes. The relevant signal to determine the weak value's imaginary part is the phase shift between $I_{z\pm}$. Since it is expected to be 2α , it can be resolved with less relative error in the strong interaction case.

5.2.2.2 Results

Figure 5.8 shows the results of the weak value determination using weak interactions. In general a very good agreement between the theoretical prediction and the experimentally obtained results is observed.

The weak value's real part is bunched around zero. It is not surprising that no solid flat line is observed in the experiment. That is every point of the two $I_{y\pm}$ intensity modulations would need to be identical, which is hard to achieve experimentally. The weak value's imaginary part can be inferred from the phase shift of two interference fringes. The interferometer is well suited to determine phase shifts and therefore the measurement results of $\text{Im} [\langle \hat{\sigma}_z^p \rangle_w]$ agree well with the theoretical prediction. The largest deviation between theory and experiment are observed in the determination of the weak value's modulus, where especially small values deviate from the theoretical prediction. This is due to the fact that in a coupling between two two-level quantum systems, the weak value's modulus appears as a second order term. This makes it hard to resolve, in the weak interaction case, especially whenever its value becomes small.

Figure 5.9 shows the results of the weak value determination using strong interactions. Again a very good agreement between theory and experiment is observed. Note that now also the weak value's modulus is resolved with smaller deviation from the expected curve also for very small values, because the relative error for larger α is small. That is, if the absolute uncertainty for the spin manipulation during the spin path coupling is 2° , the relative uncertainty for the weak interaction measurement is $\sim 13\%$, while it is only $\sim 2\%$ for the strong interaction measurement. This small relative uncertainty manifests itself in small error bars in the weak value determination.

The results presented in this section will later be used to reconstruct the interferometer's preselected path vector. The strong and weak interaction approach will be compared in terms of accuracy and precisions. Qualitative arguments from the

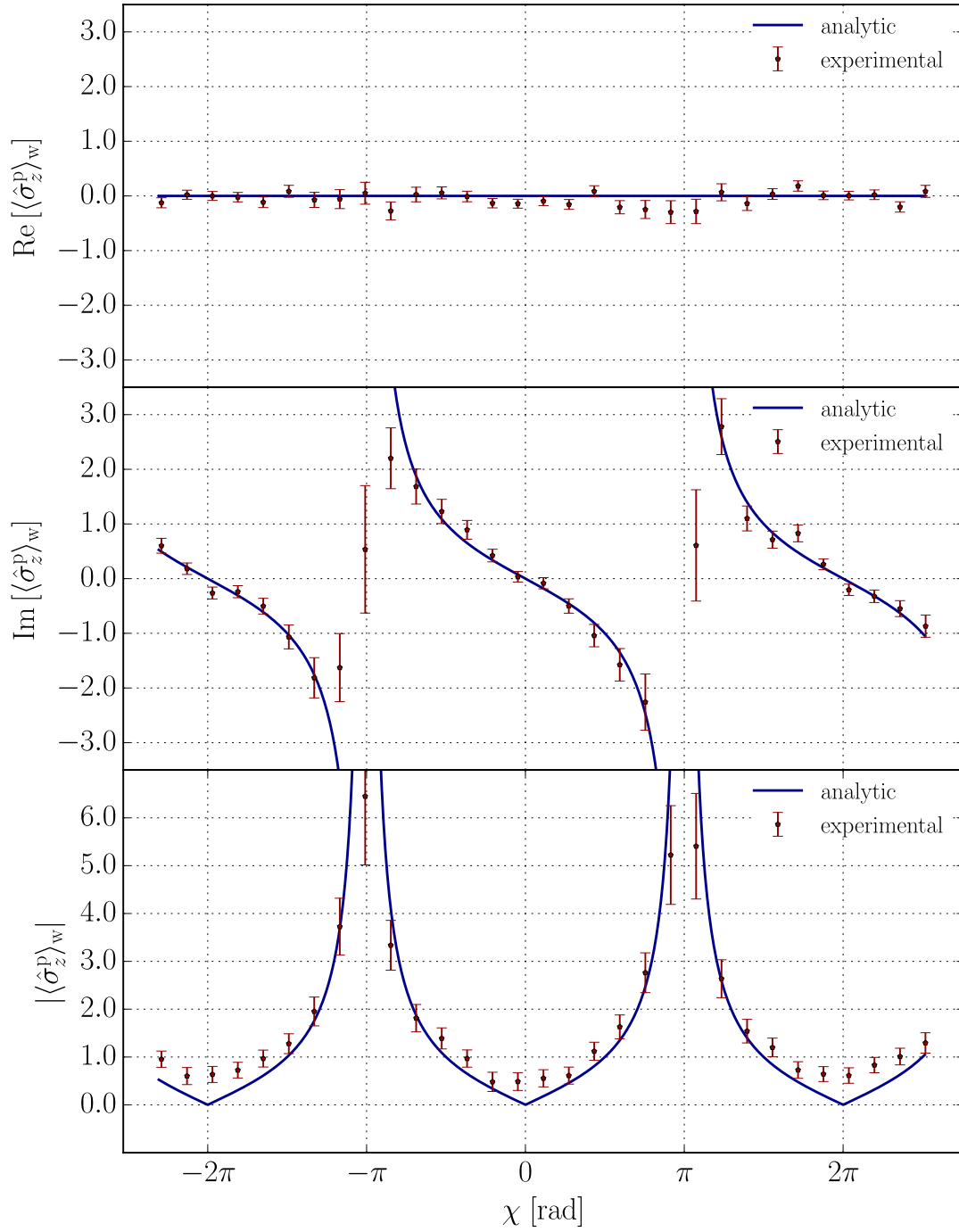


Figure 5.8: Measurement results for $\langle \hat{\sigma}_z^P \rangle_w$ for weak interaction: Measurement results (red) and theoretical predictions (blue) for the path operator's weak value. The error bars represent one standard deviation.

interference fringes and the obtained weak values is then quantified, namely that strong interactions outperform weak ones in both precision and accuracy.

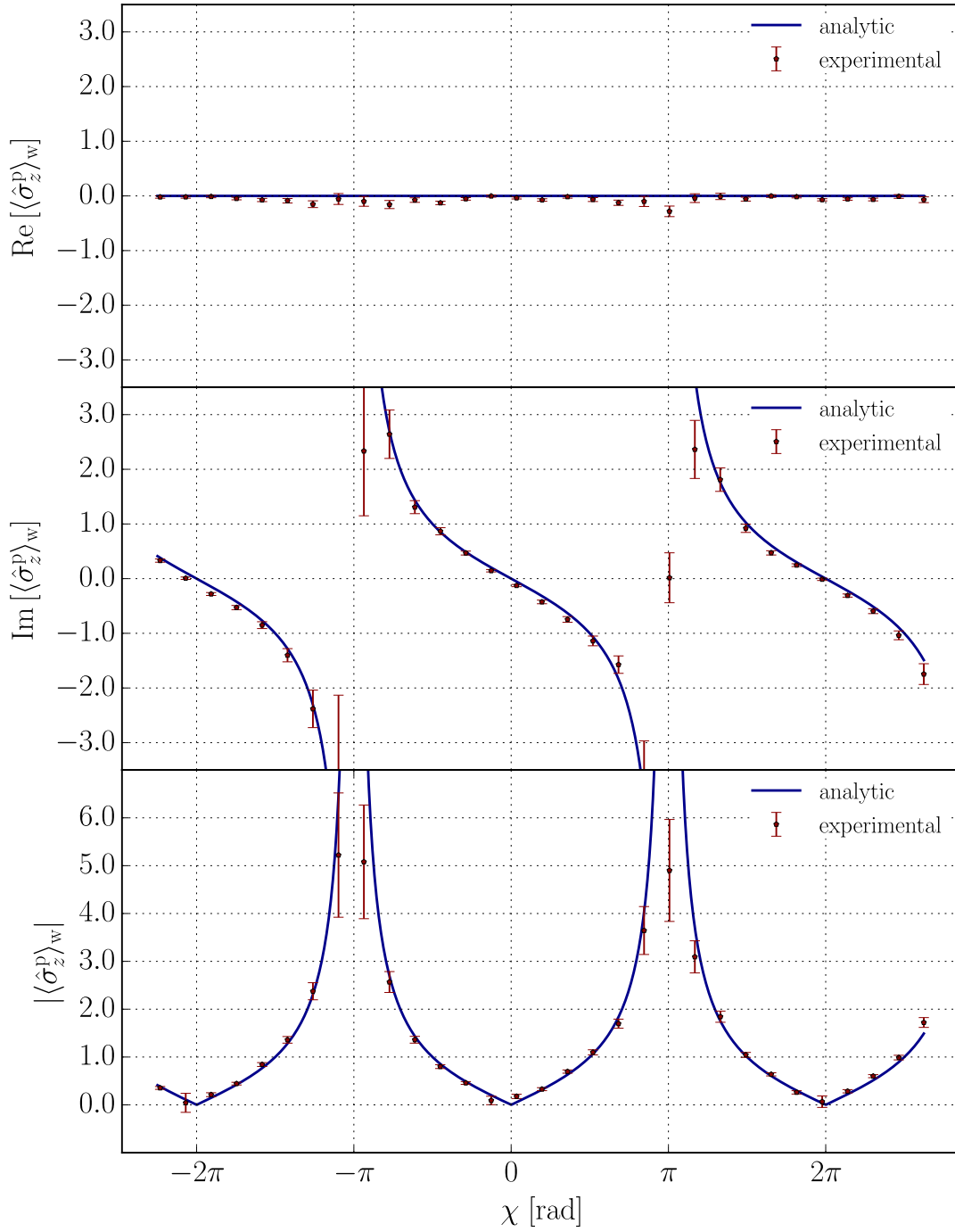


Figure 5.9: Measurement results for $\langle \hat{\sigma}_z^p \rangle_w$ for strong interaction: Measurement results (red) and theoretical predictions (blue) for the path operator's weak value. The error bars represent one standard deviation.

5.2.3 Measurement of projection operators

In the previous section the measurement results for the Pauli path operator's weak value $\langle \hat{\sigma}_z^p \rangle_w$ are presented. Using these results it is possible to also reconstruct the path projection operator's weak values. Furthermore, it is also possible to directly measure those operators. For this the experiment has only to be minimally changed. While in the previous section the spin path interaction is symmetric along both paths, one has to turn the interaction on along only either one of the paths to measure $\langle \hat{\Pi}_{z\pm}^p \rangle_w$, so that the interaction Hamiltonian is turned in the same form as Eq. (5.4). Taking the general initial path state given by Eq. (5.1) and again assuming equally weighted path eigenstates, the projection operators' weak values are expected to be

$$\langle \hat{\Pi}_{z\pm}^p \rangle_w = \frac{\langle P_f | \hat{\Pi}_{z\pm}^p | P_i \rangle}{\langle P_f | P_i \rangle} = \frac{1}{2} \mp \frac{i}{2} \tan\left(\frac{\chi}{2}\right). \quad (5.10)$$

As with the Pauli operator's weak value also the projection operators' weak value has a constant real component. Now it is one half. Again the imaginary part is of the form of a tangent function. Note the opposing signs of $\text{Im} \left[\langle \hat{\Pi}_{z\pm}^p \rangle_w \right]$ for the respective path eigenstate.

All components of $\langle \hat{\Pi}_{z\pm}^p \rangle_w$ are determined experimentally using the same setup as described above. The weak value determination is only performed for maximum measurement strength, i.e. for $\alpha = -180^\circ$ ^b. The relations given by Eqs. (3.65a) to (3.65c) are used to extract the weak value from the recorded intensities. In the subsequent sections the data as well as the final results for the weak value determination are presented.

5.2.3.1 Data

To fully determine $\langle \hat{\sigma}_z^p \rangle_w$ it is necessary to evaluate the meter system along six spin directions. For the determination of the projection operator's weak value only five directions of spin postselection are necessary. They are set by $-x$, $\pm y$ and $\pm z$. The intensities are calculated from the initial and final state. Assuming perfect

^bThe interaction parameter was chosen to be negative for experimental reasons. Negative angles of rotation correspond to positive magnetic fields. Applying a magnetic field which induces a positive spin rotation of 180° reduces the guide field and can lead to depolarization of the neutron spin, which would in turn lead to annoying effects in the experiment.

circumstances, a spin rotation along path I yields the five intensities

$$I_{x-}^I = \frac{1}{8} [1 - \cos(\alpha)] \quad (5.11a)$$

$$I_{y+}^I = \frac{1}{8} \left\{ 2 + 2 \cos(\chi) \left[\cos\left(\frac{\alpha}{2}\right) + \sin\left(\frac{\alpha}{2}\right) \right] + \sin(\alpha) \right\} \quad (5.11b)$$

$$I_{y-}^I = \frac{1}{8} \left\{ 2 + 2 \cos(\chi) \left[\cos\left(\frac{\alpha}{2}\right) - \sin\left(\frac{\alpha}{2}\right) \right] - \sin(\alpha) \right\} \quad (5.11c)$$

$$I_{z+}^I = \frac{1}{4} \left[1 + \cos\left(\frac{\alpha}{2} + \chi\right) \right] \quad (5.11d)$$

$$I_{z-}^I = \frac{1}{2} \cos \left[\frac{1}{4} (\alpha - 2\chi) \right]^2 \quad (5.11e)$$

These intensities listed are valid for arbitrary values of α . If it is set to $\alpha = -\pi$ I_{x-}^I is expected to show a flat line and no intensity modulation. $I_{y\pm}^I$ are expected to be phase shifted by π showing full contrast. The $I_{x\pm}$ and $I_{y\pm}$ intensities switched their roles when the measurement of the Pauli and the projection operators is compared to each other. In the first case I_{x+} acts as a normalization factor. In the latter this role is taken by I_{y-}^I . Also while for maximum measurement strength zero contrast is expected for the $I_{y\pm}^I$, if the Pauli operator is of interest, the I_{x-}^I intensity shows no modulation during the measurement of the path projection operators. $I_{z\pm}^I$ are also expected to show full contrast and a phase shift of π .

If the spin rotation is performed along path II of the interferometer the expected intensities are

$$I_{x-}^{II} = \frac{1}{8} [1 - \cos(\alpha)] \quad (5.12a)$$

$$I_{y+}^{II} = \frac{1}{8} \left\{ 2 + 2 \cos(\chi) \left[\cos\left(\frac{\alpha}{2}\right) + \sin\left(\frac{\alpha}{2}\right) \right] + \sin(\alpha) \right\} \quad (5.12b)$$

$$I_{y-}^{II} = \frac{1}{8} \left\{ 2 + 2 \cos(\chi) \left[\cos\left(\frac{\alpha}{2}\right) - \sin\left(\frac{\alpha}{2}\right) \right] - \sin(\alpha) \right\} \quad (5.12c)$$

$$I_{z+}^{II} = \frac{1}{2} \cos \left[\frac{1}{4} (\alpha - 2\chi) \right]^2 \quad (5.12d)$$

$$I_{z-}^{II} = \frac{1}{4} \left[1 + \cos\left(\frac{\alpha}{2} + \chi\right) \right] \quad (5.12e)$$

I_{x-}^I and I_{x-}^{II} as well as $I_{y\pm}^I$ and $I_{y\pm}^{II}$ are equal for both cases. Those intensities are necessary to determine the modulus and the real part of the path projection operators' weak value, which are equal for both paths. Therefore it is only reasonable that also the intensities are the same. $I_{z\pm}^I$ and $I_{z\pm}^{II}$ are exchanged so that $I_{z+}^I = I_{z-}^{II}$ and vice versa. The z -intensities are crucial in the determination of the weak value's imaginary part, which is equal for path I and II up to an opposite sign. The change of sign is due to the fact that the $I_{z\pm}$ intensities depend in which path the rotation

is performed.

In the experiment five IN intensities, with a spin rotation inside the interferometer, are recorded for each path projection operator. Furthermore six OUT measurements with no spin rotation inside the interferometer are performed. In total 16 interferograms are recorded in a nested way. The IN intensities are plotted in Fig.5.10. I_{x-}^I and I_{x-}^{II} show only negligible small contrast. $I_{y\pm}^I$ and $I_{y\pm}^{II}$ are phase shifted by

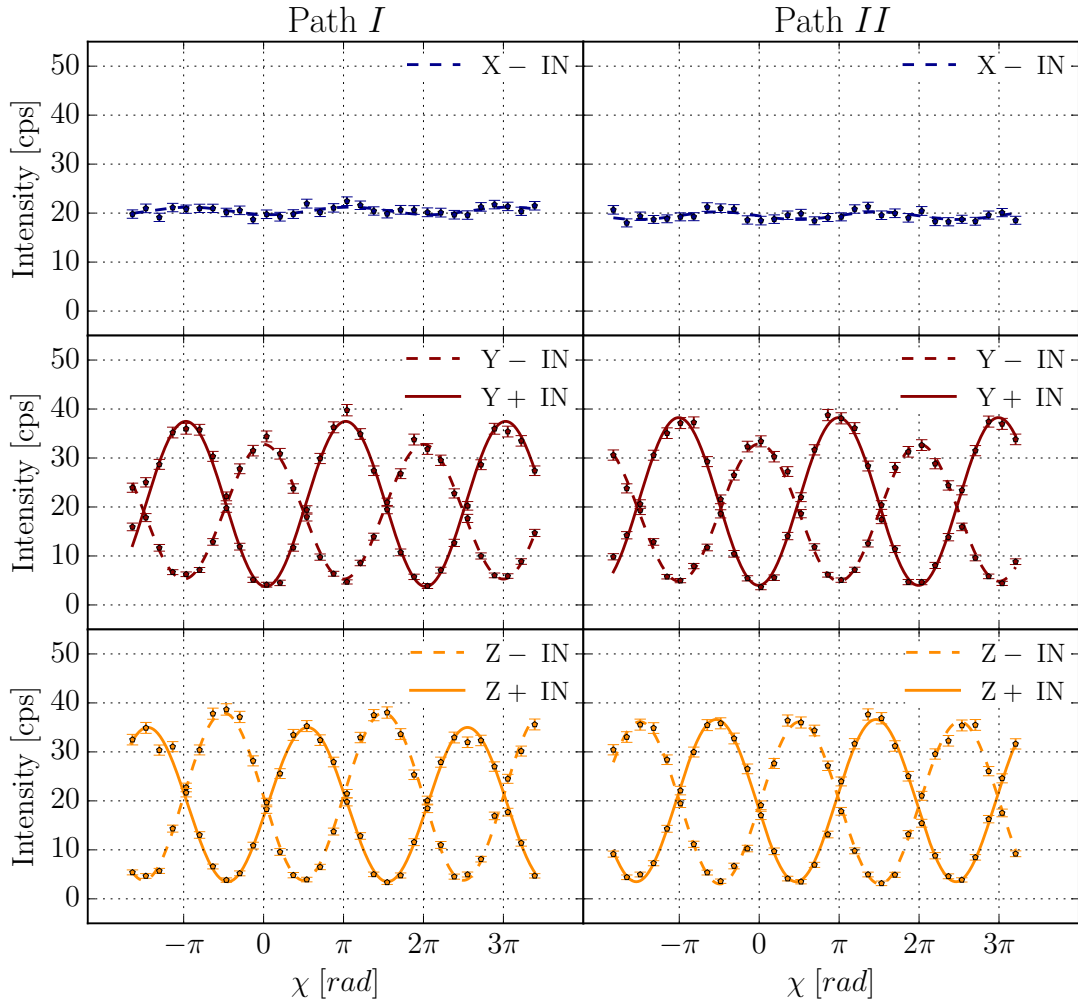


Figure 5.10: Intensity modulations obtained in the χ -scan for the measurement of the path projection operators: The intensities $I_{y\pm}$ and $I_{z\pm}$ are phase shifted by $\sim \pi$ with the same average count rate. I_{x-} show only negligible small contrast. The error bars show one standard deviation. Background has been subtracted for all measurements. The lines represent minimizing χ^2 -fits to the data.

π . Note that the intensity I_{y-}^{II} has a little less count rate than I_{y+}^{II} . This suggests a small misalignment in the spin postselection or the spin manipulation inside the

interferometer^c. It will manifest itself in the final result as a deviation from the theoretical curve for phase values close to odd multiples of π . The $I_{z\pm}$ intensities are phase shifted by π for both paths and in average they show the same count rate as expected.

5.2.3.2 Results

The intensities presented in Fig.5.10 are inserted point to point into Eqs. (3.65a) to (3.65c) to determine the path projection operators' weak values. The results are depicted in Fig. 5.11 A very good agreement between experiment and theory is

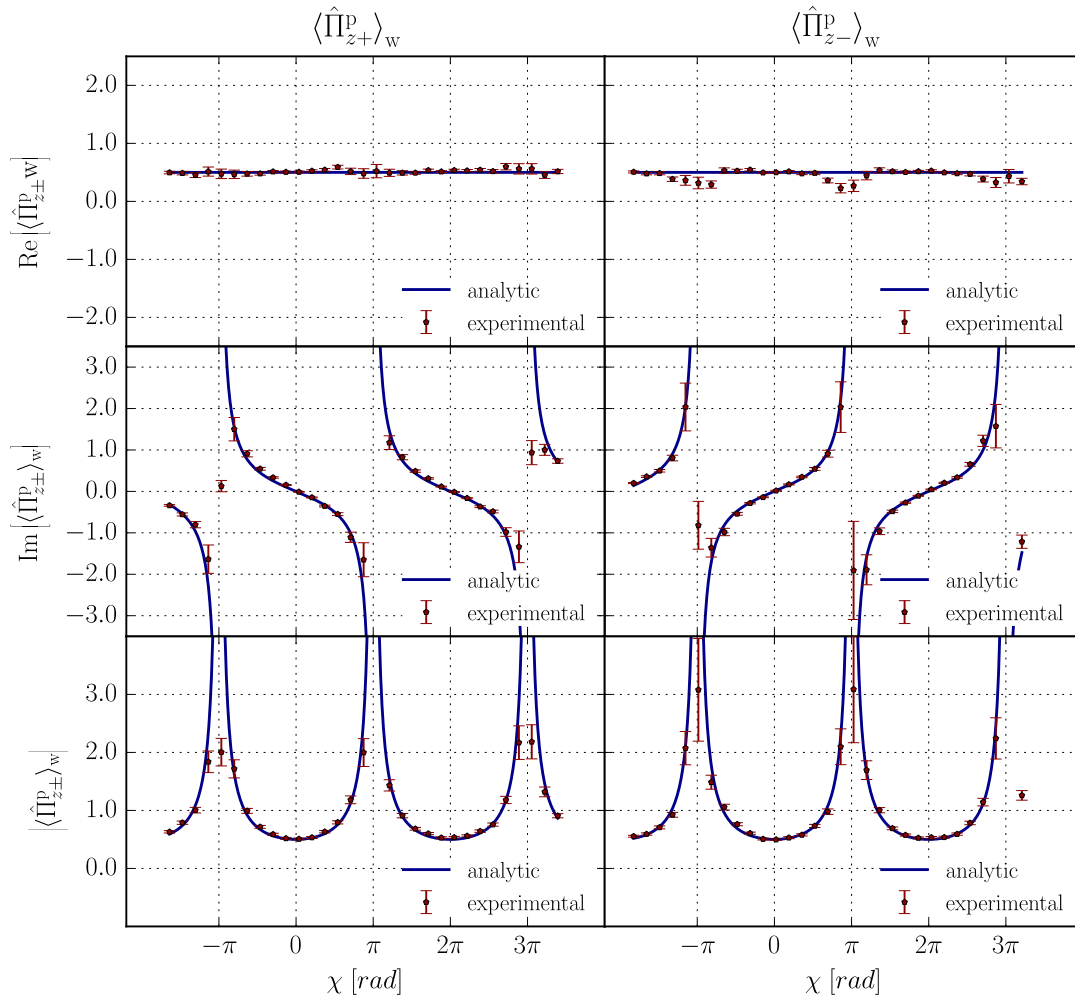


Figure 5.11: Measurement Results for $\langle \hat{\Pi}_{z\pm}^p \rangle_w$. Theoretical predictions (blue) and measurement results (red) for the projection operators' weak value. The error bars represent one standard deviation.

^cAn inaccuracy generated during the spin manipulation is more likely. If it were made during the postselection I_{y-} should show the same behavior also for path I .

observed. The real part of $\langle \hat{\Pi}_{z\pm}^p \rangle_w$ is expected to be constant one half. While the measurement very accurately produces this result for $\langle \hat{\Pi}_{z+}^p \rangle_w$, small deviations from the theoretical expectations are observed for $\langle \hat{\Pi}_{z-}^p \rangle_w$ for phase values close to odd multiples of π . This is because the average count rate of the recorded intensity I_{y-}^{II} is less than expected, as was already suggested above, manifesting itself in the weak value's real part being smaller than one would expect.

The imaginary part of $\langle \hat{\Pi}_{z\pm}^p \rangle_w$ is accurately determined for both paths, showing the opposite signs. Only for almost orthogonal pre and postselected states, deviations between the theoretical predictions and the measured values are observed.

The weak value's modulus is directly extracted from the data. Note that the minima in the theoretical curve are clearly resolved with only minimal deviation. The good results for $\left| \langle \hat{\Pi}_{z\pm}^p \rangle_w \right|$ are due to the large interaction strength of $\alpha = -180^\circ$, making it possible to resolve the second order effect precisely.

5.2.4 Summary and conclusion

The results presented in section 5.2.2 confirm the validity of the measurement protocol to fully determine a Pauli operator's weak value using arbitrary measurement strengths, which is established theoretically in chapter 3. It is tested in the weak and strong regime and a very good agreement between the experimental results and the theoretical prediction is observed. It has to be stressed that the measurement results show that it is possible to determine weak values without making any approximations due to neglected terms in a series expansion.

In section 5.2.3 the experiment is adapted so that the weak value of projection operators can be determined using maximum measurement strengths. Again the strong measurement protocol is successfully implemented and its validity is confirmed in the experiment.

One of the advantages of weak interactions in a measurement is, that the preselected state only gets minimally disturbed during the system evolution caused by the measurement process. This allows for example to validate counterfactual statements made by the ABL formula. Tuning the measurement strength to maximum invalidates this concept, because the strong measurement changes the probability of postselection [Brodtch and Cohen, 2016]. The strong measurement scheme is therefore not a suitable measurement protocol to investigate pre and postselection paradoxes. However, recent theoretical works suggest that the quantum state is ontic [Leifer, 2014]. Following that reasoning, the properties of a quantum state are elements of reality, which exist independently of any observer. Then if a quantum

system is successfully pre and postselection weak values of its observables also exists independently of the amount of disturbance introduced by the measurement. Consequently, for any experiment which has the sole purpose to determine the weak value of a pre and postselected system, strong interactions are favorable, since large experimental inaccuracies due to weak interactions can be avoided.

As with the measurements of the Pauli spin operator one might claim that determining weak value's of the neutron's path degree of freedom is a purely academic exercise without any practical use to it. However as the measurement protocol is completely general, its successful experimental realization makes an application in a wide range of quantum systems possible. Furthermore the experimental results can be used to perform a so called “direct” state characterization which will be subject of the following section.

5.3 “Direct” state characterization

In chapter 1 the concept of the so called direct state characterization is presented. In the following it will be shown how the measurement results obtained in section 5.2.2 can be used to perform a characterization of the neurons path state using both weak and strong interactions. Experimental evidence is given that strong interactions outperform weak ones for tomographic purposes in both accuracy and precision. The newly established method makes it possible to keep the experimental advantages of a state tomography via weak values without dealing with weak interactions. These results are also reported in [Denkmayr et al., 2016].

5.3.1 Characterizing the preselected path state via weak values

Here a short overview of the “direct” state characterization procedure for two-level quantum systems with special respect to the path system is presented.

Given a complete N -dimensional orthonormal basis, the preselected state vector $|\Psi_i\rangle$ of a quantum system can be written as

$$|\Psi_i\rangle = \sum_{a'} c_{a'} |a'\rangle, \quad (5.13)$$

with the basis states $|a'\rangle$, $|a''\rangle$, ... up to $|a^{(N)}\rangle$. The expansion coefficients $c_{a'}$ are the probability amplitudes of the state vector. They are given by,

$$c_{a'} = \langle a' | \Psi_i \rangle. \quad (5.14)$$

As an example we consider the neutron’s path degree of freedom. Its dimension is $N = 2$ with the basis given by $|a'\rangle = |P_z; +\rangle$ and $|a''\rangle = |P_z; -\rangle$. We set the neutron’s preselected path state to

$$|\Psi_i\rangle = \sum_{a'} c_{a'} |a'\rangle = c_{a'} |a'\rangle + c_{a''} |a''\rangle \equiv c_+ |P_z; +\rangle + c_- |P_z; -\rangle, \quad (5.15)$$

with probability amplitudes c_+ and c_- of to the eigenstates of path *I* and *II* respectively.

We now connect the weak value to the state vector of our quantum system. Let $|\Psi_f\rangle$ its postselected state. The weak value of a projection operator $\hat{\Pi}_{a'}$ on the state $|a'\rangle$ is then defined as

$$\langle \hat{\Pi}_{a'} \rangle_w = \frac{\langle \Psi_f | \hat{\Pi}_{a'} | \Psi_i \rangle}{\langle \Psi_f | \Psi_i \rangle} = \frac{\langle \Psi_f | a' \rangle \langle a' | \Psi_i \rangle}{\langle \Psi_f | \Psi_i \rangle}. \quad (5.16)$$

Using basic algebra we can rearrange Eq. (5.16) to

$$\langle a' | \Psi_i \rangle = \frac{\langle \Psi_f | \Psi_i \rangle}{\langle \Psi_f | a' \rangle} \langle \hat{\Pi}_{a'} \rangle_w \quad (5.17)$$

Comparing the relations given by Eq. (5.14) and (5.17) we see that the probability amplitude can be connected to the weak values of the projection operators. The system’s pre selected state vector is then given by

$$|\Psi_i\rangle = \sum_{a'} c_{a'} |a'\rangle = \frac{\langle \Psi_f | \Psi_i \rangle}{\langle \Psi_f | a' \rangle} \langle \hat{\Pi}_{a'} \rangle_w |a'\rangle + \frac{\langle \Psi_f | \Psi_i \rangle}{\langle \Psi_f | a'' \rangle} \langle \hat{\Pi}_{a''} \rangle_w |a''\rangle \quad (5.18)$$

Again considering the interferometer’s path, the projection operators given by $\hat{\Pi}_{z+}^p = |P_z; +\rangle \langle P_z; +|$ and $\hat{\Pi}_{z-}^p = |P_z; -\rangle \langle P_z; -|$ lead to

$$|\Psi_i\rangle = \frac{\langle \Psi_f | \Psi_i \rangle}{\langle \Psi_f | P_{z;+} \rangle} \langle \hat{\Pi}_{z+}^p \rangle_w |P_z; +\rangle + \frac{\langle \Psi_f | \Psi_i \rangle}{\langle \Psi_f | P_{z;-} \rangle} \langle \hat{\Pi}_{z-}^p \rangle_w |P_z; -\rangle. \quad (5.19)$$

The preselected state vector is directly proportional to the projection operator’s weak values. To fully characterize the initial state $|\Psi_i\rangle$, the prefactors $\frac{\langle \Psi_f | \Psi_i \rangle}{\langle \Psi_f | P_{z;+} \rangle}$ and $\frac{\langle \Psi_f | \Psi_i \rangle}{\langle \Psi_f | P_{z;-} \rangle}$ have to be determined as well. If the measurement of the weak value and the

post selection are mutually unbiased, they are identical [Wootters and Fields, 1989]. The z -basis of the path degree of freedom is mutually unbiased with respect to the x -basis [Salvail et al., 2013]. Therefore the preselected state vector given by Eq. (5.19) can be simplified to

$$|\Psi_i\rangle = \epsilon \left(\left\langle \hat{\Pi}_{z+}^p \right\rangle_w |P_z; +\rangle + \left\langle \hat{\Pi}_{z-}^p \right\rangle_w |P_z; -\rangle \right), \quad (5.20)$$

with $\epsilon \equiv \frac{\langle \Psi_f | \Psi_i \rangle}{\langle \Psi_f | P_z; + \rangle} = \frac{\langle \Psi_f | \Psi_i \rangle}{\langle \Psi_f | P_z; - \rangle}$. Finally the state vector needs to be normalized, i.e. $\langle \Psi_i | \Psi_i \rangle = 1$. This leads to

$$\begin{aligned} \langle \Psi_i | \Psi_i \rangle &= \epsilon^* \epsilon \left(\left\langle \hat{\Pi}_{z+}^p \right\rangle_w^* \left\langle \hat{\Pi}_{z+}^p \right\rangle_w + \left\langle \hat{\Pi}_{z-}^p \right\rangle_w^* \left\langle \hat{\Pi}_{z-}^p \right\rangle_w \right) = 1 \\ &= |\epsilon|^2 \left(\left| \left\langle \hat{\Pi}_{z+}^p \right\rangle_w \right|^2 + \left| \left\langle \hat{\Pi}_{z-}^p \right\rangle_w \right|^2 \right) = 1 \\ \Rightarrow \nu \equiv |\epsilon| &= \sqrt{\frac{1}{\left| \left\langle \hat{\Pi}_{z+}^p \right\rangle_w \right|^2 + \left| \left\langle \hat{\Pi}_{z-}^p \right\rangle_w \right|^2}} \end{aligned} \quad (5.21)$$

The neutron's preselected path state $|\Psi_i\rangle$ is directly proportional to quantities that can be accessed experimentally, namely through real and imaginary part as well as the modulus of the path projection operators' weak values. Furthermore, as has been successfully demonstrate by the experiments presented previously, we do not have to rely on weak measurements to determine $\langle \hat{\Pi}_{z\pm}^p \rangle_w$. We can perform measurements with arbitrary interaction strengths.

As was already mentioned above, a general preselected path state is given by Eq. (5.7). Using the method of equating the coefficients, one can relate the polar and azimuthal angle of Eq. (5.7) to the probability amplitudes c_+ and c_- of Eq. (5.15) by the relations

$$\rho = \arg(c_+) - \arg(c_-), \quad (5.22a)$$

$$\kappa = \arccos(|c_+|^2 - |c_-|^2). \quad (5.22b)$$

The probability amplitudes c_+ and c_- are directly related to the path projection operator's weak values and therefore to experimentally accessible quantities. Using the relations given by Eqs. (5.22a) and (5.22b) they can be linked to a general preselected path state making a “direct” state characterization possible.

5.3.2 Results

In section 5.2.2 the measurement results for the Pauli path operator’s weak value $\langle \hat{\sigma}_z^p \rangle_w$ are presented. The weak value is determined using weak and strong interaction. As was explained above, the measurement results of $\langle \hat{\sigma}_z^p \rangle_w$ can be used to reconstruct the preselected path state by a so-called “direct” state characterization. The results of such a characterization are shown in Fig. 5.12. The left column

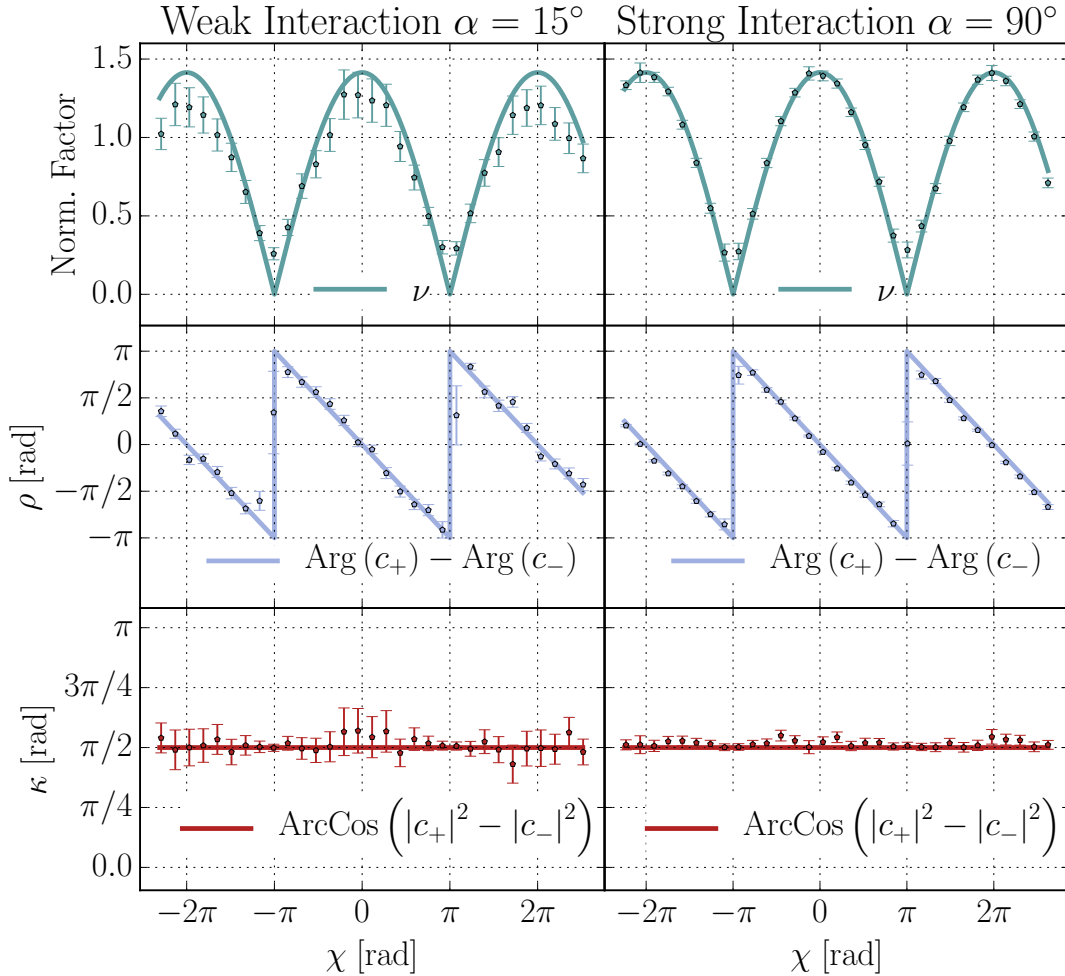


Figure 5.12: Results of the “direct” state characterization of the neutron’s path degree of freedom using weak ($\alpha = 15^\circ$) and strong interactions ($\alpha = 90^\circ$): The error bars show one standard deviation. The solid lines are the theoretical predictions

shows the results for weak interactions ($\alpha = 15^\circ$), the right one that for maximum strength interactions ($\alpha = 90^\circ$). In the upper two panels the state vector’s normalization factor ν is plotted. In the middle two panels the relative phase ρ between the path eigenstates is depicted. In the lower two panels the factor κ is shown, which

describes the relative weighting of the path eigenstates. The solid lines represent theoretical predictions based upon the adjustment of the experimental setup. For the final results the imperfect contrast of the interferometer is considered.

Both measurements are in good agreement with the theory. The normalization factor is expected to oscillate between zero and square root of two, showing a maximum for even multiples of π and a minimum for odd ones. The relative phase ρ between the two paths is expected to vary linearly between $-\pi$ and π with the phase introduced by the phase shifter. Again the reconstructed preselected state shows exactly this behavior. Finally the parameter κ , the relative weighting between the path eigenstates is expected to be constant, since the phase shifter only changes the preselected path state in the xy -plane of the Path Bloch sphere. The experiment fully confirms this theoretical prediction.

While both measurement approaches are in good agreement with the theoretical prediction, it is already visible to the naked eye that the strong interaction approach works better in terms of accuracy and precision. It is clearly visible that the error bars of the weak interaction approach are larger than those of the strong interaction one. Also looking at the upper two panels one can see that the experimental results are closer to the theoretical prediction for the strong interaction measurements.

Using the theoretical prediction and the measurement results we can make quantitative statements about the accuracy and the precision of both measurements. The precision is a measure of fluctuation and can be quantified by the root mean square statistical error $\bar{\sigma}$

$$\bar{\sigma} = \sqrt{\frac{1}{N} \sum_i^N |\sigma_i|^2}, \quad (5.23)$$

where σ_i are the standard deviations of each individual data point. The accuracy is a measure of the deviation from the theoretical prediction. The root mean square deviation $\bar{\Delta}$ can be defined as

$$\bar{\Delta} = \sqrt{\frac{1}{N} \sum_i^N |t_i - m_i|^2}, \quad (5.24)$$

where t_i is the theoretical prediction for each measurement point and m_i is the experimentally obtained value [Vallone and Dequal, 2016].

Using $\bar{\sigma}$ and $\bar{\Delta}$ a quantitative comparison between the weak and the strong interaction approach is performed. The values calculated from the results of our measure-

ment are listed in Table 5.1. The strong interaction approach performs significantly

Table 5.1: Quantitative comparison of precision $\bar{\sigma}$ and accuracy $\bar{\Delta}$ of the weak and the strong interaction approach. The strong interaction approach performs significantly better in terms of accuracy and precision.

Precision $\bar{\sigma}$			Accuracy $\bar{\Delta}$		
	Weak	Strong		Weak	Strong
ν	0.100	0.036	ν	0.152	0.062
θ	0.191	0.065	θ	0.100	0.067
ϕ	0.355	0.159	ϕ	0.860	0.580

better in terms of accuracy and precision. This shows that the statistical fluctuation and the deviation from the theoretical predictions is smaller for strong interactions measurements. It also gives experimental evidence that strong interactions outperform weak ones for tomographic purposes.

What has not been considered yet is the measurement time. While it took 540s to obtain one point of the weak interaction measurement, it took only 290s for one of the strong interaction measurement. This is mainly due to the fact that I_{x-}^w , i.e. the intensity for orthogonal pre and postselected spin states, is very close to zero in the weak interaction approach. Therefore it takes a long time to resolve it from the background. From the signal extent, we simply estimate the gain of equivalent measurement time by 3 for the strong interaction case.

In the publication [Gross et al., 2015] the merits of then direct state characterization method are critically evaluated in terms of novelty, efficacy and foundational significance. In terms of novelty and significance it is concluded that the direct state tomography (DST) “*adds very little to a tomographic framework based on random one-dimensional orthogonal projective measurements*”. The discussion of novelty and significance is of theoretical nature and not of prime importance to an experimentalist. From an experimental point of view it can be added that certain protocols may be easier to implement in an actual experiment than others given certain setup boundary conditions. Regarding efficacy it is found theoretically that the weakness of the interaction actually decreases the performance of the DST protocol and that stronger interactions are superior. In particular the information gain about the investigated system is very slow when weak measurements are used. Our experimental results fully support this statement. For the strong interaction approach significantly less measurement time was needed than for the weak interaction measurements.

5.4 Summary and perspective

In this chapter experiments determining the weak value's of path operators's is presented. In section 5.2.2 the measurement results of the Pauli path operator $\langle \hat{\sigma}_z^P \rangle_w$ are shown for both weak and strong interactions. Additionally in section 5.2.3 the weak value of the projection operators $\hat{\Pi}_{z\pm}$ on the path eigenstates is successfully performed. The measurement results are presented. The results of both sections give experimental confirmation that the weakness of a measurement is not a necessary condition to determine weak values.

Furthermore the measurement data of section 5.2.2 is used to perform a “direct” state characterization as is shown in section 5.3. Accuracy and precision of the strong and the weak interaction approach are quantitatively compared, showing that strong interactions outperform weak ones for both parameters.

The results presented in this chapter are not limited to the neutron and its degrees of freedom, because they are obtained using the measurement protocol of chapter 3, which is in fact general and can be applied to a wide range of two-level quantum systems.

It is interesting to note that the “direct” state characterization via weak values can be extended to mixed states also for strong interactions. It would be very interesting to test if the benefits of the strong interactions are also present for this case. Nevertheless, a mixed path state is difficult to grasp conceptually and also difficult to realize experimentally. It would therefore be advantageous to switch the roles of the spin and path once again, so that the neutron's path degree of freedom serves as a meter and the spin is the investigated system. Then one could generate for example a completely mixed spin state by removing the polarizing prisms. A partially mixed spin state would be generated by misaligning the prisms. This is easy to implement experimentally and offers a good repeatability.

CHAPTER 6

The quantum Cheshire cat effect

“Well! I’ve often seen a cat without a grin,” thought Alice; “but a grin without a cat! It’s the most curious thing I ever saw in my life!”

said Alice in Wonderland [Carroll, 1965]. Alice’s surprise stems from her experience that an object and its property cannot exist independently. It seems to be impossible to find a grin without a cat. However, the laws of quantum mechanics tell us that under very specific circumstances it is indeed possible to create a quantum ensemble that behaves as if it was spatially separated from one of its properties, a phenomenon which is strikingly analogous to the Cheshire Cat story and consequently named quantum Cheshire cat.

The so called quantum Cheshire Cat effect was proposed by Aharonov *et. al* [Aharonov and Rohrlich, 2008, Aharonov et al., 2013b] and has been experimentally demonstrated for the first time in 2014 using neutron interferometry [Denkmayr et al., 2014, Sponar et al., 2016]. In this chapter a brief review of the theoretical concept of the quantum Cheshire Cat is given. Subsequently the experimental results are presented. At the end possible future experiments are discussed.

6.1 Theory

Cats, being classical objects of our everyday world, are not well suited to perform quantum mechanical experiments. We therefore use a neutron passing through a Mach-Zehnder type interferometer. In the quantum Cheshire cat experiment the

cat is substituted by the neutron itself and the cat's grin is replaced by the neutrons z -spin component. It is now possible to create a pre and postselected quantum ensemble that behaves in average as if the neutron and its spin component are spatially separated. While the neutrons (the cat) take the upper beam path their spin components (the grin) travel along the lower one. An artistic depiction of this behavior is shown in Fig. 6.1. In order to create a quantum Cheshire cat the initial

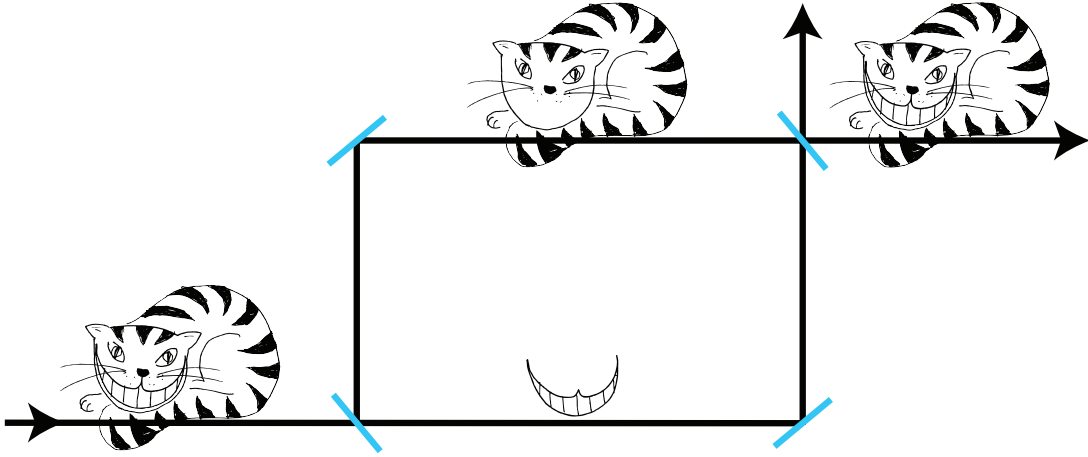


Figure 6.1: Artistic depiction of the quantum Cheshire Cat phenomenon. Figure courtesy of Leon Filter [Denkmayr et al., 2014].

state has to be preselected in a state is given by a superposition of the two path eigenstates with orthogonal spin states. The preselected state is then given by

$$|\Psi_i\rangle = \frac{1}{\sqrt{2}} (|P_z; +\rangle |S_x; +\rangle + |P_z; -\rangle |S_x; -\rangle). \quad (6.1)$$

The system's postselected state in turn is given by

$$|\Psi_f\rangle = \frac{1}{\sqrt{2}} (|P_z; +\rangle + |P_z; -\rangle) |S_x; -\rangle, \quad (6.2)$$

i.e. only particles with a spin aligned along the negative x -direction and leaving the interferometer in forward direction are considered. We now want to ask about the location of the neutron between pre- and postselection. For this we calculate the

weak values of the path projection operators $\hat{\Pi}_{z\pm}^P$. They are given by

$$\left\langle \hat{\Pi}_{z+}^P \right\rangle_w = \frac{\langle \Psi_f | \hat{\Pi}_{z+}^P | \Psi_i \rangle}{\langle \Psi_f | \Psi_i \rangle} = 0, \quad (6.3a)$$

$$\left\langle \hat{\Pi}_{z-}^P \right\rangle_w = \frac{\langle \Psi_f | \hat{\Pi}_{z-}^P | \Psi_i \rangle}{\langle \Psi_f | \Psi_i \rangle} = 1. \quad (6.3b)$$

The weak values of the projection operators tell us that any weak coupling to the path dependent part of the system's state vector will behave as if there were no neutrons travelling along path *I* but only along path *II*. Since $\hat{\Pi}_{z\pm}^P$ are dichotomic operators this result will also hold in the strong limit, because it can be shown that if the weak value of a dichotomic operator equals one of its eigenvalues, then the outcome of a strong measurement of the operator is that same eigenvalue with probability one [Aharonov and Vaidman, 1991].

To reveal the Cheshire cat we not only have to locate the particle itself but also its property: the spin's *z*-components. For this we have to calculate the weak values of the operator product $\hat{\sigma}_z^s \hat{\Pi}_{z\pm}^P$, i.e. the spin's *z*-components conditioned on the path. They are

$$\left\langle \hat{\sigma}_z^s \hat{\Pi}_{z+}^P \right\rangle_w = \frac{\langle \Psi_f | \hat{\sigma}_z^s \hat{\Pi}_{z+}^P | \Psi_i \rangle}{\langle \Psi_f | \Psi_i \rangle} = 1, \quad (6.4a)$$

$$\left\langle \hat{\sigma}_z^s \hat{\Pi}_{z-}^P \right\rangle_w = \frac{\langle \Psi_f | \hat{\sigma}_z^s \hat{\Pi}_{z-}^P | \Psi_i \rangle}{\langle \Psi_f | \Psi_i \rangle} = 0. \quad (6.4b)$$

This result tells us that in the weak regime any coupling to the neutrons spin's *z*-component is only effected on path *I* while there is no effect on path *II*. At the same time we found that a coupling to the spatial part of the wave function is only effective along path *II*. We can create a quantum ensemble that behaves in average as if it were separated from one of its properties: a quantum Cheshire cat emerges! A typical criticism of the argument presented above is that it is counterfactual since ideal successive quantum measurements in the interferometer are not feasible. They contradict with postselection. To overcome this kind of criticism weak measurements have to be used to reveal the quantum Cheshire cat. They can be performed simultaneously on the same ensemble since, at least in theory, they do not disturb each other. Also they do not prevent the ensemble from being successfully post-selected. Therefore, all the counterfactual statements can be verified weakly on the same ensemble. One has to bear in mind that weak values have a limitation

though: they can only make assertions about an ensemble average as is the case for the measurement of expectation values. They are not the outcome of individual (weak) measurements performed on individual particles. They are averages over many outcomes, of individual weak measurements on ensembles of equally prepared individual particles. Therefore weak values are only properties of an ensemble of measurement outcomes, not of individual measurement outcomes. Because of that one has to be careful with the statements one makes about the quantum Cheshire cat. Nevertheless, if a quantum system is successfully preselected in an the initial state given by Eq. (6.1) and postselected into the state given by Eq. (6.2), we can state, that it will in average behave as if the neutron and its spin z -component are travelling along different paths inside the interferometer.

6.2 Experiment

The experimental realization of the quantum Cheshire cat effect using neutron interferometry was performed during reactor cycle 169 in May 2013 at the interferometer beam line S18 at the research reactor of ILL. The experimental setup is almost identical to that presented in chapter 4. The only extension is the use of small absorbing foils. Since a detailed explanation of the adjustment procedure of this setup has already been given previously is not be repeated here. Figure 6.2 shows an artistic depiction of the experimental setup. The incident neutron spin state is prepared by a combination of the polarizing prisms and a DC coil. Inside the interferometer small coils in Helmholtz configuration in each beam path are used to probe the location of the neutron spin components. In comparison to the setup used to measure the spin weak values, the Cheshire cat setup additionally uses indium foils which are weak absorbers to probe the neutron's location inside the interferometer. The phase shifter inserted into the setup is used to tune the relative phase between the two path eigenstates. A general postselected path state is given by

$$|P_f\rangle = \frac{1}{\sqrt{2}} (|P_z; +\rangle + e^{i\chi} |P_z; -\rangle). \quad (6.5)$$

In the experiment of the quantum Cheshire cat effect, only the postselected state $|P_f\rangle = |P_x; +\rangle$ ($\chi = 0$) is of interest. However it would be very difficult experimentally to set and keep the phase shifter to this exact position. Instead phase shifter scans are performed. The intensity for $\chi = 0$ is extracted from least square fits to the data and is used to directly determine the weak values of interest. The spin postselection is performed by a combination of a DC coil mounted on a translation

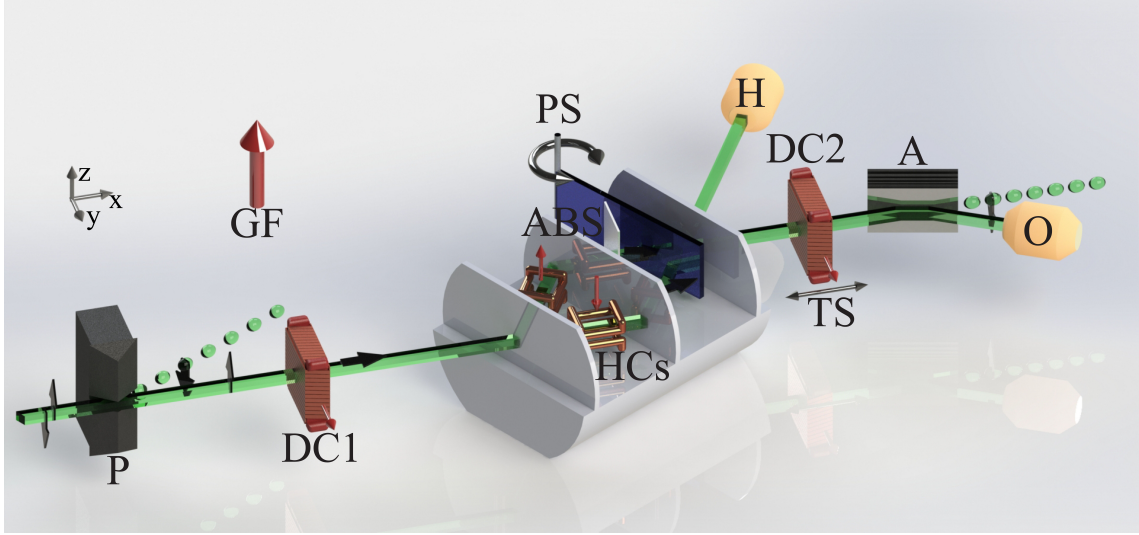


Figure 6.2: Artistic depiction of the experimental setup: The neutron beam passes polarizing magnetic prisms (P). To prevent depolarization a magnetic guide field (GF) is applied around the whole setup. Before the neutrons enter the interferometer a DC coil (DC1) prepares the initial spin state $|S_i\rangle$. At the interferometer's first plate the neutron beam gets separated into path *I* and *II*, preparing $|P_i\rangle$ and thereby completing the preselection process. In each beam path small coils in Helmholtz configuration (HCs) make it possible to manipulation the neutron spin in the xy -plane. They can be used to probe for the spin's location. The phase shifter (PS) tunes the relative phase χ between *I* and *II* and selects the state $|P_f\rangle$. Weak absorbers can be inserted into the interferometer's paths to probe the neutron's location. The postselection on the state $|S_f\rangle$ is performed using the second DC coil (DC2) on a translation stage (TS) in combination with a CoTi supermirror analyzer (A). Of the two outgoing beams from the interferometer, only the O-beam is spin analyzed (O). Both detectors (O & H) are ^3He counter tubes.

stage and a CoTi supermirror analyzer as has already been described several times in previous sections.

6.2.1 Probing the location of the neutrons

To reveal the quantum Cheshire cat, first the location of the neutron inside the interferometer is probed. This is done by performing a phase shifter scan of the empty interferometer with no interaction between pre and postselection to establish a reference. The initial state is given by Eq. (6.1). This is a fully entangled state with orthogonal spin states in path *I* and *II*. Full which-way information can be revealed and thus no interference is observed [Englert, 1996, Banaszek et al., 2013]. Subsequently a 0.25 mm thick Indium foil is put into the interferometer. The transmissivity of the foil is $T = 0.79(1)$. When the foil is put in the lower beam path

(path *I*), no significant drop in intensity is observed, as compared to the reference intensity. In the third measurement the absorber is taken out of the lower beam path and put into the upper one (path *II*). Now the observed intensity drops to about 80% of the reference intensity. The measurement results are depicted in Fig. 6.3. The absorber interacts with the spatial part of the neutron's wave func-

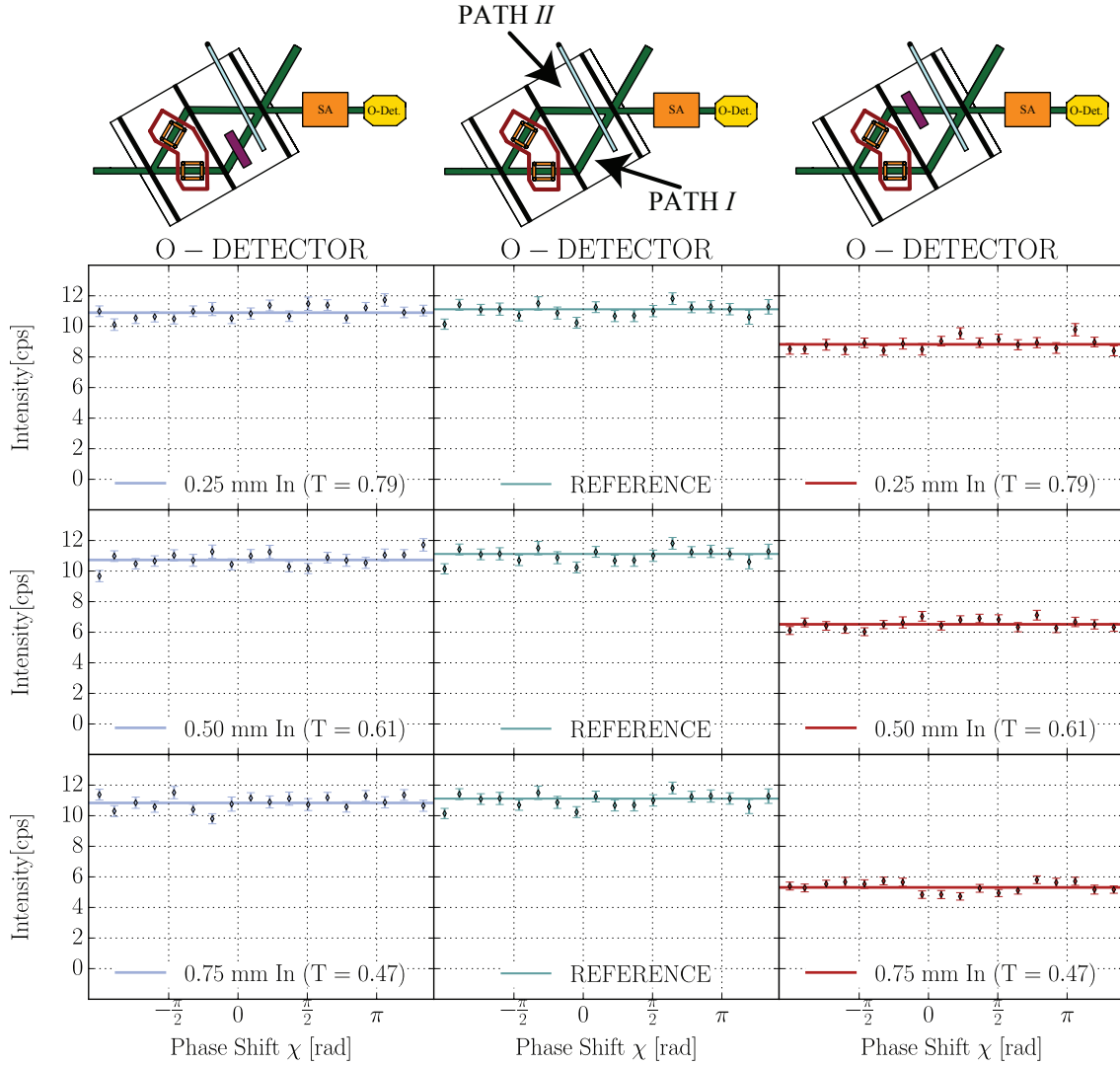


Figure 6.3: Results of the path measurement: The middle panels depicts a reference measurement with no interaction between pre and postselection. When the absorbers are put into the lower beam path no significant change in count rate can be observed (left panels). In contrast to that the count rate drops according to the transmissivity of the absorbers, when they are put into the upper beam path (right panels). Error bars represent one standard deviation. The lines represent minimizing χ^2 -fits to the data.

tion. As one would expect when looking at the weak values, the absorber influences the obtained intensity pattern only when it is put into the upper beam path and none when it is put in the lower one. Furthermore the theorem about weak values

of dichotomic operators presented above applies to the path projection operators. Because of that the same result is also expected for strong absorptions, i.e. $T=0$. To test stronger absorptions the same measurement is repeated with 0.5 mm and 0.75 mm thick Indium foils. Those absorbers have a transmission of $T = 0.61(1)$ and $T = 0.47(1)$ respectively. Again the same effect is observed. The absorbers do not influence the obtained intensity pattern when they are put into path I , but the count rate reduces to $\sim 59\%$ and $\sim 48\%$ of the reference intensity (obtained without absorbers) respectively, if they are put into path II . The measurement results for stronger absorptions are also depicted in Fig. 6.3. From the absorber measurement results we can conclude that the neutrons travel along the upper beam path of the interferometer.

Note that the observed behavior is solely due to the spin postselection. This can be easily recognized when looking at the H-detector interference fringes obtained during the absorber measurement, which are depicted in Fig.6.4. The H-detector is not spin analyzed. Hence the particles detected there do not get spin postselected. When an absorber is put in either one of the beams the intensity decreases and no path dependency of the absorption is observed.

6.2.2 Probing the location of the neutrons' spin component

To probe the location of the neutrons' spin component small magnetic fields pointing in the z -direction are applied in either one of the beam paths. The magnetic field cause a spin rotation, which allows us to check for a magnetic moment (the neutrons' spin component). If there is a magnetic moment present in one of the interferometer's arms then the externally applied magnetic field should have an effect on it. If there is no spin component present the applied field should not have any effect.

In the experiment the field strength is set so that it is equivalent to a spin rotation of $\alpha = 20^\circ$. Again first a reference measurement with no spin rotation at all is performed. Then the magnetic field is applied in the upper beam path. Since $\langle \hat{\sigma}_z^s \hat{\Pi}_{z-}^p \rangle_w = 0$, we expect nothing to happen. Finally the a magnetic field with the same magnitude is applied in the lower beam path. The results of such a measurement is depicted in Fig. 6.5. The results are what one would expect from the weak value calculation. When no magnetic field is applied between pre and postselection, a flat intensity without a sinusoidal pattern is recorded. When a magnetic field is applied to the lower beam path an interference fringe with $\sim 30\%$ contrast appears. Obviously a magnetic moment is present in the lower beam path, because otherwise

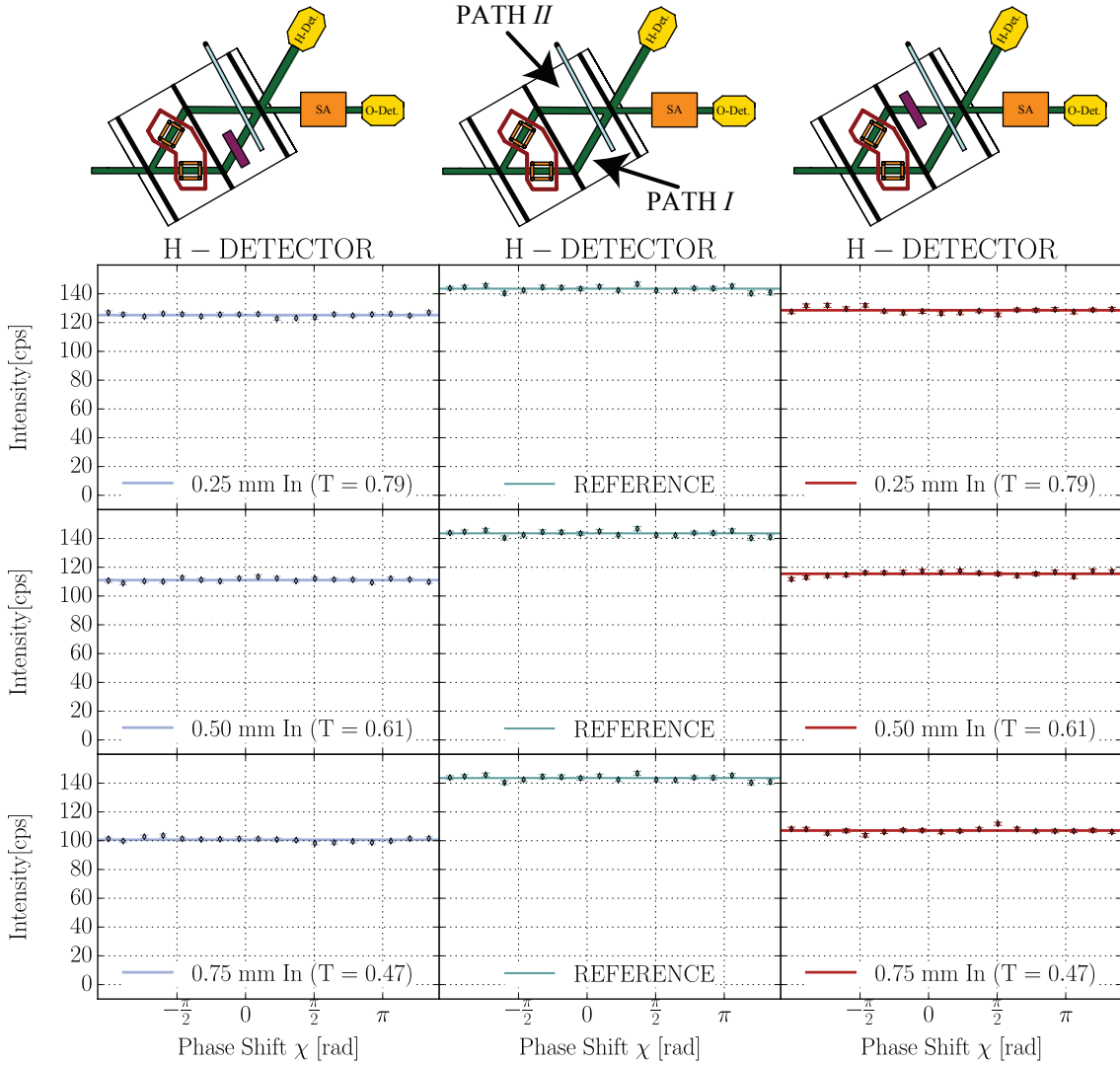


Figure 6.4: Results of the path measurement at the H-detector: The reference measurement shows no interference pattern, also for the H-detector, because of the orthogonal spin states inside the interferometer (middle panel). When an absorber is put in either one of the beam paths the observed intensity decreases. Error bars represent one standard deviation. The lines represent minimizing χ^2 -fits to the data.

the magnetic field would not have any effect. If the same magnetic field is now applied to the upper beam path no significant change in the interference fringes is observed. There is a very tiny oscillation with $\sim 4\%$ contrast, due to imperfections in the experimental apparatus, but this is negligibly small.

From the absorber measurement and the measurements with the magnetic field, we conclude that the absorber is only effective when it is put in the upper beam path. At the same time a magnetic field has only an effect on the measurement results when it is applied in the lower beam path and vice versa. Using pre and postselec-

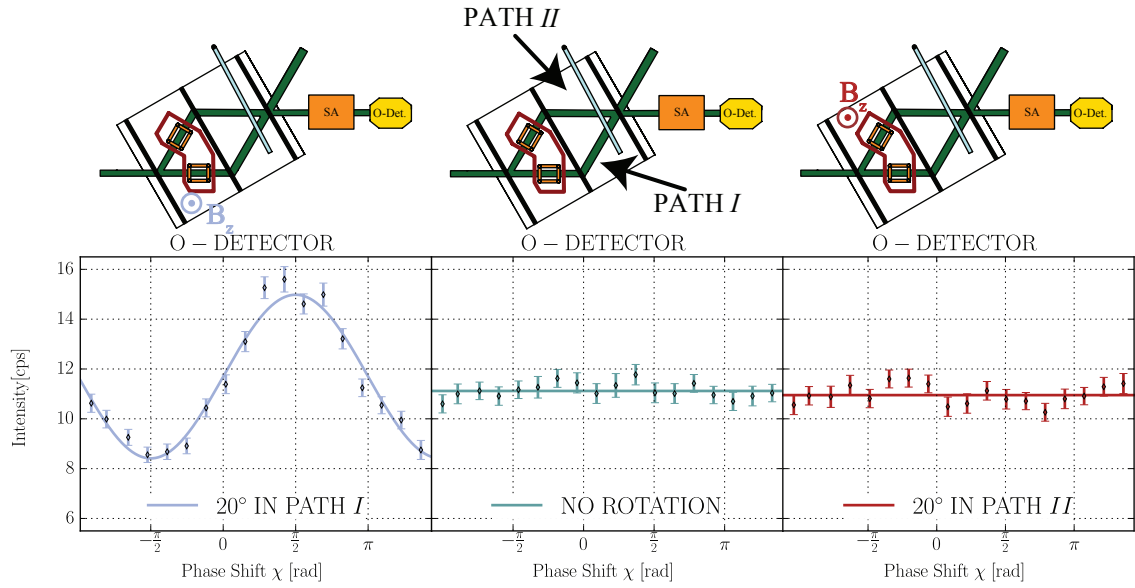


Figure 6.5: Result of the spin measurement at the O-Detector: First a reference measurement without any spin rotation is performed, which shows no contrast due to orthogonal spin states inside the interferometer (middle panel). If a magnetic field is applied in the lower beam path a sinusoidal interference fringe appears (left panel). If the same magnetic field is applied at the upper beam path no significant change in the recorded intensity is detected (right panel). Error bars represent one standard deviation. The lines represent minimizing χ^2 -fits to the data.

tion we have created a quantum system that behaves in average as if a particle (the neutron) and one of its properties (the spin z -component) are spatially separated: the quantum Cheshire cat is revealed!

To confirm the fact that the quantum Cheshire cat is really an effect of postselection, the the H-detector's intensity modulation is studied once again. In our experiment only the O-detector is spin analyzed. Figure 6.6 shows the H-detector interferograms of the same measurements as in Fig. 6.5. Since the H-detector is not spin analyzed, the neutrons detected there are not postselected and therefore the behavior of the interference fringes is different. For the reference measurement no modulation emerges like at the O-detector, since this is due to the orthogonality of the spin states inside the interferometer and not an effect of postselection. If a magnetic field is applied in either of the beam paths an interference pattern with a contrast in the same order of magnitude appears and the Cheshire cat effect, i.e. the spin travels only along one path, is not observed. The H-detector can be used as a monitor for phase fluctuations and count rate normalization.

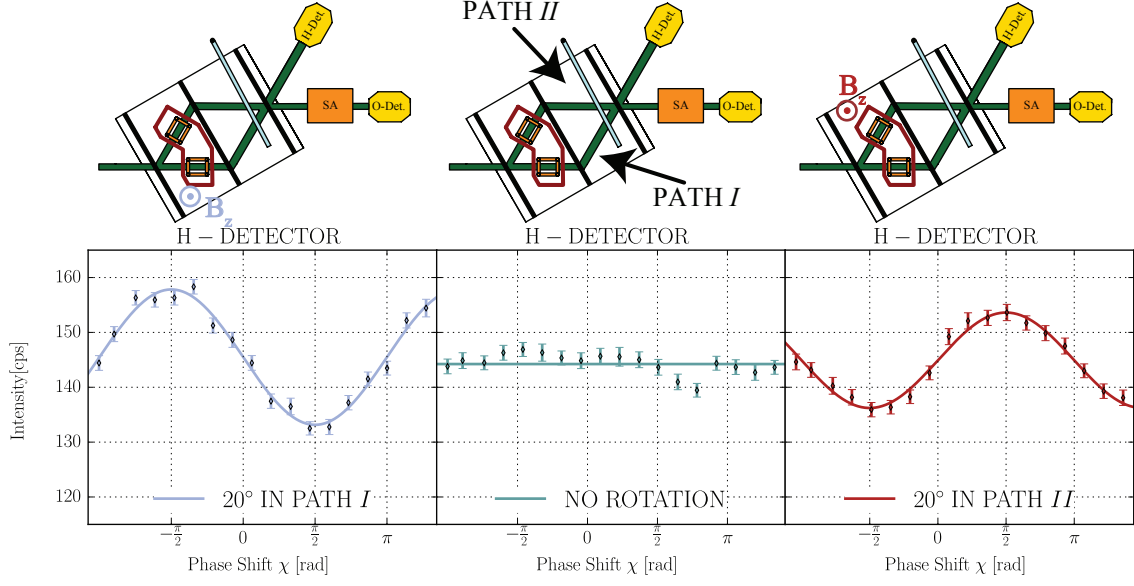


Figure 6.6: Result of the spin measurement at the H-Detector: The reference measurement shows no interference pattern, also for the H-detector, because of the orthogonal spin states inside the interferometer (middle panel). When a magnetic field is applied in either one of the beam paths, sinusoidal interference fringes appear for both. Error bars represent one standard deviation. The lines represent minimizing χ^2 -fits to the data.

6.2.3 Quantifying the results

Using the fits to the obtained data, weak values are extracted for the measurement result.

The measurement of $\langle \hat{\Pi}_{z\pm}^p \rangle_w$ is performed using indium foils with a high transmissivity. As was already explained in chapter 2, an absorption is described by an imaginary potential. Conditioned on the respective path eigenstate it is given by

$$\hat{V}_{z\pm} = -i\mu_{z\pm}(r)\hat{\Pi}_{z\pm}^p, \quad (6.6)$$

where the absorption coefficient is given by $M_{z\pm} = \int \mu_{z\pm}(r)dr$ for the respective path eigenstate with r being integrated on the absorber's thickness. For $M_{z\pm} \ll 1$ the absorption coefficient can be related to the transmissivity $T_{z\pm}$ through $M_{z\pm} \approx 1 - \sqrt{T_{z\pm}}$. After the interaction with the absorber the evolved state vector is given by

$$|\Psi'\rangle = e^{-i \int dr \hat{V}_{z\pm}} |\Psi_i\rangle \approx \left[1 - M_{z\pm} \hat{\Pi}_{z\pm}^p + \dots \right] |\Psi_i\rangle \quad (6.7)$$

Using the definition of the path projectors' weak value the obtained intensity after postselection is given by

$$I_{z\pm}^{\text{ABS}} = |\langle \Psi_f | \Psi_i \rangle|^2 \left[1 - 2M_j \langle \hat{\Pi}_{z\pm}^p \rangle_w \right]. \quad (6.8)$$

The above calculation assumes that a possible contribution from an imaginary part of $\langle \hat{\Pi}_{z\pm} \rangle_w$ can be neglected. This requires that the pre and postselected state are prepared correctly in the experiment. A deviation from the ideal initial and final state in any direction on the Bloch sphere, would manifest itself in the appearance of intensity modulations during the reference measurements. Since in the experiment the average contrast of the reference measurements was below 3%, it is reasonable to assume that the ensemble is pre and postselected in the correct states, namely in those given by Eqs. (6.1) and (6.2). Since $I^{\text{REF}} = |\langle \Psi_f | \Psi_i \rangle|^2$, the weak values can be extracted from the observation of $I_{z\pm}^{\text{ABS}}/I^{\text{REF}}$, i.e. from the recorded intensity with absorbers present in the interferometer and from the reference measurement.

The weak values of $\hat{\sigma}_z^s \hat{\Pi}_{z\pm}^p$ are determined using path conditioned spin rotations. To determine $\langle \hat{\sigma}_z^s \hat{\Pi}_{z\pm}^p \rangle_w$, a small magnetic field is applied in either path *I* or *II*. The interaction Hamiltonian for this measurement is

$$\hat{H}_{z\pm} = -\vec{\mu} \cdot \vec{B} \hat{\Pi}_{z\pm}^p \quad (6.9)$$

where $\vec{\mu}$ is the neutron's moment and $\vec{B} = (0, 0, B_z)$ is an externally applied magnetic field. As in interaction Hamiltonians of previous experiments $\hat{\Pi}_{z\pm}$ denotes the fact that the magnetic field is applied only along one of the paths. The effect of the interaction Hamiltonian upon the initial state of the composite system is given by

$$|\Psi'\rangle = e^{-i \int dt \hat{H}_{z\pm}} |\Psi_i\rangle = e^{i\alpha \hat{\sigma}_z^s \hat{\Pi}_{z\pm}^p / 2} |\Psi_i\rangle \approx \left[1 + \frac{i\alpha}{2} \hat{\sigma}_z^s \hat{\Pi}_{z\pm}^p + \dots \right] |\Psi_i\rangle. \quad (6.10)$$

Taking the interaction parameter into account up to α^2 , the intensity after postselection is given by

$$I_{z\pm}^{\text{MAG}} = |\langle \Psi_f | \Psi' \rangle|^2 = |\langle \Psi_f | \Psi_i \rangle|^2 - \frac{\alpha^2}{4} \langle \Psi_f | \hat{\Pi}_{z\pm}^p | \Psi_i \rangle \langle \Psi_i | \Psi_f \rangle + \frac{\alpha^2}{4} \left| \langle \Psi_f | \hat{\sigma}_z^s \hat{\Pi}_{z\pm}^p | \Psi_i \rangle \right|^2, \quad (6.11)$$

Again it is assumed that a possible contribution from any imaginary part can be neglected. Again this is justified by the average maximal contrast of the empty

interferometer and we get

$$I_{z\pm}^{\text{MAG}} = |\langle \Psi_f | \Psi_i \rangle|^2 \left[1 - \frac{\alpha^2}{4} \langle \hat{\Pi}_{z\pm}^{\text{P}} \rangle_{\text{w}} + \frac{\alpha^2}{4} \left| \langle \hat{\sigma}_z^{\text{s}} \hat{\Pi}_{z\pm}^{\text{P}} \rangle_{\text{w}} \right|^2 \right] \quad (6.12)$$

The weak values of $\hat{\Pi}_{z\pm}^{\text{P}}$ are known from the absorber measurements and because $I^{\text{REF}} = |\langle \Psi_f | \Psi_i \rangle|^2$ the weak values are extracted from the measurements of the intensities with the magnetic field applied along path *I* and applied along path *II* as well as with the magnetic field turned off (for further details see also [Denkmayr, 2013] and “Methods” in [Denkmayr et al., 2014]).

Due to experimental limitations the weak values are not determined by coupling spin and path to a meter system. Only the absolute square of the joint weak value $\langle \hat{\sigma}_z^{\text{s}} \hat{\Pi}_{z\pm}^{\text{P}} \rangle_{\text{w}}$ is determined. For the given pre and postselected states in the Cheshire cat experiment, the weak values for any operator of interest are either one or zero per definition and because of that the absolute square of the weak values will equal the weak value itself. Since we know from the reference measurements that the states are correctly pre and postselected, it is reasonable to assume that the absolute square of the weak values will equal the weak value itself also in the experiment. The intensities $I_{z\pm}^{\text{ABS}}$, $I_{z\pm}^{\text{MAG}}$ and $I_{z\pm}^{\text{REF}}$ are extracted from the fits to the data. The final results are given by: $I^{\text{REF}} = 11.25(5)$, $I_{z+}^{\text{ABS}} = 10.90(9)$, $I_{z-}^{\text{ABS}} = 8.83(8)$, $I_{z+}^{\text{MAG}} = 11.57(6)$ and $I_{z-}^{\text{MAG}} = 10.93(6)$ (all in counts per second)^a. Using these intensities the weak values are determined. The results are listed in Table 6.1.

Table 6.1: Results for the weak value determination in the Cheshire Cat experiment:

	Path <i>I</i>	Path <i>II</i>
$\langle \hat{\Pi}_{z\pm}^{\text{P}} \rangle_{\text{w}}$	0.14 ± 0.04	0.96 ± 0.06
$\left \langle \hat{\sigma}_z^{\text{s}} \hat{\Pi}_{z\pm}^{\text{P}} \rangle_{\text{w}} \right ^2$	1.07 ± 0.25	0.02 ± 0.24

The theoretically predicted results for the weak values are $\langle \hat{\Pi}_{z+}^{\text{P}} \rangle_{\text{w}} = 0$ and $\langle \hat{\Pi}_{z-}^{\text{P}} \rangle_{\text{w}} = 1$, as well as $\left| \langle \hat{\sigma}_z^{\text{s}} \hat{\Pi}_{z+}^{\text{P}} \rangle_{\text{w}} \right|^2 = 1$ and $\left| \langle \hat{\sigma}_z^{\text{s}} \hat{\Pi}_{z-}^{\text{P}} \rangle_{\text{w}} \right|^2 = 0$. Also the path projection operators must sum up to unity. The experiment confirms the predictions within the errors of the measurement. The observed deviations from the theoretically predicted values is due to imperfections in the setup, such as misalignments during the spin manipulation and a degree of polarization below one.

^aThese intensities are the average of all performed measurements.

6.2.4 Discussion

There are several important points that have to be kept in mind concerning the quantum Cheshire cat effect. Most importantly it has to be stressed that everything all arguments presented so far are within standard quantum mechanics. The weak values and the prediction made by them do not violate quantum mechanics. All calculations followed from standard quantum mechanics and the only the way to interpret the obtained results is open to debate.

The weak values are a powerful tool that give an heuristic insight into the dynamical behavior between pre and postselected quantum ensembles [Popescu, 2010]. Since $\langle \hat{\Pi}_{z+}^p \rangle_w = 0$ and $\langle \hat{\Pi}_{z-}^p \rangle_w = 1$ one expects that a coupling to the neutron itself will only be effective along path *II*. Because of $\langle \hat{\sigma}_z^s \hat{\Pi}_{z+}^p \rangle_w = 1$ and $\langle \hat{\sigma}_z^s \hat{\Pi}_{z-}^p \rangle_w = 0$, a coupling to the spin component should only show an effect along path *I*. This is exactly the behavior observed in the experiment. The weak values give a simple prediction, which is found to be correct.

To gain a deeper understanding of the experiment, one can now think of the reason why the system behaves the way it does following the evolution of the system in the interferometer. Inside the interferometer the spin is aligned along the positive *x*-direction in path *I* and aligned along the negative one along path *II*. The spin postselection only lets particles with a spin aligned along the negative *x*-direction pass to the detector. This is the reason why the absorber has no effect in path *I*. It only takes away neutrons that would never pass through the postselection anyways. The behavior of the system under the influence of the magnetic field is more subtle to understand. The magnetic field minimally alters the spin state inside the interferometer so that a part in the systems wave function is created that can show interference. But again the spin postselection has to be considered: If the spin manipulation is performed along path *I*, the $|S_x; +\rangle$ state will be turned away from orthogonality towards the spin postselection direction. Thus a certain part contributing interference will be able to pass postselection. Therefore we see an interference fringe arising. If a magnetic field is applied along path *II* the spin state $|S_x; -\rangle$ is altered, with the spin actually turning away from the postselection direction and any part created which would contribute interference cannot pass the spin postselection. Therefore no interference fringes appear if a magnetic field is applied along the upper beam path. If the postselection direction is changed from $|S_x; +\rangle$ to $|S_x; -\rangle$ the role of the paths switches. In that case the system will behave as if neutrons were travelling along path *II*, while their spin moves along path *I*. It is also interesting to note that the effect of the spin rotation on the recorded

intensity scales with $\sin(\alpha/2)$ in path *I* and with $\cos(\alpha/2)$ in path *II*. Also the operators $\langle \hat{\sigma}_z^s \hat{\Pi}_{z\pm}^p \rangle_w$ are not dichotomic, so that they can only be evaluated weakly. If one would turn the neutron spin by $\alpha = 90^\circ$ along the upper beam path one would see the intensity drop to zero.

We see that the experiment has a perfectly simple explanation in terms of standard quantum interference. However it is long winded and not very intuitive. At the same time the weak values give a quick and easy to understanding of the phenomena in the experiment.

6.3 Summary and perspective

Investigating a spin/path pre and postselected ensemble in a neutron interferometer made it possible to observe the quantum Cheshire cat effect proposed by Aharonov *et al.*. Using absorbers and magnetic fields it has been shown that the system behaves as if the neutrons and their property took a different path through the interferometer. If an absorbing foil is inserted into the lower beam path it shows no effect on the recorded intensity. At the same time a weak magnetic field shows only an effect at the lower beam path while it has none in the upper one. This is exactly what one expects from the theoretical predictions. While the experiment can be understood in terms of simple quantum interference the weak values give an easier understanding of what is happening in the experiment.

The experimental realization of the Cheshire cat effect published in [Denkmayr et al., 2014] was the first of its kind and therefore received a lot of coverage in the media and popular science magazines (see e.g. [Ananthaswamy, 2014] and [Lemmel, 2014]). There has also been a lot of interest from the scientific community, which lead to the observation of the Cheshire cat effect in other systems [Atherton et al., 2015, Ashby et al., 2016]. In addition the experiment has been reconstructed by event to event simulations [Michielsen et al., 2015].

There are also several possible future experiments that would be very interesting to perform: In the first version of the Cheshire cat experiment the weak values were not determined by coupling the system to an external meter. So it would be interesting to extend the measurement protocol established in chapter 3 to three degrees of freedom and then to perform the experiment. For this either the neutron's energy degree of freedom [Sponar et al., 2008] or the recently demonstrated angular momentum degree of freedom [Clark et al., 2015] could be used.

As a next step the scheme can then be extended to measure the observable simul-

taneously, i.e. one would need to measure the four pairs $\langle \hat{\Pi}_{z+}^P \rangle_w$ and $\langle \hat{\sigma}_z^s \hat{\Pi}_{z+}^P \rangle_w$, $\langle \hat{\Pi}_{z+}^P \rangle_w$ and $\langle \hat{\sigma}_z^s \hat{\Pi}_{z-}^P \rangle_w$, $\langle \hat{\Pi}_{z-}^P \rangle_w$ and $\langle \hat{\sigma}_z^s \hat{\Pi}_{z+}^P \rangle_w$, as well as $\langle \hat{\Pi}_{z-}^P \rangle_w$ and $\langle \hat{\sigma}_z^s \hat{\Pi}_{z-}^P \rangle_w$. To perform the simultaneous weak measurements the neutrons energy degree of freedom is a promising choice. One could put a small RF spin turner in each beam path and perform time resolved measurements (see also the dissertation project of H. Geppert). A qualitative analysis of the effect could then be done by analyzing the Fourier transform of the time resolved signal. To give a quantitative description using weak values the mathematical formalism developed in chapter 3 would have to be adopted.

In the Cheshire cat experiment only one spin component is regarded, but there is also an experimental proposal in which all spin components are seemingly separated from a particle [Guryanova et al., 2012, Aharonov et al., 2013a]. In the original proposal the state vector of an entangled system is regarded. This is not a feasible approach for neutron interferometry since sources of entangled neutron pairs are not available. A similar state vector, but in a mixture form, can also be created if the DC coils, which pre and postselect the spin coils are switched rapidly between the states $|S_x; \pm\rangle$. The switching would have to be faster than the detector resolution (above 10 kHz) for the experiment to work.

In a recent proposal extends the Cheshire cat effect to a dynamical situation [Aharonov et al., 2015]. While the gedankenexperiment presented therein is also not feasible using the technique of neutron interferometry, it might be possible to extend the experimental scheme of [Schuster et al., 1990] to investigate the a dynamical Cheshire cat.

Finally it would be interesting to perform a delayed choice version of the quantum Cheshire cat experiment. This would open up the possibility of investigating the so called two-state vector formalism of quantum mechanics.

CHAPTER 7

Conclusion and outlook

In this thesis weak values and weak measurements have been studied in neutron optical experiments:

In chapter 3 several measurement schemes are derived which make it possible to fully determine the weak value of either Pauli or projection operators using a coupling between two two-level quantum systems. It is shown that weakness is not a necessary condition to determine weak values. An intuitive geometric picture of the physical content of weak value derivation is developed.

In chapter 4 various experimental implementations of the previously derived measurement scheme are described. The results of the weak value determination of the Pauli spin operator $\hat{\sigma}_z^s$ for one preselected and many different postselected states are shown. The newly established experimental technique is used to generate ensembles with a purely imaginary weak value. The results are used to show the quantum pigeon hole effect.

In chapter 5 the results of a neutron interferometric experiment is presented in which the weak value the Pauli operator $\hat{\sigma}_z^p$ for the path degree of freedom in a Mach-Zehnder interferometer is fully determined using both weak and strong interactions. The results are used to reconstruct the neutron's preselected path state using the "direct" state tomography method. A quantitative comparison for weak and strong interactions is performed and experimental evidence is given that strong interactions outperform weak ones in terms of accuracy and precision. Additionally the measurement results for the weak values of path projection operators $\langle \hat{\Pi}_{z\pm}^p \rangle_w$ are presented. They are obtained by slightly altering the experimental scheme so

that $\langle \hat{\Pi}_{z\pm}^p \rangle_w$ are determined using maximum measurement strengths.

Chapter 6 shows the results of the experimental investigation of the so called quantum Cheshire cat effect. A pre and postselected ensemble is created, which behaves in average as if the neutron and one of its properties (the spin z -component) are spatially separated inside the interferometer. To quantify the behavior of the system, weak values are utilized.

At the time of their performance, the experiments presented in this thesis were the first of their kind using massive particles. The newly developed experimental technique described here opens a window into previously unexplored realms of the study of quantum mechanics foundations: The experimental schemes presented in chapters 4 and 5 can be combined to perform a “direct” state characterization of mixed states. For such an experiment the neutron spin degree of freedom would be the system under investigation and the neutrons path degree of freedom would serve as a meter system. The (partially) mixed spin states can be created by intentionally misaligning the polarizing prisms in the interferometric setup.

It would also be of great interest to extend the measurement protocol of chapter 3 including additional meters, so that more complicated weak measurements can be performed. While this seems quite easy to do on paper, the actual experimental implementation will be the far more tricky part. Possible candidates for additional meters are the neutron orbital angular momentum and the neutron energy.

Concerning the quantum Cheshire cat effect it would be interesting to “simultaneously” measure the location of the neutrons and their spin components. This would require two additional meters. Also the observation of a complete Cheshire cat is still lacking, which will be an interesting future experimental challenge.

Implementing additional meter systems in the experiment will also make the simultaneous determination of several weak values of quantum systems other than of the Cheshire cat possible. While for positive operator valued measures (POVM) considerable disturbance is unavoidable, weak measurements are a new way to investigate quantum systems. In their realm the study of dynamical and complementary properties of quantum systems is possible. The ultimate goal of our studies is to reach new possibilities to get to know and to control quantum systems.

Bibliography

- [Abele, 2008] Abele, H. (2008). The neutron. its properties and basic interactions. *Progress in Particle and Nuclear Physics*, 60(1):1 – 81.
- [Aharonov et al., 1988] Aharonov, Y., Albert, D. Z., and Vaidman, L. (1988). How the result of a measurement of a component of the spin of a spin-1/2 particle can turn out to be 100. *Physical review letters*, 60(14):1351.
- [Aharonov et al., 1964] Aharonov, Y., Bergmann, P. G., and Lebowitz, J. L. (1964). Time symmetry in the quantum process of measurement. *Physical Review*, 134(6B):B1410.
- [Aharonov et al., 2002] Aharonov, Y., Botero, A., Popescu, S., Reznik, B., and Tollaksen, J. (2002). Revisiting hardy’s paradox: counterfactual statements, real measurements, entanglement and weak values. *Physics Letters A*, 301(3–4):130 – 138.
- [Aharonov et al., 2015] Aharonov, Y., Cohen, E., and Popescu, S. (2015). A current of the cheshire cat’s smile: Dynamical analysis of weak values. *arXiv preprint arXiv:1510.03087*.
- [Aharonov et al., 2016] Aharonov, Y., Colombo, F., Popescu, S., Sabadini, I., Struppa, D. C., and Tollaksen, J. (2016). Quantum violation of the pigeonhole principle and the nature of quantum correlations. *Proceedings of the National Academy of Sciences*, 113(3):532–535.
- [Aharonov et al., 2013a] Aharonov, Y., Nussinov, S., Popescu, S., and Vaidman, L.

- (2013a). Peculiar features of entangled states with postselection. *Physical Review A*, 87(1):014105.
- [Aharonov et al., 2013b] Aharonov, Y., Popescu, S., Rohrlich, D., and Skrzypczyk, P. (2013b). Quantum cheshire cats. *New Journal of Physics*, 15(11):113015.
- [Aharonov et al., 2010] Aharonov, Y., Popescu, S., and Tollaksen, J. (2010). A time-symmetric formulation of quantum mechanics. *Physics Today*, 63(11):27–32.
- [Aharonov and Rohrlich, 2008] Aharonov, Y. and Rohrlich, D. (2008). *Quantum paradoxes: quantum theory for the perplexed*. John Wiley & Sons.
- [Aharonov and Vaidman, 1989] Aharonov, Y. and Vaidman, L. (1989). Aharonov and vaidman reply. *Phys. Rev. Lett.*, 62:2327–2327.
- [Aharonov and Vaidman, 1991] Aharonov, Y. and Vaidman, L. (1991). Complete description of a quantum system at a given time. *Journal of Physics A: Mathematical and General*, 24(10):2315.
- [Allen and Eberly, 2012] Allen, L. and Eberly, J. H. (2012). *Optical resonance and two-level atoms*. Courier Corporation.
- [Ananthaswamy, 2014] Ananthaswamy, A. (2014). Lost and found. *New Scientist*, 223(2979):32 – 35.
- [Ashby et al., 2016] Ashby, J. M., Schwarz, P. D., and Schlosshauer, M. (2016). Observation of the quantum paradox of separation of a single photon from one of its properties. *Phys. Rev. A*, 94:012102.
- [Atherton et al., 2015] Atherton, D. P., Ranjit, G., Geraci, A. A., and Weinstein, J. D. (2015). Observation of a classical cheshire cat in an optical interferometer. *Optics letters*, 40(6):879–881.
- [Badurek et al., 2000] Badurek, G., Buchelt, R., Kroupa, G., Baron, M., and Villa, M. (2000). Permanent magnetic field-prism polarizer for perfect crystal neutron interferometers. *Physica B: Condensed Matter*, 283(4):389 – 392.
- [Badurek et al., 1979] Badurek, G., Rauch, H., Wilfing, A., Bonse, U., and Graeff, W. (1979). A perfect-crystal neutron polarizer as an application of magnetic prism refraction. *J. Appl. Cryst.*, 12(2):186–191.

- [Banaszek et al., 2013] Banaszek, K., Horodecki, P., Karpiński, M., and Radzewicz, C. (2013). Quantum mechanical which-way experiment with an internal degree of freedom. *Nature communications*, 4.
- [Bartosik et al., 2009] Bartosik, H., Klepp, J., Schmitzer, C., Sponar, S., Cabello, A., Rauch, H., and Hasegawa, Y. (2009). Experimental test of quantum contextuality in neutron interferometry. *Physical review letters*, 103(4):040403.
- [Basu et al., 2001] Basu, S., Bandyopadhyay, S., Kar, G., and Home, D. (2001). Bell’s inequality for a single spin-1/2 particle and quantum contextuality. *Physics Letters A*, 279(5):281–286.
- [Bliokh et al., 2013] Bliokh, K. Y., Bekshaev, A. Y., Kofman, A. G., and Nori, F. (2013). Photon trajectories, anomalous velocities and weak measurements: a classical interpretation. *New Journal of Physics*, 15(7):073022.
- [Brodtch and Cohen, 2016] Brodtch, A. and Cohen, E. (2016). A scheme for performing strong and weak sequential measurements of non-commuting observables. *Quantum Studies: Mathematics and Foundations*, pages 1–15.
- [Carroll, 1965] Carroll, L. (1965). *Alice’s Adventures In Wonderland*. Penguin Books, London, the annotated alice edition.
- [Clark et al., 2015] Clark, C. W., Barankov, R., Huber, M. G., Arif, M., Cory, D. G., and Pushin, D. A. (2015). Controlling neutron orbital angular momentum. *Nature*, 525(7570):504–506.
- [Cohen-Tannoudji et al., 1977] Cohen-Tannoudji, C., Diu, B., and Laloë, F. (1977). Quantum mechanics.
- [Colella et al., 1975] Colella, R., Overhauser, A. W., and Werner, S. A. (1975). Observation of gravitationally induced quantum interference. *Phys. Rev. Lett.*, 34:1472–1474.
- [Cormann et al., 2016] Cormann, M., Remy, M., Kolaric, B., and Caudano, Y. (2016). Revealing geometric phases in modular and weak values with a quantum eraser. *Phys. Rev. A*, 93:042124.
- [Demtröder, 2013] Demtröder, W. (2013). *Statische Magnetfelder*, pages 83–121. Springer Berlin Heidelberg, Berlin, Heidelberg.

- [Denkmayr, 2013] Denkmayr, T. (2013). Spin and path weak values in neutron optical experiments. Master’s thesis, TU Wien.
- [Denkmayr et al., 2016] Denkmayr, T., Geppert, H., Lemmel, H., Waegell, M., Dressel, J., Hasegawa, Y., and Sponar, S. (2016). Experimental demonstration of direct path state characterization by strongly measuring weak values in a matter-wave interferometer. *arXiv preprint arXiv:1604.04102*.
- [Denkmayr et al., 2014] Denkmayr, T., Geppert, H., Sponar, S., Lemmel, H., Matzkin, A., Tollaksen, J., and Hasegawa, Y. (2014). Observation of a quantum cheshire cat in a matter-wave interferometer experiment. *Nat Commun*, 5.
- [Dixon et al., 2009] Dixon, P. B., Starling, D. J., Jordan, A. N., and Howell, J. C. (2009). Ultrasensitive beam deflection measurement via interferometric weak value amplification. *Physical review letters*, 102(17):173601.
- [Dressel, 2015] Dressel, J. (2015). Weak values as interference phenomena. *Physical Review A*, 91(3):032116.
- [Dressel et al., 2014] Dressel, J., Malik, M., Miatto, F. M., Jordan, A. N., and Boyd, R. W. (2014). Colloquium: Understanding quantum weak values: Basics and applications. *Rev. Mod. Phys.*, 86:307–316.
- [Duck et al., 1989] Duck, I., Stevenson, P., and Sudarshan, E. (1989). The sense in which a” weak measurement” of a spin-1/2 particle’s spin component yields a value 100. *Physical Review D*, 40(6):2112.
- [Englert, 1996] Englert, B.-G. (1996). Fringe visibility and which-way information: An inequality. *Physical review letters*, 77(11):2154.
- [Erdösi et al., 2013] Erdösi, D., Huber, M., Hiesmayr, B. C., and Hasegawa, Y. (2013). Proving the generation of genuine multipartite entanglement in a single-neutron interferometer experiment. *New Journal of Physics*, 15(2):023033.
- [Ferrie and Combes, 2014a] Ferrie, C. and Combes, J. (2014a). How the result of a single coin toss can turn out to be 100 heads. *Physical review letters*, 113(12):120404.
- [Ferrie and Combes, 2014b] Ferrie, C. and Combes, J. (2014b). Weak value amplification is suboptimal for estimation and detection. *Physical review letters*, 112(4):040406.

- [Folger, 2009] Folger, T. (2009). Is quantum mechanics tried, true, wildly successful, and wrong? *Science*, 324(5934):1512–1513.
- [Geppert et al., 2014] Geppert, H., Denkmayr, T., Sponar, S., Lemmel, H., and Hasegawa, Y. (2014). Improvement of the polarized neutron interferometer setup demonstrating violation of a bell-like inequality. *Nuclear Instruments and Methods in Physics Research Section A: Accelerators, Spectrometers, Detectors and Associated Equipment*, 763(0):417 – 423.
- [Goggin et al., 2011] Goggin, M., Almeida, M., Barbieri, M., Lanyon, B., O’Brien, J., White, A., and Pryde, G. (2011). Violation of the leggett–garg inequality with weak measurements of photons. *Proceedings of the National Academy of Sciences*, 108(4):1256–1261.
- [Gross et al., 2015] Gross, J. A., Dangniam, N., Ferrie, C., and Caves, C. M. (2015). Novelty, efficacy, and significance of weak measurements for quantum tomography. *Physical Review A*, 92(6):062133.
- [Guryanova et al., 2012] Guryanova, Y., Brunner, N., and Popescu, S. (2012). The complete quantum cheshire cat. *arXiv preprint arXiv:1203.4215*.
- [Hainbuchner and Jericha, 2001] Hainbuchner, M. and Jericha, E. (2001). Neutron scattering lengths. <http://www.ati.ac.at/~neutropt/scattering/table.html>.
- [Hardy, 1992] Hardy, L. (1992). Quantum mechanics, local realistic theories, and lorentz-invariant realistic theories. *Physical Review Letters*, 68(20):2981.
- [Hasegawa et al., 2003] Hasegawa, Y., Loidl, R., Badurek, G., Baron, M., and Rauch, H. (2003). Violation of a bell-like inequality in single-neutron interferometry. *Nature*, 425(6953):45–48.
- [Hasegawa et al., 2006] Hasegawa, Y., Loidl, R., Badurek, G., Baron, M., and Rauch, H. (2006). Quantum contextuality in a single-neutron optical experiment. *Physical Review Letters*, 97(23):230401.
- [Hasegawa et al., 2010] Hasegawa, Y., Loidl, R., Badurek, G., Durstberger-Rennhofer, K., Sponar, S., and Rauch, H. (2010). Engineering of triply entangled states in a single-neutron system. *Phys. Rev. A*, 81:032121.
- [Hasegawa et al., 2001] Hasegawa, Y., Loidl, R., Baron, M., Badurek, G., and Rauch, H. (2001). Off-diagonal geometric phase in a neutron interferometer experiment. *Physical review letters*, 87(7):070401.

- [Hasegawa and Rauch, 2011] Hasegawa, Y. and Rauch, H. (2011). Quantum phenomena explored with neutrons. *New Journal of Physics*, 13(11):115010.
- [Herstein, 1964] Herstein, I. (1964). *Topics in Algebra*. Blaisdell Publishing Company, Waltham.
- [Hosten and Kwiat, 2008] Hosten, O. and Kwiat, P. (2008). Observation of the spin hall effect of light via weak measurements. *Science*, 319(5864):787–790.
- [Johansen, 2004] Johansen, L. M. (2004). What is the value of an observable between pre-and postselection? *Physics Letters A*, 322(5):298–300.
- [Johansen, 2007] Johansen, L. M. (2007). Reconstructing weak values without weak measurements. *Physics Letters A*, 366(4–5):374 – 376.
- [Jordan et al., 2014] Jordan, A. N., Martínez-Rincón, J., and Howell, J. C. (2014). Technical advantages for weak-value amplification: When less is more. *Phys. Rev. X*, 4:011031.
- [Kastner, 1999] Kastner, R. E. (1999). The three-box “paradox” and other reasons to reject the counterfactual usage of the abl rule. *Foundations of Physics*, 29(6):851–863.
- [Kedem and Vaidman, 2010] Kedem, Y. and Vaidman, L. (2010). Modular values and weak values of quantum observables. *Physical review letters*, 105(23):230401.
- [Kittel, 2004] Kittel, C. (2004). *Introduction to Solid State Physics*. John Wiley and Sons Ltd, 8th edition.
- [Klepp et al., 2014] Klepp, J., Sponar, S., and Hasegawa, Y. (2014). Fundamental phenomena of quantum mechanics explored with neutron interferometers. *Progress of Theoretical and Experimental Physics*, 2014(8):082A01.
- [Knoll, 2010] Knoll, G. F. (2010). *Radiation detection and measurement*. John Wiley & Sons.
- [Kochen and Specker, 1967] Kochen, S. and Specker, E. P. (1967). The problem of hidden variables in quantum mechanics. *J. Math. Mech.*, 17:59.
- [Kocsis et al., 2011] Kocsis, S., Braverman, B., Ravets, S., Stevens, M. J., Mirin, R. P., Shalm, L. K., and Steinberg, A. M. (2011). Observing the average trajectories of single photons in a two-slit interferometer. *Science*, 332(6034):1170–1173.

- [Kroupa et al., 2000] Kroupa, G., Bruckner, G., Bolik, O., Zawisky, M., Hainbuchner, M., Badurek, G., Buchelt, R., Schricker, A., and Rauch, H. (2000). Basic features of the upgraded {S18} neutron interferometer set-up at {ILL}. *Nuclear Instruments and Methods in Physics Research Section A: Accelerators, Spectrometers, Detectors and Associated Equipment*, 440(3):604 – 608.
- [Ku, 1966] Ku, H. (1966). Notes on the use of propagation of error formulas. *Journal of Research of the National Bureau of Standards*, 70(4).
- [Leggett, 1989] Leggett, A. (1989). Comment on “how the result of a measurement of a component of the spin of a spin-(1/2 particle can turn out to be 100”. *Physical review letters*, 62(19):2325.
- [Leifer, 2014] Leifer, M. S. (2014). Is the quantum state real? an extended review of ψ -ontology theorems. *Quanta*, 3(1):67–155.
- [Lemmel, 2014] Lemmel, H. (2014). Das quantengrinsen der cheshire-katze. *Physik in unserer Zeit*, 45(6):266–267.
- [Littrell et al., 1997] Littrell, K. C., Allman, B. E., and Werner, S. A. (1997). Two-wavelength-difference measurement of gravitationally induced quantum interference phases. *Phys. Rev. A*, 56:1767–1780.
- [Lundeen and Steinberg, 2009] Lundeen, J. and Steinberg, A. (2009). Experimental joint weak measurement on a photon pair as a probe of hardy’s paradox. *Physical review letters*, 102(2):020404.
- [Lundeen and Bamber, 2012] Lundeen, J. S. and Bamber, C. (2012). Procedure for direct measurement of general quantum states using weak measurement. *Physical review letters*, 108(7):070402.
- [Lundeen et al., 2011] Lundeen, J. S., Sutherland, B., Patel, A., Stewart, C., and Bamber, C. (2011). Direct measurement of the quantum wavefunction. *Nature*, 474(7350):188–191.
- [Malik et al., 2014] Malik, M., Mirhosseini, M., Lavery, M. P. J., Leach, J., Padgett, M. J., and Boyd, R. W. (2014). Direct measurement of a 27-dimensional orbital-angular-momentum state vector. *Nat Commun*, 5.
- [Mermin, 1990] Mermin, N. D. (1990). Simple unified form for the major no-hidden-variables theorems. *Phys. Rev. Lett.*, 65:3373–3376.

- [Mezei, 1972] Mezei, F. (1972). Neutron spin echo: A new concept in polarized thermal neutron techniques. *Zeitschrift für Physik*, 255(2):146–160.
- [Mezei, 1976] Mezei, F. (1976). Novel polarized neutron devices: supermirror and spin component amplifier. *Communications on Physics (London)*, 1(3):81–85.
- [Michielsen et al., 2015] Michielsen, K., Lippert, T., and De Raedt, H. (2015). Mysterious quantum cheshire cat: an illusion. In *SPIE Optical Engineering+ Applications*, pages 95700O–95700O. International Society for Optics and Photonics.
- [Mirhosseini et al., 2014] Mirhosseini, M., Magaña Loaiza, O. S., Hashemi Rafsanjani, S. M., and Boyd, R. W. (2014). Compressive direct measurement of the quantum wave function. *Phys. Rev. Lett.*, 113:090402.
- [Piacentini et al., 2015] Piacentini, F., Levi, M., Avella, A., Cohen, E., Lussana, R., Villa, F., Tosi, A., Zappa, F., Gramegna, M., Brida, G., et al. (2015). Measuring incompatible observables of a single photon. *arXiv preprint arXiv:1508.03220*.
- [Popescu, 2010] Popescu, S. (2010). Dynamical quantum non-locality. *Nature Physics*, 6(3):151–153.
- [Pryde et al., 2005] Pryde, G., O’Brien, J., White, A., Ralph, T., and Wiseman, H. M. (2005). Measurement of quantum weak values of photon polarization. *Physical review letters*, 94(22):220405.
- [Pusey, 2014] Pusey, M. F. (2014). Anomalous weak values are proofs of contextuality. *Physical review letters*, 113(20):200401.
- [Rauch et al., 2002] Rauch, H., Lemmel, H., Baron, M., and Loidl, R. (2002). Measurement of a confinement induced neutron phase. *Nature*, 417(6889):630–632.
- [Rauch and Suda, 1974] Rauch, H. and Suda, M. (1974). Intensitätsberechnung für ein neutronen-interferometer. *physica status solidi (a)*, 25(2):495–505.
- [Rauch et al., 1974] Rauch, H., Treimer, W., and Bonse, U. (1974). Test of a single crystal neutron interferometer. *Physics Letters A*, 47(5):369 – 371.
- [Rauch and Werner, 2015] Rauch, H. and Werner, S. A. (2015). *Neutron Interferometry: Lessons in Experimental Quantum Mechanics, Wave-Particle Duality, and Entanglement*. Oxford University Press, USA.

- [Rauch et al., 1975] Rauch, H., Zeilinger, A., Badurek, G., Wilfing, A., Bauspiess, W., and Bonse, U. (1975). Verification of coherent spinor rotation of fermions. *Physics Letters A*, 54(6):425 – 427.
- [Resch et al., 2004] Resch, K., Lundeen, J., and Steinberg, A. (2004). Experimental realization of the quantum box problem. *Physics Letters A*, 324(2–3):125 – 131.
- [Ritchie et al., 1991] Ritchie, N., Story, J., and Hulet, R. G. (1991). Realization of a measurement of a “weak value”. *Physical review letters*, 66(9):1107.
- [Romito et al., 2016] Romito, A., Jordan, A. N., Aharonov, Y., and Gefen, Y. (2016). Weak values are quantum: you can bet on it. *Quantum Studies: Mathematics and Foundations*, 3(1):1–4.
- [Sakurai and Napolitano, 2011] Sakurai, J. J. and Napolitano, J. (2011). *Modern quantum mechanics*. Addison-Wesley.
- [Salvail et al., 2013] Salvail, J. Z., Agnew, M., Johnson, A. S., Bolduc, E., Leach, J., and Boyd, R. W. (2013). Full characterization of polarization states of light via direct measurement. *Nat Photon*, 7(4):316–321.
- [Schärpf, 1980] Schärpf, O. (1980). *The polarised neutron technique of neutron spin echo*, pages 27–52. Springer Berlin Heidelberg, Berlin, Heidelberg.
- [Schuster et al., 1990] Schuster, M., Rauch, H., Seidl, E., Jericha, E., and Carlile, C. (1990). Test of a perfect crystal neutron storage device. *Physics Letters A*, 144(6):297 – 300.
- [Sears, 1989a] Sears, V. F. (1989a). *Neutron optics: an introduction to the theory of neutron optical phenomena and their applications*, volume 3, chapter 7.1 Two-beam interferometers, pages 219–225. Oxford University Press, USA.
- [Sears, 1989b] Sears, V. F. (1989b). *Neutron optics: an introduction to the theory of neutron optical phenomena and their applications*, volume 3, chapter 7.2 Perfect-crystal neutron interferometer, pages 225–231. Oxford University Press, USA.
- [Sears, 1989c] Sears, V. F. (1989c). *Neutron optics: an introduction to the theory of neutron optical phenomena and their applications*, volume 3, chapter 3.2 Transmission, pages 75–78. Oxford University Press, USA.
- [Sears, 1989d] Sears, V. F. (1989d). *Neutron optics: an introduction to the theory of neutron optical phenomena and their applications*, volume 3, chapter 7.5 Multiple-beam interference, pages 252–258. Oxford University Press, USA.

- [Sokolovski, 2015] Sokolovski, D. (2015). The meaning of “anomalous weak values” in quantum and classical theories. *Physics Letters A*, 379(16):1097–1101.
- [Sponar et al., 2016] Sponar, S., Denkmayr, T., Geppert, H., and Hasegawa, Y. (2016). Fundamental features of quantum dynamics studied in matter-wave interferometry—spin weak values and the quantum cheshire-cat. *Atoms*, 4(1):11.
- [Sponar et al., 2015] Sponar, S., Denkmayr, T., Geppert, H., Lemmel, H., Matzkin, A., Tollaksen, J., and Hasegawa, Y. (2015). Weak values obtained in matter-wave interferometry. *Physical Review A*, 92(6):062121.
- [Sponar et al., 2008] Sponar, S., Klepp, J., Loidl, R., Filipp, S., Badurek, G., Hasegawa, Y., and Rauch, H. (2008). Coherent energy manipulation in single-neutron interferometry. *Physical Review A*, 78(6):061604.
- [Sponar et al., 2010] Sponar, S., Klepp, J., Loidl, R., Filipp, S., Durstberger-Rennhofer, K., Bertlmann, R. A., Badurek, G., Rauch, H., and Hasegawa, Y. (2010). Geometric phase in entangled systems: A single-neutron interferometer experiment. *Phys. Rev. A*, 81:042113.
- [Suda, 2005] Suda, M. (2005). *Quantum interferometry in phase space: theory and applications*. Springer Science & Business Media.
- [Summhammer et al., 1983] Summhammer, J., Badurek, G., Rauch, H., Kischko, U., and Zeilinger, A. (1983). Direct observation of fermion spin superposition by neutron interferometry. *Phys. Rev. A*, 27:2523–2532.
- [Summhammer et al., 1987] Summhammer, J., Rauch, H., and Tuppinger, D. (1987). Stochastic and deterministic absorption in neutron-interference experiments. *Physical Review A*, 36(9):4447.
- [Svensson, 2013] Svensson, B. E. Y. (2013). What is a quantum-mechanical “weak value” the value of? *Foundations of Physics*, 43(10):1193–1205.
- [Utsuro and Ignatovich, 2010] Utsuro, M. and Ignatovich, V. K. (2010). *Handbook of neutron optics*. John Wiley & Sons.
- [Vallone and Dequal, 2016] Vallone, G. and Dequal, D. (2016). Strong measurements give a better direct measurement of the quantum wave function. *Physical review letters*, 116(4):040502.

- [von Neumann, 1932] von Neumann, J. (1932). *Mathematische Grundlagen der Quantenmechanik*. Springer Berlin.
- [Waegell and Tollaksen, 2015] Waegell, M. and Tollaksen, J. (2015). Contextuality, pigeonholes, cheshire cats, mean kings, and weak values. *arXiv preprint arXiv:1505.00098*.
- [Wagh et al., 1997] Wagh, A. G., Rakhecha, V. C., Summhammer, J., Badurek, G., Weinfurter, H., Allman, B. E., Kaiser, H., Hamacher, K., Jacobson, D. L., and Werner, S. A. (1997). Experimental separation of geometric and dynamical phases using neutron interferometry. *Phys. Rev. Lett.*, 78:755–759.
- [Werner et al., 1975] Werner, S. A., Colella, R., Overhauser, A. W., and Eagen, C. F. (1975). Observation of the phase shift of a neutron due to precession in a magnetic field. *Phys. Rev. Lett.*, 35:1053–1055.
- [Williams and Jordan, 2008] Williams, N. S. and Jordan, A. N. (2008). Weak values and the leggett-garg inequality in solid-state qubits. *Phys. Rev. Lett.*, 100:026804.
- [Wootters and Fields, 1989] Wootters, W. K. and Fields, B. D. (1989). Optimal state-determination by mutually unbiased measurements. *Annals of Physics*, 191(2):363 – 381.
- [Wu, 2013] Wu, S. (2013). State tomography via weak measurements. *Scientific reports*, 3.
- [Yokota et al., 2009] Yokota, K., Yamamoto, T., Koashi, M., and Imoto, N. (2009). Direct observation of hardy’s paradox by joint weak measurement with an entangled photon pair. *New Journal of Physics*, 11(3):033011.
- [Yurke et al., 1986] Yurke, B., McCall, S. L., and Klauder, J. R. (1986). $Su(2)$ and $su(1,1)$ interferometers. *Phys. Rev. A*, 33:4033–4054.
- [Zeilinger, 1981] Zeilinger, A. (1981). General properties of lossless beam splitters in interferometry. *American Journal of Physics*, 49(9):882–883.
- [Zhang et al., 2016] Zhang, Y.-X., Wu, S., and Chen, Z.-B. (2016). Coupling-deformed pointer observables and weak values. *Physical Review A*, 93(3):032128.

Curriculum Vitae

TOBIAS DENKMAYR

Address

Habichergasse 19/28
1160 Wien
Austria

Phone: +43-664-88583168
Email: tobias.denkmayr@gmail.com

Personal details

Gender: Male
Date of birth: 14th of March, 1988
Place of birth: Braunau am Inn, Austria
Present Citizenship: Austria
Children: Samuel Tobias Denkmayr (*17. April 2016)

Education

2013–2016 TU Wien
– Doctor of Engineering Sciences in Physics, 2016

2010–2013 TU Wien

- Master of Science, 2013
- Physics major with distinction

2007–2010 TU Wien

- Bachelor of Science, 2010
- Physics major with distinction

2002–2006 Gymnasium Ried im Innkreis High School

- Graduation (Matura) with distinction, 2006

Work experience

2013–2016 Project assistant at the Institute of Atomic and Subatomic Physics

- Assistance in a project of the Austrian Science Fund (FWF)

2005–2016 Part-time paramedic for the Red Cross Upper Austria

- Executed pre-hospital emergency medical services
- Attained teaching qualification for technical rescue
- Special training in radiation protection
- One year of full time employment (including alternative service)

2010 Tutor at the Institute of Solid State Physics, TU Wien

- Taught freshmen physics students
- Oversaw and corrected tests

Honors and achievements

2015-2016 TUtheTOP

- Participation in the High Potential Program of TU Wien

2012 ERASMUS Student Mobility Scholarship for Placements

- Research internship at the Munich University of Technology

2011 American European Exchange in Engineering, Joint Study Scholarship

- Exchange semester at the University of Tulsa, OK
- GPA of 4.0
- Mention on the university's honor roll

2010 Academic Excellence Scholarship

- Granted to honor extraordinary academic achievements

Languages

- ▷ German (First language)
- ▷ English (Fluent; TOEFL internet based test score: 111)
- ▷ Italian (Working knowledge)
- ▷ Latin

List of publications (peer reviewed)

Related to this thesis

- ▷ Denkmayr, T., Geppert, H., Sponar, S., Lemmel, H., Waegell, M., Dressel, J. & Hasegawa, Y. Experimental demonstration of direct path state characterization by strongly measuring weak values in a matter-wave interferometer. *arXiv*, 1604.04102 (2016)
- ▷ Sponar, S., Denkmayr, T., Geppert, H., Lemmel, H., Matzkin, A., Tollaksen, J. & Hasegawa, Y. Weak values obtained in matter-wave interferometry. *Phys. Rev. A* **92**, 062121 (2015)
- ▷ Denkmayr, T., Geppert, H., Sponar, S., Lemmel, H., Matzkin, A., Tollaksen, J. & Hasegawa, Y. Observation of a quantum Cheshire Cat in a matter-wave interferometer experiment. *Nat. Comm.* **5**, 4492 (2014)

Others

- ▷ Sponar, S., Denkmayr, T., Geppert, H. & Hasegawa, Y. Fundamental Features of Quantum Dynamics Studied in Matter-Wave Interferometry – Spin Weak Values and the Quantum Cheshire-Cat. *Atoms* **4**, 11 (2016)
- ▷ Geppert, H., Denkmayr, T., Sponar, S., Lemmel, H. & Hasegawa, Y. Improvement of the polarized neutron interferometer setup demonstrating violation of a Bell-like inequality. *Nucl. Instrum. Meth. A* **763**, 417–423 (2014)